NUMERICAL INVESTIGATION OF THE GAS/SPRAY JET INTERACTION WITH FLUIDIZED BEDS

by

Tingwen Li

B.Sc., Peking University, 2001

M.Sc., Peking University, 2004

A THESIS SUBMITTED IN PARTIAL FULFILLMENT OF

THE REQUIREMENTS FOR THE DEGREE OF

DOCTOR OF PHILOSOPHY

in

The Faculty of Graduate Studies

(Mechanical Engineering)

THE UNIVERSITY OF BRITISH COLUMBIA

(Vancouver)

March, 2009

ABSTRACT

In many industrial fluidized bed reactors, for example fluid catalytic cracking units, coaters and fluid cokers, the reactant feed is introduced into the system in the form of a gas jet or spray for different purposes. A good understanding of the interaction between the feed injection and the bed can lead to improved reactor design and operation. Despite the fact that numerical models and simulations have been used extensively to investigate fluidization processes, still little is known about the interactions of the jet/spray with fluidized beds.

In this thesis, gas jets and liquid spray in several gas-solid systems are numerically studied. The Eulerian-Eulerian multi-fluid model with appropriate closure correlations is employed, and two- and three-dimensional numerical simulations are performed accordingly. The numerical simulations can be divided into two groups: two-phase (gas-solid) and three-phase (gas-liquid-solid) simulations. First, a three-dimensional numerical simulation of a single gas jet injection in a cylindrical bubbling fluidized bed is performed and is compared favorably to available experimental data and empirical correlations. After that, the injection of multiple gas jets into a small bubbling fluidized bed is numerically investigated. The influence of the secondary gas injection on the flow hydrodynamics, as well as interactions between the gas jet and the surrounding gas, solids, bubbles, and other jets is studied numerically, and the mixing of the secondary gas with the bed materials is also analyzed. To study the liquid spray in gas-solid systems, several three-phase systems of the low-flow-rate bottom spray into a flat-based spouted bed with a draft tube (DTSB), an evaporating gas-liquid spray into a uniform gas-solid crossflow, and an evaporative water spray into a hot riser are simulated, respectively. Appropriate models are chosen to describe the interactions between spray droplets and particles, as well as the inter-phase heat and mass transfer. While implementing the models in the numerical code, careful comparison with the available experimental data is performed. General features of the

spray are properly predicted, and the interaction of the liquid spray with the gas-solid flows is investigated.

TABLE OF CONTENTS

LIST OF TABLES

LIST OF FIGURES

NOMENCLATURE

A_{drop}	surface area of droplet	m^2
$B^b(l;\vec{x},t)$	volumetric birth rate of droplet due to breakup	$(m^3\text{-}s)^{-1}$
$B^c(l;\vec{x},t)$	volumetric birth rate of droplet due to coalescence	$(m^3\text{-}s)^{-1}$
B_M	Spalding mass transfer number	-
C	scale factor	-
C	tracer concentration	%volume
C_0	tracer gas concentration defined in equation (4.10)	%volume
C_1, C_2	model constants of $k-\varepsilon$ turbulence model	-
C_k	dimensionless number defined in equation (6.16)	-
C_p	specific heat	J/kg-K
C_μ	model constant of $k-\varepsilon$ turbulence model	-
d_l	droplet diameter	m
$d_{l,inlet}$	droplet diameter at spray inlet	m
d_p	particle diameter	m
$d_{p,d}$	dry particle diameter	m
$d_{v,90}$	droplet diameter	m
$D^b(l;\vec{x},t)$	death rate of droplet due to breakup	$(m^3\text{-}s)^{-1}$
$D^c(l;\vec{x},t)$	death rate of droplet due to coalescence	$(m^3\text{-}s)^{-1}$
D_j	nozzle diameter	m

$D_{l,t}$	turbulent dispersion coefficient of liquid	m^2/s
D_p	self-diffusion coefficient of particles	m^2/s
$\bar{\bar{D}}_p$	rate of deformation tensor	s^{-1}
D_v	binary diffusivity of vapour in gas phase	m^2/s
erf	error function	-
e_{lp}	coefficient of restitution for droplet-particle collision	-
e_p	coefficient of restitution for particle collision	-
E	energy	J
$E(t)$	exit age distribution	s^{-1}
f	volume fraction of agglomerates in dense phase	-
f_{lp}	frequency of collisions per unit volume	$(m^3\text{-}s)^{-1}$
$F(t)$	cumulative distribution function	-
g	gravitational acceleration	m/s^2
$g_{0,p}$	radial distribution function	-
G	production of turbulent kinetic energy	$kg/m\text{-}s^3$
G	droplet growth rate based on diameter	m/s
G_V	droplet volume growth rate	m^3/s
h	gap height	m
h_g	gas specific enthalpy	J/kg
h_p	solid specific enthalpy	J/kg
h_{total}	total enthalpy	J/kg
$\hbar_{drop}$	heat transfer coefficient for single droplet	$W/m^2\text{-}K$

$\hbar_{gl}$	volumetric heat transfer coefficient between gas and liquid	W/m^3-K
$\hbar_{gp}$	volumetric heat transfer coefficient between gas and solid	W/m^3-K
$\hbar_{pl}$	volumetric heat transfer coefficient between liquid and solid	W/m^3-K
H	bed height	m
H_0	static bed height	m
H_g	energy transfer to gas phase due to phase change	W/m^3
H_p	energy transfer to solid phase due to phase change	W/m^3
I_{2D}	second invariant of $\overline{\overline{D}}_p$	s^{-2}
I_g	momentum transfer to gas phase due to phase change	kg/m^2-s^2
I_l	momentum transfer to liquid phase due to phase change	kg/m^2-s^2
I_p	momentum transfer to solid phase due to phase change	kg/m^2-s^2
k	turbulent kinetic energy of gas phase	J/kg
k_g	thermal conductivity of gas	W/m-K
k_{gl}	covariance of the velocities of gas phase and droplet phase	J/kg
k_l	turbulent kinetic energy of liquid phase	J/kg
l	diameter	m
L	latent heat	J/kg
L_j	jet penetration length	m
$L_{S,l}$	surface area concentration of liquid	m^{-1}
m_l	mass of droplet	kg
$\dot{m}_l$	rate of droplet evaporation	kg/s

M_g	molecular weight of gas	g/mol
M_l	molecular weight of liquid	g/mol
M_{gp}	gas-solid momentum exchange rate	kg/m^2-s^2
M_{lg}	liquid-gas momentum exchange rate	kg/m^2-s^2
M_{lp}	liquid-solid momentum exchange rate	kg/m^2-s^2
M_{pg}	solid-gas momentum exchange rate	kg/m^2-s^2
M_{pl}	solid-liquid momentum exchange rate	kg/m^2-s^2
$n(l;\vec{x},t)$	droplet number density function	m^{-3}
n_l	number density of droplet	m^{-3}
n_p	number density of particle	m^{-3}
N_{lp}	number of collisions per second in unit volume	(m^3-s)$^{-1}$
Nu_{drop}	Nusselt number for droplet	-
Nu_{part}	Nusselt number for particle	-
P	pressure	Pa
P_{Fs}	vapour pressure at drop surface	Pa
$P_{s,fric}$	solid frictional pressure	Pa
$P_{s,vis}$	solid pressure based on kinetic granular theory	Pa
Pr_g	Prandtl number	-
q_g	mass transfer rate to gas	kg/m^3-s
$\vec{q}_g$	heat flux of gas phase	W/m^2
q_l	mass transfer rate to liquid	kg/m^3-s

$q_{lg,drop}$	mass transfer rate from liquid to gas	kg/m^3-s
q_p	mass transfer rate to solid	kg/m^3-s
$\vec{q}_p$	heat flux of solid phase	W/m^2
Q_g	total gas flow rate	m^3/s
Q_{spray}	spray volume flow rate	m^3/s
Q_{tracer}	volumetric flow rate of tracer gas	m^3/s
Q_{gp}	heat transfer between gas and solid phase	W/m^3
Q_{pg}	heat transfer between solid and gas phase	W/m^3
r_l	droplet radius	m
R	universal gas constant	J/K-mol
Re	Reynolds number	-
Re_l	droplet Reynolds number	-
Re_p	particle Reynolds number	-
Re_l^*	effective Reynolds number	-
Re_t	terminal Reynolds number	-
$S(l;\vec{x},t)$	source term in population balance model	(m^3-s)$^{-1}$
Sc	Schmidt number	-
Sh	Sherwood number	-
$\overline{\overline{S}}_p$	deviator tensor of strain rate	s^{-1}
t	time	s
T_g	gas temperature	K
T_l	liquid temperature	K

T_p	solid temperature	K
T_{ref}	reference temperature	K
u_{crit}	critical impact velocity	m/s
u_{slip}	slip velocity	m/s
u_{spray}	liquid spray velocity	m/s
u_t	terminal velocity	m/s
U_g	fluidizing gas velocity	m/s
U_j	jet velocity	m/s
$U_{j,g}$	gas velocity in particle-laden jet	m/s
$U_{j,p}$	particle velocity in particle-laden jet	m/s
U_{mb}	minimum bubbling velocity	m/s
U_{mf}	minimum fluidization velocity	m/s
U_p	primary superficial gas velocity	m/s
$\vec{v}_{l,dr}$	drift velocity of droplet	m/s
V	volume	m^3
$\vec{V}_g$	velocity of gas phase	m/s
$\vec{V}_l$	velocity of liquid phase	m/s
$\vec{V}_{lp,R}$	relative velocity between droplets and particles	m/s
$\vec{V}_p$	velocity of solid phase	m/s
W	bed loading	kg
We	Weber number	-

y	error function parameter	-
X , Y	Cartesian coordinates	m
Y	vapour mass fraction in free stream	-
Y_s	vapour mass fraction at droplet surface	-
z	axial distance above distributor	m
Z	coordinate	m

Greeks

α_g	gas volume fraction	-
α_l	liquid volume fraction	-
α_p	solid volume fraction	-
$\alpha_{p,l}$	volume fractions of liquid adhering to particles	-
$\alpha_{p,loosepack}$	volume fraction of particles at loosely packing state	-
$\alpha_{p,\min}$	solid volume fraction to activate frictional model	-
$\alpha_{p,\max}$	maximum solid volume fraction	-
β_{gp}	gas-solid drag coefficient	kg/m^3-s
β_{gl}	gas-liquid drag coefficient	kg/m^3-s
β_{lp}	liquid-solid drag coefficient	kg/m^3-s
ε	voidage	-
ε	dissipation rate of gas phase turbulent kinetic energy	m^2/s^3
ε_0	initial bed voidage	-
ε_a	volume fraction of agglomerates	-
ε_e	volume fraction of emulsion	-

ε_g	volume fraction of gas	-
ε_{mf}	bed voidage at minimum fluidization	-
ε_{mb}	bed voidage at minimum bubbling fluidization	-
ϕ	internal angle of friction	degree
ϕ	lump number	-
ϕ_b, ϕ_c, ϕ_v	source terms in equation (6.42)	$(m\text{-}s)^{-1}$
ϕ_{gp}	granular energy exchange between gas and solid phase	$J/m^3\text{-}s$
ϕ_w	specularity coefficient	-
φ	lump parameter in equation (7.2)	-
φ	adhesion efficiency	-
γ	particles collection efficiency	-
γ_Θ	dissipation of granular energy	$J/m^3\text{-}s$
$\kappa_{p,\Theta}$	diffusion coefficient for granular energy	kg/m-s
λ_{fric}	solid frictional bulk viscosity	Pa-s
λ_p	solid bulk viscosity	Pa-s
μ_g	gas viscosity	Pa-s
$\mu_{g,t}$	turbulent viscosity of gas	Pa-s
μ_{fric}	solid frictional viscosity	Pa-s
μ_l	liquid viscosity	Pa-s
μ_p	solid shear viscosity	Pa-s
θ	jet expansion angle	degree

θ_{lp}	contact angle	degree
Θ_p	granular temperature	J/kg
ρ_g	fluidizing gas density	kg/m^3
ρ_j	jetting gas density	kg/m^3
ρ_p	particle density	kg/m^3
ρ_{vapor}	vapour density	kg/m^3
σ	standard deviation of residence time	s
σ	surface tension	N/m
σ_k	model constant of $k-\varepsilon$ turbulence model	-
$\bar{\bar{\sigma}}_p$	solid stress tensor	Pa
$\bar{\bar{\sigma}}_{p,fric}$	solid frictional stress	Pa
$\bar{\bar{\sigma}}_{p,vis}$	solid stress tensor based on granular kinetic theory	Pa
σ_ε	model constant of $k-\varepsilon$ turbulence model	-
τ	residence time	s
$\bar{\bar{\tau}}_{g,\text{eff}}$	gas stress tensor	Pa
$\tau_{g,t}$	characteristic time of large turbulent eddies of gas phase	s
$\bar{\bar{\tau}}_l$	liquid stress tensor	Pa
$\tau_{l,F}$	droplet response time	s
$\tau_{l,t}^0$	fluid Lagrangian integral time scale	s
τ_L	Lagrangian time scale	s
$\bar{\bar{\tau}}_{p,vis}$	solid stress tensor based on granular kinetic theory	Pa

Subscript

g	gas phase
i	bin number
j	jet
l	liquid/droplet phase
p	particle/solid phase
s	particle/solid phase

Abbreviations

BC	boundary condition
CFB	circulating fluidized bed
CFD	computational fluid dynamics
DEM	discrete element method
DPM	discrete particle model
DTSB	spouted bed with a draft tube
FBR	fluidized bed reactor
FCC	fluid catalytic cracking
MFIX	Multiphase Flow with Interphase eXchanges
NETL	National Energy Technology Laboratory
PISO	Pressure Implicit with Split Operator
RTD	residence time distribution
SGS	sub-grid scale
TFM	two-fluid model
UBC	University of British Columbia
UDF	user-defined functions
UDS	user-defined scalar

ACKNOWLEDGEMENTS

I would like to thank all those great people who have given me support to make this work possible.

I would like to thank my outstanding supervisor, Dr. Martha Salcudean for all her gracious support, warm encouragement and timely guidance throughout the course of my Ph.D. work. It was a great honor to work under her supervision. I would also like to thank my co-supervisor, Dr. Dana Grecov, for her guidance and help.

I would like to thank my research committee members, Dr. Sheldon Green and Dr. John Grace, for their advice and helpful suggestions.

I would also like to thank all my colleagues at UBC. In particular, thanks to Konstantin Pougatch for sharing his code and experience, and his suggestions and constructive criticisms. Thanks to Xiaosi Feng, Yaoguo Fan, Kai Liu, Pirooz Darabi, Sara Hormozi for their help and friendship. I owe much thanks to Maureen Phillips for carefully reviewing the manuscript and making the text more readable.

I would like to express my endless gratitude to my parents for their constant support and dedication to my education. I also would like to give the thanks to my brother and sisters for their support. Finally, I thank my wife, Yue Su, for her love, understanding and encouragement.

To my parents

Chapter 1. INTRODUCTION

In this chapter, an introduction of some basic concepts of fluidization is presented first. After that, a comprehensive literature review of previous research on jet and fluidized bed interaction is conducted. Then, several typical industrial applications of gas/liquid jet in fluidized beds are described briefly. Finally, the research objectives and thesis structure are outlined.

1.1 BASIC CONCEPTS OF FLUIDIZATION

1.1.1 Fluidized bed reactor

A Fluidized Bed Reactor (FBR) is a type of reactor that can be used to carry out a variety of multiphase chemical reactions. In this type of reactor, a fluid is passed through a granular solid material at high enough velocities to suspend the solid and cause it to behave as a fluid. This process, known as fluidization, imparts many important advantages, such as excellent gas-solid contact, and superior mass and heat transfer characteristics. Because of this, fluidized bed reactors are among the most important reactors in the process industries.

Fluidized bed reactors are a relatively new tool in the industrial engineering field. In the 1920s, a fluidized bed gas generator was developed by Fritz Winkler in Germany which represented the first large-scale, commercially significant use of the fluidized bed (Kunii and Levenspiel, 1991). The fluidized bed reactor was first introduced into the petroleum industry through the fluid catalytic cracking (FCC) process by the Standard Oil Company of New Jersey (now ExxonMobil) in 1942. The FCC process, which converted heavy petroleum into gasoline, reduced waste and increased flexibility, provided greater control over the mix of fuels and chemicals produced by refineries. It was an economical means of producing more gasoline, the product in most demand. Continual efforts were made to improve the process and successive modifications led to the

construction of new plants. By 1945, there were 34 cracking units online which were producing 240,000 barrels per day - roughly 45% of US production (Kunii and Levenspiel, 1991). The initial FBR successes spawned much interest in fluidization, and a variety of new processes and applications have been developed. Nowadays, fluidized beds are widely used in many industrial applications, such as the metallurgical, pharmaceutical, food, chemical and petrochemical industries as well as coal combustion, paper making etc. In the following paragraphs, the fundamentals of fluidized bed are briefly reviewed.

1.1.2 Geldart's classification of powders

The fluidization phenomena of gas–solid systems depend on the type of powders employed. By employing the fluidization data obtained at ambient condition, Geldart (1972) was the first to classify particles into four groups (groups A, B, C and D) in terms of the density difference between the particles and the fluidizing medium, and the mean particle size. The widely used particle's classification proposed by Geldart is shown in Figure 1-1.

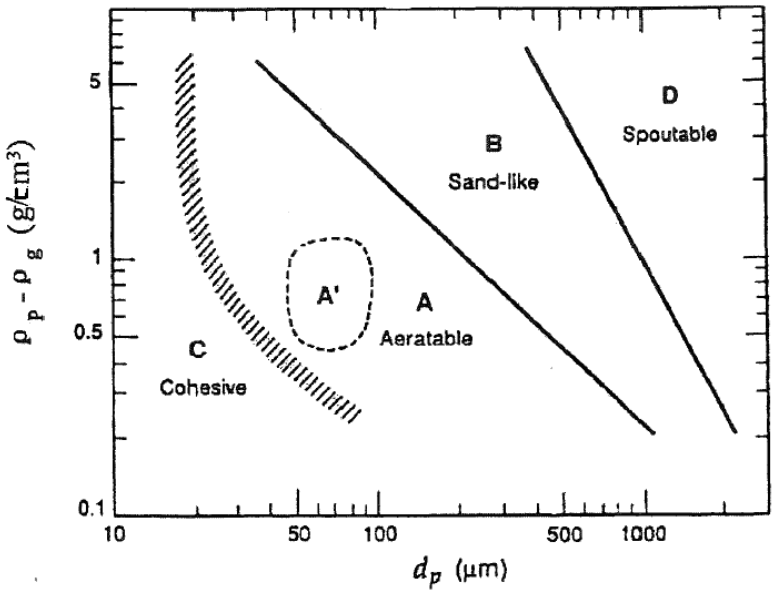

Figure 1-1. Diagram of Geldart's classification of powders. (Adapted from Kunii and Levenspiel, 1991)

As shown in the diagram, very fine particles (usually <30 μm) belonging to group C, are very cohesive and difficult to fluidize. Particles with a size in the range of 20~100 μm and a density of less than about 1400 kg/m^3 belong to group A, which manifests smooth expansion over a range of fluidizing gas velocities before bubbling begins. Group B particles are generally within the size range of 40~500 μm and the density range of 1400~4500 kg/m^3. For group B particles, free bubbling occurs immediately when the bed is fluidized. Group D particles are of greater size and density than other groups. Hence, they require higher gas velocities to fluidize the bed. When the gas velocity is high and the gas is admitted only through a centrally positioned hole, group D particles can be made to spout. In addition, the bubble rising velocity is smaller than the interstitial velocity of the gas in the dense phase, which leads to a different mixing pattern in the bed from that observed in the beds of group A or B particles.

Geldart's classification of powders is not applicable at elevated pressure and temperature or for beds fluidized by a medium other than air. To develop a generalized powder classification, several criteria have been proposed in literature which are not presented here (Molerus, 1982; Grace, 1986; Goossens, 1998; Yang, 2007).

1.1.3 Fluidization regimes

When gas is introduced from the gas distributor at the bottom of the bed, several fluidization regimes can be observed as the gas flow rate increases from zero. The typical regimes are packed bed, bubbling fluidization, slugging fluidization, turbulent fluidization, fast fluidization and dilute pneumatic conveying regimes as shown in Figure 1-2 (Grace, 1986). Among them, the bubbling fluidization regime is one of the most studied in gas-solid fluidization, which has been dealt with in numerous books and papers. The transitions between different fluidization regimes are often not sharp. Different criteria have been proposed to define the transition velocities to distinguish different fluidization regimes (Howard, 1989; Bi et al., 2000; Smolders and Baeyens,

2001). For groups C and D particles, channelling and spouting patterns are often observed, not shown in the figure.

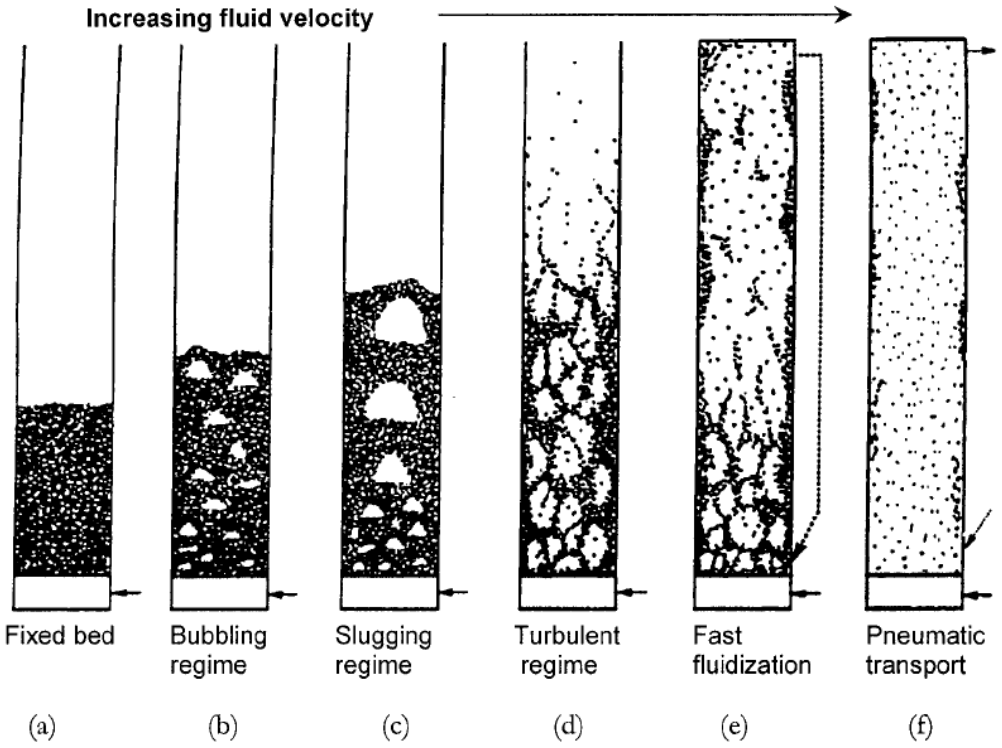

Figure 1-2. Diagram of gas-solid fluidization regimes. (Adapted from Grace, 1986)

1.2 LITERATURE REVIEW OF JETS IN FLUIDIZED BEDS

In fluidized beds, gas jets form at the distributor or from tubes inserted into the beds. Gas jets introduced through the distributor orifices or upward nozzles have been studied extensively (Merry, 1975; Yang and Keairns, 1979; Filla et al., 1983; Grace and Lim, 1987; Cleaver et al., 1995; Vaccaro, 1997; Vaccaro et al., 1997; Musmarra, 2000; Hong et al., 2003; Zhang et al., 2004). In the current research, we focus mainly on horizontal gas jets and two-phase jet/spray in fluidized beds. A literature survey in related fields is conducted and some work is reviewed here.

1.2.1 Horizontal gas jets in fluidized beds

In industrial fluidized bed reactors, reactant gases are often introduced from lateral nozzles at a certain height above the distributor plate for different purposes: to supplement the reactant, enhance mixing, stimulate solids flow, control NO_x emission and temperature, or maintain the reacting mixture outside explosion limits (Rajan and Christoff, 1982; Varol and Atimtay, 2007). Understanding the hydrodynamics of the gas and solids movements resulting from the introduction of gas jets can have considerable significance in improving reactor design and process optimization.

There is a voluminous literature dealing with the horizontal injection of gas jets into fluidized beds (Shakhova, 1968; Zenz, 1968; Merry, 1971; Rajan and Christoff, 1982; Xuereb et al., 1991a; Xuereb et al., 1991b; Chyang et al., 1997; Hong et al., 1997; Copan et al., 2001; Al Sherehy, 2002; Donald et al., 2004). A brief summary of these experimental studies is presented in Table 1-1.

Merry (1971) measured the penetration length of horizontal air jets into fluidized beds of sand, kale seed and steel shot, under atmospheric conditions. Different nozzle diameters (2.54 to 14.3 mm) and jet velocities (40 to 300 m/s) were used. A semi-theoretical expression for predicting the jet penetration length, which correlated a wide range of data reasonably well, was derived.

Rajan and Christoff (1982) investigated the solids circulation and mixing patterns produced by a horizontal jet stream penetrating into a bench-scale fluidized-bed combustor. It was reported that the presence of a horizontal air jet markedly influenced the solids circulation pattern in the fluidized bed.

Xuereb et al. (1991a) carried out experiments to study the behaviour of horizontal or inclined jets in a two-dimensional bed. The interactions between the jet and the bubbles resulting from the

fluidization, as well as the inherent fluctuations of the jet were examined by a cinematographic technique. The values of morphological parameters characterizing the jet, including penetration length and expansion angle, were measured from photographs and movies for inclined and horizontal jets. The effects of the fluidization velocity, gas injection velocity, and particle diameter were studied in these configurations. Xuereb et al. (1991b) also measured local gas velocities in a horizontal jet with a Pitot-tube. The gas velocity radial profiles were reported to be asymmetric with a tendency for the jet to deviate upward.

Chen and Weinstein (1993) studied the shape and extent of the void area formed by a horizontal jet in a rectangular fluidized bed with an X-ray system. Their experimental observations showed the horizontal jet formed three regions in the fluidized bed: a coherent void, i.e. the jet, bubble trains, and a surrounding compaction zone.

Chyang et al. (1997) conducted studies of the gas discharge modes including bubbling and jetting at a single horizontal nozzle in a two-dimensional gas fluidized bed by visual observation. When gas was injected into the fluidized bed from a horizontal nozzle, a chain of bubbles or a permanent jet plume with bubbles would form in the bed, which mainly depended on the material properties, bed configuration, and operating conditions. In their studies, gas discharge modes were analyzed by high-speed cine photography, and the effects of nozzle diameter, gas velocity through the nozzle, particle diameter, and the static bed height were studied. A phase diagram of bubbling, jetting, and transition zones were drawn by using a modified Froude number and the ratio of the nozzle diameter to the particle size.

Table 1-1. Summary of experimental conditions in the literature for experimental studies of horizontal jets in gas-fluidized beds.

Reference	**Column type**	**Bed material**	**Nozzle diameter (mm)**	**Jet velocity (m/s)**
Shakhova (1968)	3D	Co-polymer: $d_p = 4$ mm, $\rho_p = 1000$ kg/m^3	4~6	52~303
Zenz (1968)	2D	Sand: $d_p = 0.05 \sim 2$ mm, $\rho_p = 2600$ kg/m^3	14.0	2.8~6.6
		Mill scale: $d_p = 0.17$ mm, $\rho_p = 2600$ kg/m^3	7.9	75~118
Merry (1971)	3D	Sand: $d_p = 0.18$ and 0.33 mm, $\rho_p = 2640$ kg/m^3	2.54, 6.35, 14.3	5~20
	3D	Sand: $d_p = 0.18$ and 0.33 mm, $\rho_p = 2640$ kg/m^3	3.175	40~300
		Steel shot: $d_p = 0.28$ mm, $\rho_p = 7430$ kg/m^3	3.175	40~300
		Kale seeds: $d_p = 2$ mm, $\rho_p = 1000$ kg/m^3	3.175	40~300
Rajin and Christoff (1982)	3D	Limestone: $d_p = 1.125$ mm	4.8, 6.4, 8.7	-
Xuereb et al. (1991a, b)	2D	Polystyrene: $d_p = 0.41$ mm, $\rho_p = 1020$ kg/m^3	8	35~125
		Polystyrene: $d_p = 0.605$ and 1.13 mm, $\rho_p = 1020$ kg/m^3	8	63~125

Reference	Column type	Bed material	Nozzle diameter (mm)	Jet velocity (m/s)
		Polystyrene: $d_p = 0.725$ mm, $\rho_p = 1020$ kg/m^3	8	47~125
		Polystyrene: $d_p = 1.64$ mm, $\rho_p = 1020$ kg/m^3	8	54~105
Chen and Weinstein (1993)	3D	FCC: $d_p = 0.059$ mm, $\rho_p = 1450$ kg/m^3	6.4, 12.7	23~69
Chyang et al. (1997)	2D	Glass bead: $d_p = 0.214$, 0.545, 0.775 and 0.92 mm, $\rho_p = 2600$ kg/m^3	3~9	21~129
Hong et al. (1997)	2D	Millet: $d_p = 1.43$ mm, $\rho_p = 1402$ kg/m^3	5, 7, 8, 10	26.2~189.7
		Sand: $d_p = 2.25$ mm, $\rho_p = 1354$ kg/m^3	5, 7, 8, 10	26.2~218
		Sand: $d_p = 1.43$ mm, $\rho_p = 1582$ kg/m^3	5, 8, 10	35~196.7
Copan et al. (2001)	3D	Polyethylene: $d_p = 0.37$ mm, $\rho_p = 930$ kg/m^3	3.81	-
Al-Sherehy (2002)	3D	FCC: $d_p = 0.061$ mm, $\rho_p = 1460$ kg/m^3	4.3	0.2~226
Donald et al. (2004)	3D	FCC: $d_p = 0.084$ mm, $\rho_p = 1720$ kg/m^3	4.4, 7.5, 9.2	50~170

Hong et al. (1997) analyzed the inclined jet in a two-dimensional gas-solid fluidized bed with experimental observation and numerical simulation. The influences of bed structure (voidage), particle properties (density, diameter), and jet characteristics (jet velocity, nozzle diameter, nozzle inclined angle, and nozzle position) on the jet penetration length were examined and a correlation for the inclined jet penetration length was derived.

To study the distributed addition of gaseous reactants in fluidized beds, Al-Sherehy (2002) measured horizontal jet penetration depth of a single nozzle into a bubbling fluidized bed of FCC particles and the effect of primary air superficial velocity on jet penetration was evaluated. The gas mixing resulting from a single horizontal jet injection was investigated. It was reported that the distribution of injected gas was non-uniform at the injection level, especially at smaller injection velocities. However, the injected gas became uniformly distributed within a short distance above the injection level.

Donald et al. (2004) investigated horizontal jet penetration for a single jet, interacting pairs of jets and five jets entering together a bubbling fluidized bed of FCC particles. They found that a jet was affected more by another jet below it than by the neighbouring jets at the same level, and the influence from the jet above it was minimal. Jets issuing from nozzles at the same level influenced each other when the jets overlapped.

Among all the parameters describing gas jets issuing into fluidized beds, the jet penetration length is one of the most important, since it determines the length of the effective interaction zone of the gas jet and emulsion phase. Several correlations for predicting the penetration lengths of horizontal gas jets have been developed based on theoretical analysis and experimental data (Shakhova, 1968; Zenz, 1968; Merry, 1971; Benjelloun et al., 1995; Hong et al., 1997). Zenz (1968) presented a curve to predict the horizontal jet penetration length. Shakhova (1968) derived an expression for the horizontal jet penetration length. Merry (1971) measured the

penetration depths of horizontal air jets injected into fluidized beds of sand, kale seed, and steel shot and derived a simple model for jet penetration length. Hong et al. (1997) derived a correlation for the inclined jet penetration length. These studies have consistently reported that the horizontal jet penetration length increases with increasing velocity of gas injection and nozzle diameter, and is dependent on properties of bed material (gas and solid densities, viscosity, and particle diameter) and operation conditions (bed heights, fluidizing gas velocity, void fraction, etc.). A summary of existing correlations for horizontal jet penetrations in the literature is given in Table 1-2. There are various definitions of jet penetration length. Among correlations listed in Table 1-2, the penetration depth, L_j, is the maximum jet penetration except for Shakhova's correlation in which the mean value of the maximum and minimum penetration length was used.

Table 1-2. Correlations for horizontal jet penetration length.

$\frac{L_j}{D_j} = 7.8\left(\frac{\rho_j}{\rho_p}\frac{U_j}{\sqrt{gD_j}}\right)$	Zenz (1968)
$0.044\frac{L_j}{D_j} + 1.57 = 0.5\log(\rho_j U_j^2)$	Shakhova (1968)
$\frac{L_j}{D_j} + 4.5 = 5.25(\frac{\rho_j U_j^2}{(1-\varepsilon)\rho_p g d_p})^{0.4}(\frac{\rho_g}{\rho_p})^{0.2}(\frac{d_p}{D_j})^{0.2}$	Merry (1971)
$\frac{L_j}{D_j} = 5.52(\frac{\rho_j U_j^2}{(\rho_p - \rho_g) g D_j})^{0.27}$	Benjelloun et al. (1995)
$\frac{L_j}{D_j} + 3.8 = 1.64\times10^{-6}(\frac{\rho_j U_j^2}{(1-\varepsilon)\rho_p g d_p})^{0.327}(\frac{\rho_g}{\rho_p})^{1.974}(\frac{d_p}{D_j})^{-0.04}$	Hong et al. (1997)

The expansion angle is another important parameter describing the jet behaviour. It must be used as an input parameter for the application of hydrodynamic models of the jet region and it may influence the prediction of the gas and particle entrainment rate into the jet. Measurements of jet

angles have been conducted in the context of work investigating gas jet features. Most of the measurements focus mainly on the vertical gas jets in fluidized beds (Massimilla, 1985; Cleaver et al., 1995; Vaccaro, 1997). As far as a horizontal gas jet is concerned, only limited work has been published and a systematic investigation is still lacking (Demichele et al., 1976; Xuereb et al., 1991a; Copan et al., 2001; Ariyapadi et al., 2003).

1.2.2 Gas/liquid sprays in fluidized beds

In many industrial fluidized bed reactors, for example fluid catalytic cracking units, coaters and fluid cokers, the reactant is introduced into the system in the form of gas/liquid spray. Considerable effort has been devoted to better understanding the feed injection into industrial processes in experimental, theoretical, and numerical studies. Skouby (1999) performed the hydrodynamics measurements in a 0.45-m riser with liquid feed injection through two different nozzles. Different performances for the two nozzles with respect to solid mass flux, particle velocity, and concentration were observed. Zhu et al. (2000) investigated the liquid nitrogen spray jets in dilute gas-solid flows to illustrate the effect of solid concentration on microstructures of the evaporative liquid jets, especially the jet evaporation length. The study indicated the jet evaporation length significantly decreased with an increase in the solid concentration. Zhu et al. (2002) also developed a parametric model for the study of mixing characteristics of an evaporating liquid jet in gas–solid suspension flows. Numerical simulations of evaporative spray jets in concurrent gas-solid pipe flows and gas-solid crossflows with Lagrangian-Eulerian approach were conducted (Wang et al., 2004; Qureshi and Zhu, 2006). Fan et al. (2001) studied the fundamental characteristics of evaporative liquid jets in gas-liquid-solid systems for both dilute and dense solid phase conditions.

Ariyapadi et al. (2003) investigated horizontal injection of gas, gas-liquid, and liquid jets into fluidized beds using a sophisticated digital X-ray imaging system. Their results showed that the jet expansion angle was considerably reduced for a gas-liquid jet when compared to that of a gas

jet. The gas-liquid jet also appeared to penetrate deeper than a gas jet with the same momentum. Furthermore, when a liquid feed was introduced into a fluidized bed of particles, the particles might agglomerate if they were wet-enough to form liquid bridges. A new correlation, which included the effect of nozzle geometry, was developed to predict the horizontal jet penetration of gas-liquid sprays injected into gas-solid fluidized beds (Ariyapadi et al., 2004).

To study the mechanism of liquid injection into fluidized bed reactors, Bruhns and Werther (2005) measured the bed temperature and vapour concentration of a pilot-scale bubbling fluidized bed with injections of water and ethanol, respectively. In their experimental investigation, the injected liquid was found to form agglomerates with the bed particles at the nozzle exit and become transported into the bed interior by the large-scale mixing of solids. A three-dimensional model was developed to describe the injection of liquid reactants into fluidized bed reactors operating in the bubbling fluidization regime (Werther and Bruhns, 2004).

Gehrke and Wirth (2007a, 2007b, 2008) investigated liquid feed injection into a high-density circulating fluidized bed at elevated temperatures. By employing fast-responding thermocouples, capacitance and conductivity probes, the solid concentration and velocity were measured and the spray zone was characterized. Effects of bed temperature, solids mass flux, spray flow rate, and spray cone angle were examined.

Extensive experimental work has been done on coating and agglomeration in both top spray and bottom spray coaters (deOliveira et al., 1997; Dewettinck et al., 1998; Dewettinck and Huyghebaert, 1998; Maronga and Wnukowski, 2001; Turton et al., 2001; Donida and Rocha, 2002; Hemati et al., 2003; Saleh et al., 2003; Donida et al., 2005; Paulo et al., 2006). However, most of them only focus on the particle growth rate, coating efficiency, and agglomerate size. Only limited information can be found on detailed interaction between the spray and the bed.

Maronga and Wnukowski (1998) measured the distribution of gas humidity and temperature for a top-spray particulate coating device using a single non-submerged spray nozzle. The measurements indicated that during the process, pockets of low temperature and high humidity formed deep inside the bed. The shape and size of low temperature and high humidity profiles depended on the type of particles used and the operating conditions. Two general shapes were formed by the temperature profile, funnel-shaped and bell-shaped profiles.

Saadevandi and Turton (2004) investigated particle motion in a semicircular spouted-fluidized bed coating device by measuring the radial and axial particle velocity and voidage profiles with computer-based video imaging techniques and a custom software. To investigate the effect of liquid droplets on fluidized particles in the spray region, measurements were carried out both with and without an atomized water spray fed to the bed. It was reported in their study that there was no difference in velocity and voidage measurements with or without spray, when a small amount of liquid spray was injected into the system.

With significant improvements in computational power and numerical algorithms, numerical modeling has become an attractive tool for studying fluidization problems. In order to predict the performance of FCC systems, several numerical simulations of three-phase flow have been reported in the literature. Gao et al. (2001) developed a 3-D, gas-liquid-solid three-phase flow-reaction model by extending their 3-D, two-phase turbulent flow-reaction model with a set of governing equations for the feed-spray droplets. Their model predictions were compared with performance data from commercial riser reactors. Gupta and Rao (2001) developed a three-phase model for predicting conversions and yield patterns in a FCC riser taking into account the effect of feed atomization. With this model, an entire FCC unit comprised of a riser and a generator was simulated and the effect of feed atomization on the unit performance was evaluated (Gupta and Rao, 2003). Nayak et al. (2005) simulated the simultaneous heat transfer, evaporation, and cracking reactions in a FCC riser reactor with the Eulerian–Lagrangian approach to understand

the influences of key design and operating parameters on the reactor performance. A three-dimensional, three-phase reacting flow computational fluid dynamics code, ICRKFLO, was developed in Argonne National Laboratory, and it was used to study the interactions of multiphase hydrodynamics, droplet evaporation, and cracking reactions in FCC riser reactors (Chang et al., 2001; Chang and Zhou, 2003). Despite the fact that numerical models and simulations have been extensively used to investigate the fluidization processes, little is known about the interactions of the spray with fluidized beds.

1.3 TYPICAL INDUSTRIAL APPLICATIONS

As already stated, fluidized beds with secondary gas/liquid injection from nozzles are found in many industrial applications. Three types of typical industrial applications of a gas/liquid injection system are briefly described in this section.

1.3.1 Spouted bed coater

Spouted beds are applied in various industrial applications such as drying, coating and granulation, as they provide a means of good mixing and circulation for particles of relatively large size and narrow size distribution. Coating is one of the most important applications of spouted beds, which is common in pharmaceutical and food industries. Figure 1-3 shows a schematic of a spouted bed coater, where two types of spray – top spray and bottom spray, are illustrated.

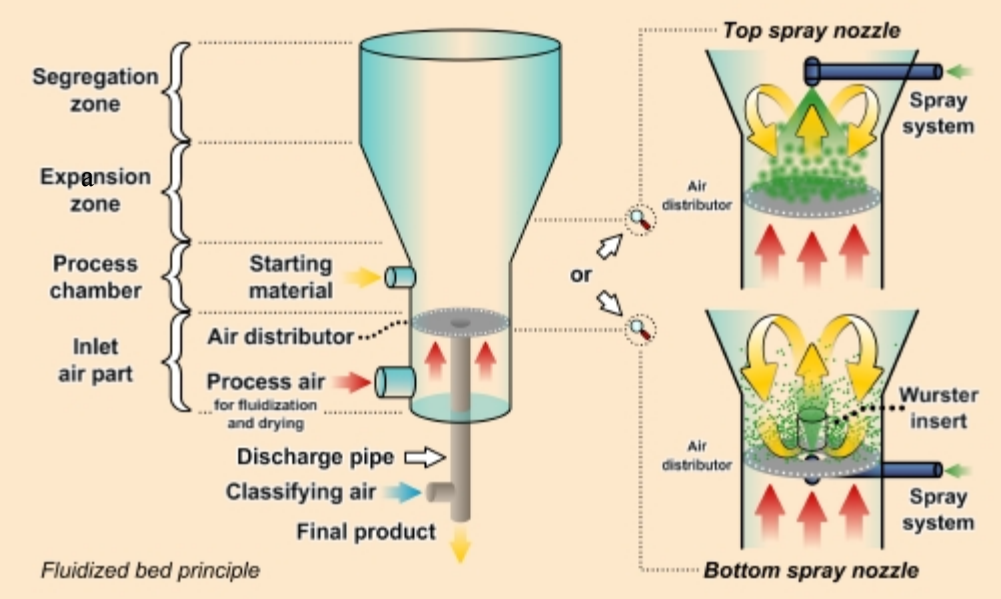

Figure 1-3. Schematic of spouted bed coater. (From www.gate2tech.com)

The conventional top spray coater is very popular in the food industry owing to its high versatility, relatively high batch size and relative simplicity (Dewettinck and Huyghebaert, 1999). Moreover, it can be easily used for both coating and agglomeration. In a top spray coater, the particles are accelerated from the product container past the nozzle, which sprays the coating liquid counter-currently onto the randomly fluidized particles. Coated particles travel through the process chamber (coating zone) into the expansion zone, and then they fall back into the container. Bottom spray coaters, generally known as Wurster coaters (Wurster, 1953), have been extensively utilized in the pharmaceutical industry for coating small particulates, especially pellets. In a Wurster coater, a vertical draft tube is inserted into the bed producing several advantageous characteristics. It overcomes the limitations of conventional spouted beds like spouting instabilities caused by the maximum spoutable bed height. The draft tube also allows accurate control of gas and solids residence times by separating the spout and the annulus. Furthermore, smaller particles can be successfully spouted after the insertion of a draft tube in spouted beds, which greatly improves the design and operation flexibility. The spray droplets induced from the bottom travel co-currently with particles in the draft tube, providing excellent heat and mass transfer and helping to form uniform coating (Aulton et al., 1995).

In coaters, typical nozzles are binary or pneumatic: a liquid is supplied at a low pressure and is sheared into droplets by atomizing gas (for example air-assist atomizer, air blast atomizer). With this type of spray nozzles, the droplet size and distribution are more controllable, especially at a low spray flow rate (Lefebvre, 1989).

1.3.2 Fluid Catalytic Cracking

Fluid Catalytic Cracking (FCC) is one of the key processes for production of gasoline and diesel fuels. In many refineries, the fluid catalytic cracking unit serves as the primary conversion unit, converting, or cracking, low-value crude oil heavy ends into a variety of higher value, light products. World-wide, there are approximately 400 FCC units in operation. They have a total processing capacity of 1.9 million metric ton per day, no less than 17 % of the total oil refining capacity (Jones et al., 2006).

The FCC unit consists of a catalyst section and a fractionating section that operate together as an integrated processing unit. The catalyst section contains the reactor and the regenerator, which, with standpipes and riser, form the catalyst circulation unit as shown in Figure 1-4. The fluid catalyst is continuously circulated between the reactor and the regenerator using air, oil vapours, and steam as the conveying media. A typical FCC process involves mixing a preheated hydrocarbon charge with hot, regenerated catalysts. The feed is usually injected into the bottom section of the riser. By contacting with extremely hot catalyst particles, the feed is vaporized and cracking reactions take place to break down the high molecular weight (or heavy) oil into gasoline and other light products. All these processes take place in the riser. The mixture is then transported into the stripper, where the product stream (cracked product) is separated and then charged to a fractionating column. Spent catalyst particles are transported to the regenerator through the stand pipe. In the regenerator, most of the coke deposits on the catalyst particles are burnt off at the bottom where preheated air and spent catalyst are mixed. During this process,

fresh catalyst is added and deactivated catalyst is removed continuously to optimize the cracking process.

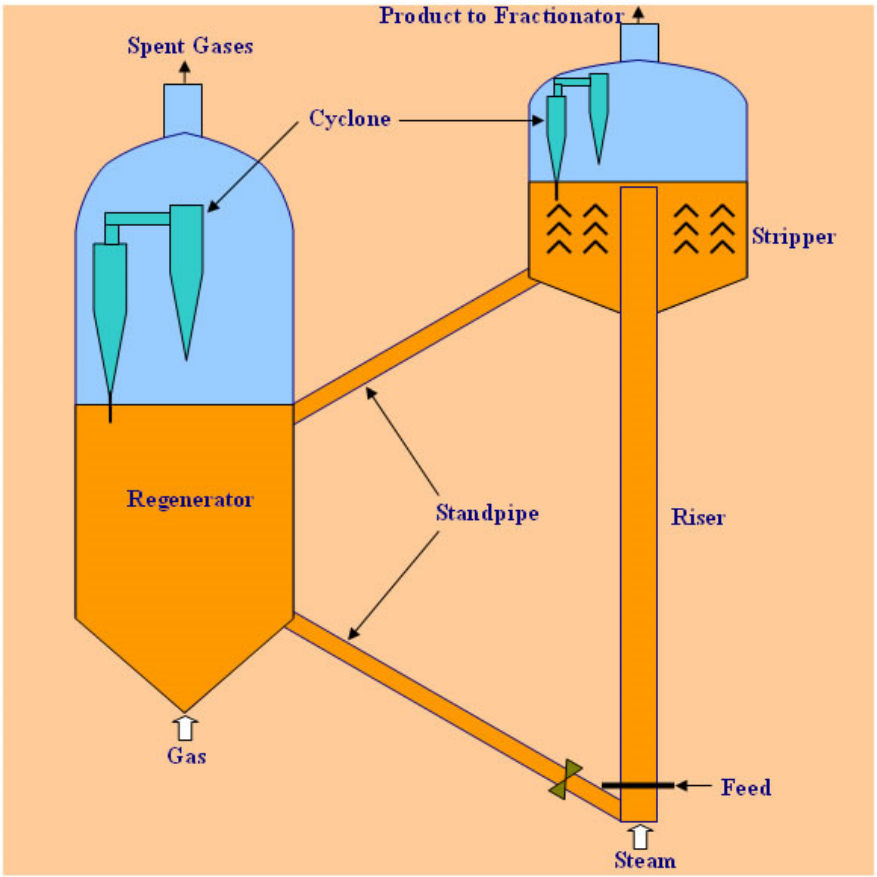

Figure 1-4. Schematic diagram of catalyst section of FCC unit (Kunii and Levenspiel, 1991).

As mentioned at the beginning of this chapter, the FCC process has been commercially deployed for over 60 years. The technology continues to evolve to meet new challenges, which include processing more difficult feedstocks and meeting more stringent environmental regulations. Considerable efforts have been devoted to better understand the complexity of riser reactors, including theoretical and experimental studies, pilot plants, and commercial tests. There is condiderable FCC research and development in the industry focusing on further improvement of the product. An important aspect of the research is to improve the understanding of the interaction between feed spray and catalyst particles, which has an important impact on the conversion (Chen, 2006).

1.3.3 Fluid coker

Fluid coking is a process that utilizes a fluidized bed of hot coke particles to thermally crack bituminous feeds. Fluid coking was developed by extending the earlier thermal conversion technology through the adaptation of fluid-solid technology from catalytic cracking, after World War II and into the early 1950s (Hammond et al., 2003). This technology is currently used by Syncrude Canada Ltd (http://www.syncrude.ca). The fluid coking system consists mainly of a fluidized bed reactor and a fluidized bed burner. In the reactor, operating at temperatures in the range of 500~550 $°C$, the bitumen feed, heating to 350 $°C$ and consisting of heavy bituminous hydrocarbons, is atomized with steam and injected into the reactor of hot coke particles through a series of nozzles horizontally mounted on the wall of the bed. Through spraying onto the bed of hot coke, the feed is thermally cracked into a full range of lighter products, from gases to gas oils, and by-product coke. Gas oil, naphtha, and lighter liquids are the desirable products which can then be mixed to form the synthetic crude oil. The coke is then recycled to the burner, where part of it is burnt off to provide the heat for cracking. A schematic of the fluid coking process is shown in Figure 1-5.

During the fluid coking process, it has been reported that a number of process variables are significant. Among these variables, the mixing behaviour of gas, bitumen feed and hot cokes in the fluidized bed are very important to the overall coking performance to achieve high conversion and selectivity. Despite the long history of fluid coking, the complex interactions between hydrodynamics, liquid feed injection, reaction kinetics, and heat transfer continue to provide fertile opportunities for significant process improvements (Gray, 2002).

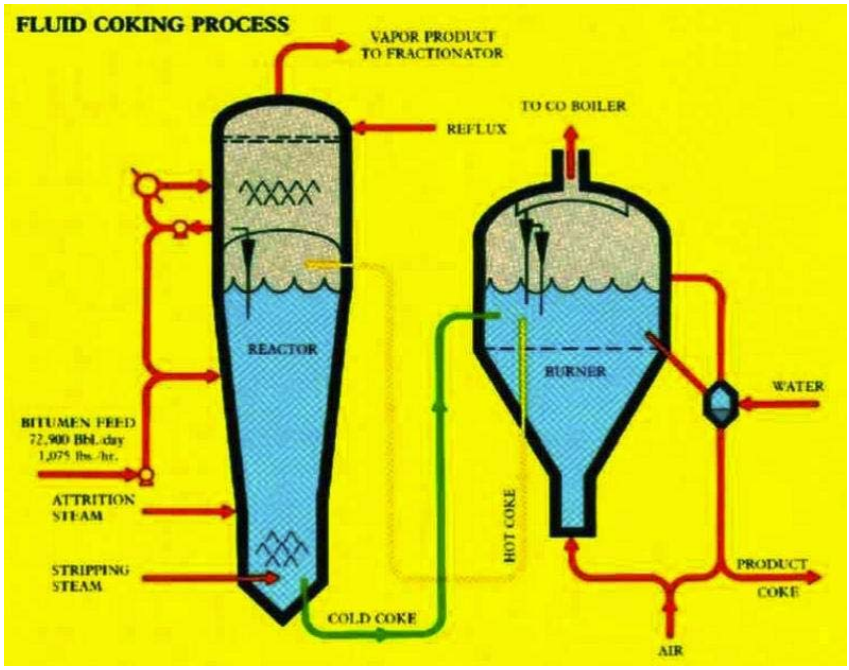

Figure 1-5. Schematic of fluid coking process (Felli et al., 2003).

1.4 RESEARCH OBJECTIVES

In the current research, we want to improve our understanding of jet-bed interaction with the aid of CFD tools. Key objectives are to:

- Conduct numerical simulations of the horizontal gas jet injection into bubbling fluidized beds and improve our understanding of this process. In an effort to validate our numerical simulations, the results are compared with available experimental data as well as empirical correlations. After that, we study the hydrodynamics of horizontal gas jets in bubbling fluidized beds. This includes studying the jet behaviours as well as the interactions between the gas jet and the surrounding gas, solids, bubbles, or other jets for multiple-jet injection; evaluating the effect of secondary gas injection through horizontal jets on the flow hydrodynamics for different conditions; and analyzing the mixing of secondary gas injection with bed materials.

- Develop models to simulate the liquid spray injection into gas-solid flows and investigate the spray interaction with different gas-solid systems. To do this, a simple model is implemented first to simulate a dilute liquid spray into the gas-solid flow in a spouted bed. Further extension is made to take into account the evaporation of the liquid spray. Finally, a complete model is developed to model the hydrodynamics of the evaporative spray in hot gas-solid flows. Sub-models for the interaction between droplets and particles including momentum exchange and heat, mass transfer in the light of available experimental observations and analytical and CFD results are proposed. During the development and implementation of the models, necessary comparison with available experimental data in each step is performed.

1.5 THESIS LAYOUT

Chapter 2 summarizes the basic numerical models used in simulations of different fluidized bed systems. The governing equations for the Eulerian-Eulerian approach are presented with closure correlations of granular kinetic theory, frictional models, and inter-phase drag models.

In **Chapter 3**, a three-dimensional numerical simulation of a single horizontal gas jet entering a cylindrical fluidized bed of laboratory scale is conducted. A scaled drag model is proposed and implemented into the simulation of a bubbling fluidized bed of FCC particles. The gas and particle flows in the fluidized bed are investigated by analyzing the transient simulation results. The jet penetration lengths of different jet velocities are predicted and compared with published experimental data, as well as with predictions of empirical correlations. Furthermore, the expansion angles of the gas jet are also obtained from the simulations and their dependence on the jet gas velocity is evaluated.

In **Chapter 4**, the behaviours of single and multiple horizontal gas jets entering a rectangular bubbling fluidized bed are studied with three-dimensional numerical simulations. The jet

penetrations, as well as the interactions between the jet and the surrounding gas, solids, bubbles, and other jets are investigated. The effect of the secondary gas injection on the flow hydrodynamics in the bed is examined for multiple-jet injections with different jetting velocities and arrangements. In addition, the mixing behaviour of secondary injected gas with bed materials is studied by introducing a tracer gas into the secondary gas injection. Both unsteady and steady analyses of the mixing behaviour are performed.

Chapter 5 presents numerical simulations of the gas-solid flow in a flat-based spouted bed with a draft tube (DTSB). The hydrodynamics of the flow in DTSB is investigated and compared with experimental data. The effect of the gas velocity on the particles circulation rate is evaluated, and parametric studies of the restitution coefficient are performed. In addition, several different frictional models are tested. A model for the liquid spray injection into a gas-solid flow is proposed and implemented into Fluent 6.3. The liquid spray introduced through the bottom nozzle is simulated and the influence of spray rate on solids concentration and velocity inside the draft tube is examined.

In **Chapter 6**, three-dimensional simulations of an evaporating gas-liquid spray into a gas-solid crossflow are presented. The gas, solid, and liquid phases are modeled with a Eulerian-Eulerian model, and appropriate correlations for inter-phase interaction and heat transfer are used. The implementation of these models into Fluent 6.3 is evaluated with available experimental data. General features of the evaporative spray and qualitative trends are predicted by numerical simulations.

In **Chapter 7**, we propose a model capable of accounting for the interaction between droplets and particles including the momentum exchange and heat, mass transfer in light of available experimental observations and CFD results in the literature. Several parameters are introduced to model the complex interaction between the cold evaporative spray and the hot gas-solid flow.

With this model, numerical simulation of an evaporative water spray through a hollow cone spray nozzle in a riser operated at an elevated temperature is conducted and comparison with available experimental measurements of the spray expansion is performed. The influences of the adjustable parameters in the model are investigated in the parametric study, and possible values for those parameters are suggested. In addition, effects of operating conditions such as droplet size, bed temperature, and spray angle are evaluated.

Finally, the current research is summarized in **Chapter 8**, and key conclusions drawn from these studies are presented. In addition, some recommendations for future work in both experimental and numerical aspects are given.

Appendix A presents the derivation of the expression for droplet-particle momentum transfer due to collisions.

Chapter 2. NUMERICAL MODELS FOR GAS-SOLID FLOW

2.1 INTRODUCTION

With the fast development of high speed computers, modeling and numerical simulations of fluidized beds have become an expanding subject and are playing an important role in understanding and predicting the hydrodynamics of fluidization applications. Considerable progress has been achieved in hydrodynamic modeling of fluidized beds in the last decade. Basically, there are two different categories of models for gas-solid flows: Lagrangian-Eulerian models and Eulerian-Eulerian models. Our current research is conducted mainly with the latter one, which is the focus of this chapter. The Lagrangian-Eulerian models are only briefly reviewed here.

2.2 LAGRANGIAN-EULERIAN APPROACH

The Lagrangian approach, also known as the discrete particle model (DPM) or the discrete element method (DEM), describes the solid phase at a particle level and the gas phase as a continuum. The Newtonian equation for each individual particle or swarm of particles taking into account the effect of particle collisions and forces acting on particles by gas has to be solved with Navier Stokes equations for the gas phase. Particle-particle collisions are modeled with the hard sphere model (Hoomans et al., 1996) or the soft sphere model (Tsuji et al., 1993). In the hard sphere model, any collision between particles is assumed to be pair-wise additive and instantaneous. The trajectories of the particles are determined by employing the collision laws to account for the energy dissipation due to non-ideal particle interactions. In the soft sphere model, the collision between particles is treated as a continuous process that takes place over a finite time. The contact force is calculated as a continuous function of the distance between colliding

particles based on physically realistic interaction laws using empirical spring stiffness, dissipation constant, and friction coefficient. Both hard sphere and soft sphere models are widely applied in numerical modeling of fluidized beds (Tsuji et al., 1993; Hoomans et al., 1996; Rhodes et al., 2001; Li and Kuipers, 2002; Limtrakul et al., 2003; Yu and Xu, 2003; Link et al., 2007). The Lagrangian approach is a very powerful tool for studying the details of flow phenomena in fluidized beds (Deen et al., 2007). However, the Lagrangian approach requires a large amount of computational resources for a large system of particles. The simulations reported in the literature are restricted to systems that are either very dilute or very small, such that the total number of particles is limited, usually no more than $\sim 10^7$.

2.3 EULERIAN-EULERIAN APPROACH

The Eulerian-Eulerian approach is based on the two-fluid model (TFM) that treats each phase as an interpenetrating continuum. Conservation equations of mass, momentum, and energy for both the particulate and fluid phases are derived by some form of averaging method (Anderson and Jackson, 1967; Ishii, 1975). Eulerian-Eulerian models require closure laws for particle interactions, and there is an absence of consensus concerning the stress terms in the particulate momentum equation. Various non-Newtonian models for the internal stresses of the solid phase have been proposed (Gidaspow and Ettehadieh, 1983; Gidaspow, 1986; Tsuo and Gidaspow, 1990). These stresses were correlated with experimental observations and some of them were summarized by Enwald et al. (1996). However, many two-fluid models in the literature suffer from uncertainties in prescribing the viscosity and the normal stress of the solid phase. The uncertainties in empirical correlations of solid viscosity and the need for a more systematic way to prescribe viscosity lead to the popularity of granular kinetic theory, based on kinetic theories of non-uniform dense gases. Constitutive relations for the solid phase stress tensor can be derived based on the kinetic theory (Chapman and Cowling, 1970; Jenkins and Savage, 1983; Lun et al., 1984; Johnson and Jackson, 1987; Gidaspow, 1994). Many research groups have been

involved in simulations with granular kinetic theory, and encouraging results have been reported in the literature (Jenkins and Savage, 1983; Enwald et al., 1996; Samuelsberg and Hjertager, 1996; Lu and Gidaspow, 2003; Syamlal and O'Brien, 2003; Hansen et al., 2004; Johansson et al., 2006).

2.3.1 Governing equations

There are many ways, depending on the averaging procedures and the closure laws adopted, to formulate a two-fluid model. The general idea is to first formulate the integral balances of mass, momentum, and energy for a fixed control volume containing both phases. The balance must be satisfied at any time and at any point in space, and thus reduces to two types of local equations, one being the local instantaneous equations for each phase and the other an expression of the local instantaneous jump conditions, i.e. the interactions between phases at the interface. The local instantaneous equations are then averaged in a suitable way, in space, in time, or ensemble to form the governing equations in the Eulerian-Eulerian approach. Based on local space-averaging and time-averaging procedures, Anderson and Jackson (1967), and Ishii (1975) have derived governing equations for the two-fluid model, respectively, which are referred to by most researchers (van Wachem et al., 2001). Here, the final governing equations are presented, and details on the derivation of these equations can be found in Gidaspow (1994).

The mass conservation equations for gas and solid phase are written as

$$\frac{\partial}{\partial t}(\alpha_g \rho_g) + \nabla \cdot (\alpha_g \rho_g \vec{V}_g) = q_g \tag{2.1}$$

$$\frac{\partial}{\partial t}(\alpha_p \rho_p) + \nabla \cdot (\alpha_p \rho_p \vec{V}_p) = q_p \tag{2.2}$$

The subscripts g, p stand for gas and solid phases, respectively; α is the volume fraction with the constraint: $\alpha_g + \alpha_p = 1$, and ρ, $\vec{V}$ are density and velocity. On the right-hand side of equations (2.1) and (2.2), q is the source term due to mass transfer between phases.

The momentum equations for gas and solid phases are written as

$$\frac{\partial}{\partial t}(\alpha_g \rho_g \vec{V}_g) + \nabla \cdot (\alpha_g \rho_g \vec{V}_g \vec{V}_g) = \nabla \cdot \bar{\bar{\tau}}_{g,\text{eff}} - \alpha_g \nabla P + \alpha_g \rho_g \vec{g} + M_{pg} + I_g \quad (2.3)$$

$$\frac{\partial}{\partial t}(\alpha_p \rho_p \vec{V}_p) + \nabla \cdot (\alpha_p \rho_p \vec{V}_p \vec{V}_p) = \nabla \cdot \bar{\bar{\sigma}}_p - \alpha_p \nabla P + \alpha_p \rho_p \vec{g} + M_{gp} + I_p \quad (2.4)$$

where P is the gas pressure; $\vec{g}$ is the gravitational acceleration; and M_{gp} and M_{pg} are the inter-phase momentum exchanges between gas and particles, and I accounts for the momentum transfer resulting from mass transfer. $\bar{\bar{\tau}}_g$ and $\bar{\bar{\sigma}}_p$ are stress tensors for gas and solid phases, respectively.

To describe the conservation of energy in Eulerian multiphase applications, a separate enthalpy equation can be written for each phase (Fan and Zhu, 1998).

$$\frac{\partial}{\partial t}(\alpha_g \rho_g h_g) + \nabla \cdot (\alpha_g \rho_g \vec{V}_g h_g) = -\alpha_g \frac{\partial P}{\partial t} - \nabla \cdot \vec{q}_g + \bar{\bar{\tau}}_g : \nabla \vec{V}_g - Q_{gp} + H_g \quad (2.5)$$

$$\frac{\partial}{\partial t}(\alpha_p \rho_p h_p) + \nabla \cdot (\alpha_p \rho_p \vec{V}_p h_p) = -\alpha_p \frac{\partial P}{\partial t} - \nabla \cdot \vec{q}_p + \bar{\bar{\sigma}}_p : \nabla \vec{V}_p - Q_{pg} + H_p \quad (2.6)$$

where h and T are the specific enthalpy and temperature, $\vec{q}$ is the heat flux from boundary or radiation, Q stands for the heat transfer between two phases, and H represents the inter-phase energy transfer due to phase change. The first terms on the right-hand side of equations (2.5) and (2.6) can be neglected since the flow velocity is usually far below the sound velocity and no combustion is taking place. The second term on the right-hand side of each energy equation is the heat flux, and the third is the energy dissipation term.

2.3.2 Closure relations

2.3.2.1 Turbulence model

In two-phase flows, turbulence of the carrier phase plays an important role in the transport or mixing of the dispersed phase. For dense gas-solid flows (including fluidized beds), the

turbulence of the particulate phase is usually modeled with a granular temperature based on granular kinetic theory (Gidaspow, 1994). The turbulence of the carrier phase is not of primary concern as particle-particle collisions dominate the flow (Crowe et al., 1996). Furthermore, it has been reported that the inertia of particles damps out the turbulence in the carrier phase, and the turbulence of carrier phase can be ignored (Enwald et al., 1996; Portela and Oliemans, 2006). In dilute flows, the turbulent fluid-particle interaction becomes important and complex. Considerable work has been done to modify the turbulence of gas phase by taking interfacial turbulent momentum transfer into account (Reeks, 1991; Cao and Ahmadi, 1995; Simonin, 1996; de Bertodano, 1998; Xu and Subramaniam, 2006). However, a generally applicable turbulence model for two-phase flow is not available, and it is still a challenging problem in CFD. Several turbulence models have been used in our numerical simulations as discussed in detail in the following chapters.

2.3.2.2 Granular kinetic theory

In granular kinetic theory, it is assumed that the random motion of particles is analogous to the thermal motion of molecules in a gas and a so-called granular temperature, proportional to the mean square of the random particle velocity based on the Maxwellian velocity distribution, is defined to model the turbulent fluctuating energy of the solid phase. Constitutive relations for the solid phase stress can thus be derived based on the kinetic theory concepts (see Lun et al., 1984), which allows for the inelastic nature of particle collisions.

According to Gidaspow (1994), the transport equation of granular temperature derived from kinetic theory is

$$\frac{3}{2}\left[\frac{\partial}{\partial t}(\alpha_p \rho_p \Theta_p) + \nabla \cdot (\alpha_p \rho_p \vec{V}_p \Theta_p)\right] = (-P_{s,vis}\overline{\overline{I}} + \overline{\overline{\tau}}_{p,vis}) : \vec{V}_p + \nabla \cdot \left(\kappa_{p,\Theta} \nabla \Theta_p\right) - \gamma_\Theta + \phi_{gp} \tag{2.7}$$

The first term on the right-hand side of equation (2.7) is the generation of granular energy; the second term is the diffusion of granular temperature; the third term is the dissipation of granular energy due to particle-particle inelastic collisions; the last term represents energy exchange between the gas and solid phase.

The solid pressure $P_{s,vis}$, which represents the solid phase normal forces due to particle collisions, was originally introduced by Anderson and Jackson (1969) in modeling the stability of a homogeneous fluidized bed. In granular kinetic theory, the solid pressure has the following form.

$$P_{s,vis} = \alpha_p \rho_p \Theta_p \left(1 + 2\alpha_p g_{0,p}(1+e_p)\right) \tag{2.8}$$

where e_p is the coefficient of restitution for particle collisions; $g_{0,p}$ is the radial distribution function, which is introduced to take into account the increase in number of collisions when the volume fraction of particles approaches the packing limit. It can be noted that the solids pressure is composed of a kinetic term and a second term due to particle collisions. There exist several expressions for the radial distribution function (Carnahan and Starling, 1969; Lun and Savage, 1986; Sinclair and Jackson, 1989; Ahmadi and Ma, 1990; Syamlal et al., 1993; Gidaspow, 1994; Gera et al., 1998; Iddir and Arastoopour, 2005). Some of these were reviewed by van Wachem et al., (2001). Here, we use the expression given by Gidaspow (1994)

$$g_{0,p} = \frac{3}{5}\left[1 - \left(\frac{\alpha_p}{\alpha_{p,\max}}\right)^{\frac{1}{3}}\right]^{-1} \tag{2.9}$$

where $\alpha_{p,\max}$ is the maximum volume fraction of particles.

The stress for the solid phase is

$$\overline{\overline{\sigma}}_{p,vis} = -P_{s,vis}\overline{\overline{I}} + \overline{\overline{\tau}}_{p,vis} \tag{2.10}$$

where $\overline{\overline{\tau}}_{p,vis}$ is the solid shear stress tensor

$$\bar{\bar{\tau}}_{p,vis} = \mu_p[\nabla\vec{V}_p + (\nabla\vec{V}_p)^T] + (\lambda_p - \frac{2}{3}\mu_p)\bar{\bar{I}}\cdot\nabla\cdot\vec{V}_p \qquad (2.11)$$

λ_p and μ_p are the solid bulk viscosity and solid shear viscosity, respectively.

There are various expressions for the solid shear viscosity (Lun et al., 1984; Ahmadi and Ma, 1990; Syamlal et al., 1993; Gidaspow, 1994; Hrenya and Sinclair, 1997), which differ mainly in the dilute region. We show only one of them, taken from Gidaspow (1994).

$$\mu_p = \frac{4}{5}\alpha_p^2\rho_p d_p g_{0,p}(1+e_p)\sqrt{\frac{\Theta_p}{\pi}} + \frac{\frac{5\sqrt{\pi}}{48}\rho_p d_p\sqrt{\Theta_p}}{(1+e_p)g_{0,p}}[1+\frac{4}{5}g_0\alpha_p(1+e_p)]^2 \qquad (2.12)$$

The solid bulk viscosity λ_p, accounting for the resistance of granular particles to compression and expansion, is calculated according to Lun et al. (1984) from.

$$\lambda_p = \frac{4}{3}\alpha_p^2\rho_p d_p g_{0,p}(1+e_p)\sqrt{\frac{\Theta_p}{\pi}} \qquad (2.13)$$

The diffusion coefficient according to Gidaspow (1994) for granular temperature is

$$\kappa_{p,\Theta} = \frac{150\rho_p d_p\sqrt{\Theta_p\pi}}{384(1+e_p)g_{0,p}}\left[1+\frac{6}{5}\alpha_p g_{0,p}(1+e_p)\right]^2 + 2\rho_p\alpha_p^2 d_p(1+e_p)\sqrt{\frac{\Theta_p}{\pi}} \qquad (2.14)$$

Other expressions for the diffusion coefficient can also be found in the literature (Lun et al., 1984; Syamlal et al., 1993; Cao and Ahmadi, 1995; Simonin, 1996).

The dissipation of granular energy, γ_Θ, is given (Lun et al., 1984) by the following model.

$$\gamma_\Theta = \frac{12(1-e_p^2)g_{0,p}}{d_p\sqrt{\pi}}\rho_p\alpha_p^2\Theta_p^{\frac{3}{2}} \qquad (2.15)$$

The transfer of the kinetic energy of random fluctuations in particle velocity from the solid phase to the gas phase is modeled (Gidaspow, 1994) as

$$\phi_{gp} = -3\beta_{gp}\Theta_p \qquad (2.16)$$

where β_{gp} is the inter-phase drag coefficient.

Instead of solving the complete balance equation (1.14) for the granular temperature, an algebraic expression was proposed by Syamlal et al. (1993). This approach assumes that the granular energy is dissipated locally, neglecting the convection and diffusion, and retaining only the generation and dissipation terms. The granular temperature thus is given by an algebraic expression.

$$\Theta_p = \left[\frac{-(K_1\alpha_p + \rho_p)Tr(\overline{\overline{D}}_p) + \sqrt{(K_1\alpha_p + \rho_p)^2 Tr^2(\overline{\overline{D}}_p) + 4K_4\alpha_p[2K_3 Tr(\overline{\overline{D}}_p^2) + K_2 Tr^2(\overline{\overline{D}}_p)]}}{2K_4\alpha_p} \right]^2 \tag{2.17}$$

where $\overline{\overline{D}}_p$ is the rate of deformation tensor and with the abbreviations

$$K_1 = 2(1+e_p)\rho_p g_{0,p} \tag{2.18}$$

$$K_2 = \frac{4}{3\sqrt{\pi}} d_p \rho_p (1+e_p) g_{0,p} \alpha_p - \frac{2}{3} K_3 \tag{2.19}$$

$$K_3 = \frac{d_p \rho_p}{2} \left\{ \frac{\sqrt{\pi}}{3(3-e_p)} \left[1 + \frac{2}{5}(1+e_p)(3e_p - 1) g_{0,p} \alpha_p \right] + \frac{8\alpha_p}{5\sqrt{\pi}} g_{0,p}(1+e_p) \right\} \tag{2.20}$$

$$K_4 = \frac{12(1-e_p^2)\rho_p g_{0,p}}{d_p \sqrt{\pi}} \tag{2.21}$$

2.3.2.3 Frictional model

At high solids concentration, usually $\alpha_p > 0.5$, the particles start to endure long, sliding and rubbing contact. In this regime, the flow is slow and the surface friction between individual particles becomes significant. This reflects the transition between two limiting flow regimes: rapid flow regime and quasi-static regime. It is extremely difficult to construct theoretical models

for this frictional flow regime. Savage (1983) first suggested presenting the total stress as the sum of a rate-independent frictional part and a rate-dependent viscous part obtained from granular kinetic models.

$$\bar{\bar{\sigma}}_p = \bar{\bar{\sigma}}_{p,vis} + \bar{\bar{\sigma}}_{p,fric} \tag{2.22}$$

where $\bar{\bar{\sigma}}_p$ is the total solid stress, $\bar{\bar{\sigma}}_{p,vis}$ is the viscous stress modeled with granular kinetic theory, and $\bar{\bar{\sigma}}_{p,fric}$ stands for the frictional stress, for which the constitutive models are largely based on soil mechanics (Schaeffer, 1987; Tardos, 1997; Dartevelle, 2004). This *ad hoc* patching approach unifies the available models for the rapid flow regime and the quasi-static regime.

Under a normal stress, a granular material will yield only when the shear stress attains a critical value, i.e. the yield condition. A large number of powders obey the yield condition as long as they undergo continuous deformation (Tardos, 1997). This state is usually called "the critical state". In most simulations, the frictional model proposed by Schaeffer (1987), derived from the von Mises yield conditions and the coaxiality flow rule according to critical-state soil mechanics (see Atkinson and Bransby, 1978 for details on critical-state soil mechanics), is employed to calculate the frictional component of solid stress. The expression for $\bar{\bar{\sigma}}_{p,fric}$ is written as

$$\bar{\bar{\sigma}}_{p,fric} = -P_{s,fric}\left(\bar{\bar{I}} - \frac{\sin\phi}{\sqrt{I_{2D}}}\bar{\bar{D}}_p\right) \tag{2.23}$$

where $P_{s,fric}$ is the normal frictional stress or frictional pressure, usually calculated based on empirical correlations (Johnson and Jackson, 1987; Johnson et al., 1990; Syamlal et al., 1993). ϕ is the internal angle of friction; its typical value for spherical glass beads falls between 24 and 30 degrees (Johnson and Jackson, 1987; Johnson et al., 1990). $\bar{\bar{D}}_p$ is the rate of deformation tensor and I_{2D} is the second invariant of $\bar{\bar{D}}_p$.

$$\bar{\bar{D}}_p = \frac{1}{2}\left(\nabla\vec{V}_p + (\nabla\vec{V}_p)^T\right) \tag{2.24}$$

$$I_{2D} = \frac{1}{6}\left[\left(D_{p,11} - D_{p,22}\right)^2 + \left(D_{p,22} - D_{p,33}\right)^2 + \left(D_{p,33} - D_{p,11}\right)^2 + D_{p,12}^2 + D_{p,23}^2 + D_{p,31}^2\right] \quad (2.25)$$

Accordingly, the frictional viscosity for Schaeffer's model is of the form

$$\mu_{fric} = \frac{P_{s,fric} \sin\phi}{\sqrt{I_{2D}}} \quad (2.26)$$

The frictional pressure is calculated from the correlation suggested by Johnson et al. (1990).

$$P_{s,fric} = \begin{cases} 0 & \alpha_p < \alpha_{p,\min} \\ Fr \dfrac{(\alpha_p - \alpha_{p,\min})^n}{(\alpha_{p,\max} - \alpha_p)^p} & \alpha_p \geq \alpha_{p,\min} \end{cases} \quad (2.27)$$

with empirical material constants $Fr = 0.05$, $n = 2$ and $p = 5$. $\alpha_{p,\min}$ is the solid volume fraction when frictional stress becomes important. Nolan and Kavanagh (1992) reported $\alpha_{p,\min} = 0.509$ in their computer-simulation of random packing hard-spheres. In our study, the value of 0.5 suggested by Johnson et al. (1990), which has been commonly applied in numerical simulations, is used.

Savage (1998) argued that some fluctuations existed in the strain rate associated with the formation of shear layers even in a purely quasi-static flow. He also suggested that these fluctuations reduced the shear stress in solids flow and could be related to the granular temperature. A frictional model was proposed by Srivastava and Sundaresan (2003) taking into account the strain rate fluctuations in a simple manner. The simplified version of this model is given in equation (2.28) by invoking the critical state hypothesis. This was found to be reasonably accurate in simulations and improved the computational speed (Srivastava and Sundaresan, 2003).

$$\bar{\bar{\sigma}}_{p,fric} = -P_{s,fric}\left(\bar{\bar{I}} - \sqrt{2}\frac{\sin\phi}{\sqrt{\bar{\bar{S}}_p : \bar{\bar{S}}_p + \Theta_p / d_p^2}}\bar{\bar{S}}_p\right) \quad (2.28)$$

where $\bar{\bar{S}}_p$, the deviator of strain rate, is defined as

$$\overline{\overline{S}}_p = \frac{1}{2}(\nabla \vec{V}_p + (\nabla \vec{V}_p)^T) - \frac{1}{3}(\nabla \cdot \vec{V}_p)\overline{\overline{I}} \tag{2.29}$$

Dartevelle (2004) reviewed the plastic-frictional theory and presented a set of constitutive equations for frictional granular flows. These equations were derived from the yield function formulated by Pitman and Schaeffer (1987) and Gray and Stiles (1988) based on Plastic Potential Theory (Schofield and Wroth, 1968). The frictional stress is written as

$$\overline{\overline{\sigma}}_{p,fric} = -P_{s,fric}\overline{\overline{I}} + (2\mu_{fric}\overline{\overline{S}} + \lambda_{fric}\nabla \cdot \vec{V}_p\overline{\overline{I}}) \tag{2.30}$$

where the frictional shear viscosity μ_{fric} and the bulk viscosity λ_{fric} are given by

$$\mu_{fric} = \frac{P_{s,fric}\sin^2\phi}{\sqrt{4\sin^2\phi I_{2D} + (\nabla \cdot \vec{V}_p)^2}} \tag{2.31}$$

$$\lambda_{fric} = \frac{P_{s,fric}}{\sqrt{4\sin^2\phi I_{2D} + (\nabla \cdot \vec{V}_p)^2}} \tag{2.32}$$

The detail of Dartevelle's review of the plastic-frictional theory can also be found at http://www.granular-volcano-group.org/frictional_theory.html.

2.3.2.4 Inter-phase momentum exchange

In momentum equations, the terms for the inter-phase momentum exchanges should include the effects of drag, Saffman lift, virtual mass, Basset and Magnus forces etc. (Fan and Zhu, 1998). For dense particles/droplets flows, which have $\rho_p / \rho_g \gg 1$, the drag force becomes the dominant effect characterizing the momentum exchange between the continuous phase and dispersed phase. Generally, the drag force acting on particles in fluid-solid systems is represented by the product of a drag coefficient β and the slip velocity $(V_s - V_g)$ between two phases. Simply, we have

$$M_{gp} = -M_{pg} = \beta_{gp}(\vec{V}_g - \vec{V}_p) \tag{2.33}$$

where β_{gp} is the drag coefficient. The correlations proposed for the drag coefficient are based mostly on experimental measurements for homogeneous systems, such as fluidization and sedimentation of the liquid-solid system or the gas-solid fixed bed. To date, several drag models have been developed to predict the inter-phase drag coefficient (Wen and Yu, 1966; Syamlal et al., 1993; Difelice, 1994; Gidaspow, 1994; Gibilaro, 2001; Hill et al., 2001; Benyahia et al., 2006). For the gas-particle drag force, the Gidaspow drag model following the correlation of Wen and Yu (1965) and Ergun (1952) equation, which has been extensively applied in numerical simulations of gas-solid systems, is given here.

$$\beta_{gp} = \begin{cases} 150\dfrac{\alpha_p(1-\alpha_g)\mu_g}{\alpha_g d_p^2} + 1.75\dfrac{\alpha_p \rho_g \left|\vec{V}_p - \vec{V}_g\right|}{d_p} & \text{if } \alpha_g < 0.8 \\ \dfrac{3}{4} C_{D,p} \alpha_g^{-2.65} \dfrac{\alpha_p \alpha_g \rho_g \left|\vec{V}_p - \vec{V}_g\right|}{d_p} & \text{if } \alpha_g \geq 0.8 \end{cases} \tag{2.34}$$

where

$$C_{D,p} = \begin{cases} \dfrac{24}{\mathrm{Re}_p \cdot \alpha_g}(1 + 0.15(\mathrm{Re}_p \cdot \alpha_g)^{0.687}) & \text{if } \mathrm{Re}_p \cdot \alpha_g < 1000 \\ 0.44 & \text{if } \mathrm{Re}_p \cdot \alpha_g \geq 1000 \end{cases} \tag{2.35}$$

In equation (2.35), the particle Reynolds number is defined as

$$\mathrm{Re}_p = \frac{\rho_g \left|\vec{V}_p - \vec{V}_g\right| d_p}{\mu_g} \tag{2.36}$$

2.4 SUMMARY

All the governing equations and constitutive correlations, which form what can be called the original, default, or standard model, have been presented in this chapter. In the following chapters, numerical predictions with alterations of some of the constitutive equations or additional models will be presented for specific problems.

In our study, different CFD solvers have been utilized to solve the above governing equations. An in-house serial Fortran code is firstly used to simulate the gas jet in a cylindrical bubbling fluidized bed in **Chapter 3**. Considering the extremely heavy computational load of the three-dimensional simulation of fluidization systems, two parallel CFD solvers, Fluent, and MFIX, are employed in the following simulations. Numerical simulations in **Chapter 5, 6,** and **7** are conducted by a commercial CFD software-Fluent on an IBM eServer cluster-Glacier, hosted by the University of British Columbia. This cluster is an important part of WestGrid computing facilities (www.westgrid.ca) and under heavy load everyday. To overcome the restrictions of Fluent parallel computing license and long queue waiting-time on the Glacier cluster, the most time-consuming simulations in **Chapter 4** are performed by MFIX on a PC cluster in the Physics and Astronomy Department at the same time. Valuable experience in CFD, from in-house code to commercial software and open-source software, has been learnt during the research. In addition, preliminary verification of each solver is performed by comparing simulation results of a simple bubbling fluidized bed with one another.

Chapter 3. SINGLE GAS JET IN A BUBBLING FLUIDIZED BED

3.1 INTRODUCTION

As already mentioned in **Chapter 1**, understanding of the hydrodynamics of gas and solids movement resulting from the introduction of gas jets could have considerable significance in improving reactor design and process optimization. With the significant improvements in computational power and numerical algorithms, numerical modeling has become an attractive tool for studying fluidization. Although there is a considerable amount of literature dealing with the horizontal injection of gas jets into fluidized beds (Merry, 1971; Rajan and Christoff, 1982; Xuereb et al., 1991b; Chyang et al., 1997; Hong et al., 1997; Al-Sherehy, 2002), there are only a few numerical studies of the hydrodynamic aspect of horizontal jet penetration into fluidized beds. Hong et al. (1997) performed two-dimensional simulations with an Eulerian-Eulerian model to study the mechanism of the formation of a jet when gas was injected through an inclined nozzle into a fluidized bed. In their article, simulation results regarding only the jet penetration length were reported, which agreed well with their experimental measurements. From experimental observations, it has been shown that the penetration of the horizontal jet issuing from a long slot in a two-dimensional fluidized bed differed remarkably from that of the jet issuing from a round orifice, as the fluidizing gas and solid particles can move around the sides of the jet in the latter case (Chen and Weinstein, 1993). For this reason, Tyler and Mees (1999) conducted three-dimensional simulations to investigate the interaction of a horizontal jet on fluidized bed hydrodynamics, but only preliminary results were reported. So far, no complete three-dimensional numerical simulation of horizontal jet penetration has been reported.

The objective of this study is to simulate horizontal gas injection into a cylindrical fluidized bed of FCC particles using a three-dimensional multiphase CFD code. The code is based on an

Eulerian-Eulerian granular kinetic model. Different jet velocities are simulated, and the results of these simulations are compared with the available experimental data.

3.2 NUMERICAL METHOD

3.2.1 Hydrodynamic model

A finite volume CFD code utilizing curvilinear coordinate transformation (He and Salcudean, 1994; Nowak and Salcudean, 1996) was extended to multi-phase flows by Pougatch (2005). A multi-fluid Eulerian-Eulerian model is adopted, as it is the most suitable for fluidized bed simulations. The continuous phase – air – and the discrete one – solid particles – are interpenetrating. The flow is assumed to be isothermal, the gas phase is incompressible, there is no mass transfer between phases, and particles are spherical and mono-sized. The governing equations and constitutive correlations summarized in **Chapter 2** are solved, and the algebraic form of granular temperature is used in the simulation. The solution method is an extension of a PISO procedure to multiple phases (Spalding, 1980). The momentum equations for each curvilinear velocity are solved simultaneously for both phases to account implicitly for inter-phase friction. The relationships for the velocity corrections are obtained from the coupled momentum equations by solving the matrix equations. To construct a pressure correction equation, each phase momentum equation is divided by the corresponding phase density before they are added together. As the sum of all volume fractions equals unity, the transient term of the final total mass conservation equation is simplified. The velocity correction equations are substituted into this equation to produce a pressure correction equation in a manner described by Patankar (1980). The solution of this equation serves to improve the velocity corrections by accounting for the influence of the velocity and pressure in the neighboring cells, and the improved values are again used in the pressure correction equation. These are PISO iterations, and their numbers can be controlled. Detailed information can be found in Pougatch (2005).

3.2.2 Simulation setup

An experimental study of the horizontal gas jet penetration into a cylindrical fluidized bed of FCC particles was conducted by Al-Sherehy at UBC (Al-Sherehy, 2002; Al-Sherehy, 2004). In Al-Sherehy's experiments, the fluidized bed was made of two sections, a main (lower) section of 152 mm diameter, 2056 mm in height, and an expanded (upper) section of 229 mm diameter, 315 mm in height with a smooth conical transition between these two sections, as shown in Figure 3-1. The column, 1150 mm in height, was filled with FCC particles at rest, and the fluidizing air was injected uniformly from the bottom at a superficial velocity of 5.1 mm/s. Secondary gas was injected into the fluidized bed through a small tube mounted on the wall 560 mm above the distributor. The inside diameter of the tube was 4.3 mm. In the experiments, different jet penetration lengths were measured by visual observation with varying gas injection velocities through the nozzle.

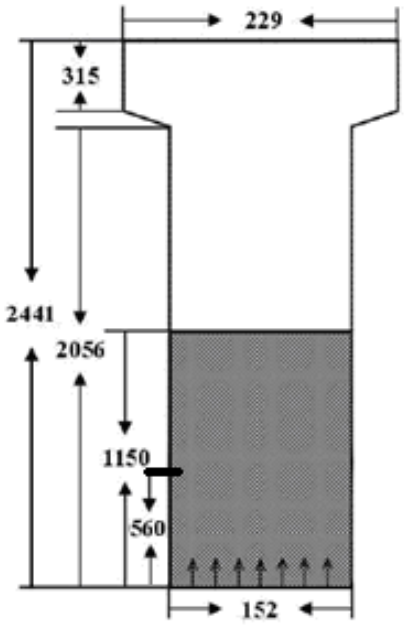

Figure 3-1. Geometry of the fluidized bed (unit: mm).

The material properties and operating conditions are listed in Table 3-1; most of them are obtained from Al-Sherehy's experiments, while the value of the restitution coefficient is taken from the literature (McKeen and Pugsley, 2003a). According to the experimental measurement of Chyang et al. (1997), the shape of a nozzle orifice has minimal effect on the jet penetration length. To simplify the problem and decrease the computational load, a nozzle of rectangular cross-section 4×3.63 mm, which has the same cross-section area as that of the nozzle employed in Al-Sherehy's experiments, is used in our simulations.

Table 3-1. Material properties and operating conditions.

Property	**Value**
Particle average diameter d_p	61 μm
Particle density ρ_p	1460 kg/m^3
Minimum fluidization velocity U_{mf}	0.003 m/s
Voidage at minimum fluidization ε_{mf}	0.48
Minimum bubbling velocity U_{mb}	0.007 m/s
Static bed height H_0	1.15 m
Fluidization velocity U_g	0.0051 m/s
Jet velocity U_j	50 m/s, 78.5 m/s, 156 m/s
Nozzle diameter D_j	4.3 mm
Restitution coefficient e_p	0.95
Gas density ρ_g	1.225 kg/m^3
Gas viscosity μ_g	1.789 e-5 Pa·s

As the modeled geometry and flow conditions are symmetric with the plane through the axes of the nozzle and the cylinder, only half of the domain needs to be simulated. A non-uniform curvilinear structured grid, which is fine near the nozzle orifice and coarse away from it, was developed as shown in Figure 3-2. The boundary conditions utilized in the simulations are also schematically shown in the figure. The lateral walls of a fluidized bed are modeled using a no-slip boundary condition for the gas phase and a free slip boundary condition for the solid phase, assuming purely elastic collisions (van Wachem et al., 2001; Peirano et al., 2002). Constant pressure is assumed at the top of the freeboard and particles are free to leave the system. At the distributor and the nozzle inlet, the uniform gas velocities are specified and no particles enter the domain.

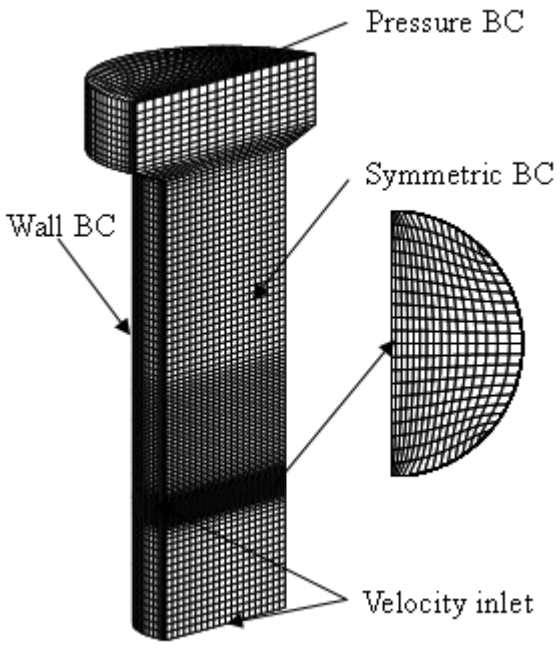

Figure 3-2. Non-uniform grid and boundary conditions used in the simulation.

As an initial condition of the simulation, the main section of the fluidized bed is partially filled with particles at a volume fraction of 0.6. The bed is then fluidized by air injected uniformly

from the bottom distributor. During the computation, the volume fraction of the solid phase is assumed not to be smaller than 10^{-5} to avoid numerical problems.

3.3 RESULTS AND DISCUSSION

3.3.1 Preliminary study and grid resolution

In Al-Sherehy's experiments, the static bed of 1.15 m in height was fluidized by air from the bottom distributor at a velocity of 5.1 mm/s, which was between the minimum fluidization velocity, $U_{mf} = 3$ mm/s, and the minimum bubbling velocity, $U_{mb} = 7$ mm/s, measured experimentally. In our preliminary study, an axisymmetric two-dimensional fluidized bed is simulated. As expected, the bed expands homogeneously and the overall voidage is about 0.49, higher than the minimum fluidization voidage, $\varepsilon_{mf} = 0.48$. To accelerate the three-dimensional simulation, the average voidage of 0.49 and the corresponding bed height obtained from the two-dimensional simulation are set as the initial conditions for the following computations. The bed is then fluidized for several seconds to approach a pseudo-steady state prior to injection of the gas jet.

In order to check the grid independence of the solution, three sets of non-uniform grid were generated. The simulation results obtained with the use of these grids during a short time period are compared. Because of the heavy computational load for three-dimensional simulation, even with the coarse grid, only one jet velocity of 50 m/s is tested with these three sets of mesh to study the grid independence.

Since the behavior of the gas jet is of most concern in the current study, the gas jet penetration lengths, defined as the horizontal distance from the orifice to the farthest point of the void with $\varepsilon_g = 0.8$ on different meshes and CPU times at $t = 0.5$ s after the start of the injection, are

compared in Table 3-2. It can be seen that the jet penetration lengths are similar on medium and fine meshes, while the result on the coarse mesh shows an obvious deviation from the others. By examining the voidage distribution in the jet region, the simulation on fine grid manifests the best bubble resolution, but the longest CPU time. The computations are carried out with a fixed time step of 1×10^{-4} s on a P4 Xeon 2.4 GHz processor with 2 GByte of RAM. As a compromise between time and accuracy, further simulations are conducted on the medium grid.

Table 3-2. Jet penetration lengths and CPU times for 0.5 second simulation on different meshes.

	Fine	**Medium**	**Coarse**
Grid nodes	45,696	29,835	19,773
Time (days)	12	8	4.3
Penetration (mm)	50.2	48.4	70.6

3.3.2 Bed expansion

Bed expansion is an important characteristic of the fluidized bed and it can be used as a measure to evaluate how well numerical simulations capture the hydrodynamic behavior of the bed. The bed expansion ratio is defined as $(H-H_0)/H_0$, where H and H_0 are the bed heights at the expanded and static state, respectively. For jetting velocities of 50 m/s and 78.5 m/s, the average bed heights are 2.1 m and 2.28 m, respectively. The corresponding bed expansion ratios, 0.82 and 0.98, are much higher than the expected value, which should be less than 0.4 based on experimental observations (Al-Sherehy, 2002). A similar overestimation of bed expansion in numerical simulations of bubbling fluidized beds of FCC particles has also been reported by other researchers (McKeen and Pugsley, 2003a; Zimmermann and Taghipour, 2005). These poor simulation results may be due to the reduced gas-particle drag forces due to the existence of agglomerates caused by the strong inter-particle forces between fine Geldart A particles.

Generally, the drag force acting on particles in fluid – solid systems is represented by the product of the drag coefficient β and the slip velocity $(V_p - V_g)$ between the two phases. To date, several drag models have been developed to predict the inter-phase drag coefficient and some of them are summarized in Table 3-3. These models are compared quantitatively in Figure 3-3 at a slip velocity of 0.1 m/s for the FCC particles used in the current study. There is no substantial deviation between drag coefficients predicted by each model at various solid phase volume fractions. With these similar drag models, the over-prediction of bed height for fine particles does not depend on the model choice. It has been demonstrated that the drag laws of Gidaspow (1994) and Syamlal and O'Brien (1989) predicted similar bed expansions and flow patterns in simulations of a bubbling fluidized bed of FCC particles (Zimmermann and Taghipour, 2005). In our study, a preliminary comparison of bed expansion predicted by the drag laws of Gidaspow (1994) and Gibilaro (2001) is also performed in the two-dimensional simulation of a bubbling fluidized bed of FCC particles, and no apparent difference in bed heights can be observed. As it is impossible to avoid over-prediction of bed height and correspondingly unrealistic voidages by any of the existing drag models, further modifications taking into account the effect of agglomeration on gas-solid drag force must be introduced.

Table 3-3. Correlations for drag coefficient plotted in Figure 3-3.

Wen and Yu, (1966)

$$\beta = \frac{3}{4} C_D \alpha_g^{-2.65} \frac{\alpha_p \alpha_g \rho_g \left|\vec{V}_p - \vec{V}_g\right|}{d_p}$$

$$C_D = \begin{cases} \dfrac{24}{\mathrm{Re}\cdot\alpha_g}(1 + 0.15(\mathrm{Re}\cdot\alpha_g)^{0.687}) & \text{if } \mathrm{Re}\cdot\alpha_g < 1000 \\ 0.44 & \text{if } \mathrm{Re}\cdot\alpha_g \geq 1000 \end{cases}$$

$$\mathrm{Re} = \frac{\rho_g \left|\vec{V}_p - \vec{V}_g\right| d_p}{\mu_g}$$

Gidaspow, (1994)

$$\beta = \begin{cases} 150\dfrac{\alpha_p^2 \mu_g}{\varepsilon_g d_p^2} + 1.75\dfrac{\alpha_p \rho_g \left|\vec{V}_p - \vec{V}_g\right|}{d_p} & \text{if } \alpha_p > 0.2 \\ \dfrac{3}{4} C_D \alpha_g^{-2.65} \dfrac{\alpha_p \alpha_g \rho_g \left|\vec{V}_p - \vec{V}_g\right|}{d_p} & \text{if } \alpha_p \le 0.2 \end{cases}$$

$$C_D = \begin{cases} \dfrac{24}{\mathrm{Re}\cdot\alpha_p}(1 + 0.15(\mathrm{Re}\cdot\alpha_p)^{0.687}) & \text{if } \mathrm{Re}\cdot\alpha_g < 1000 \\ 0.44 & \text{if } \mathrm{Re}\cdot\alpha_g \ge 1000 \end{cases}$$

Syamlal and O'Brien, (1989)

$$\beta = \frac{3}{4} C_D \frac{\alpha_p \alpha_g \rho_g}{V_r^2 d_p} \left|\vec{V}_p - \vec{V}_g\right|$$

$$C_D = \left(0.63 + 4.8\sqrt{\frac{V_r}{\mathrm{Re}}}\right)^2$$

$$V_r = 0.5\left[a - 0.06\,\mathrm{Re} + \sqrt{(0.06\,\mathrm{Re})^2 + 0.12\,\mathrm{Re}(2b - a) + a^2}\right]$$

$$a = \alpha_g^{4.14}$$

$$b = \begin{cases} P\alpha_g^{1.28} & \text{if } \alpha_g \le 0.85 \\ \alpha_g^{Q} & \text{if } \alpha_g > 0.85 \end{cases}$$

$P = 0.8$ and $Q = 2.65$ by default

Gibilaro, (2001)

$$\beta = \left(\frac{17.3}{\mathrm{Re}\,\alpha_g} + 0.336\right)\frac{\rho_g \left|\vec{V}_p - \vec{V}_g\right|}{d_p}\alpha_p \alpha_g^{-1.8}$$

Di Felice, (1994)

$$\beta = \frac{3}{4 d_s} C_D \alpha_p \alpha_g \rho_g \left|\vec{V}_p - \vec{V}_g\right| \alpha_g^{\eta}$$

$$C_D = \left(0.63 + 4.8\sqrt{\frac{1}{\mathrm{Re}\,\alpha_g}}\right)^2$$

$$\eta = 3.5 - 0.65\exp\left(-\frac{(1.5 - \log(\mathrm{Re}\,\alpha_g))^2}{2}\right)$$

Modified Hill-Koch-Ladd drag correlation (Benyahia et al., 2006)

$$\beta = \begin{cases} 1 + 0.375\,\mathrm{Re}' & \alpha_p \le 0.01 \text{ and } \mathrm{Re}' \le \dfrac{F_2 - 1}{0.375 - F_3} \\ F_0 + F_1(\mathrm{Re}')^2 & \alpha_p > 0.01 \text{ and } \mathrm{Re}' \le \dfrac{F_3 + \sqrt{F_3^2 - 4F_1(F_0 - F_2)}}{2F_1} \\ F_2 + F_3\,\mathrm{Re}' & \begin{cases} \alpha_p \le 0.01 \text{ and } \mathrm{Re}' > \dfrac{F_2 - 1}{0.375 - F_3} \\ \alpha_p > 0.01 \text{ and } \mathrm{Re}' > \dfrac{F_3 + \sqrt{F_3^2 - 4F_1(F_0 - F_2)}}{2F_1} \end{cases} \end{cases}$$

$$F_0 = \begin{cases} (1-w)\dfrac{1 + 3\sqrt{0.5\alpha_p} + 2.11\alpha_p \ln(\alpha_p) + 17.14\alpha_p}{1 + 0.681\alpha_p - 8.48\alpha_p^2 + 8.16\alpha_p^3} + w\dfrac{10\alpha_p}{\alpha_g^3} & 0.01 < \alpha_p < 0.4 \\ \dfrac{10\alpha_p}{\alpha_g^3} & \alpha_p \ge 0.4 \end{cases}$$

$$F_1 = \begin{cases} \dfrac{\sqrt{0.5\alpha_p}}{40} & 0.01 < \alpha_p \le 0.1 \\ 0.11 + 0.00051\exp(11.6\alpha_p) & \alpha_p > 0.1 \end{cases}$$

$$F_2 = \begin{cases} (1-w)\dfrac{1 + 3\sqrt{0.5\alpha_p} + 2.11\alpha_p \ln(\alpha_p) + 17.89\alpha_p}{1 + 0.681\alpha_p - 11.03\alpha_p^2 + 15.41\alpha_p^3} + w\dfrac{10\alpha_p}{\alpha_g^3} & \alpha_p < 0.4 \\ \dfrac{10\alpha_p}{\alpha_g^3} & \alpha_p \ge 0.4 \end{cases}$$

$$F_3 = \begin{cases} 0.9351\alpha_p + 0.03667 & \alpha_p < 0.0953 \\ 0.0673 + 0.212\alpha_p + \dfrac{0.0232}{\alpha_g^5} & \alpha_p \ge 0.0953 \end{cases}$$

$$\mathrm{Re}' = \frac{\rho_g \alpha_g \left|\vec{V}_p - \vec{V}_g\right| d_p}{2\mu_g}$$

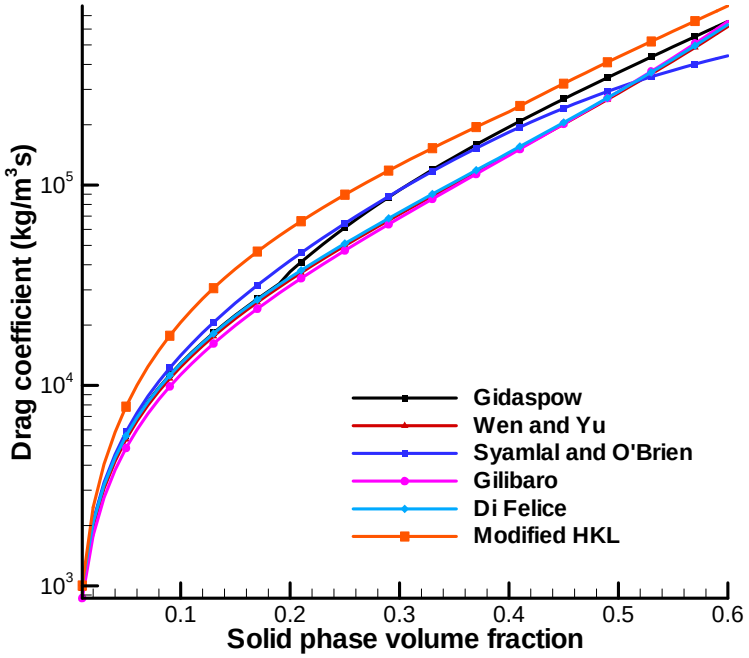

Figure 3-3. Comparison of different drag models for FCC particles for a slip velocity of 0.1 m/s.

To overcome the over-prediction of bed expansion in numerical simulations, two methods to modify the standard drag law proposed by Syamlal and O'Brien (2003) and McKeen and Pugsley (2003a) are investigated. Syamlal and O'Brien (2003) introduced a method to modify their drag law based on the minimum fluidization velocity and the minimum fluidization voidage measured in the experiment. With this method, reasonable simulation results for a bubbling fluidized bed of fine particles have been reported (Syamlal and O'Brien, 2003; Zimmermann and Taghipour, 2005). Unfortunately, the attempted implementation of the modification of Syamlal and O'Brien's drag law indicates that this method is not applicable to our problem, due to its limited range of applicability. McKeen and Pugsley (2003a) successfully adjusted Gibilaro's drag law with an empirical scale factor between 0.2 and 0.3 to simulate a bubbling fluidized bed of FCC particles. The application of this method has also been reported in numerical simulations of the cold flow FCC stripper and deaeration of FCC fluidized beds (McKeen and Pugsley, 2003b; Das Sharma et al., 2006). However, to find an appropriate scale factor, this empirical

approach requires an extensive case study for every application. Considering the expensive computation load of our three-dimensional simulation, it is impractical. Simply, a scale factor of 0.25 on Gibilaro's drag law, which has been employed many times in simulations of FCC particle flow (McKeen and Pugsley, 2003a; McKeen and Pugsley, 2003b; Das Sharma et al., 2006), is adopted directly.

In Figure 3-4, the distributions of the solid phase along the central symmetry plane for Gidaspow's drag law and scaled Gibilaro's drag law are compared. It is apparent that the bed height is substantially reduced with the scaled drag force. For jetting velocities of 50 and 78.5 m/s, the bed heights are 1.39 and 1.42 m, respectively, and the corresponding bed expansion ratios of 0.2 and 0.23, respectively, are much lower than predictions with the standard drag law of Gidaspow. In Figure 3-4(a), the volume fraction of the solid phase below the gas injection point is about 0.51, slightly lower than that at minimum fluidization. In Figure 3-4(b), however, the volume fraction of the solid phase is about 0.6, meaning that the region of bed is nearly packed. The reason for this phenomenon is that there is insufficient force in the model to fluidize the solid particles after scaling the drag relationship. This result is inconsistent with the fact that the bed is fluidized, as the gas velocity exceeds U_{mf} in the experiment. This unphysical behaviour can be attributed to the fact that the scale factor suggested by McKeen and Pugsley (2003a) is applicable to the bubbling regime only. Consequently, it is necessary to adjust the general scale factor to make it applicable to both the homogeneous expanded and bubbling regimes in our problem.

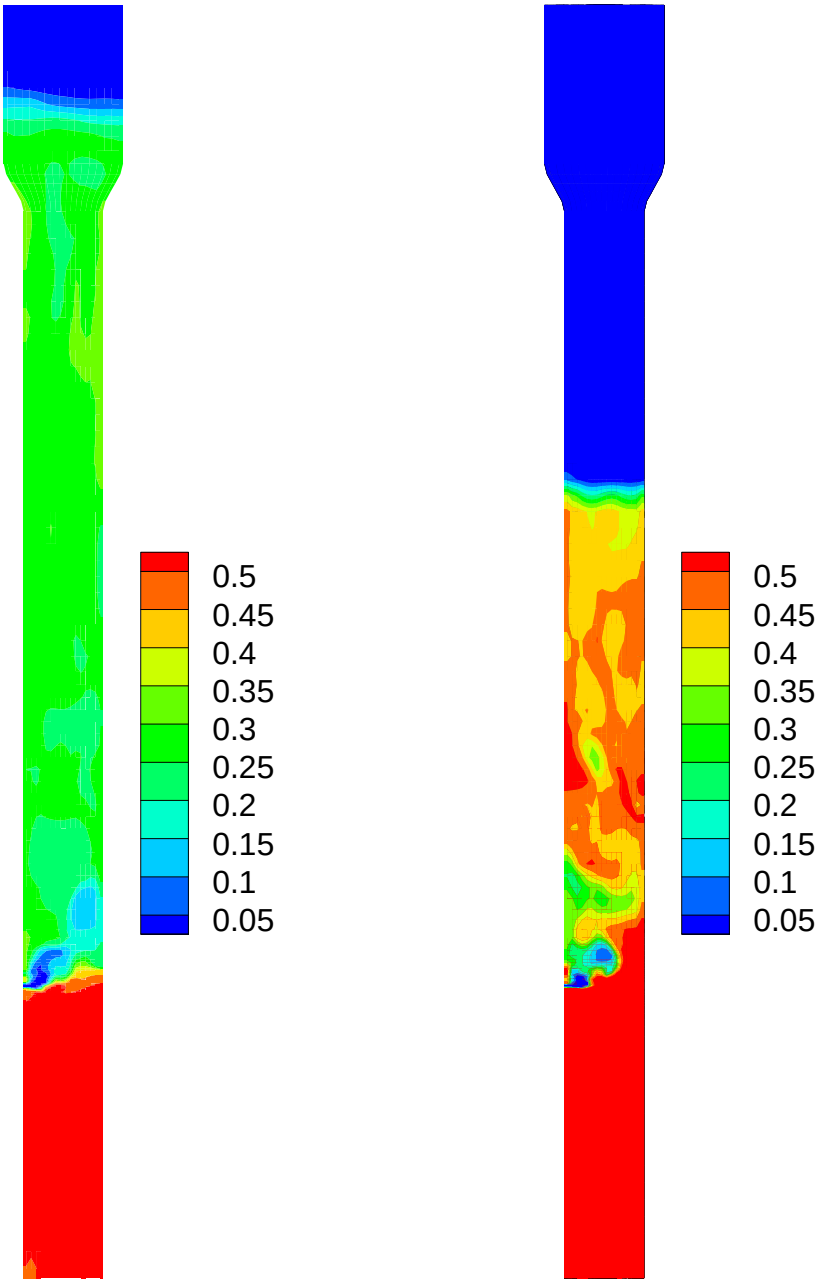

(a) (b)

Figure 3-4. Comparison of distributions of solid phase volume fraction inside bed (slice view) with different inter-phase drag models at $U_j = 78.5$ m/s. (a) Gidaspow drag law, (b) Gibilaro drag law scaled by a factor 0.25.

The correlations proposed for the drag coefficient are based mostly on the experimental measurements for homogeneous systems, such as fluidization and sedimentation of a liquid-solid system or gas-solid fixed bed. In the CFD modeling of fluidized beds, the drag coefficient is calculated in each small control volume where the distribution of the solid phase is assumed to be uniform. For most particles, such as Geldard B particles, it is possible to predict the correct drag coefficient by assuming a uniform distribution of solid particles in small control volumes. However, for fine cohesive particles in a dense flow, the formation of agglomerates due to the existence of strong inter-particle cohesive forces, such as van-der Waals force, leads to a strong heterogeneous structure (Kono, 1989). This is true even in a small control volume where the assumption of uniform distribution fails in predicting the correct effective drag coefficient with standard drag laws. To represent the reduced drag force, a scale factor applied to the standard drag law is simple and effective, but a careful adjustment should be made in regions where the flow is either extremely dense or dilute. In the control volume, as shown in Figure 3-5, the mixture comprises the agglomerate and emulsion phases with voidages ε_a and ε_e, respectively. Similar to the theoretical analysis, the agglomerate voidage is assumed to be the bed voidage at minimum fluidization (Yadav et al., 1994; Mostoufi and Chaouki, 2000).

$$\varepsilon_a = \varepsilon_{mf} \tag{3.1}$$

Then the average voidage in the region can be calculated as

$$\overline{\varepsilon} = f\,\varepsilon_{mf} + (1-f)\,\varepsilon_e \tag{3.2}$$

where f is the volume fraction of agglomerates.

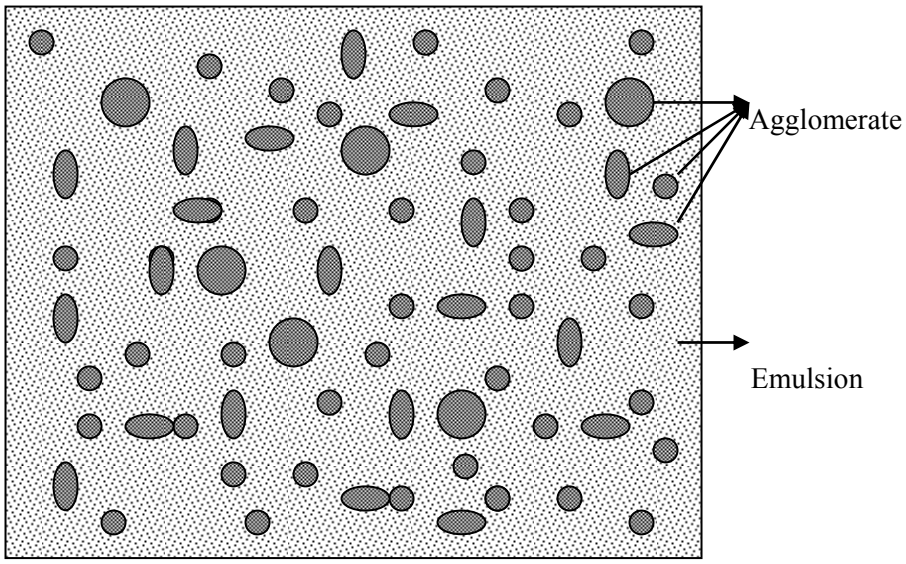

Figure 3-5. Schematic of the agglomerates and emulsion phases in a control volume.

With the preceding assumptions, the volume fraction of the agglomerates approaches unity in very dense regions where the bed voidage is close to that at minimum fluidization state. As a result, the whole region becomes a homogeneous emulsion phase where the drag force can be predicted based on existing correlations developed from measurements of homogeneous systems. In very dilute regions, there barely exists any agglomerate. Again, the drag force can be calculated by the standard drag model, which ensures the correctness of the drag force for an individual particle in fluid. However, no experimental evidence can be used to define at what point agglomerates start to disappear. Here, a voidage of 0.9 is used referring to the work by Yang et al. (2003). As little is known about the size and volume fraction of agglomerates in the medium dense region, a scale factor of 0.25 suggested in the literature (McKeen and Pugsley, 2003a; McKeen and Pugsley, 2003b; Das Sharma et al., 2006) is used in the current study to approximate the reduction of the drag force caused by the existence of the agglomerates. Finally, by fitting the transition of the scale factor from the homogeneous expanded regime to the

bubbling regime with continuous function, the expression for the scale factor C vs. voidage is correlated as follows:

$$C = \begin{cases} 1 & \text{if } \alpha_g \le \varepsilon_{mf} \\ 0.375 * \cos\left(\dfrac{\pi(\alpha_g - \varepsilon_{mf})}{\varepsilon_{mb} - \varepsilon_{mf}}\right) + 0.625 & \text{if } \varepsilon_{mf} < \alpha_g \le \varepsilon_{mb} \\ 0.25 & \text{if } \varepsilon_{mb} < \alpha_g \le 0.9 \\ 0.375 * \cos(10\pi\alpha_g) + 0.625 & \text{if } 0.9 < \alpha_g \end{cases} \tag{3.3}$$

In our simulations, the voidage at minimum bubbling of 0.55 is used, and the scale factor is plotted in Figure 3-6. With this new scale factor on Gibilaro's drag model, the average bed heights for jetting velocities of 50 and 78.5 m/s are 1.42 and 1.49 m, respectively, and the corresponding bed expansion ratios of 0.26 and 0.3 fall within the expected range. The fluidization in the lower section of the bed is achieved and satisfactory jet penetration lengths are obtained, as discussed in the following sections.

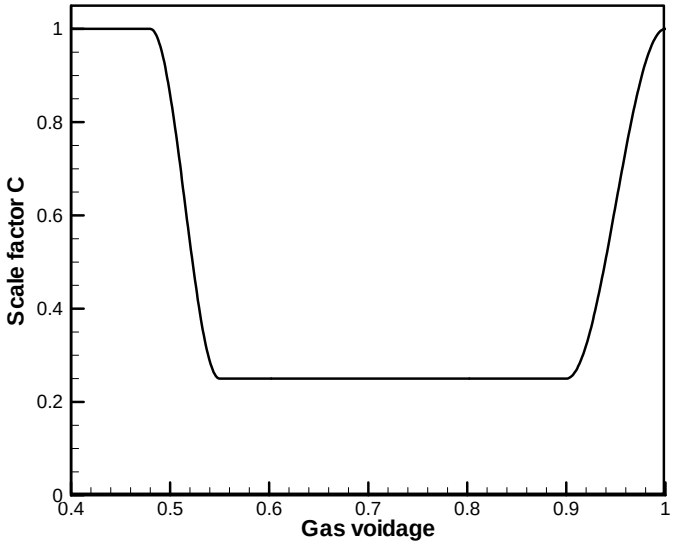

Figure 3-6. The new scale factor used in present study.

3.3.3 Jet penetration

In numerical simulations, a large bubble is formed when gas is injected into the bed horizontally. As the bubble progresses upwards, another starts to form and a fluctuating jet develops at the orifice. Due to the addition of secondary gas, the bed keeps expanding and finally reaches a statistic steady state where the bed height remains almost constant, with only small fluctuations. To avoid the transient startup phenomenon, data is recorded every 0.01 s for analysis after a statistically steady state has been reached. To measure the jet penetration length, the boundary of jet and bubbles is defined at a voidage of 0.8, which has been widely adopted by other researchers (Hong et al., 1997; Gelderbloom et al., 2003). The typical gas jet observed in the simulation is presented in Figure 3-7. In cases where the gas jet curves upwards or begins to pinch off to form a bubble, the maximum penetration length is considered to be the distance from the orifice to the end of the curvature, or the pinch point, as shown in Figure 3-7(a) and (b), which is in line with the measurement in the experiment (Xuereb et al., 1991a). The plots on the left-hand side represent the distributions of the solid phase volume fraction on the symmetry plane obtained from the simulations; on the right-hand side, the boundaries of the jets are drawn, as well as the jet penetration lengths. Results are obtained for the maximum jet penetration lengths at different times and they are averaged to obtain a representative value.

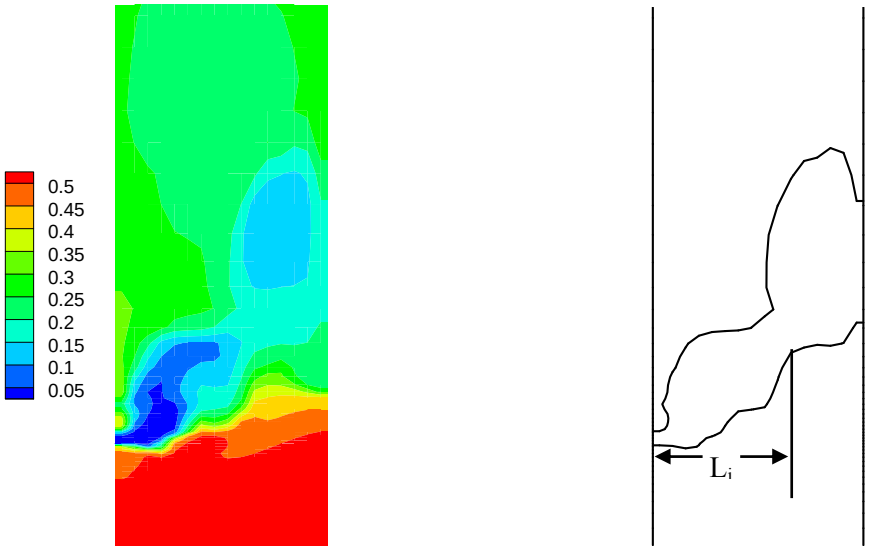

(a)

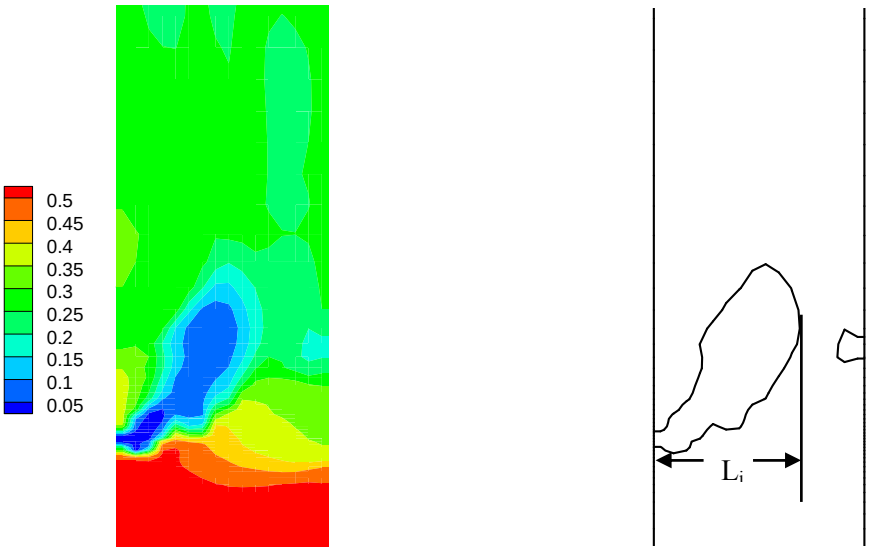

(b)

Figure 3-7. Distributions of the solid phase volume fraction in the typical jet regions (left) and the measured jet penetration lengths (right). (a) jet curves, (b) jet pinches.

To investigate the jet penetration lengths, results for both unscaled and scaled drag models are analyzed. In Figure 3-8, the penetration lengths for different jetting velocities by Gidaspow's

drag model and scaled Gibilaro's drag model are compared with the experiment and with empirical correlations. For convenience, the jet penetration length is nondimensionalized with the nozzle diameter. The predictions of Zenz (1968) and Shakhova (1968) correlations are far below the experimental data because those correlations are derived from experimental measurements for very coarse particles. In the figure, predictions of Merry (1971), Hong et al. (1997) and Benjelloun et al. (1995) correlations are plotted. The correlation of Hong et al. (1997) over-predicts the experimental data significantly, since it was developed based on measurements in a two-dimensional fluidized bed. It can be observed that Merry's correlation provides good fit to the Al-Sherehy's data for $U_j = 50$, 78.5 m/s, but over-predicts the penetration length for $U_j = 156$ m/s, while the correlation by Benjelloun et al. (1995) shows the best fit to the experimental data. A similar trend was reported by Ariyapadi et al. (2004) when they compared the experimental jet penetration data for a horizontal gas jet with existing correlations.

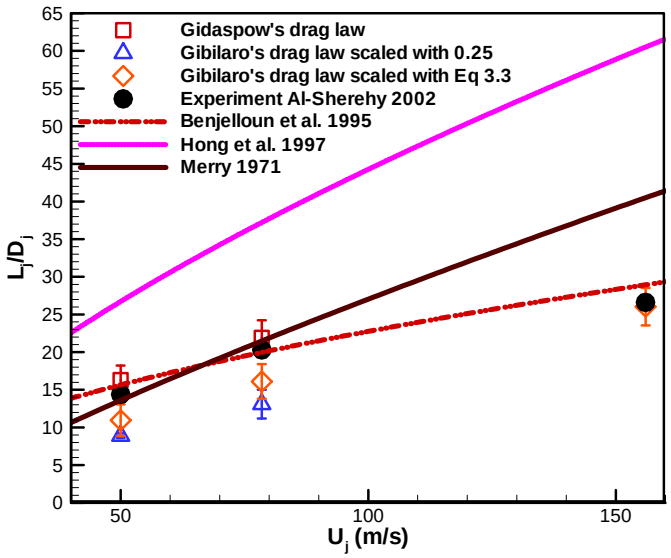

Figure 3-8. Comparison of the jet penetration lengths for scaled and unscaled drag laws with experimental data and empirical correlations (error bar indicates the standard deviation of measured data).

Comparison with the experiment shows that jet penetration lengths from the numerical simulation by Gidaspow's drag law agree well with the experimental data, though the bed expansion is over-predicted, as discussed in the preceding section. After the scaled Gibilaro's drag law with a general correction scale factor of 0.25 is implemented into the model, the jet penetration lengths decrease greatly in comparison with predictions by the standard drag law. The jet penetration lengths are under-predicted due to the existence of the almost packed region below the jet caused by the unnecessary correction of the drag force at the dense region in the lower section of the bed. Finally, the jet penetration lengths predicted by the variable-scaled Gibilaro's drag law are measured. For this particular correlation, one more case for the jetting velocity of 156 m/s is simulated. Good agreement with experimental data and empirical correlations is achieved. From Figure 3-8, we can see that both predictions by Gibilaro's drag model scaled with C from equation (3.3) agree with the experimental data. It should be pointed out here that the nozzle is usually inserted into the fluidized bed at a small distance from the wall in the experiments to eliminate the effect of the side wall on the jet behaviour (Merry, 1971; Al-Sherehy, 2002). In the current work, the nozzle is simplified as an orifice on the wall, leading to the tendency of the gas jet to sometimes cling to the wall for the low jet velocities (Coanda effect). This effect may contribute to the slight under-prediction of the jet penetration length in numerical simulations at jetting velocities of 50 and 78.5 m/s for the scaled Gibilaro's drag model.

3.3.4 Expansion angle

The jet expansion angle is dependent on the rate at which momentum is transferred from the gas jet to the entrained gas and solids. Due to the transfer of momentum, the jet cross-section increases with the decrease of the gas velocity along the jet to maintain the constant gas flow rate inside the jet (Vaccaro, 1997). In our simulations, the jet is a torch-like coherent void that bends upward because of gravity. The diameter of the jet increases after leaving the injection orifice, and then decreases towards the end of the region, finally collapsing to form bubbles. Because of

the periodical formation of bubbles at the end of the jet, the jet pattern in this region tends to oscillate.

Due to the significant importance in modeling jet behavior, the jet expansion angles are measured by analyzing the results from the numerical simulations with Gibilaro's drag model scaled with C defined in equation (3.3). The jet expansion angle can be obtained by measuring the angle between the two lines that overlay the jet boundary, as shown in Figure 3-9. Nevertheless, due to the vigorous oscillation of the jet, only a range of expansion half-angles are measured, which are of the order of 12-20 and 11-16.5 degrees for the gas jetting velocity of 78.5 and 156 m/s, respectively. The expansion angle decreases slightly when increasing the gas jetting velocity from 78.5 to 156 m/s. This phenomenon is consistent with the trend that θ decreases with increasing jetting velocity, reported for a vertical jet in a fluidized bed of fine powders in ambient conditions (Cleaver et al., 1995).

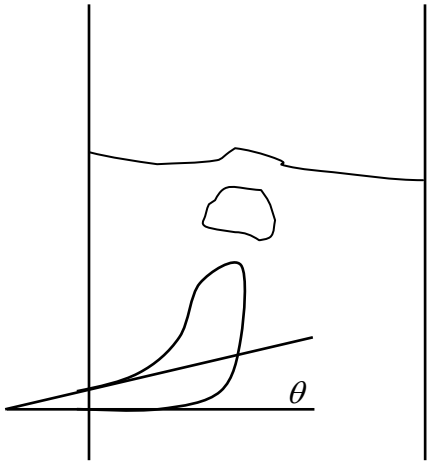

Figure 3-9. Schematic of the jet expansion angle.

The values of the jet expansion half angle predicted in current numerical simulations are consistent with the data reported in early experiments, as listed in Table 3-4, though there is an evident difference between the range of experimental configurations and operating conditions.

Table 3-4. Jet half angle of horizontal gas jets into fluidized beds.

Reference	d_p (μm)	ρ_p (kg/m^3)	D_j (mm)	U_j (m/s)	$\theta/2$ (°)
Present study	61	1460	4.3	78.5	12~20
	61	1460	4.3	156	11~16.5
Demichele et al., (1976)	-	-	-	-	13~18
Xuereb et al., (1991a)	1130	1020	8	63~125	5~19
	725	1020	8	47~125	4~14
	605	1020	8	63~125	4~14
Copan et al., (2001)	370	930	3.81	210~570	4~4.5
Ariyapadi et al., (2003)	70	1400	0.84	346	10
	150	1400	1.5	175,240	10~15

3.4 SUMMARY

A three-dimensional numerical simulation of a single horizontal round gas jet issuing into a cylindrical gas-solid fluidized bed of FCC particles is conducted with an in-house CFD code. Over-prediction of bed heights is reported and available approaches to improve the model predictions are investigated. Extension of work by McKeen and Pugsley (2003a) leads to a non-uniform scale factor on Gibilaro's interphase drag model, taking into account the effect of agglomerates on fine particle flow. This is incorporated into the simulation. The predicted bed heights and distribution of the solid phase are consistent with the observations in experiments of Al-Sherehy (2002) at UBC. The transient simulation results show that the jet penetration lengths at different jet velocities are in good agreement with published experimental data and predictions of empirical correlations. Furthermore, the expansion angles of the gas jet are also obtained from the current simulations and their dependence on the jet gas velocity is evaluated. Good consistency with the experimental findings in the literature is attained. The agreement with

experimental results demonstrates the validity of this scaled drag model in the simulation of an FCC fluidized bed.

Chapter 4. MULTIPLE GAS JETS IN A BUBBLING FLUIDIZED BED

4.1 INTRODUCTION

In **Chapter 3**, the jet penetration and expansion angle for a single horizontal gas jet in a fluidized bed were studied with numerical simulations. However, in practice, injections of multiple jets are almost always encountered. Consequently, it is necessary to investigate the interaction between jets in addition to single jet behaviour. Unfortunately, studies of the horizontal jet in fluidized bed reactors are mainly focused on a single jet. Research on multiple horizontal jets in fluidized beds is very limited. Donald et al. (2004) investigated penetration of a single jet, interacting pairs of jets, and five jets entering together into a bubbling fluidized bed of FCC particles. They found that a jet was affected more by another jet below it than by neighbouring jets at the same level, and the influence from a jet above it was minimal. Jets issuing from nozzles at the same level influenced each other when they overlapped. Several papers investigating the effects of secondary air injection through multiple nozzles on the flow hydrodynamics in circulating fluidized beds have been published (Cho et al., 1994; Marzocchella and Arena, 1996; Knoebig and Werther, 1999; Kim and Shakourzadeh, 2000). The effects of secondary gas injection on the mixing behaviour of gas and solids, as well as heat transfer, were investigated (Ran et al., 2001; Koksal and Hamdullahpur, 2004; Koksal et al., 2008). In all these studies, only the overall bed hydrodynamics such as pressure drop, solids hold-up, particle velocity, were measured to analyze the effect of secondary gas injection. The behaviour of the gas jets was not reported.

Gas mixing in fluidized beds, as in any other type of reactors, is a major concern in design (Van Deemter, 1985). Gas and solid mixing has been extensively studied with a variety of techniques (Kunii and Levenspiel, 1991; Bi et al., 2000). However, little work can be found in the literature

on the mixing of secondary feed injection in bubbling fluidized beds. Al-Sherehy et al. (2004) investigated the effect of distributing gaseous feed along a bench-scale bubbling fluidized bed with a diameter of 152 mm. In their experiment, all secondary gas was injected through a single nozzle mounted on the side wall. Both steady and unsteady-state experiments were conducted, and they showed that the secondary gas concentration profile at the injection level was almost uniform for high secondary and low primary gas velocities. The secondary gas readily mixed within a short distance above the injection level. Back-mixing of the secondary gas was detected and it was primarily influenced by the primary feed superficial gas velocity. Song et al. (2005) investigated gas mixing in the reactor section of a fluid coker cold model by using helium as tracer gas. In this experiment, secondary gas was injected into the bed through six feed rings, which contained 10-18 nozzles to achieve relatively uniform injection around the outer perimeter. The mean residence time of gas from the feed nozzles indicated intensive gas mixing inside the system. Christensen et al. (2008a, b, c) conducted both experiment and numerical simulation to study distributed secondary gas injection via a fractal injector submerged in a two-dimensional bed. Their results indicated improved gas-solid contact in a fluidized bed with secondary gas injection. However, the fractal injector used in their experiment is different from secondary feeding systems investigated previously (Koksal and Hamdullahpur, 2004; Song et al., 2004).

The objective of this part of study is to investigate numerically the horizontal gas injection into a bubbling fluidized bed. By means of three-dimensional numerical simulation, single and multiple horizontal jets issuing into the bubbling fluidized bed are investigated to obtain a better understanding of the jet behaviour. The interactions between the jet and the surrounding gas, solids, as well as the ascending bubbles in the system are analyzed and compared with available experimental observations reported in the literature. For multiple horizontal jets injected at the same level, the interaction between jets and its influence on the jet penetration are evaluated, and the effect of secondary gas injection on the hydrodynamics of the bubbling fluidized bed is determined by analyzing the solids hold-up, gas and solids velocities, and mean bubble sizes. In

addition, we also study the mixing of secondary gas with the bed materials by introducing a tracer gas with the secondary gas injections. Both unsteady and steady results are analyzed to characterize the mixing behaviour. The effects of gas injection velocity and jet arrangement on the gas-solid mixing are evaluated.

4.2 NUMERICAL METHOD

4.2.1 Numerical models

In the current study, the Multiphase Flow with Interphase eXchanges (MFIX) CFD code, available from the U.S. Department of Energy's National Energy Technology Laboratory (NETL) at http://www.mfix.org, is used to solve the partial differential equations system with closure relations from the Eulerian-Eulerian model (Syamlal et al., 1993). MFIX is a general-purpose computer code for modeling the hydrodynamics, heat transfer, and chemical reactions in fluid-solids systems, which has been successfully used for describing bubbling and circulating fluidized beds and spouted beds (McKeen and Pugsley, 2003a; Syamlal and O'Brien, 2003; Benyahia et al., 2005; Das Sharma et al., 2006). For the flow without chemical reactions, as considered in the current study, the hydrodynamic model equations are similar to the equations summarized in **Chapter 2**. The governing equations for the solid phase are closed by the kinetic granular theory and detail information about the model equations, as well as closure correlations, can be found in the MFIX documentation and in Syamlal et al. (1993) and Benyahia et al., (2007).

For dense gas-solid flows such as fluidized beds, the turbulence of the particulate phase is modeled with granular temperature based on granular kinetic theory (Gidaspow, 1994). The turbulence of the carrier phase is not of primary concern as particle-particle collisions dominated the flow (Crowe et al., 1996). Furthermore, it has been reported that the inertia of particles damps out the turbulence in the carrier phase, and the turbulence of the carrier phase can be

ignored (Enwald et al., 1996; Portela and Oliemans, 2006). In dilute flows, the turbulent fluid-particle interaction becomes important and complex. A significant amount of work has been done to modify the turbulence of the gas phase by taking into account interfacial turbulent momentum transfer (Reeks, 1991; Cao and Ahmadi, 1995; Simonin, 1996; de Bertodano, 1998; Xu and Subramaniam, 2006). However, a generally applicable turbulence model for two-phase flow is not available, and the multiphase turbulence is still a challenging problem in CFD. For simplicity, the sub-grid scale (SGS) model proposed by Deardorf (1971) is employed to model the gas phase turbulence; this has been applied extensively in numerical simulations of fluidized beds (Samuelsberg and Hjertager, 1996; Lu and Gidaspow, 2003; Hansen et al., 2004; Huanpeng et al., 2004). To study the mixing of tracer gas in the system, a species balance equation for the gas phase is solved, with an effective diffusivity calculated from turbulent viscosity.

Another important factor is the drag force between the gas and the solid phase, which characterizes the momentum exchange between the continuous phase and the dispersed phase. To date, several drag models have been developed to predict the inter-phase drag coefficient, and there is no substantial deviation between them as discussed in **Chapter 3**. In our simulation, the simulated coke particles are close to the boundary of Geldart Group A and B (Yang, 2007); hence, the inter-particle cohesive force is not as important as for fine Geldart A particles (McKeen and Pugsley, 2003a; Li et al., 2008). Therefore, the well-known Gidaspow drag model is employed.

In most numerical simulations of fluidized beds, the gas phase is treated as an incompressible phase. This is a reasonable assumption for most gas-solid fluidized bed systems operating with relatively low gas velocities. The influence of gas compressibility on numerical predictions of bubbling fluidized beds was evaluated by Johansson et al. (2006), and no significant effect was reported. In our simulations, however, the jet velocity is relatively high; therefore,

compressibility effects are included. The gas density is calculated by the ideal gas law with an assumption of constant total enthalpy.

$$P = \rho_g \frac{R}{M_g} T_g \tag{4.1}$$

$$h_{total} = C_p T_g + \frac{1}{2}\left|\vec{V}_g\right|^2 \tag{4.2}$$

where P, ρ_g, T_g, $\vec{V}_g$ and h_{total} are the pressure, density, temperature, velocity, and total enthalpy of gas; R is the universal gas constant, M_g is the molecular weight, and C_p is the specific heat capacity, respectively.

4.2.2 Simulation setup

In order to allow direct comparison with experimental measurements, the experimental setup of Ariyapadi et al. (2003) is simulated. In the experiment, a rectangular column of 0.1 m thickness and 0.5 m length was constructed to optimize X-ray image acquisition. Both gas and gas-liquid jet penetrations in a bubbling fluidized bed were investigated by taking X-ray images. We simulate only the gas injection through a small orifice. The orifice with a square cross-section and equivalent diameter 1.5 mm is used to simulate the jet penetration, since the shape has been shown to have a minimal effect on jet behavior (Chyang et al., 1997).

To save computational time, a small-scale bubbling fluidized bed is numerically constructed to match the experimental setup by Ariyapadi et al. (2003). The cross-section of the column is square, 0.1 m × 0.1 m, and the total height is 0.65 m, as shown schematically in Figure 4-1(a). The same particles and nozzle as those in Ariyapadi et al. are used in this system. For single jet injection, secondary gas is introduced from an orifice (orifice A) on the wall located 0.17 m above the distributor. For multiple jet injections, the jets arrangement is shown in Figure 4-1(b), as well as the coordinate system used in the simulation. Combinations of jets AB, AC, ABC, and

ABCD are simulated to study the multiple jet injections. Gas velocity through the orifices is adjusted to control the flow rate of secondary feed injection.

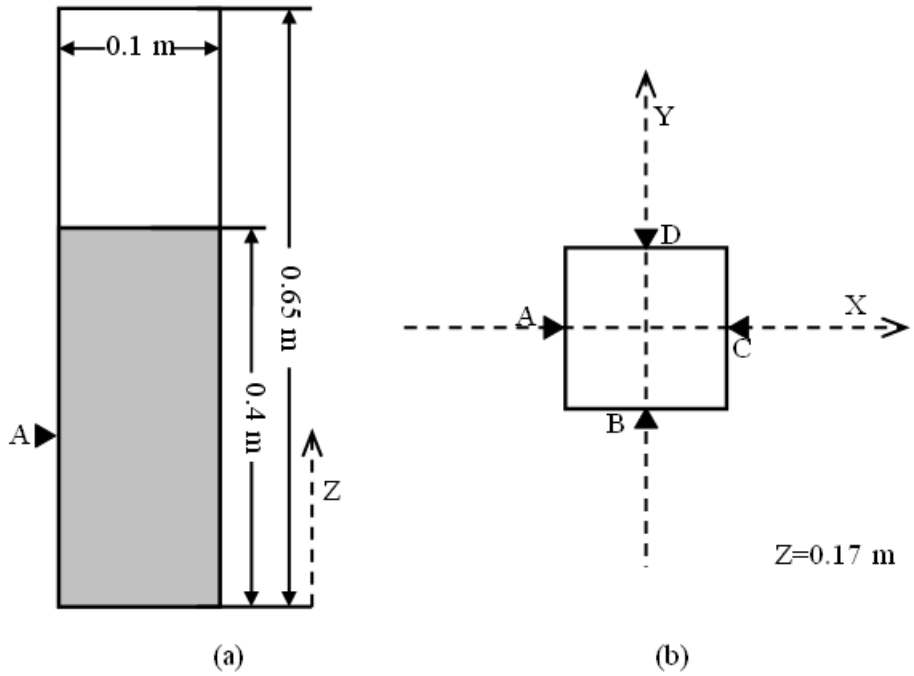

Figure 4-1. Geometry of fluidization column and arrangement of jet injections: (a) bed geometry; (b) arrangement of jets.

The material properties and operating conditions used in the simulation are summarized in Table 4-1. Except where noted otherwise, these parameters are fixed in the whole study.

Table 4-1. Bed properties and operating conditions.

Property	**Value**
Particle average diameter d_p	150 μm
Particle density ρ_p	1400 kg/m^3
Superficial gas velocity from distributor U_p	0.052 m/s
Initial voidage ε_0	0.5

Property	**Value**
Static bed height H_0	0.4 m
Nozzle diameter D_j	1.5 mm
Restitution coefficient e_p	0.95
Temperature T	293 K
Gas viscosity μ_g	1.8×10^{-5} Pa·s

A non-uniform structured grid with 139,000 grid points is employed in the simulation. It is relatively coarse in the freeboard region and fine in the bed region, with some extra refinement around the injection area. In the literature, it has been reported that the grid size of 5 mm is sufficiently small for obtaining a grid-independent numerical solution for bubbling fluidized bed of fine FCC particles with superficial gas velocities ranging from 0.05 to 0.2 m/s using the MFIX code (McKeen and Pugsley, 2003a). This grid size was also used by Cammarata et al. (2003) to perform 2D and 3D CFD simulations of bubbling fluidized beds using Eulerian-Eulerian models. In our preliminary study of the grid size, a uniform grid of 5 mm is found to be small enough to simulate a two-dimensional bubbling fluidized bed of similar bed properties and operating conditions. Consequently, the grid size in the section below the secondary gas injection is kept constant at 5 mm. To make sure the grid is fine enough in the jet region and downstream, two grid refinements are carried out in the three-dimensional simulations and axial solid holdups are compared for these two grids. From these studies, the grid is believed to be sufficient for the current simulation. Ideally, a full three-dimensional grid sensitivity study should be performed. However, the computational time would then become prohibitively long.

The following boundary conditions are adopted. The lateral wall of the bed is modeled using a non-slip boundary condition for the gas phase and a partial slip boundary condition for the solid phase (Johnson and Jackson, 1987).

$$V_{p,w} = -A\frac{\partial V_{p,w}}{\partial n} \tag{4.3}$$

where

$$A = \frac{6\mu_p \alpha_{p,\max}}{\sqrt{3}\pi\varphi\rho_p \alpha_p g_{0,p}\sqrt{\Theta_p}} \tag{4.4}$$

Here φ is the specularity coefficient, an empirical parameter qualifying the nature of particle-wall collisions. Its value ranges between zero (smooth wall) and one (rough wall). At the top boundary, constant pressure is assumed and particles are free to leave the system. For the bottom distributor and the nozzle inlet, uniform inlet gas velocities are specified with no particles entering the domain.

Initially, the column is partially filled with stationary particles to a depth of 0.4 m with a volume fraction of 0.5. The simulation is performed in three steps. In the first step, the bed is fluidized by the primary gas through the bottom distributor at a superficial gas velocity of 0.052 m/s. After fully developed bubbling fluidization has been achieved, secondary gas is introduced via the orifices on the wall. When the flow reaches a statistical steady state, simulation results are saved for the analyses of flow hydrodynamics. In the last step, tracer gases are injected through the orifices to study the mixing behaviour of the secondary feed in the reactor. All numerical simulations are performed on a PC cluster in the Physics and Astronomy Department, UBC. The PC cluster has 60 nodes connected by Myrinet network interface cards, and each node has dual P4 Xeon 2.4 GHz processors and 2 GByte of RAM. Parallel computation with 8 CPUs is carried out for most cases.

4.3 RESULTS AND DISCUSSION

4.3.1 Comparison with the experiment of Ariyapadi et al.

To verify the current numerical models, a single gas jet penetration in a rectangular bubbling fluidized bed following Ariyapadi et al.'s experiment is simulated (Ariyapadi et al., 2003). Here, two jet velocities of 175 and 250 m/s through a 1.5 mm nozzle are simulated. The simulated jet penetration lengths are presented in Table 4-2, as well as experimental data by Ariyapadi et al. (2004). The results presented in Table 4-2 show that our simulations over-predict the jet penetration lengths for both velocities. This is most likely because jet-bubble interaction was ignored when measuring the jet penetration lengths in the experiment. From the two-dimensional X-ray images, it was hard to predict whether a bubble was passing through the jet or in the same plane, but either behind or in front of the jet. In the experiment, the frames where the bubbles seemed to affect the jet morphology were excluded from the measurements of jet penetration (Ariyapadi et al., 2003). Nevertheless, interaction between the horizontal jet and bubbles was vigorous, and the entrained bubbles were found to have a significant effect (Copan et al., 2001). This interaction contributes to the increase in average jet penetration and also leads to strong fluctuation of the jet. In order to be compatible with the experimental measurements, numerical results are averaged between the front and back walls to generate a series of "X-ray" images, and the average jet penetration is obtained from these images by neglecting the frames where bubbles seem to affect the jet morphology. The new jet penetration lengths measured with this method, presented in the last column of Table 4-2, show improved agreement with the experimental results.

Table 4-2. Comparison of jet penetration lengths.

U_j **(m/s)**	L_j **exp. (cm)**	L_j **num. (cm)**	L_j^* **num. (cm)**
175	4.95 ± 0.69	5.93 ± 1.29	5.21 ± 0.73
250	5.44 ± 0.42	7.48 ± 1.71	6.53 ± 1.09

L_j^*: jet penetration length obtained by averaging numerical results between the front and back walls and ignoring the frames with bubble-jet interaction

In addition, the jet expansion angle is measured. The jet expansion half-angles are in the range of 10-15 degrees for both cases, indicating good agreement with the experimental observation (Ariyapadi et al., 2003).

In this study, it is not expected that the compressibility of the gas phase has a significant effect on the jet behaviour, since the jet velocity decreases rapidly in a very short distance as the gas exits the nozzle due to the entrainment of solid particles and surrounding gas. In our simulations, it has been demonstrated that the effect of gas compressibility is very local. By comparing the result to the simulation with an incompressible gas phase, the local influence of gas compressibility has no effect on the overall hydrodynamics. To accelerate the computation, most of our simulations in the following paragraphs are conducted with a constant gas density.

4.3.2 Flow hydrodynamics

4.3.2.1 Single jet behaviour

The snapshots of the voidage contour in the XZ plane for jet velocities of 25, 50, 75, 100, 125, and 175 m/s are shown in Figure 4-2. In simulations, a constant torch-like jet is formed at the orifice in most cases except for the case with a jet velocity of 25 m/s, where a bubble adhering to the wall appears occasionally. The diameter of the jet increases after leaving the injection orifice, and then decreases towards the end. The jet periodically collapses to form bubbles in the end. Because of the periodic formation of bubbles and the strong interaction between the jet and ascending bubbles in the crossflow, the jet tends to oscillate. It retracts back to the orifice after bubble detachment and moves forth again to form another bubble. It is also observed in the simulations that the bubble trains do not all leave from the far end of the jet. Instead, some

bubbles emerge from the jet over its length when the jet coalesces with a rising bubble in the crossflow. This prediction agrees with the observations of Chen and Weinstein (1993).

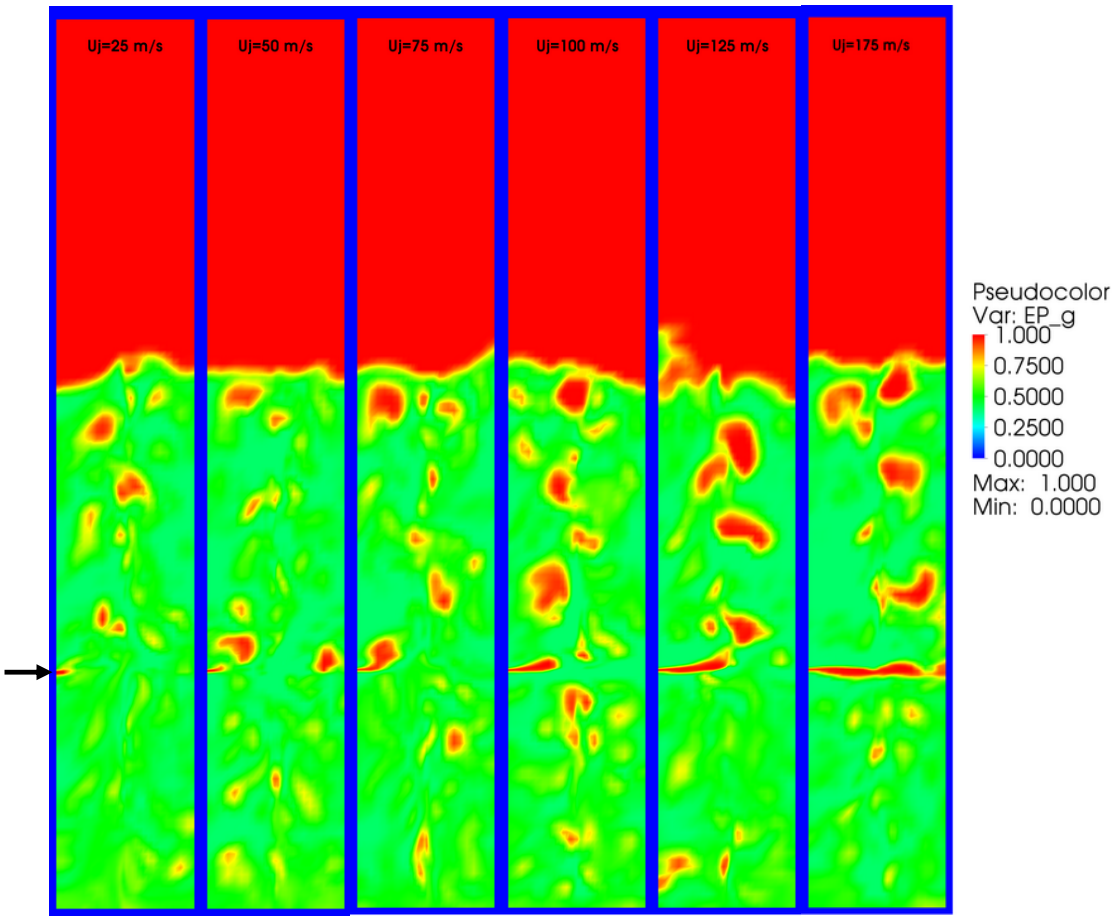

Figure 4-2. Snapshots of the voidage contour on the XZ plane, Y = 0, for different jet velocities.

In most circumstances, the jet bends upward because of the buoyancy and the upward gas-solid crossflow. However, the jet sometimes curves downwards with the downward solids circulation near the wall. Chen and Weinstein (1993) studied the shape and extent of the void area formed by a horizontal jet in a rectangular fluidized bed with an X-ray system. Their experimental observations showed that the horizontal jet formed three regions in the fluidized bed: the jet, bubble trains, and a surrounding compaction zone. In our simulation, the jet and the bubble trains are both observed. The surrounding compaction zone is not so obvious because of the strong interaction between the jet and the rising bubbles. However, we do observe a compaction

tendency as the particles are pushed away by the jetting gas and a portion of gas in the surrounding emulsion is entrained by the jet.

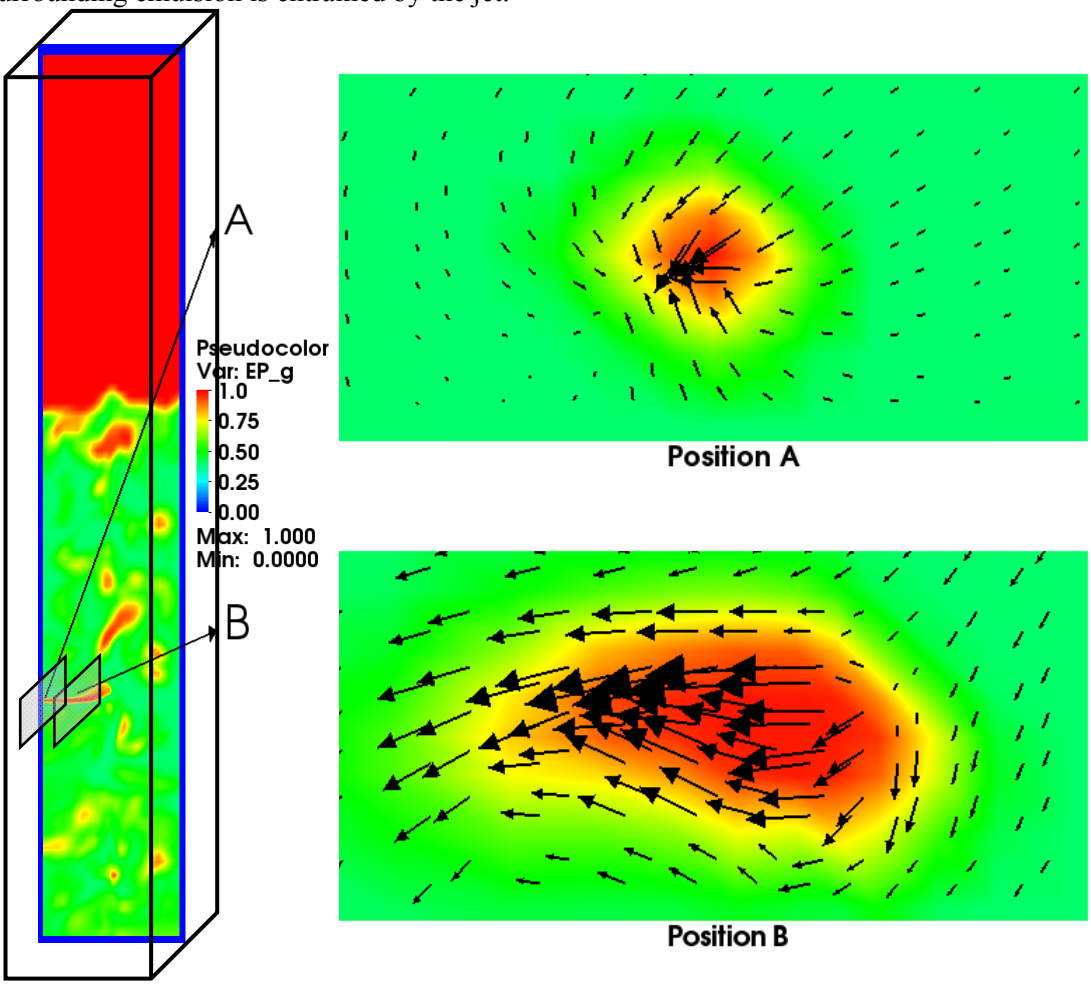

Figure 4-3. Particles entrainment and shape of the jet at different positions. (Positions A and B are shown in the left figure for single jet: $U_j = 75$ m/s; contour: voidage; vector: particle velocity.)

In experiments, the cross-sectional shape of the jet is very difficult to obtain. So far, since no experimental observation on it has been reported, the shape is naturally assumed to be round in modeling. In the present results, the shape of the jet is circular most of the time, as seen in Figure 4-3. However, the jet cross-section sometimes shows a marked deviation from the round shape, due to the strong convective effect from the crossflow as the jet penetrates deep into the bed. By examining the gas and solids velocity distributions around the jet, one can observe that the

entrainment of the surrounding gas and solids into the jet is mainly from the upstream and sides of the jet, and the rate of entrainment decreases with the distance from the injection port. Close to the injection port, the entrainment is extremely high, as gas and particles are entrained into the jet from all directions. The entrainment of particles to the jet can be illustrated in Figure 4-3. This is consistent with the experimental observation by Copan et al. (2001) that the jet behaved like a sink in the bed at the tip of the nozzle.

4.3.2.2 Single jet penetration

By defining the jet boundary at $\alpha_g = 0.8$, the jet penetration length is measured frame by frame. The predicted jet penetration length plotted against time is shown in **Error! Reference source not found.** for a 5 s interval. The strong fluctuations of the jet penetration length are clearly illustrated in the figure, which correspond to the jet oscillations. Peaks in the plot occur when a rising bubble coalesces with the jet or a bubble starts to form at the tip of the jet. The small fluctuations are most probably related to intrinsic pressure fluctuations inside the bubbling fluidized bed. For high jet velocities, the fluctuations increase as more bubbles are entrained into the jet as it penetrates deeper into the bed.

The mean jet penetration length is obtained by averaging the measurements over a sufficient time period when the flow is fully developed. The normalized jet penetration lengths for single jet injection with different jet velocities are plotted in Figure 4-5. The numerical results show reasonable agreement with both empirical correlations by Merry (1971) and Benjelloun et al. (1995). It should be noted that the empirical correlations are for the maximum penetration, whereas our measurements are for the average jet penetration. Bearing this in mind, it can be concluded that the correlation by Benjelloun et al. (1995) provides a better overall agreement with our simulation. A similar phenomenon was reported in the literature when Ariyapadi et al. (2004) compared their experimental jet penetration data with predictions from different empirical

correlations. In the simulation, it is observed that the jet can reach the opposite wall for $U_j = 175$ m/s. This may cause the undesired erosion of the wall in real applications. Though the measured jet penetration length of 6.1 cm shows good agreement with that for the jet in a large bubbling fluidized bed (See Table 4-2), it is believed that the jet is affected by the wall. Again, the computation becomes extremely time-consuming and unstable for high jet velocities. As a result, only three seconds after initiation of gas injection is simulated for $U_j = 175$ m/s.

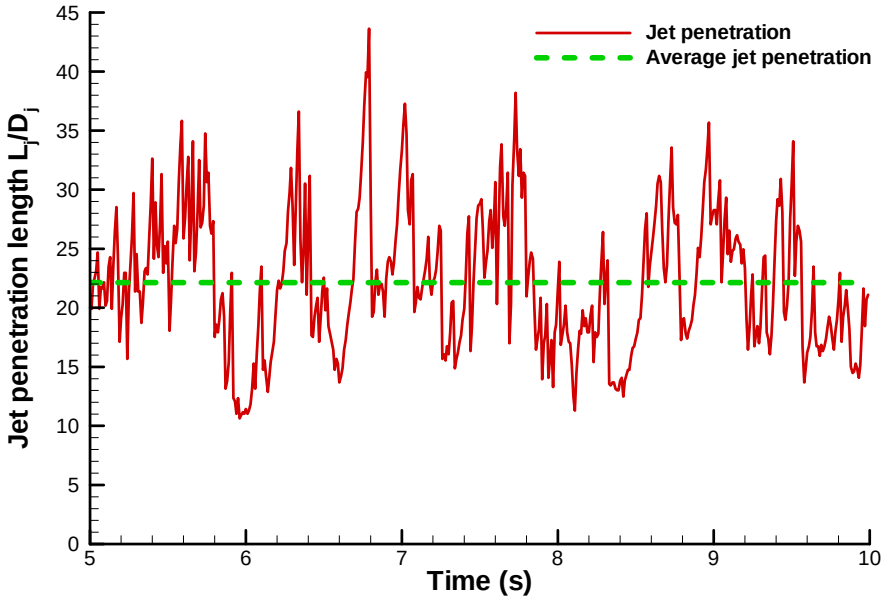

Figure 4-4. Predicted jet penetration length versus time after initiating gas injection for single jet $U_j = 75$ m/s.

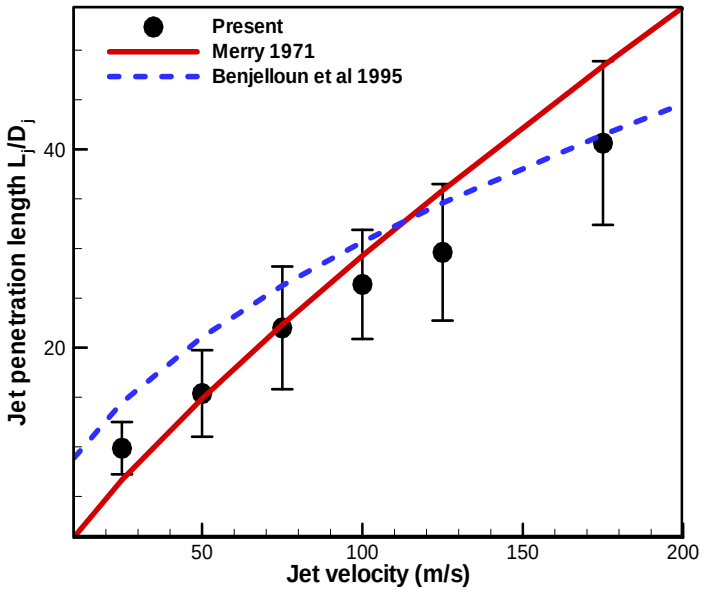

Figure 4-5. Jet penetration lengths for single jet at different velocities. (Error bars indicate ±1 standard deviation of predicted jet penetration lengths.)

In our numerical study, the jet expansion angle ranges from 15 to 35 degrees for all jet velocities except for $U_j = 25$ m/s, where the jet is not always observed and the measurement of the jet expansion angle is not feasible. Overall, the expansion angle showes a slight decrease with increasing jet velocity as expected, though this is not obvious in Figure 4-2.

4.3.2.3 Multiple-jet penetration

To study multiple-jet injections, different configurations of jet injections as shown in Figure 4-1 are simulated for various jet velocities. When multiple jets are injected together into the bed, the measurements of jet penetration are made mainly for jet A because the comparison of all jets shows that they have similar length and form in the statistical sense. When the jet velocity exceeds 100 m/s, determining jet penetration becomes very difficult because of direct contacts between neighboring jets or opposing jets. In Figure 4-6, only the jet penetration lengths for jet

velocities of 50, 75, and 100 m/s are compared. Jet penetration increases with jet velocity for all jet arrangements. More important, the penetration lengths for different jet arrangements are very similar for the same jet velocities. This is consistent with Donald et al. (2004) experimental observations suggesting that the study of penetration and other properties of a single jet can apply directly to interacting horizontal jets at the same level.

4.3.2.4 Jet-bubble and jet-jet interactions

In the bed, bubbles appear to be attracted to the jet and be entrained by it. During this process, the jet also moves towards the bubble even if it has to sometimes bend downwards. The coalescence of a bubble and the jet takes place at the end of the jet most of the time. When a bubble far from the jet is entrained, the jet usually becomes elongated, and a big bubble forms at the end of the jet afterward. The jet shrinks greatly after the bubble detaches from it. A typical cycle of the coalescence of a bubble and jet is illustrated in Figure 4-7. Sometimes, the coalescence of a bubble and jet takes place in the middle of the jet when the rising bubble rises from directly beneath. Then, after a small shift in the jet direction, the bubble emerges along the upper surface of the jet. Similar phenomena have been observed by Chen and Weinstein (1993). For a small bubble, the interaction is somewhat different; the bubble becomes smaller and smaller as it travels towards the jet. This implies that the gas in the bubble is entrained into the jet gradually. Sometimes, the small bubble disappears before it can make contact with the jet. As the jet penetrates deeper into the bed, more bubbles interact with it, and coalescence becomes more frequent.

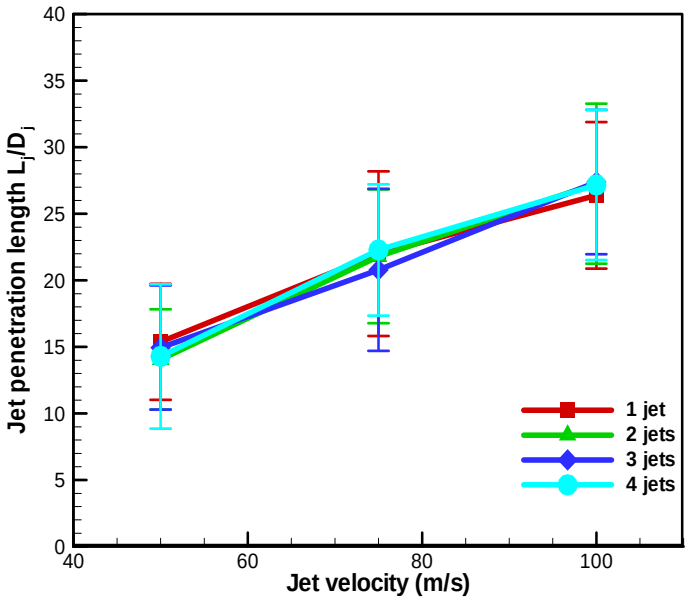

Figure 4-6. Jet penetration lengths for different jet arrangements and velocities. (Error bars indicate ±1 standard deviation of predicted jet penetration lengths.)

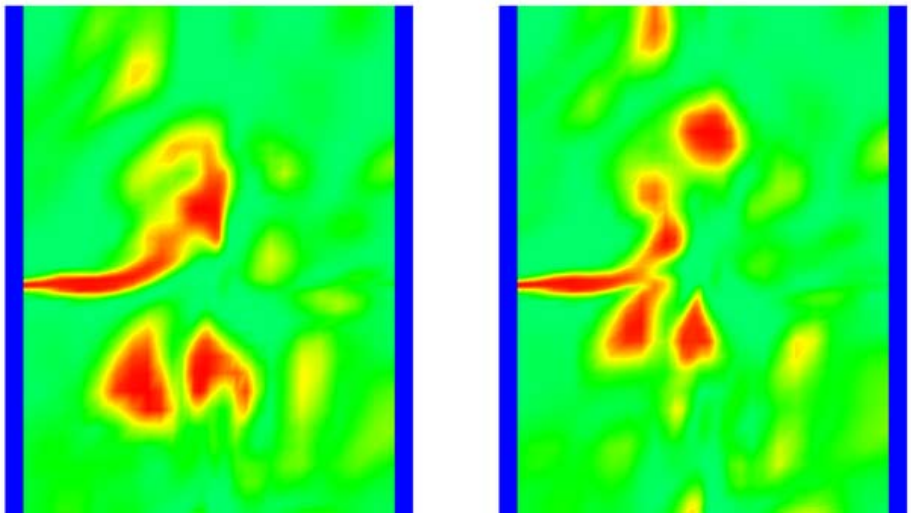

(a) (b)

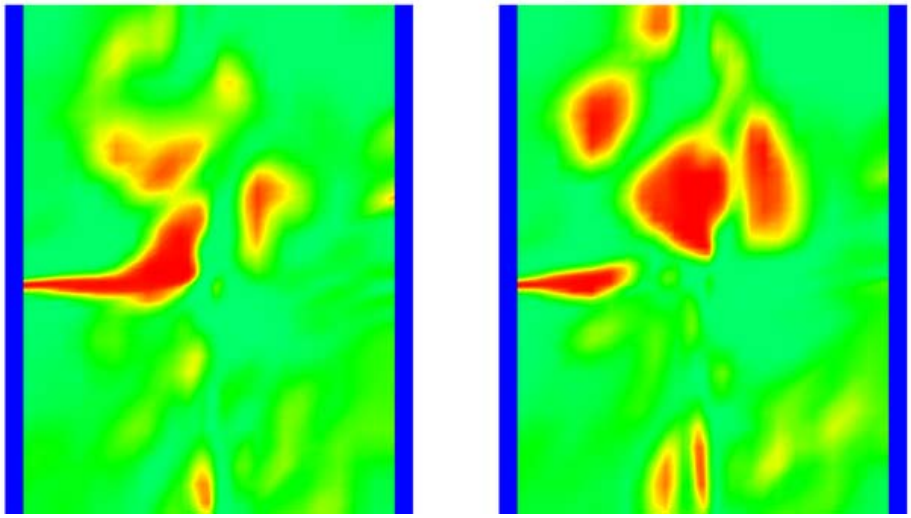

(c) (d)

Figure 4-7. Coalescence of a bubble and the jet in the bed ($U_j = 75$ m/s; time interval between two snapshots is 0.02 s).

The interaction between jets is studied by examining the jet behaviour at the injection level. For low jet velocities, such as 50 and 75 m/s, the jets barely make contact with each other. They do interact with each other through the surrounding emulsion, though there is no direct contact between them. As shown in Figure 4-8(a) and (b), the four jets show quite different shapes and penetration lengths in the injection plane. For $U_j = 100$ m/s, the jets start to touch each other or overlap occasionally. As a result, the interaction becomes strong with increasing jet velocity. However, the influence on the average jet behaviour is very limited, as already shown in Figure 4-6, where the jet penetration lengths for different jet arrangements are similar. For $U_j = 175$ m/s, the jets make contact with each other most of the time, making the measurement of jet penetration length very difficult.

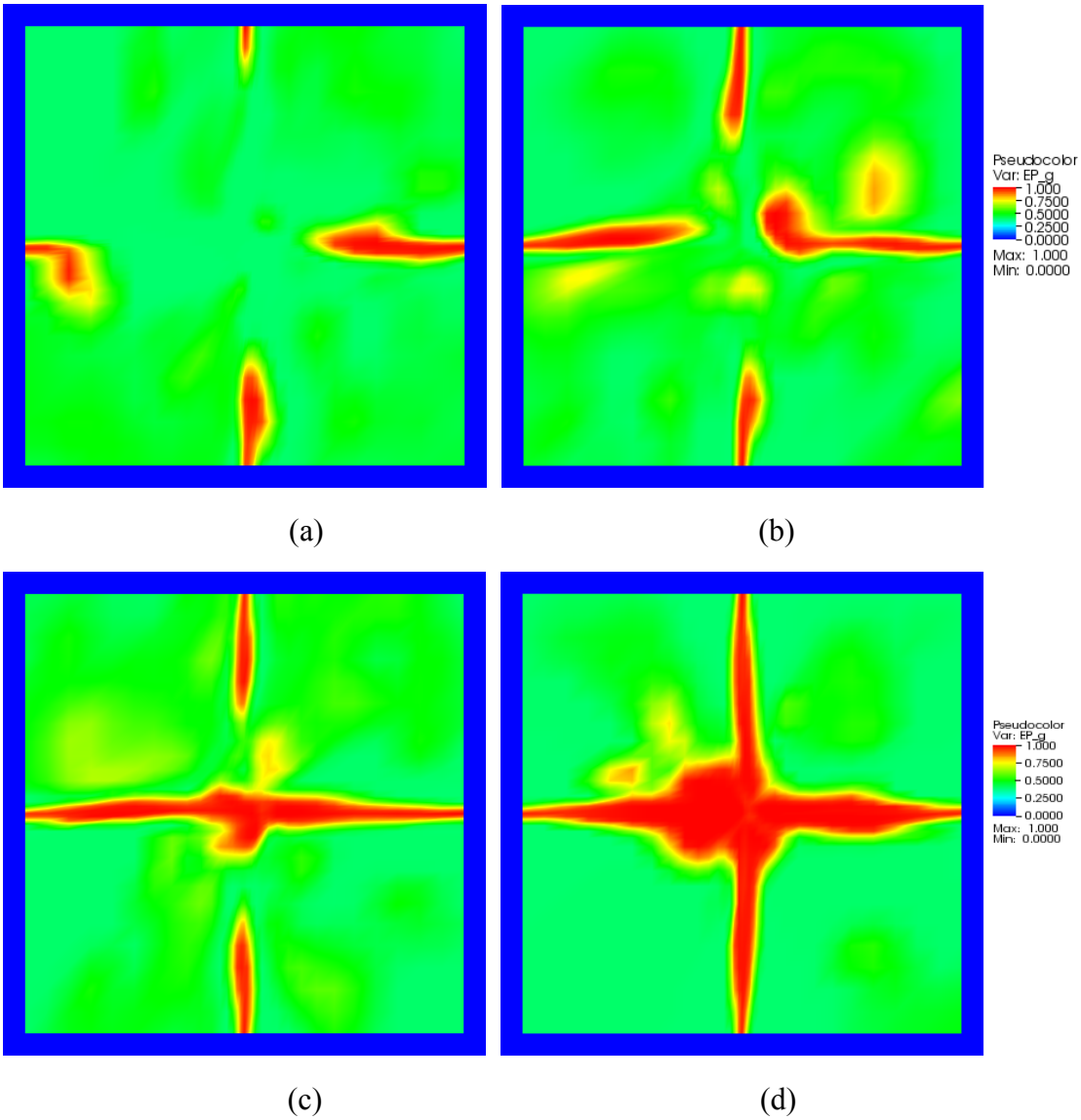

Figure 4-8. Jet interaction at the injection level Z = 0.17 m for different velocities (a, b, c, and d are for jet velocities of 50, 75, 100, and 175 m/s, respectively).

4.3.2.5 Axial solids hold-up profiles

Axial solids hold-up profiles for single jet injection with different velocities are plotted in Figure 4-9. For comparison, the solids hold-up profile without secondary gas injection is presented as a base case. The introduction of the secondary gas injection seems to have only limited influence on the solids hold-up profiles (for the jet velocities simulated), but the dilution effect on the

solids flow above the injection port can still be determined. For single jet injection, the secondary gas flow rates range from 8 to 30% of the primary gas flow rate through the bottom distributor. This is not expected to cause a significant change in the overall bed hydrodynamics. Moreover, it can be noticed that the slope of solids hold-up profiles at the bed surface decreases slightly with increasing jet velocity, which means that the interface between the dense bed and the freeboard becomes less clear as the total gas flow rate increases. This is attributed to the breakup of the increasing number of big bubbles at the bed surface, as the total superficial gas flow rate increases. If the interface between the dense bed and the freeboard is defined by $\alpha_g = 0.8$, one can also observe a slight increase in bed height due to secondary gas injection. The effect of the gas jet is quite obvious in the injection region when we examine the solids hold-up profile closely, shown in the inset in Figure 4-9. When multiple-jet injections are examined, the phenomena mentioned above become more pronounced, as shown in Figure 4-10, since more secondary gas is introduced into the system. It is evident in these figures that the secondary gas injection is predicted to have no significant effect on the solids hold-up below the injection port.

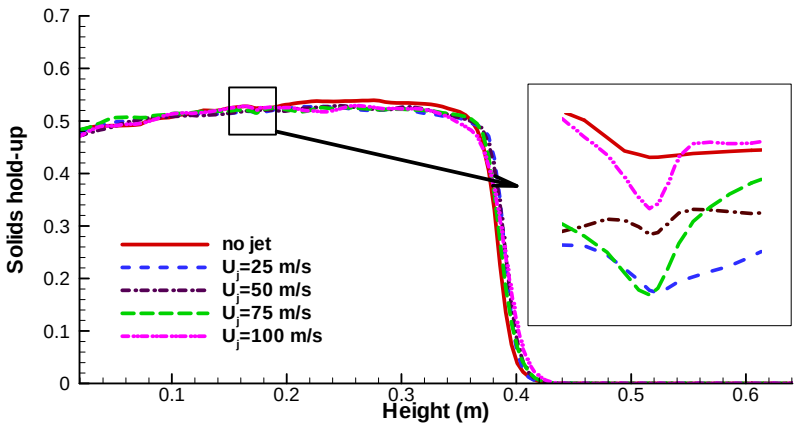

Figure 4-9. Axial solids hold-up profiles for single jet at different velocities (inset: close view of solids hold-up profiles at injection level).

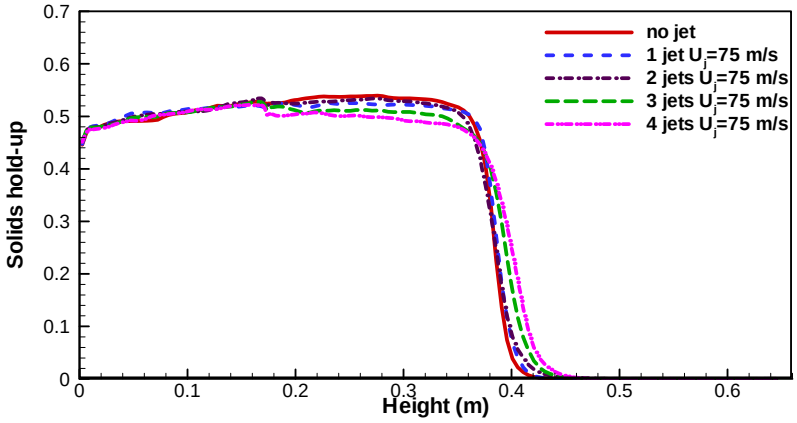

Figure 4-10. Axial solids hold-up profiles for multiple gas jets $U_j = 75$ m/s.

The above discussion shows that secondary gas injection divides the bed into two zones with different superficial gas velocities, namely the primary zone below the injection port with the superficial gas velocity denoted as U_p and a secondary zone above the injection with total superficial gas velocity denoted as U_g. Figure 4-11 shows the effect of secondary gas injection on the axial solids hold-up when the total exit air flow rate is fixed. Two exit air flow rates are simulated. For the same exit superficial gas velocity, the low gas velocity in the primary zone leads to high solids hold-up. In the upper region of the secondary zone, the solids hold-up for these four cases are very close. Since more particles are transported to the secondary zone when all gas is introduced from the bottom distributor, the bed expansion height decreases when secondary air injection is employed. In the bubbling fluidized bed, it has been reported (van Willigen et al., 2005; Christensen et al., 2008b) that the secondary injection of gas from a fractal injector significantly reduced the bubble size and decreased the rate of bubble coalescence. A similar effect can be inferred from the plots in Figure 4-11, where the steep slope at the bed surface for $U_g = 0.087$ m/s in the absence of secondary injection indicates breakup of large bubbles. However, a significant decrease in bubble size cannot be obtained for $U_g = 0.1$ m/s

with a jet velocity of 75 m/s as a high jetting flow rate and deep penetration produce large bubbles in the central region of the bed.

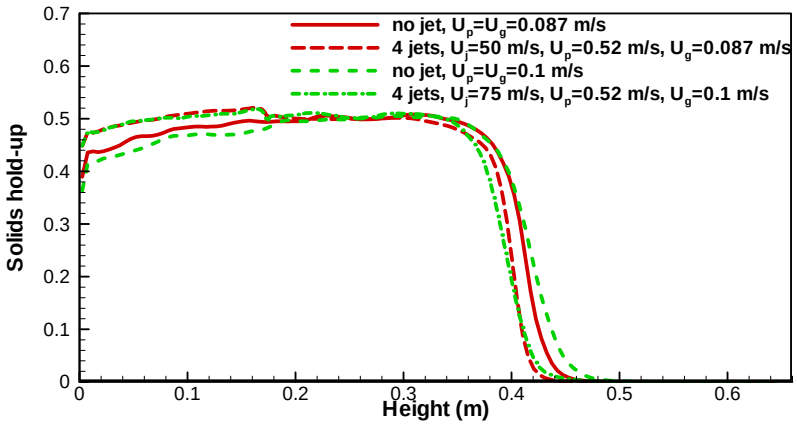

Figure 4-11. Axial solids hold-up profiles for $U_g = 0.087$ and 0.1 m/s with and without secondary gas injection.

For the same secondary gas flow rate, Figure 4-12 shows the profiles of axial solids hold-up for different jet arrangements. In this study, the same amount of gas is injected into the bed through one, two, and four nozzles (arrangement: A, AC and ABCD in Figure 4-1) with a velocity of 100, 50, and 25 m/s, respectively. It can be seen that the profiles of solids hold-up are not the same, though the gas flow rates are identical. The profile for single jet injection shows a big deviation from the other two where the solids hold-up in the secondary zone is much higher. Since the gas flow rate is constant, it suggests more fast-rising bubbles in that zone. It can also be observed from Figure 4-12 that the bed height increases slightly as we distribute the secondary gas injection to more injection ports. This implies that distributed injection results in more small slowly rising bubbles in the secondary zone or more gas in the dense phase, decreasing gas by-passing and possibly contributing to improved gas-solid contacting.

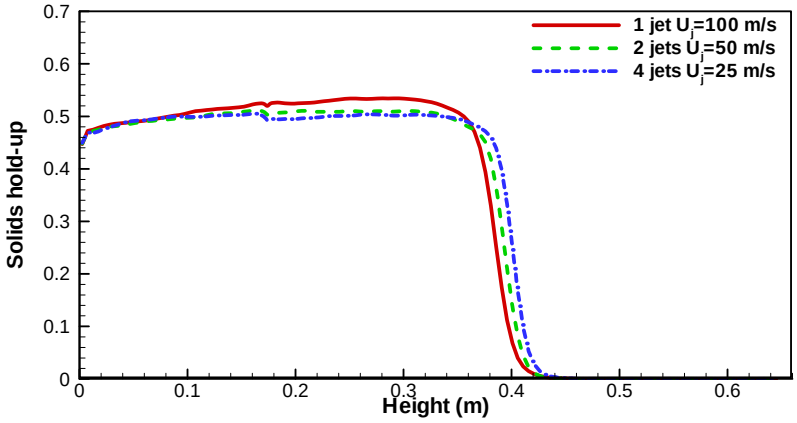

Figure 4-12. Axial solids hold-up profiles for same secondary gas flow rate with different numbers of jets (U_p = 0.052 m/s).

4.3.2.6 Voidage profiles

Considering the importance of multiple jet injections in industrial applications, the following analysis mainly focuses on multiple jet injections into the bed. The time-averaged voidage profiles at different heights in XZ and YZ planes are shown in Figure 4-13 for four-jet injections. For the sake of brevity, only results for jet velocities of 0 (no secondary injection), 50, and 100 m/s are presented. As a consequence of symmetry, the profiles in the XZ and YZ planes are similar in these plots. A dilute core region surrounded by a dense annular is predicted for all. This typical flow pattern is due to the rising bubbles in the centre and the descent of the solids close to the wall. It becomes more evident when the total superficial gas velocity increases with the secondary gas injection. At 0.02 m upstream of the injection (Z = 0.15 m), there is no substantial difference between the voidage profiles with and without secondary gas injection. Whereas, downstream of the secondary gas injection (Z = 0.2 and 0.3 m), the bed becomes more dilute at higher jet velocities. This indicates that the influence of secondary gas injection on the flow behavior is significant downstream of the injection and marginal upstream. At 0.03 m above

the injection (Z = 0.2 m), the voidage profiles for $U_j = 50$ m/s and 100 m/s show different features corresponding to the jet penetration depth. The two separate peaks in the voidage profiles for $U_j = 50$ m/s suggest that opposing jets do not impinge on each other and do not reach the bed centre. For $U_j = 100$ m/s, only one single peak is presented, indicating that the jets penetrate deeper into the bed and start to contact each other. In the far downstream region, the profiles are flatter in the centre where the flow is more developed and the jet penetration effect trails off due to radial dispersion. Although there is no distinct interface between the dilute core and the dense annular region, it can still be inferred that the thickness of the dense annular region is greater for $U_j = 100$ m/s compared with the other two cases shown in the figure. This is likely because the gas in the annular dense region is entrained into the jets and transported into the centre of the bed to form big bubbles. Increased symmetry and evenness of the voidage profiles in the core region are observed for increased injection velocity and downstream distance, reflecting the developed flow regime being achieved. The asymmetry shown in the gas fraction profiles is an indication that the time interval used to average the gas volume fraction is not long enough. A similar pattern has been reported in several numerical simulations (McKeen and Pugsley, 2003a; Taghipour et al., 2005), and it can be overcome by increasing the simulation time. However, the current averaged results are sufficient for analysis of the effect of secondary gas injection on bed hydrodynamics.

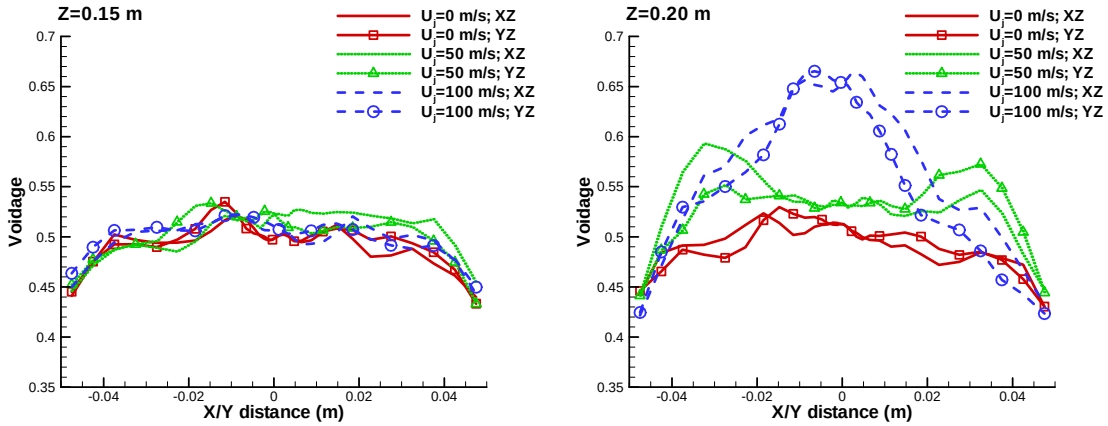

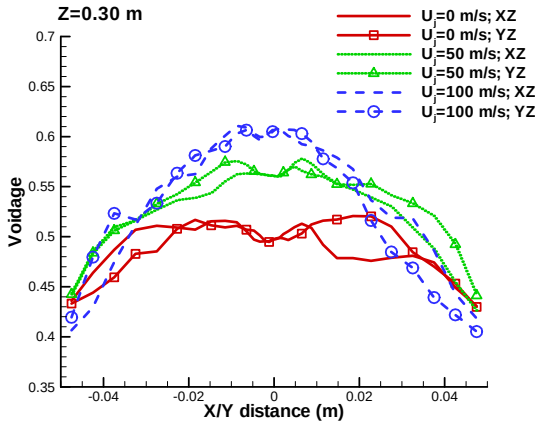

Figure 4-13. Voidage profiles at different heights in the XZ and YZ planes.

The above analyses can be illustrated by the time-averaged voidage contours, as shown in Figure 4-14. The path of bubble trains formed at the tip of the jet can be inferred from this figure (Chen and Weinstein, 1993). In Figure 4-14, the marked asymmetry presented in the contour for $U_j = 175$ m/s is due to the short time period for averaging. Here, all plots are obtained by averaging the CFD results in five seconds, except for $U_j = 175$ m/s, which is averaged for two seconds only. For all jet velocities, bubbles tend to move upward toward the centre. However, for $U_j = 25$, 50, and 75 m/s, due to the limited penetration, some bubbles have to travel up close to the wall. For high velocities of 100 and 175 m/s, big bubbles formed in the centre travel directly upward in the dilute core. Furthermore, the small bubbles in the bed are entrained by big bubbles, leading to the narrowing of the dilute core. It is also shown in Figure 4-14 that the bed heights for $U_j = 100$ and 175 m/s are lower than for the cases with low jet velocities, though the total gas flow rate increases. This is because a large number of bubbles travelling upward in the centre core tend to coalesce and cause slugging in the bed. When slugging takes place, gas bypasses through the bed and mixing of secondary gas with the bed material is limited. Slugging behavior is typically observed in columns of large height-to-diameter ratio, like the one in our simulation. In a large diameter bubbling fluidized bed, slugging does not occur, but large bubble sizes can still lead to significant gas bypassing and subsequent loss of yield (Knowlton et al.,

2005). In most processes, slugging is not desirable and should be avoided. It is also necessary to point out that the high jet flow rates tend to increase solids elutriation, which may lead to low reaction efficiency, high catalyst cost (Gray et al., 2001). In brief, the jet gas flow rate should be selected carefully, especially for small-scale fluidized bed reactors.

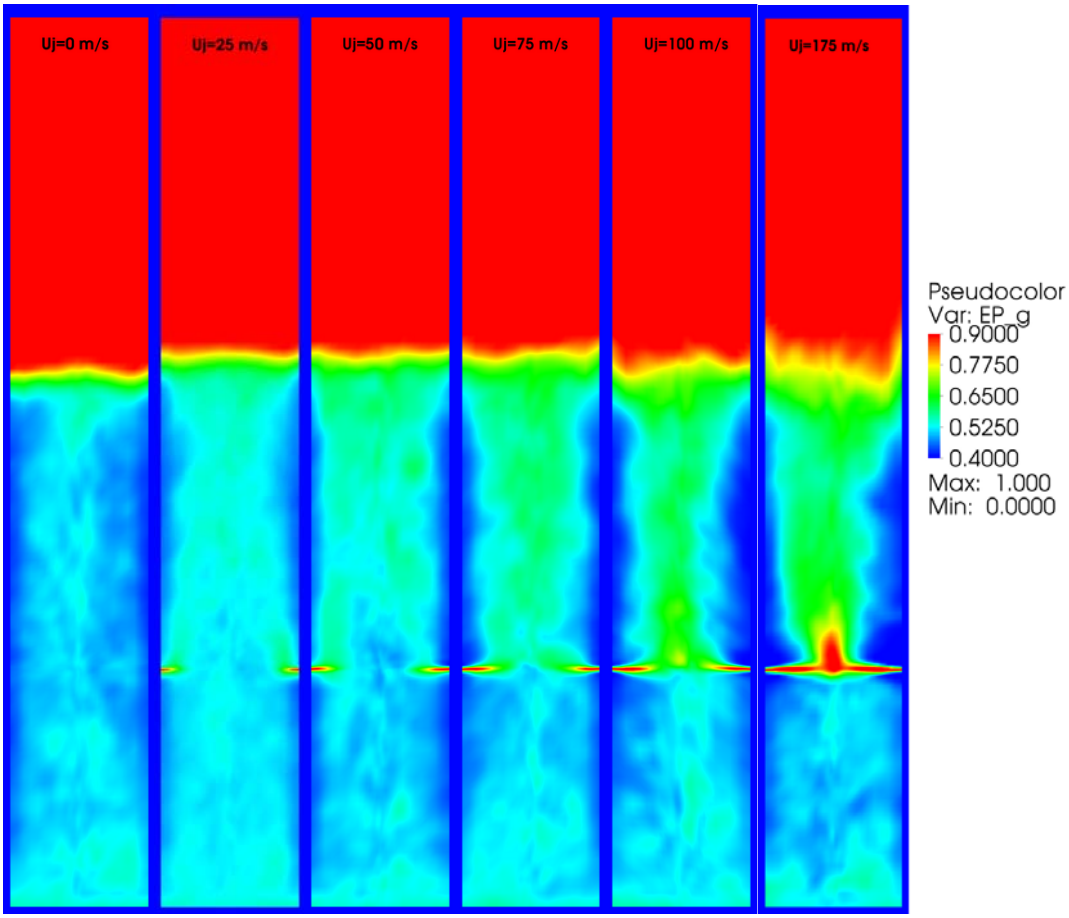

Figure 4-14. Time-averaged voidage contours in the XZ plane for different jet velocities.

The time-averaged voidage profiles at Z = 0.3 m in the XZ and YZ central planes are shown in Figure 4-15 for $U_g = 0.087$ and 0.1 m/s with and without secondary gas injection. When all the gas is introduced through the bottom distributor, more excess gas superficial velocity, ($U_p - U_{mf}$), forms more big bubbles in the lower region, and the bubbles grow as they travel upward. The big bubbles tend to accumulate at the centre and their size is further increased by coalescence. The peaks in the voidage profiles correspond to the presence of big bubbles in the

central region of the bed. When a portion of gas feed is introduced through secondary injection, the decreased gas flow rate through the bottom distributor results in fewer bubbles in the primary zone. In addition, for $U_j = 50$ and 75 m/s, as described previously, the bubbles detached from the gas jet travel upward somewhat close to the wall. This pattern delays the gulf streaming of bubbles through the bed centre; hence, the bubble coalescence is diminished. This explains the low and flatter profiles in the centre region for cases with secondary injection in Figure 4-15.

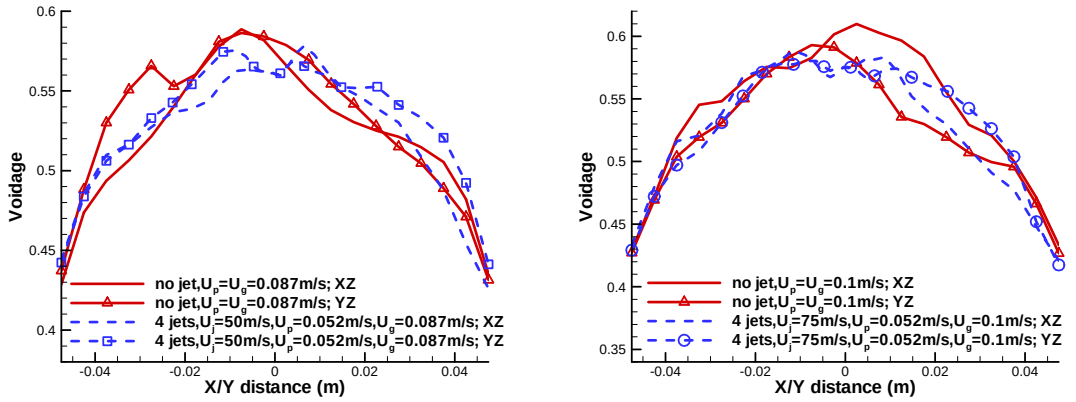

(a) (b)

Figure 4-15. Time-averaged voidage profiles at Z = 0.3 m in the XZ and YZ planes for $U_g = 0.087$ m/s (a) and 0.1 m/s (b) with and without secondary gas injection.

For the same U_p and U_g, voidage profiles at Z = 0.3 m in the XZ and YZ central planes are shown in Figure 4-16. Similar to the previous analysis, the profiles clearly present the pathway of bubbles. For single jet (U_j = 100 m/s), the jet penetrates deep into the centre of the bed. The peaks in the voidage profiles correspond to the pathway of the big bubbles detached from the jet and the bubbles formed in the central region of the primary zone. For the other two jet arrangements, the wide dilute core region corresponds to the wide pathway of bubbles. This is made more visible by plotting the voidage contours at Z = 0.3 m for the investigated cases in Figure 4-17, where the shape of the dilute core region can be clearly observed. The area of the dilute core region increases as the secondary gas injection is more distributed. It can also be

observed from Figure 4-17 that the bed seems to become more uniform as secondary gas is introduced from more distributed nozzles and low velocity.

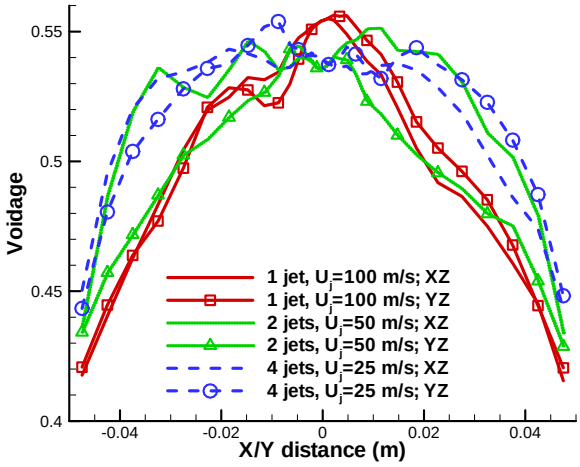

Figure 4-16. Time-averaged voidage profiles at Z = 0.3 m in the XZ and YZ planes for the same U_p and U_g with different jet arrangements (U_p = 0.052 m/s; U_g = 0.07 m/s).

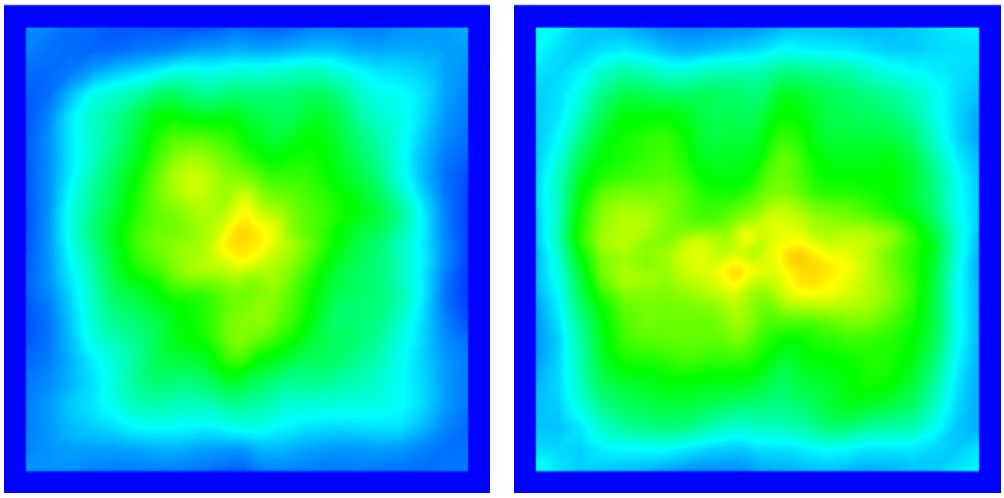

(a) (b)

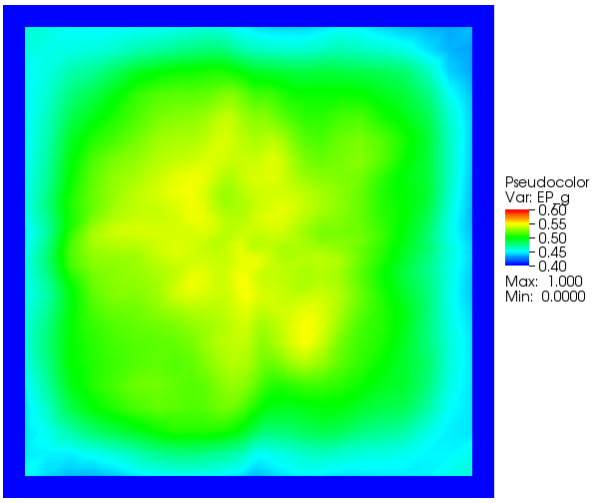

(c)

Figure 4-17. Time-averaged voidage contours at Z = 0.3 m for the same U_p and U_g with different jet arrangements: (a) one jet, U_j = 100 m/s; (b) two jets, U_j = 50 m/s; (c) four jets, U_j = 25 m/s.

4.3.2.7 Velocity profiles

Figure 4-18 shows the gas and solids velocity profiles below and above the secondary gas injection for the same operating conditions as reported in Figure 4-13 for four-jet injections with different velocities of 0, 50, and 100 m/s. It can be seen that the profiles of gas and solids mean velocities are quite similar except for their magnitudes. The typical solids circulation pattern inside the bubbling fluidized bed is obtained, with particles carried upward in the centre of the bed and descending close to the wall. Below secondary injection, the velocity profiles change little for both gas and solids. While the difference in velocity profiles is distinct everywhere above secondary injection, it is more significant in the core region than near the wall. The increasing secondary gas injection promotes the solids circulation inside the bed by bringing more particles upward in the core region. Based on the secondary gas flow rate, the total superficial gas velocities U_g above injection are calculated to be 0.052, 0.087, and 0.122 m/s, respectively. In Figure 4-18, the maximum velocity for both phases shows a dramatic increase

when U_g increases from 0.087 to 0.122 m, compared with 0.052 to 0.087 m/s. The narrow peak in downstream velocity profiles for $U_j = 100$ m/s characterizes the formation of big bubbles in the centre and shrinkage of the dilute core region, consistent with the flow pattern in Figure 4-14.

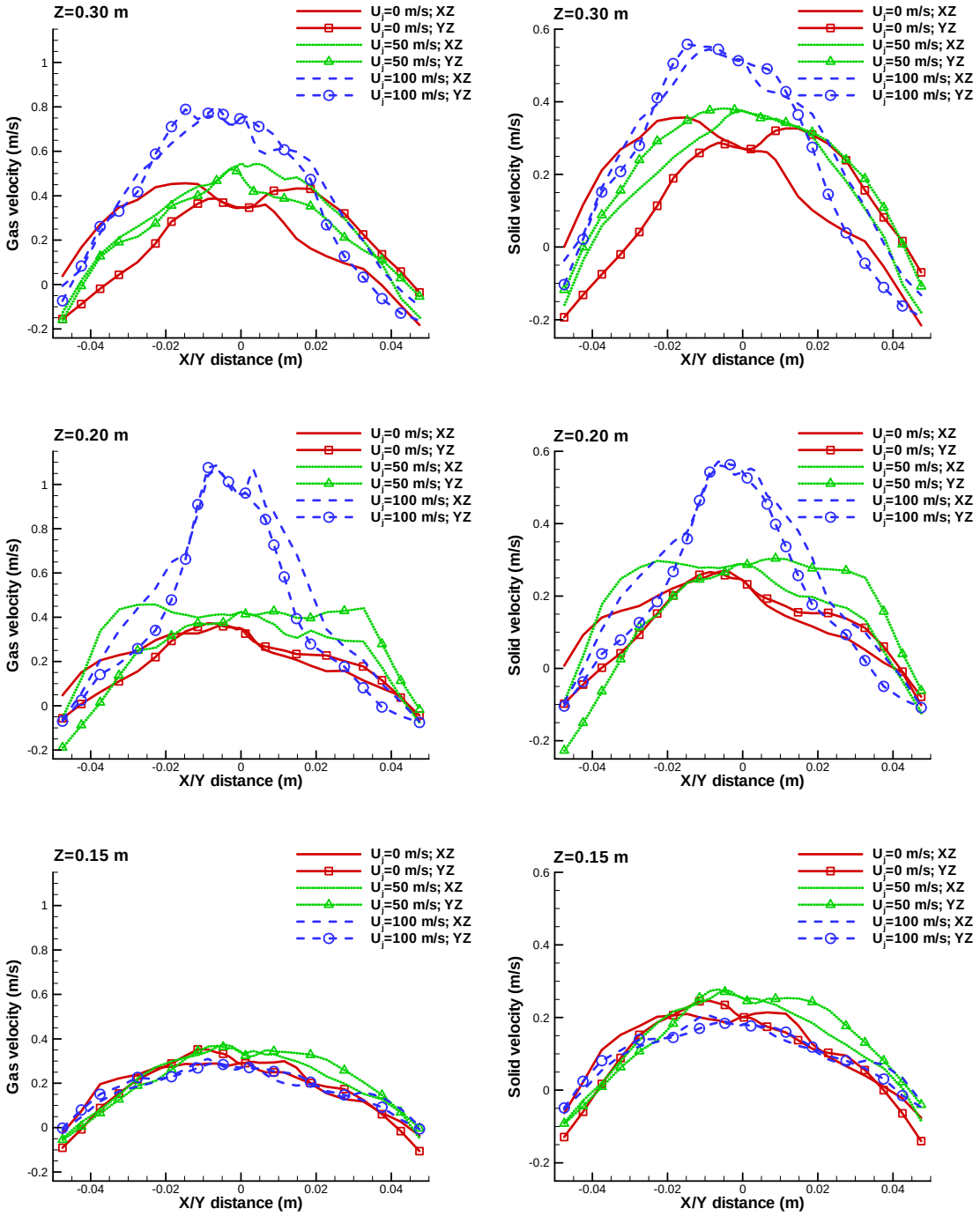

Figure 4-18. Time-averaged gas and solid velocities at different heights in the XZ and YZ planes.

The gas and solid velocity profiles at Z = 0.3 m in the XZ and YZ planes for the same U_p and U_g with different jet arrangements are shown in Figure 4-19. As can be expected, the region of high voidage with large bubbles has a high gas velocity. The velocity profiles of secondary injection with four jets show less non-uniformity since the gas phase is more uniformly distributed in the system as presented in Figure 4-17. It should be noted that the greater dissimilarity in the velocity profiles in the XZ and YZ planes is mainly due to the arrangement of the jets.

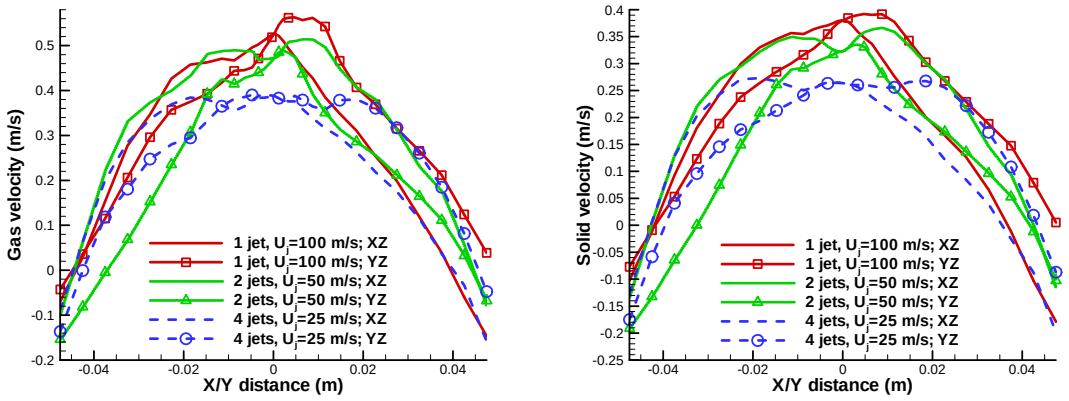

(a) (b)

Figure 4-19. Time-averaged gas (a) and solids (b) velocities at Z = 0.3 m in the XZ and YZ planes for same U_p and U_g with different jet arrangements (U_p = 0.052 m/s; U_g = 0.07 m/s).

4.3.2.8 Bubble size

In order to characterize the change in bubble size caused by the secondary gas injection, a representative bubble size is used in the following analysis. To obtain the mean bubble size at a certain height above the distributor, the voidage data at that height is extracted first for different times. The images of voidage contour are rendered with a boundary at $\varepsilon_g = 0.8$ to distinguish the bubble. Bubbles passing through the sectional plane are detected and tracked. The maximum

area projection of a bubble on the plane is used to calculate the equivalent bubble diameter. It should be noted that the bubble size measured with this approach characterizes the bubble in the XY plane only. It will under-predict the real bubble size when the bubble is elongated in the flow direction (Z direction). However, it is satisfactory for the current study since we only want to study the effect of secondary gas injection on bubble size qualitatively. The measured mean bubble size at Z = 0.3 m for cases shown in Figure 4-11 are tabulated in Table 4-3. The results confirm our previous analysis of the solids hold-up profiles that the bubble size is reduced by the secondary gas injection for $U_g = 0.087$ m/s. However, the bubble size for $U_g = 0.1$ m/s is almost unchanged when secondary gas is injected. This indicates that the decrease in bubble size caused by the horizontal gas jet injection is significantly affected by the jet velocity.

Table 4-3. Mean bubble size measured at Z = 0.3 m for $U_g = 0.087$ and 0.1 m/s with and without secondary gas injection.

Conditions	**Mean bubble size (mm)**
No jet, $U_g = 0.087$ m/s	19.1 ± 10.1
Four jets, $U_j = 50$ m/s, $U_g = 0.087$ m/s	15.4 ± 8.0
No jet, $U_g = 0.10$ m/s	21.1 ± 10.2
Four jets, $U_j = 75$ m/s，$U_g = 0.10$ m/s	21.3 ± 7.5

The mean bubble size at Z = 0.3 m for cases with the same secondary gas flow rates but different jet arrangements is shown in Table 4-4. As expected, the mean bubble size decreases as the secondary gas is injected through more jets. In our simulation, more bubbles exist when secondary gas is injected through four jets at a moderate velocity.

Table 4-4. Mean bubble size measured at Z = 0.3 m for same secondary gas flow rate with different jet arrangements ($U_p = 0.052$ m/s).

Conditions	**Mean bubble size (mm)**
One jet, $U_j = 100$ m/s	19.90 ± 8.07
Two jets, $U_j = 50$ m/s	15.91 ± 6.32
Four jets, $U_j = 25$ m/s	12.34 ± 6.26

4.3.3 Mixing

In this section, numerical results concerning the mixing of the secondary gas inside the bubbling fluidized bed are presented. As in our previous analyses, the bed is divided into two zones with different superficial gas velocities due to secondary gas injection.

4.3.3.1 Tracer measurement

Gas mixing in the bed is studied by introducing the tracer gas through jetting orifices. Figure 4-20 shows the concentration of tracer gas as well as voidage contour in the XZ plane for two opposing jet injections with $U_j = 50$ m/s. It can be seen that tracer gas is released into the flow mainly in the form of bubbles from the jets. The gas is well distributed in a short distance above the injection level indicating intensive mixing in the bed. In the primary zone, back-mixing promoted by downflow of solids near the wall can be observed.

The concentrations of tracer gas at different points, as shown in Figure 4-20, are measured to characterize the transient mixing behaviour. The tracer gas concentrations at different measurement points are plotted against time in Figure 4-21. Upstream of the injection level (Z = 0.15 m), the tracer concentration is detected to be around 0.05 though it is fluctuating. Just

downstream (Z = 0.20 m), the tracer concentration shows very strong peaks corresponding to tracer-enriched bubbles detached from the jets when jets penetrate deep into the centre of the bed. With increasing distance downstream from the injection (Z = 0.30, 0.40 m), the fluctuations become smaller and smaller due to intensive mixing. In the freeboard region (Z = 0.45 m), only very small fluctuations can be observed which tend to diminish with time, indicating that good radial and axial mixing has been achieved. Provided the tracer concentration at the bed surface is quite uniform, this curve can be used to determine the residence time distribution (RTD) in the bed.

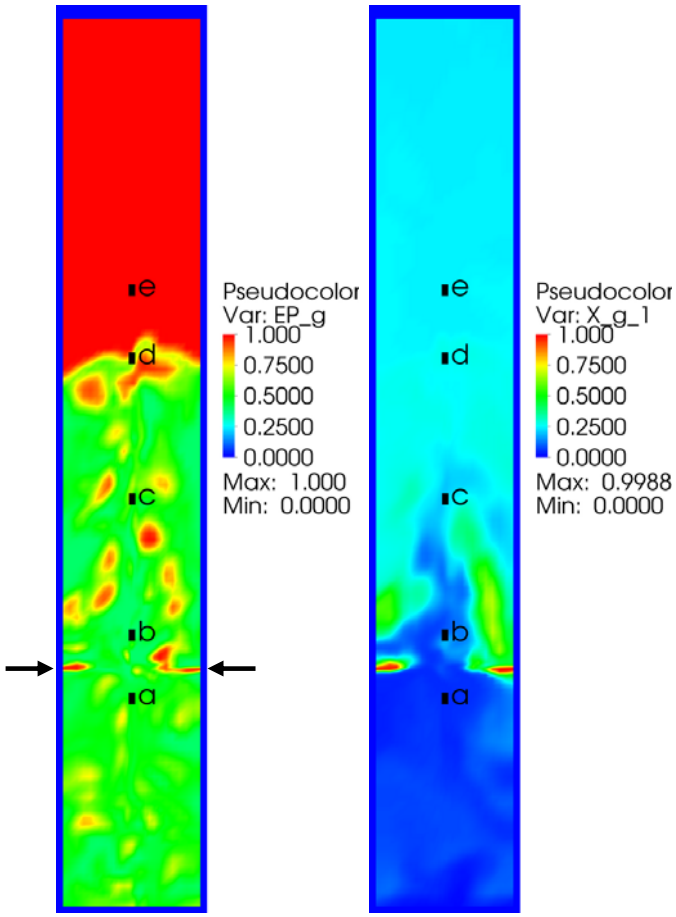

Figure 4-20. Snapshot of voidage and tracer concentration in the XZ plane for two-jet injection $U_j = 50$ m/s (a: Z = 0.15 m; b: Z = 0.20 m; c: Z = 0.30 m; d: Z = 0.40 m; e: Z = 0.45 m).

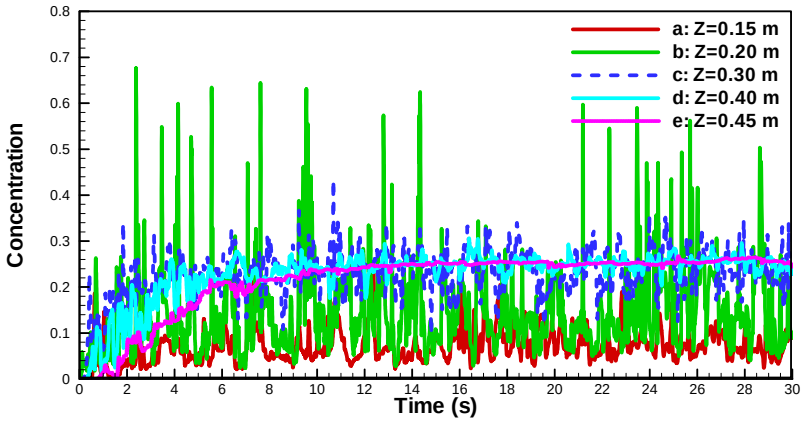

Figure 4-21. Tracer concentration at different points for two-jet injection $U_j = 50$ m/s.

4.3.3.2 Residence time

The tracer concentration measured at the bed surface, as in Figure 4-21, is subject to fluctuations and needs to be smoothed to obtain the cumulative distribution function, $F(t)$. To do this, the response curve of tracer concentration is fitted using the error function (Al-Sherehy et al., 2004)

$$erf(y) = \frac{2}{\sqrt{\pi}} \int_0^y e^{-t^2} dy \tag{4.5}$$

where

$$y = \frac{\beta - \varphi t}{\sqrt{t}} \tag{4.6}$$

In these equations, β and φ are fitting parameters, y is error function parameter and t is time. The fitting equation for $F(t)$ curve is

$$F(t) = \frac{1}{2}(1 - erf(y)) \tag{4.7}$$

The smoothed $F(t)$ curve is differentiated to calculate the exit age distribution, $E(t)$. Then the mean residence time and standard deviation can be calculated.

$$\tau = \int_0^\infty tE(t)dt \tag{4.8}$$

$$\sigma^2 = \int_0^\infty (t-\tau)^2 E(t)dt \tag{4.9}$$

To obtain the mean residence time of tracer gas in the dense bed region, the average tracer concentration at cross-section Z = 0.45 m is used. For example, the fitted $F(t)$ curve and $E(t)$ curve for two-jet injection with $U_j = 50$ m/s are shown in Figure 4-22 and Figure 4-23, respectively.

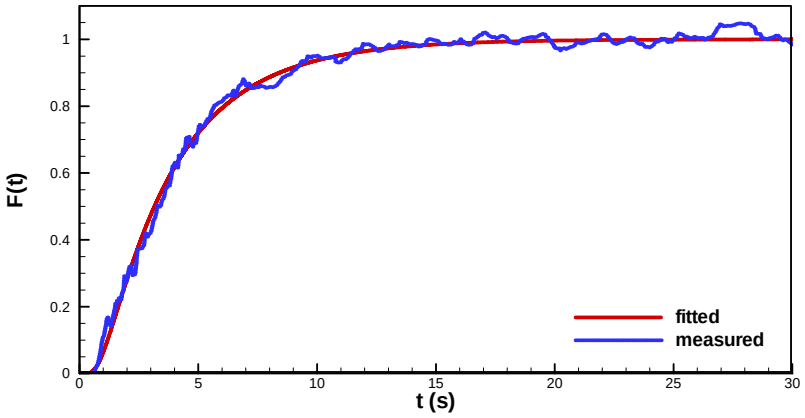

Figure 4-22. The fitted $F(t)$ curve and original scaled concentration signal for two-jet injection at $U_j = 50$ m/s at cross-section Z = 0.45 m.

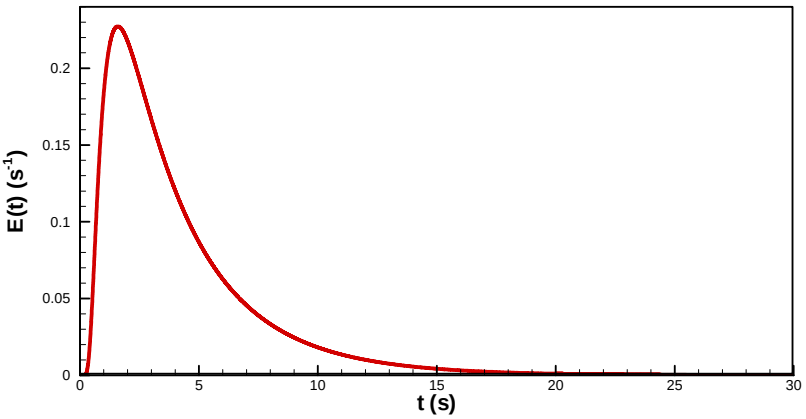

Figure 4-23. The $E(t)$ curve for two-jet injection at $U_j = 50$ m/s at cross-section Z = 0.45 m.

Error! Reference source not found. shows the mean residence time τ and the standard deviation of RTD σ of the tracer gas as a function of the jet velocity for single jet injections. As expected, the mean residence time of tracer gas decreases as the jet velocity increases, since the superficial gas velocity in the secondary zone increases with the jet velocity.

A faster decrease in mean residence time with increasing jet velocity is reported for the four-jet injection into the system, as shown in Figure 4-25. In addition, it can be noted that the standard deviation of RTD tends to decrease as the jet velocity increases. To further investigate this trend, the RTD dimensionless standard deviation σ/τ is also plotted in the figure. σ/τ or the dimensionless variance σ^2/τ^2 can be consider as a measure of the axial mixing (Missen et al., 1999). The two limiting values of σ/τ are 0 and 1, which correspond to plug flow and perfectly mixed flow. In Figure 4-25, a slight increase in σ/τ towards 1 can be observed, which reveals that the flow tends to approach perfectly mixed flow. This can be attributed to the increasing non-uniformity in gas velocity profiles as the secondary gas injection increases. As the velocity profile becomes blunter, the flow is closer to plug flow. This can be verified by the gas velocity profiles shown in Figure 4-18 for jet velocities of 50 and 100 m/s.

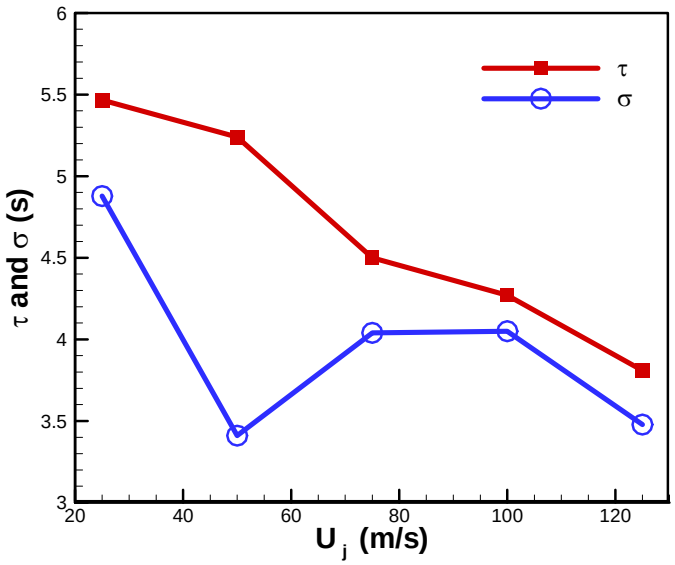

Figure 4-24. Mean residence time and standard deviation of RTD of tracer gas predicted at cross-section Z = 0.45 m for single jet injection at different velocities.

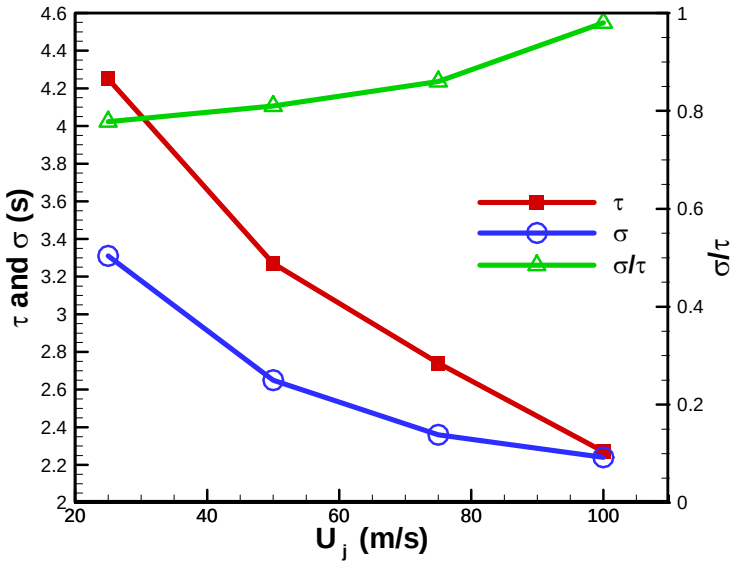

Figure 4-25. Residence time and standard deviation of RTD of tracer gas predicted at cross-section Z = 0.45 m for four-jet injection at different velocities.

Figure 4-26 shows the mean residence time of tracer gas in the dense bed when the same amount of secondary gas is injected through different jet arrangements. Here, the same amount of tracer gas is injected into the bed through one, two or four nozzles (arrangement: A, AC, and ABCD as shown in Figure 4-1) with velocities of 100, 50, and 25 m/s, respectively. Since the primary and secondary gas flow rates are identical, the mean residence time is almost the same for all jet arrangements, about 4.2 seconds. However, a decrease in σ/τ is demonstrated in the figure when secondary gas is injected through more jets with lower velocity, i.e. through four jets with $U_j = 25$ m/s, instead of one jet with $U_j = 100$ m/s. To verify this trend, the gas velocity profiles at Z = 0.3 m in the XZ and YZ planes for different jet arrangements shown in Figure 4-19 are revisited. The velocity profiles of secondary injection with four jets show less non-uniformity since the gas is more uniformly distributed. Hence it behaves closer to plug flow than the others.

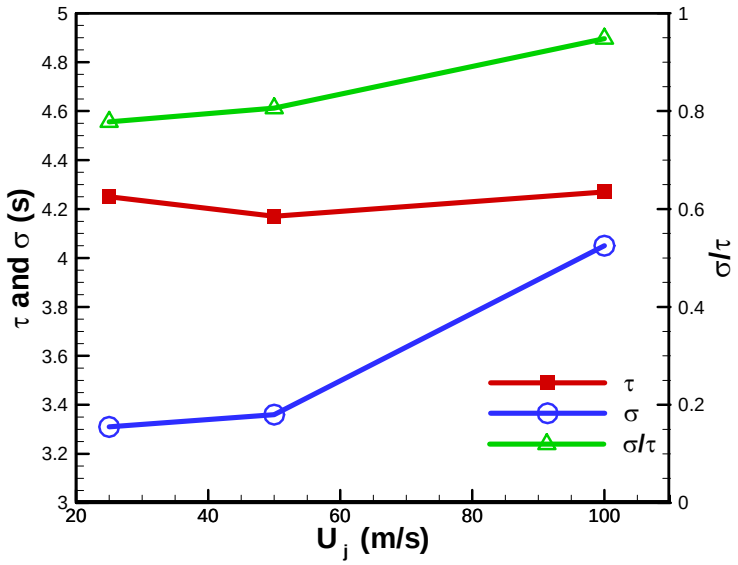

Figure 4-26. Residence time and standard deviation of RTD of tracer gas predicted at cross-section Z = 0.45 m for same amout of secondary gas injection through different numbers of jets (Jet velocities of 100, 50, 25 m/s for single, two, and four jets, respectively).

4.3.3.3 Steady concentration

Steady state tracer concentrations at different levels downstream and upstream of the secondary gas injection are analyzed to evaluate the radial mixing and back-mixing. In the current study, 30 seconds after the start of continuous tracer injection are simulated and results for the last 10 seconds are used to analyze the mixing of tracer gas at steady state. Contours of time-averaged tracer concentration in the XZ plane are shown in Figure 4-27 for single jet injection with different jetting velocities. In this figure, the tracer concentration decreases quickly away from the jet. Since the tracer is introduced through the jet, the tracer concentration contours also reflect the jet penetration depth into the bed to some extent. It is obvious that the jet penetration has a significant effect on the radial mixing of tracer gas.

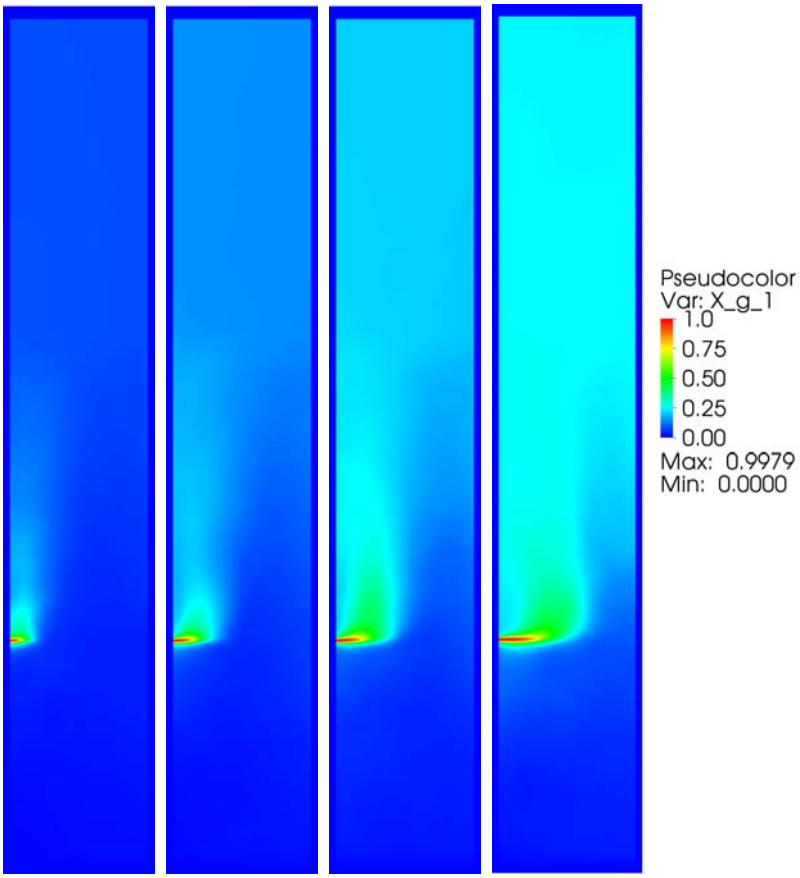

Figure 4-27. Contours of the time-averaged tracer concentration in the XZ plane for single jet injection at different velocities ($U_j = 25$, 50, 75, and 100 m/s from left to right).

Figure 4-28 shows the tracer concentration profiles at different heights in the XZ and YZ planes for single jet injection at various velocities. The tracer gas concentration is scaled with C_0.

$$C_0 = \frac{Q_{tracer}}{Q_g} \tag{4.10}$$

where Q_{tracer} is the volumetric flow rate of tracer gas and Q_g is the total gas flow rate.

For all the cases shown in Figure 4-28, there exists a bell-shaped peak at Z = 0.2 m in XZ plane, which is 0.03 m above the injection. This high tracer concentration above the jet corresponds to the tip of the curved jet or the tracer-riched bubbles generated by the jet. As the jet velocity increases, the peak migrates the centre of the bed. This pattern is in accordance with our previous results, and the jet penetration based on the measured concentration profiles compares favourably with the jet penetration depths reported in Figure 4-5. In the far downstream region, the tracer concentration profiles become flatter due to the radial diffusion. It can be seen from Figure 4-28, the tracer gas is uniformly mixed at Z = 0.40 and 0.45 m, which correspond to the bed surface region and freeboard region, respectively. At 0.02 m upstream of injection (Z = 0.15 m), the tracer gas is at a low concentration, which indicates back-mixing at that level.

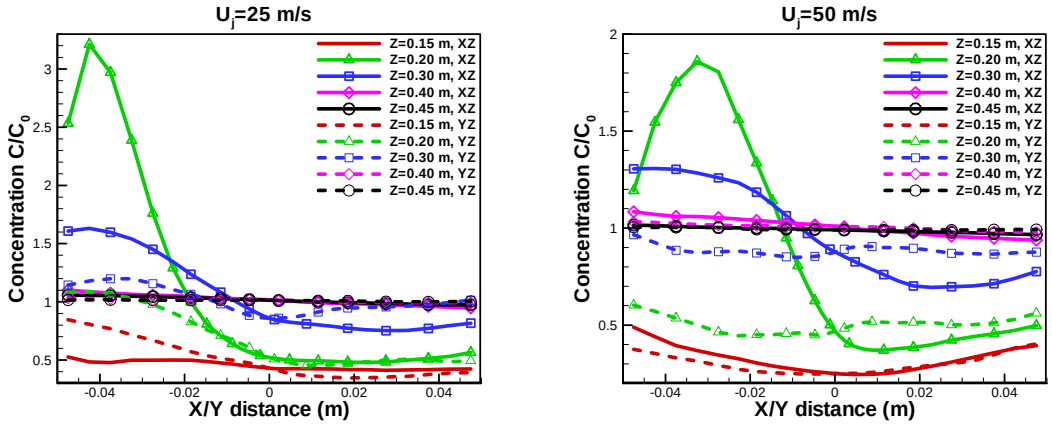

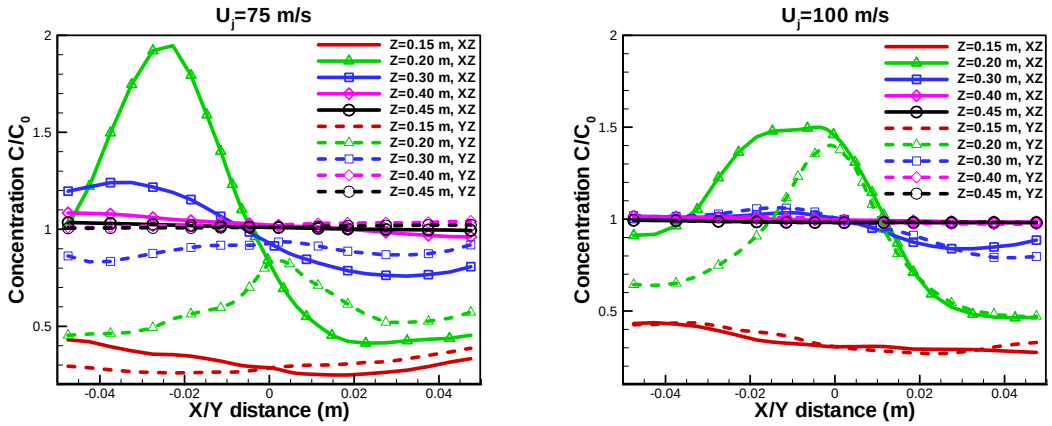

Figure 4-28. Scaled tracer concentration profiles at different heights in the XZ and YZ planes for single jet injection at different velocities.

Figure 4-29 shows the tracer concentration profiles at different heights in the XZ and YZ planes for four-jet injections at various jet velocities. In the figure, two peaks above the injection at Z = 0.20 m, corresponding to opposing jets, are observed for low jet velocities (25 and 50 m/s). The peaks move toward the centre of the bed and finally merge into one with increasing jet velocity (75 and 100 m/s). Again, flat concentration profiles are observed for Z = 0.30, 0.40 and 0.45 m, indicating good radial mixing there. In Figure 4-29, due to the short simulation time, only rough symmetry of the concentration profiles can be observed, which corresponds to the symmetric arrangement of jets. Again, back-mixing is observed for all the cases, as discussed in detail in the next section.

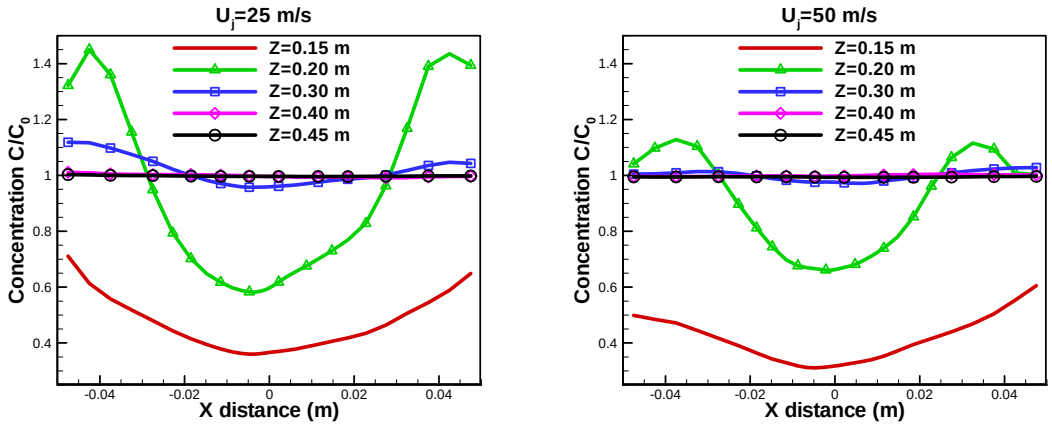

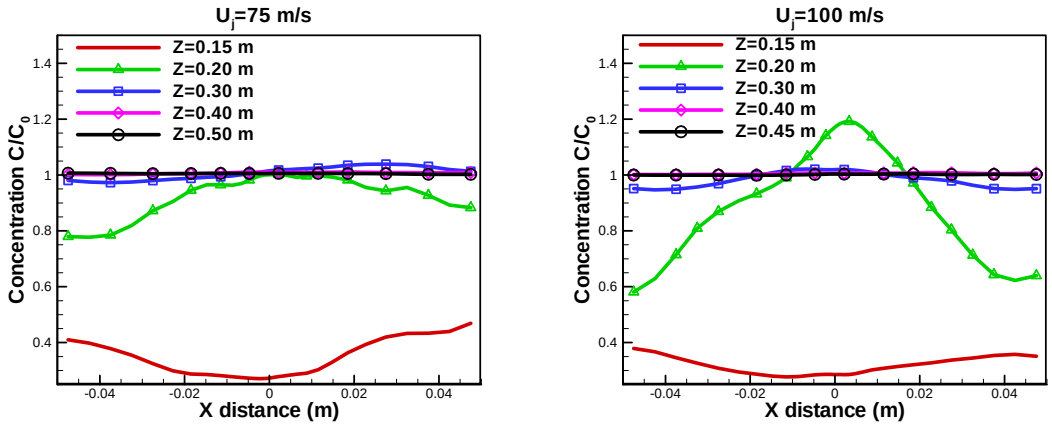

Figure 4-29. Scaled tracer concentration profiles at different heights in the XZ and YZ planes for four-jet injection at different velocities.

When the same amount of secondary gas is injected through different jet arrangements, it is not straightforward to compare the concentration profiles at certain lines. The contours of averaged tracer concentration scaled with C_0 are shown in Figure 4-30 at different levels upstream or downstream. Due to the brief time interval studied in the current steady state analysis (compared to experimental measurements which usually last a few minutes), the symmetry in bed geometry and jet arrangement is not completely reflected in the concentration contours for four-jet and two-jet configurations. As discussed above, high tracer concentration region for each jet can be seen 0.03 m above the jet injection (Z = 0.20 m). For Z = 0.30 m, relatively good mixing between the tracer gas and the primary gas has been achieved. However, the effect of jet arrangement is still visible from the concentration contour. For regions further downstream, Z = 0.40 and 0.45 m, the tracer gas is well mixed and the influence of jet arrangement fades away.

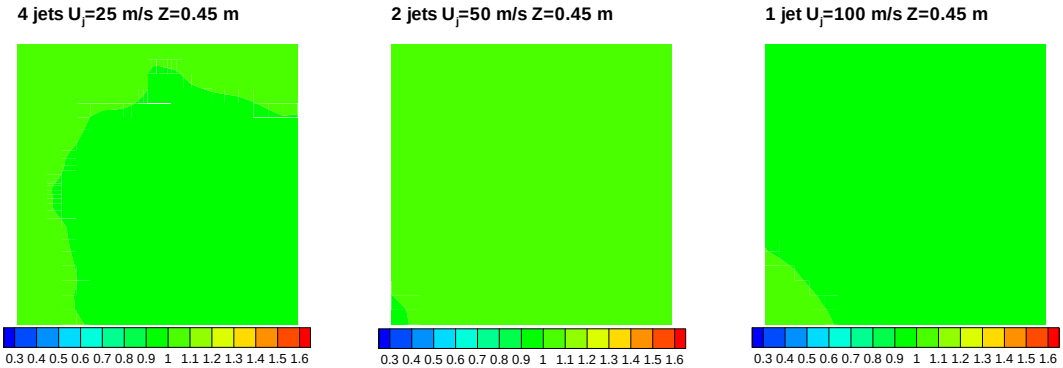

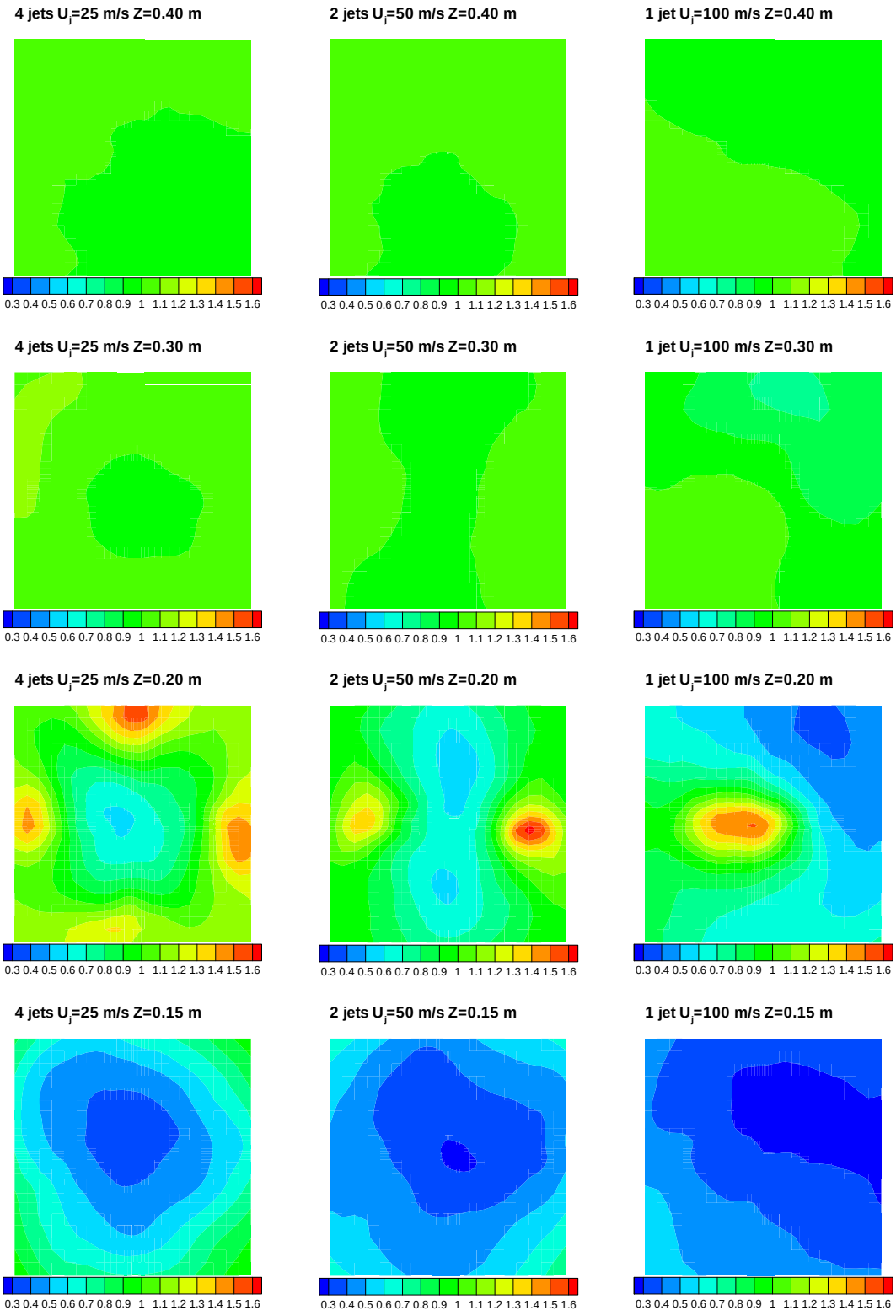

Figure 4-30. Contours of the scaled tracer concentration at different heights for single, two-, and four-jet injections at different velocities.

4.3.3.4 Back-mixing

In fluidized bed chemical reactors, the axial gas back-mixing can significantly decrease conversion and selectivity, and it is consequently undesirable in most applications. It has been suggested that there are two mechanisms for the axial back-mixing of gas in bubbling fluidized beds (Deshmukh et al., 2007). In most studies, gas back-mixing is due to the dense solids downflow, which drags gas downwards when the solids descending velocity exceeds the interstitial gas velocity (Stephens et al., 1967; Nguyen et al., 1977; Nguyen et al., 1981; Li and Weinstein, 1989; Deshmukh et al., 2007).

In this section, back-mixing of tracer gas is discussed. As already shown for the tracer concentration plots at Z = 0.15 m in previous analyses, back-mixing takes place in all the cases simulated. To further study this phenomenon, the tracer concentration profiles at different levels upstream Z = 0.05, 0.10, and 0.15 m, which are 0.12, 0.07, and 0.02 m below the injection respectively, are measured. Again, the tracer concentration is scaled with C_0.

For single jet injection, as shown in Figure 4-31, the concentration of tracer gas is high right below the point of injection, and it becomes more uniform and lower farther upstream. Generally, back-mixing of tracer gas seems stronger for low jet velocities (25 and 50 m/s) than for high jet velocities (75 and 100 m/s). However, no obvious trend can be obtained from these plots.

For four-jet injections shown in Figure 4-32, the high tracer concentration close to the wall indicates that back-mixing near the wall is prominent compared to that in the core region. This is mainly because of the downflow of solids near the wall, in which gas is entrained. This finding agrees with an experimental observation that back-mixing increased when a tracer was injected at the wall compared to when it was injected at the centre of a column (Gilliland and Mason,

1952). However, the prominence of back-mixing close to the wall is damped as the jet velocity increases and the concentration profile becomes more uniform. In addition, we can observe the decrease in back-mixing for high jet velocities as the tracer gas is transported deep into the bed. This is consistent with the results of Christensen et al. (2008a) that back-mixing decreased with increasing secondary gas injection. Furthermore, back-mixing is stronger in the corners, where the wall effect is most significant, as shown in the tracer concentration contour at Z = 0.15 in Figure 4-30.

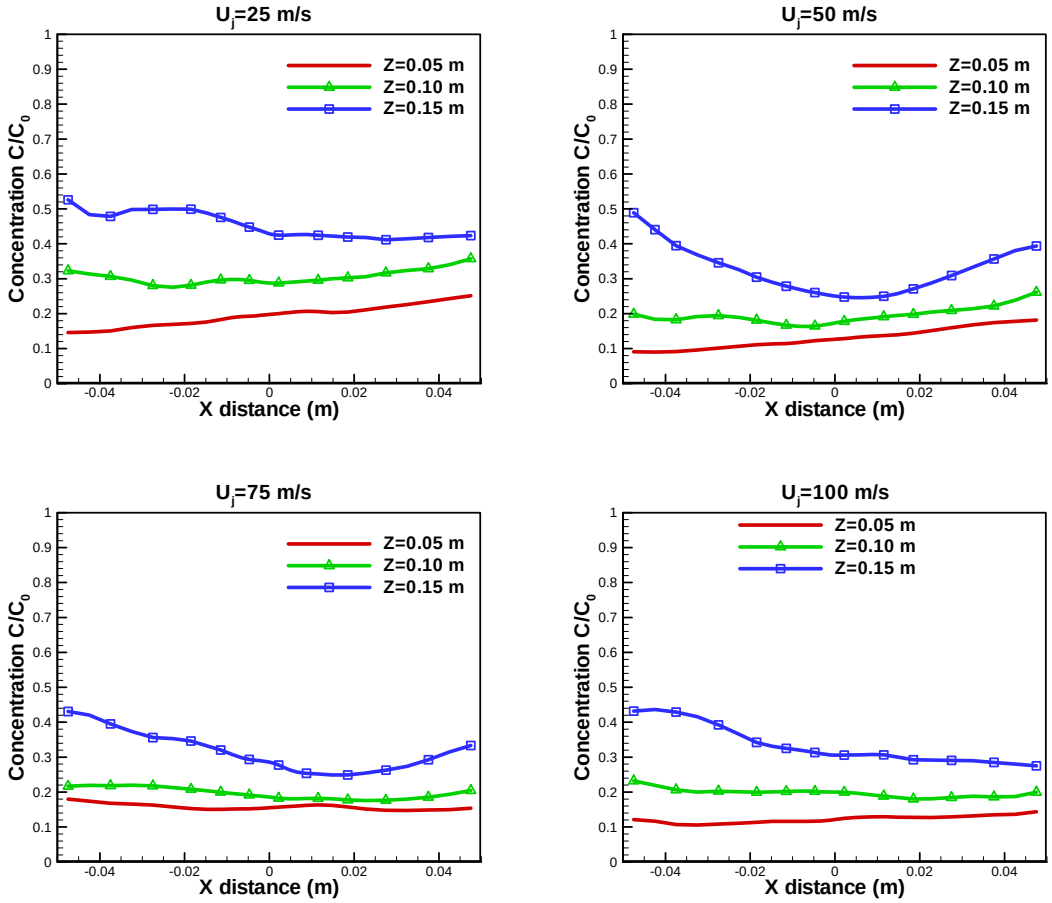

Figure 4-31. Scaled tracer concentration profiles at different levels upstream in the XZ plane for single jet injection at different velocities.

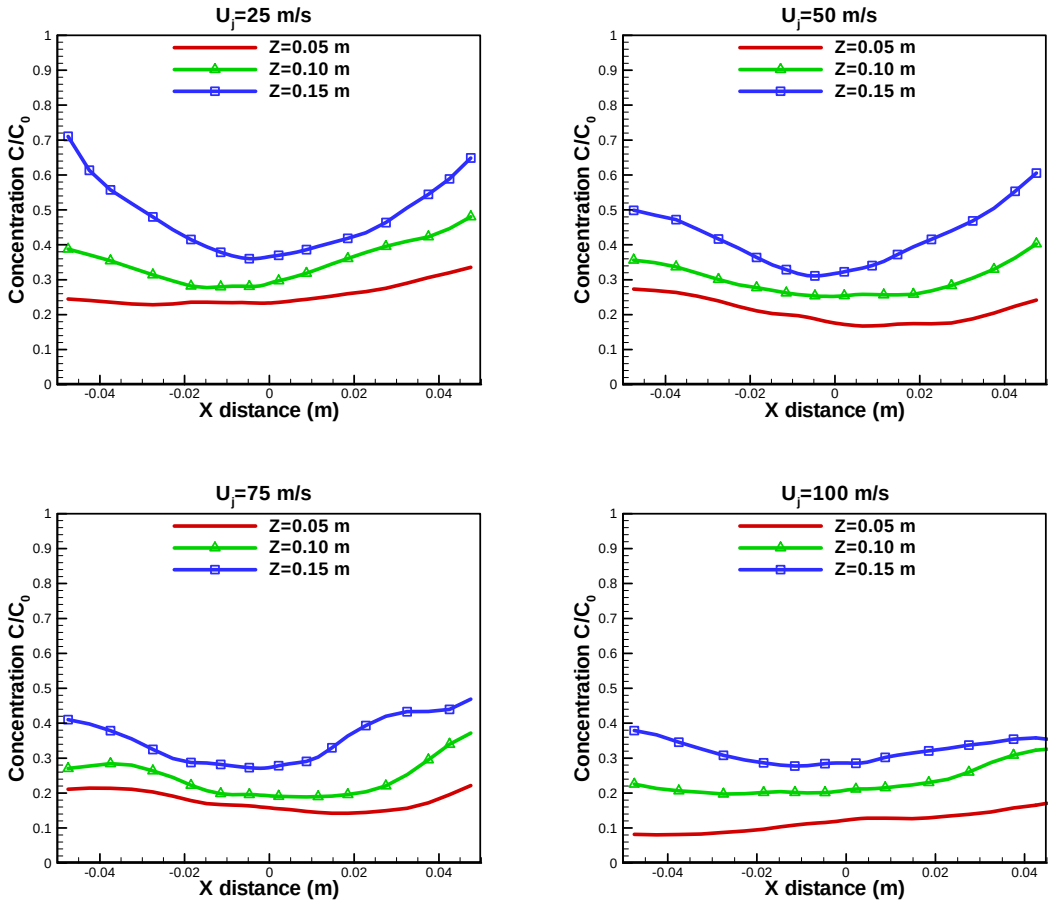

Figure 4-32. Scaled tracer concentration profiles at different levels upstream in the XZ plane for four-jet injections at different velocities.

When the secondary gas is injected through one, two, and four jets with the same flow rate, the tracer back-mixing is more significant for four jets injection than for the other two cases, as shown in Figure 4-33. This is because more tracer gas is entering the downward solids flow close to the wall due to the limited jet penetration into the bed.

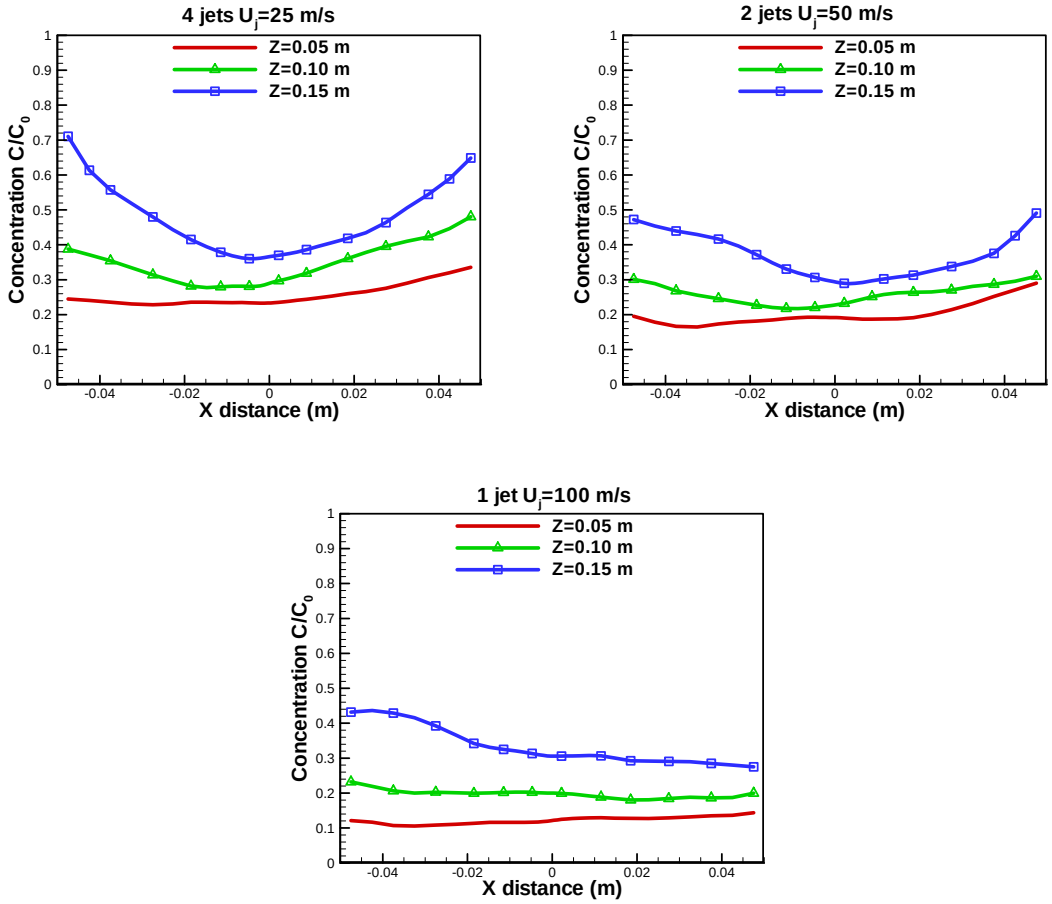

Figure 4-33. Scaled tracer concentration profiles at different levels upstream in XZ plane for single, two-, and four-jet injections with same total flow rate and different velocities.

4.3.3.5 Tracer/solid mixing

To characterize the contact between the solids and the secondary gas, the dependence between the tracer gas volume fraction and the solid volume fraction at different heights above the secondary gas injection is analyzed. A plot of the tracer volume fraction versus the solid volume fraction is shown in Figure 4-34, for four-jet injection with $U_j = 50$ m/s. The data points in the Z = 0.3 m plane are obtained for a 10 s simulation with a data recording frequency of 100 Hz. The tracer volume fraction averaged in classes of different solid volume fractions is also shown in the figure with the standard deviation as an error bar.

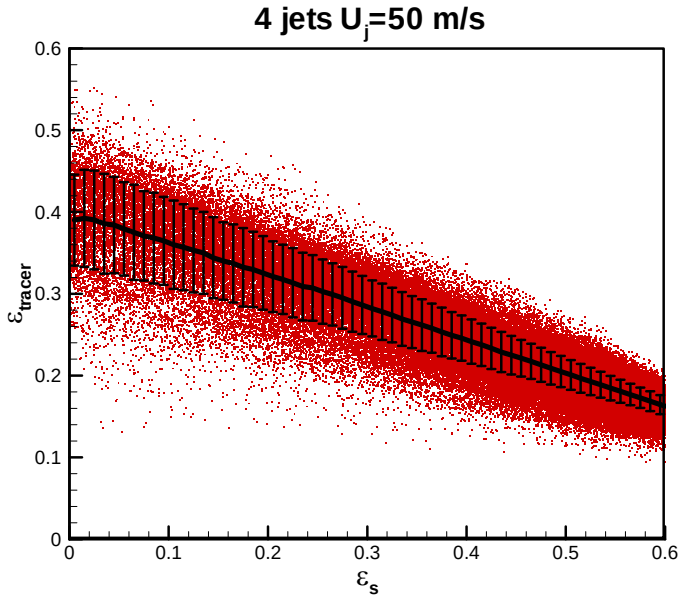

Figure 4-34. Tracer volume fraction versus solid volume fraction at Z = 0.3 m for four-jet injection $U_j = 50$ m/s.

Figure 4-35 shows the plots of the averaged tracer volume fraction versus the solid volume fraction at different heights for four-jet injections with various velocities. These plots can be used to reveal the effect of tracer mixing in the gas phase on tracer/solids mixing. Generally, the volume fraction of tracer decreases with increasing solid volume fraction. At Z = 0.2 m, most tracer gas exists in the form of bubbles detaching from the tip of gas jet. This leads to a high tracer volume fraction in the relatively dilute region ($\varepsilon_s < 0.25$) and a low value in the dense region. Higher above the injection level, the profiles become straight and the standard deviation decreases because of fast mixing of the tracer. This indicates that the contact between tracer and solids is totally governed by the gas-solid mixing inside the bed at high levels. Moreover, the pattern mentioned above is more evident for the injection with high jet velocities than for injection at low jet velocities.

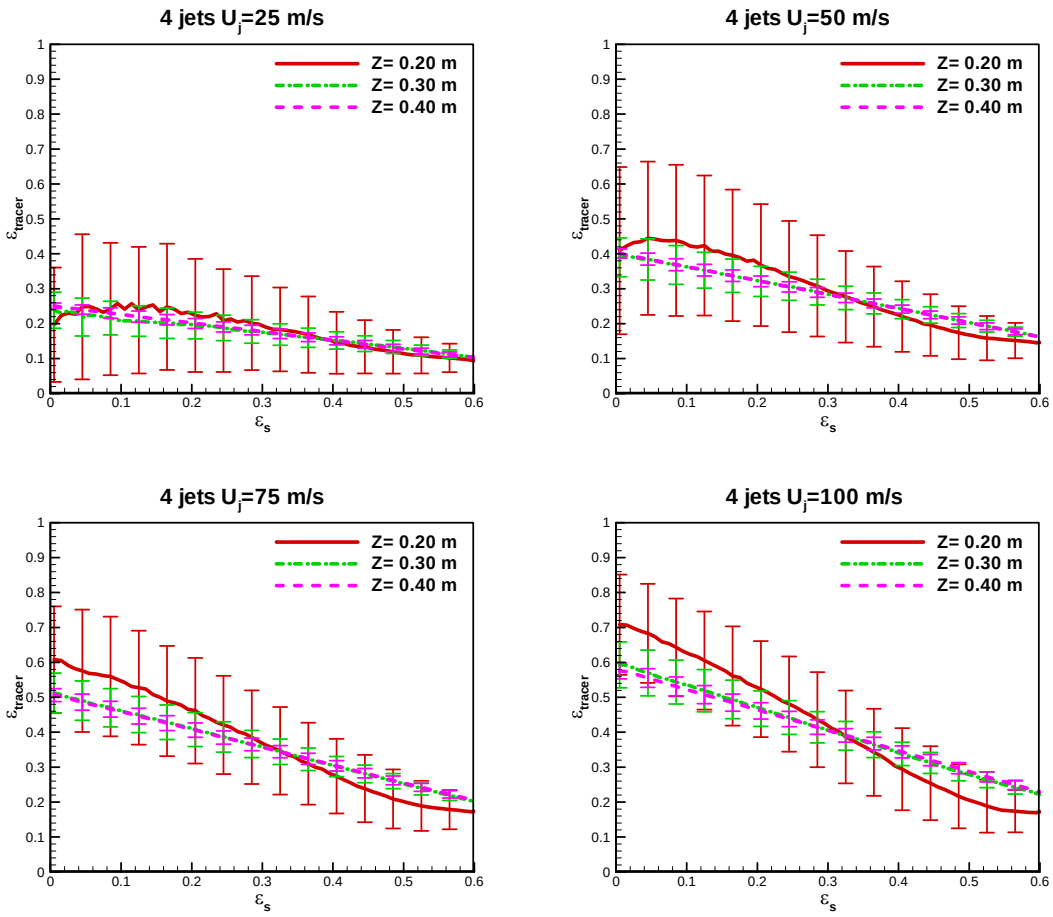

Figure 4-35. Tracer volume fraction versus solid volume fraction at different heights for four-jet injection at different velocities.

Similarly, the tracer volume fraction versus the solid volume fraction at different heights for single, two-, and 4-jet injections with identical secondary gas flow rate is plotted in Figure 4-36. For Z = 0.20 m, there is a very significant difference between the profiles in both the average value and the standard deviation. It can be concluded that the tracer tends to enter the emulsion phase for distributed injections with low jet velocities. Christensen et al. studied the distributed secondary gas injection in a bubbling fluidized bed via a fractal injector and concluded that secondary gas tends to stay in the dense phase and that gas-solid contact is improved (Christensen et al., 2008b; Christensen et al., 2008c). Our result is consistent with that of Christensen et al.

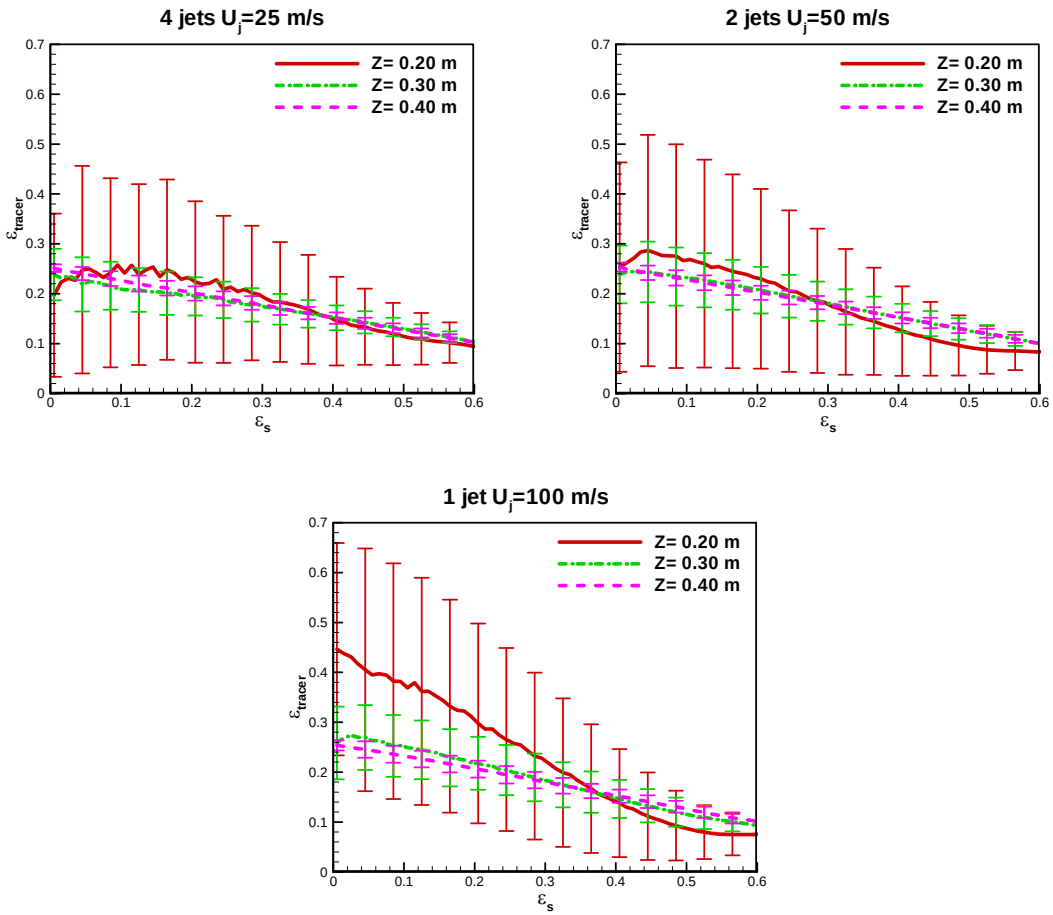

Figure 4-36. Tracer volume fraction versus solid volume fraction at different heights for single, two- and four-jet injections.

The contact between the tracer gas and the solids is further investigated by comparing the bubble hold-up at Z = 0.3 m for different jet arrangements in Figure 4-37. The tracer volume fraction versus the solid volume fraction for different jet arrangements is also presented in Figure 4-37 to aid the analysis. As already discussed, less tracer gas exists in the dilute region and more in the dense region when it is introduced into the system through four jets with $U_j = 25$ m/s instead of one jet with $U_j = 100$ m/s. From the bubble hold-up plot in Figure 4-37, it is evident that less gas is in the form of bubbles for the distributed secondary gas injections (two- and four-jet injections). Summing up these two phenomena and accounting for the bubble size being small

for four-jet injection shown in Table 4-4, it can be concluded that gas and solid contacting is greatly improved for four-jet injection when compared to single jet injection.

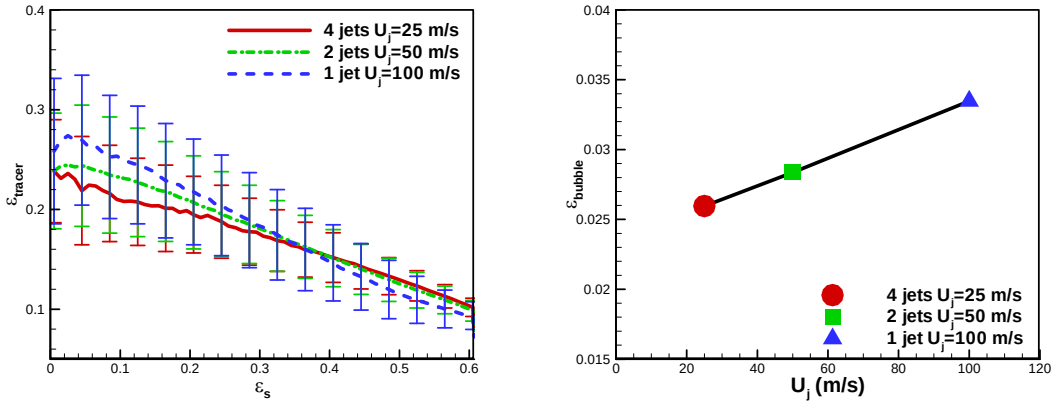

(a) (b)

Figure 4-37. Tracer volume fraction versus solid volume fraction plot (a) and average bubble hold-up (b) at Z = 0.30 m for single, two- and four-jet injections.

4.4 SUMMARY

In this chapter, single and multiple horizontal gas jet injections into a rectangular bubbling fluidized bed has been numerically studied. Various jet velocities and jet arrangements have been simulated. The predicted jet penetration length increases with the jet velocity for both single and multiple-jet injections. For the multiple gas jets investigated, limited influence of each jet on the others is observed until the jets start to overlap. Various phenomena predicted by our numerical simulations agree qualitatively with experimental observations. The interactions between the gas jet and surrounding gas, solids, bubbles, and other jets that are difficult to investigate experimentally are studied numerically. A better understanding of jet behaviour is achieved through the numerical simulation.

The influence of the secondary gas injection on flow hydrodynamics in the bubbling fluidized bed is examined. It is shown that secondary gas injection can strongly affect the hydrodynamics of the upper part above the injection level if the secondary injection flow rate is high enough, whereas its effect is nearly negligible below the injection level. According to the investigations of voidage and velocity distribution resulting from the secondary gas injection, the jet penetration depth plays an important role in affecting the bed hydrodynamics. When jets penetrate deep into the bed, it is found that the introduction of secondary gas injection can promote solids circulation inside the bed by bringing more particles upward in the core region. However, at even higher jetting flow rates and deeper penetrations, slugging tends to take place which may lead to gas bypassing. In our simulations, the decrease in mean bubble size is observed for low-flow-rate secondary gas injections, and it is more significant when the secondary gas is injected through more jets with moderate penetration depth. This decrease in bubble size leads to improved gas-solid contact, hence it is expected to increase the conversion for mass-transfer limited reaction.

Finally, the mixing of secondary gas with bed materials is studied by introducing a tracer gas from the secondary injections. Both unsteady and steady results are analyzed to understand the mixing behaviour. At the injection level, the tracer distribution is non-uniform. Within a short distance above the injection, the tracer becomes uniformly distributed. Gas back-mixing is observed in all simulations prominent near the wall due to the downward flow of solids. For the cases studied, the gas back-mixing tends to decrease as the secondary gas flow rate increases. For the same secondary gas flow rate, it appears that better contacting between the tracer gas and solid particles is achieved when the secondary gas is injected through distributed jet arrangement.

Chapter 5. SPRAY IN A COATING DEVICE

5.1 INTRODUCTION

Spouted beds have been utilized in various industrial applications such as drying, coating, and granulation, as they provide a means of good mixing and circulation of particles of relatively large size and narrow size distribution (Mathur and Epstein, 1974). In spouted beds, the maximum spoutable bed height is an important operational characteristic; beyond this height stable spouting can not be achieved for any spouting gas velocity. This property is directly related to the amount of material that can be processed by restricting the bed loading. The modification of conventional spouted beds by inserting a vertical draft tube into the bed produces several advantages (Muir et al., 1990). It overcomes the maximum spoutable bed height limitation of traditional spouted beds. The draft tube also allows more accurate control of gas and solids residence times by separating the spout and annulus. Furthermore, fine particles can be successfully spouted after the insertion of a draft tube in spouted beds, improving the design and operational flexibility (Hattori and Takeda, 1978). Spouted Beds with a Draft Tube (DTSB) have been extensively used in industrial processes, such as coating tablets, granulation and agglomeration of fine powders, grain drying, blending and mixing, low temperature carbonization of coal, devolatilization of coking coal, and heavy crude oil gasification (Arsenijevic et al., 2004; Adegoroye et al., 2004; Dewettinck and Huyghebaert, 1999; Hemati et al., 2003: Jono et al., 2000; Konduri et al., 1999).

For DTSB, the solids circulation rate is an important variable in predicting the performance of the system. The effects of design and operation conditions such as the draft tube diameter, gas velocity, entrainment height, etc., on the solids circulation rate have been investigated in numerous experiments (Berruti et al., 1988; Muir et al., 1990; Ijichi et al., 1998; Hattori et al.,

2004). However, not much work has been reported on the detailed flow behaviour inside a DTSB system. Saadevandi and Turton (2004) measured particle velocity and voidage using a computer-based video imaging technique in a semicircular DTSB. Zhao et al. (2006) measured the vertical particle velocity profiles in a full-column cylindrical conical spouted bed with and without a draft tube to study the effect of draft tubes on particle velocity.

With significant improvements in computational power and numerical algorithms, numerical modelling has become a powerful tool for obtaining detailed information about complex gas-solid systems. Marschall and Mleczko (1999) performed a numerical investigation of a draft tube gas-spouted bed of fine particles. They investigated the effect of the inlet gas velocity on the pressure drop in the draft tube, particle residence time, and voidage distribution along the axis of the draft tube. Szafran et al. carried out a series of numerical simulations of spouted beds with a draft tube; the hydrodynamics of the flow were investigated and numerical results were validated with experimental data (Szafran and Kmiec, 2004; Szafran et al., 2005; Szafran and Kmiec, 2007).

In this part of the work, we simulate the flow in a flat-based DTSB based on the experimental setup of Saadevandi and Turton (2004) with an Eulerian-Eulerian granular kinetic model. The hydrodynamics of the gas-solid flow in DTSB is investigated and compared with experimental observations. The effect of the gas velocity on the solids circulation rate is evaluated and parametric studies of the restitution coefficient are performed. A model for liquid spray injection into a gas-solid flow is proposed and implemented into a commercial CFD software package, Fluent 6.3. The liquid spray introduced through the bottom nozzle is simulated and the influence of the spray rate on particle volume fraction and velocity inside the draft tube is examined.

5.2 SAADEVANDI AND TURTON'S EXPERIMENTS

In Saadevandi and Turton's experiments, the apparatus consisted of a semicircular spouted bed column with a draft tube as shown in Figure 5-1. The column diameter was 22.9 cm and the draft tube mounted in the centre region was 10.2 cm in diameter. To reduce the flow of particles towards the spray nozzle and assist the upward flow pattern through the spray zone, the bottom of the draft tube was angled at 60 degree from the horizontal, shown as inset in Figure 5-1. The distributor was divided into two sections: an inner section and an outer section, with independently controllable air supplies to introduce the fluidizing gas into the system. The bed was equipped with a half spray nozzle at the centre of the distributor plate. Water was the model spray liquid, and spray conditions were chosen to avoid agglomeration of particles during the experiments. The whole equipment was a typical small-scale fluidized bed coating apparatus cut in half. Detailed information of this system can be found in Saadevandi (1996). 700g closely sized glass beads were loaded into the bed. Particle velocity and voidage profiles were measured from the front transparent glass face with computer-based video imaging techniques and custom software. By adjusting the gap between the draft tube and the bottom distributor, measurements for low and high solids circulation rates corresponding to gap heights of 5 and 10 mm, respectively, were conducted.

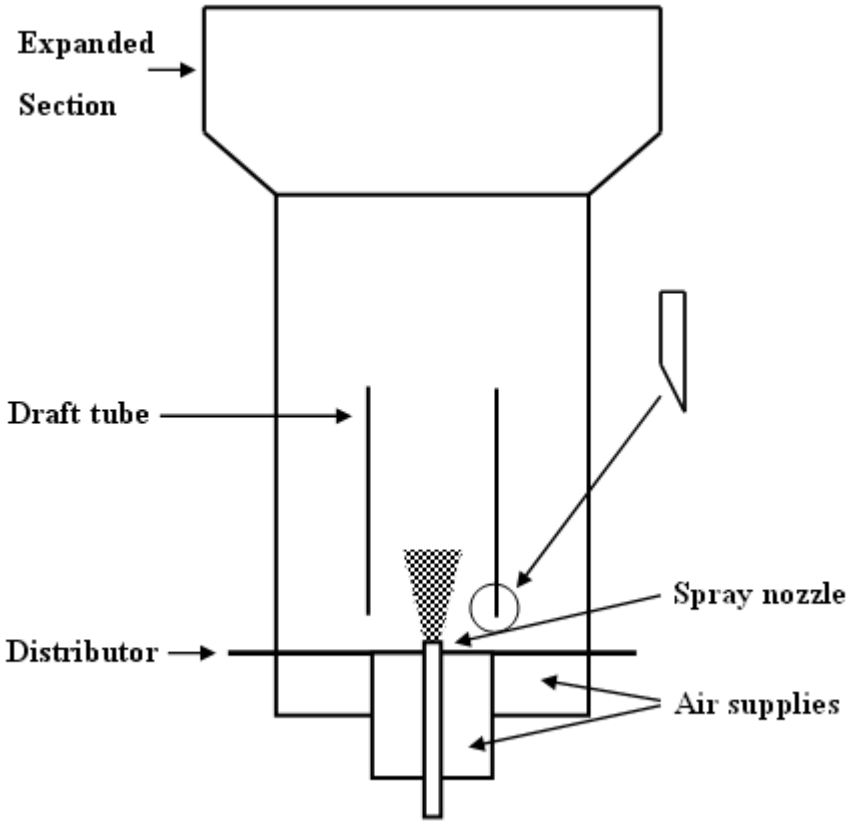

Figure 5-1. Schematic diagram of the Saadevandi and Turton (2004) experimental setup.

5.3 NUMERICAL METHOD

5.3.1 Governing equations

The multi-fluid, Eulerian-Eulerian model based on granular kinetic theory is employed in the numerical simulation; each phase is treated as an inter-penetrating continuum. The flow is assumed to be isothermal and the gas phase is incompressible. The conservation equations of mass and momentum for each phase and constitutive relations, including granular kinetic models and frictional models, as summarized in **Chapter 2** are employed. To minimize repetition, only new models employed in the current study are described here.

5.3.2 Model of liquid spray

We model the atomized liquid spray as a dispersed phase with uniform droplet size in the Eulerian approach. Governing equations of mass and momentum are solved for the droplet phase.

$$\frac{\partial}{\partial t}(\alpha_l \rho_l) + \nabla \cdot (\alpha_l \rho_l \vec{V}_l) = q_l \tag{5.1}$$

$$\frac{\partial}{\partial t}(\alpha_l \rho_l \vec{V}_l) + \nabla \cdot (\alpha_l \rho_l \vec{V}_l \vec{V}_l) = \nabla \cdot \bar{\bar{\tau}}_l - \alpha_l \nabla P + \alpha_l \rho_l \vec{g} + M_{lg} + I_l \tag{5.2}$$

In the above equations, l stand for the liquid droplets, α, ρ are the volume fraction and density, and $\vec{V}$ is the velocity. In the mass conservation equation, q_l is the mass transfer from droplet phase to particulate phase due to coalescence upon collision. P is the gas pressure shared by all phases, and $\vec{g}$ is the gravitational acceleration. M_{lg} is the inter-phase momentum exchange between gas and droplets, and I_l accounts for the momentum transfer resulting from mass transfer.

To obtain the inter-phase momentum exchange, the gas-droplet drag coefficient β_{gl} is calculated following Issa and Oliveira (1996).

$$\beta_{gl} = \alpha_g \alpha_l \frac{3\rho_g \left|(\vec{V}_g - \vec{V}_l)\right| C_{D,l}}{4 d_l} \tag{5.3}$$

where

$$C_{D,l} = \begin{cases} \dfrac{24}{\mathrm{Re}_l \cdot \alpha_g}(1 + 0.15(\mathrm{Re}_l \cdot \alpha_g)^{0.687}) & \text{if } \mathrm{Re}_l \cdot \alpha_g < 1000 \\ 0.44 & \text{if } \mathrm{Re}_l \cdot \alpha_g \geq 1000 \end{cases} \tag{5.4}$$

An additional model is employed to include the interaction between spray droplets and solid particles. Without considering the breakup of a droplet, when a droplet collides with a particle, they can stick together or bounce depending on the material properties as well as the impact

velocity. The fraction of droplets that adhere on the particle surface is expressed by an adhesion efficiency φ. To calculate the adhesion efficiency, an expression for critical impact velocity u_{crit}, above which the drop rebounds, for drops impacting a horizontal dry plate, developed by Link (1996) and reported by Panda (2001) is employed.

$$u_{crit} = \frac{4\mu_l \left(3\tan(\theta_{lp}/2) + \tan^3(\theta_{lp}/2)\right)^{2/3}}{d_l \rho_l \tan^2(\theta_{lp}/2)} \tag{5.5}$$

and φ is defined as

$$\varphi = \begin{cases} 0 & u < u_{crit} \\ 1 & u \geq u_{crit} \end{cases} \tag{5.6}$$

where θ_{lp} is the contact angle. When coalescence is the outcome of the collision between a droplet and a particle, the liquid is assumed to spread over the particle surface and form a thin film in the presence of good wettability. No agglomeration of solid particles can take place if only a small amount of liquid is introduced through fine spray. This assumption is appropriate for this work, because the experimental spray conditions were chosen to avoid agglomeration of particles. The formation of liquid film on particles is expected to affect the restitution coefficient. However, no relationship between the liquid film thickness and restitution coefficient is reported. In the current work, the influence of water film on particle restitution coefficient is neglected since the film is very thin.

According to the mechanisms mentioned above, the mass transfer rate from droplet phase to particulate phase is proportional to the number of collisions of solid particles and liquid droplets per unit volume, which can be calculated by (Nayak et al., 2005)

$$N_{lp} = \frac{\pi}{4} n_l n_p (d_p + d_l)^2 \left|\vec{V}_{lp,R}\right| \tag{5.7}$$

where n_l and n_p are the number densities of droplets and particles, and d_l, d_p are their diameters. $\vec{V}_{lp,R}$ is the relative velocity between droplets and the particulate phase.

Rewriting n_l and n_p in terms of volume fraction, equation (5.7) becomes

$$N_{lp} = \frac{\pi}{4}\left(\frac{6\alpha_l}{\pi d_l^3}\right)\left(\frac{6\alpha_p}{\pi d_p^3}\right)(d_p + d_l)^2 \left|\vec{V}_{lp,R}\right| \tag{5.8}$$

Hence, the mass transfer from the dispersed liquid droplet phase to the particulate phase due to collisions is

$$q_{lp} = \varphi m_l N_{lp} \tag{5.9}$$

where m_l is the mass of a single droplet, i.e.

$$m_l = \frac{1}{6}\rho_l \pi d_l^3 \tag{5.10}$$

In the current model, the particulate phase is treated as a mixture of wet and dry particles. A transport equation for liquid adhering to wet particles is written as

$$\frac{\partial}{\partial t}(\alpha_{p,l}\rho_l) + \nabla\cdot(\alpha_{p,l}\rho_l\vec{V}_p) = \nabla\cdot(D_p\nabla(\alpha_{p,l}\rho_l)) + q_{lp} \tag{5.11}$$

where $\alpha_{p,l}$ is the volume fractions of liquid adhering to the particles. The first term in the right-hand side of equation (5.11) stands for the diffusion of liquid in the particulate phase and the second term is the source term due to collisions between droplets and particles. As the deposited liquid travels with wet particles, the diffusion coefficient of the liquid is assumed to be the same as the self-diffusion coefficient of particles. In this model, the transport of liquid from one particle to another particle due to their collisions is neglected since the liquid film is too thin to wet other particles. The self-diffusion coefficient of particles has been extensively studied in sheared granular flows (Campbell, 1997; Henrique et al., 2001; Valverde et al., 2001; Utter and Behringer, 2004). Generally, the diffusion coefficient is a second order symmetric tensor, which has been demonstrated in shear flows. With the basic assumptions of granular kinetic theory, namely binary collisions, uniform particle size distribution, and isotropic granular temperature, the diffusion coefficient can be treated as a scalar. The expression of Hsiau and Hunt (1993) is employed.

$$D_p = \frac{d_p \sqrt{\pi \Theta_p}}{8(1+e_p)\alpha_p g_{0,p}} \tag{5.12}$$

The diameter of particle increases when liquid accumulates on the surface of a particle. The average diameter of the particulate phase can be calculated by

$$d_p = d_{p,d} \left(\frac{\alpha_p}{\alpha_p - \alpha_{p,l}}\right)^{\frac{1}{3}} \tag{5.13}$$

where $d_{p,d}$ is the diameter of the dry particle.

5.3.3 Simulation setup

The equations presented in the above paragraphs are solved by a finite control volume technique with a commercial CFD software package, Fluent 6.3. The frictional model and liquid spray model are incorporated into Fluent 6.3 with user-defined functions (UDF). A $k-\varepsilon$ dispersed turbulence model is used to model the flow turbulence based on Tchen's theory of dispersion of discrete particles by homogeneous turbulence (Fluent, 2006). The domain of numerical simulation follows the experimental device. This problem is simplified as an axisymmetric problem, and non-uniform structured grid is adapted as illustrated in Figure 5-2. The entire computational domain is represented by 9616 control volumes. Two more grids are generated to carry out the grid independence study, and the flow properties such as solids concentration and velocity are compared. The comparison indicates that the current grid size is adequate to capture the flow behaviour of this system. Figure 5-3 shows the profiles of cross-sectional particle volume fraction in the draft tube for different grids.

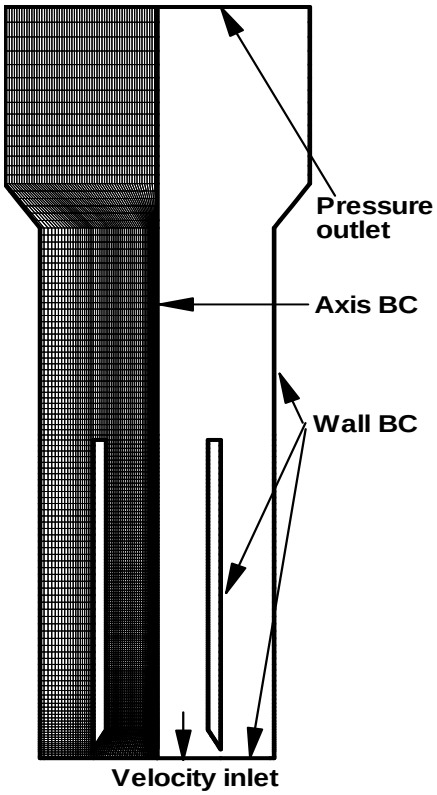

Figure 5-2. Distribution of the grids and sketch of boundary conditions.

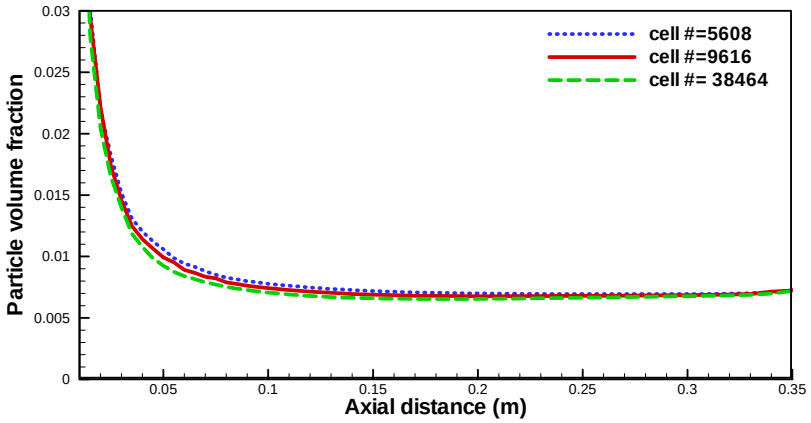

Figure 5-3. Profiles of cross-sectional particle volume fraction in the draft tube for different grids.

The parameters for numerical simulations are listed in Table 5-1. Parametric studies were performed for the restitution coefficient and are discussed below.

Table 5-1. Conditions for numerical simulation.

Parameter	**Description**	**Experiment**	**Simulation**
W	Bed loading	700 g	700 g
h	Gap height	10 mm	10 mm
d_p	Particle diameter	1.086 mm	1.086 mm
d_l	Droplet diameter	34.8 μm	34.8 μm
ρ_p	Density of particles	2500 kg/m^3	2500 kg/m^3
ρ_l	Density of droplets	1000 kg/m^3	1000 kg/m^3
ρ_g	Density of gas	1.2 kg/m^3	1.2 kg/m^3
e_p	Restitution coefficient	-	0.9~0.99
μ_g	Viscosity of gas	1.8e-5 Pa.s	1.8e-5 Pa.s
$\alpha_{p,loosepack}$	Volume fraction for loose packing	0.588	-
$\alpha_{p,\max}$	Maximum solids packing volume fraction	-	0.64

The boundary conditions are illustrated in Figure 5-2. At the axis of symmetry, the gradients of all flow variables along the radial direction are set to zero. The distributor is divided into two parts. The inner part, where the fluidizing gas is introduced, is treated as uniform gas flow, and the outer part is treated as a wall since there is no gas fed in the experiment. A non-slip boundary condition is set for all the walls for the gas phase. For the particulate phase, the partial slip boundary condition suggested by Johnson and Jackson (1987) is applied. In the simulation of the

liquid spray, a free slip boundary condition for the droplet phase is set for the wall. Since droplets are very small and usually travel with the gas, no collision between droplets and the wall is expected. In addition, spray droplets can hardly reach the wall due to interaction with particles. As for the top gas outlet, the pressure outlet boundary condition is used, which allows the particles and droplets to exit the bed freely.

Initially, the spouted bed is partially filled with a certain amount of solid particles and zero velocities are set to all the phases. The spouting gas is introduced from the centre region of the bottom distributor and transient simulation is performed. Time-averaged results are analyzed when fully developed flow has been achieved.

5.4 RESULTS AND DISCUSSION

5.4.1 Gas-solid system

5.4.1.1 Flow hydrodynamics

The system without liquid spray is simulated first. The mean particle volume fraction in the bed is shown together with particle velocity vectors in Figure 5-4 for a gas inlet velocity of 8 m/s. It can be seen that most particles accumulate in the bottom region of the outer annulus. Since no aeration is used, the particles are loosely packed in the annular region. In our simulation, the average solid volume fraction of the packed region is predicted to be about 0.58, consistent with the measured value of 0.588 for loose packing reported by Saadevandi and Turton (2004). The solids flow in the draft tube is dilute. Above the draft tube, the numerical simulation predicted a typical fountain.

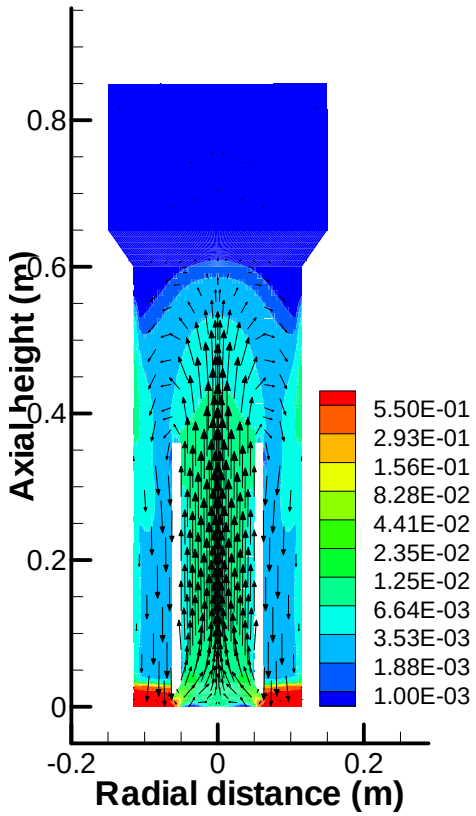

Figure 5-4. Mean particle volume fraction contours and velocity vectors inside the bed.

The particles accumulate at the bottom of the annulus due to gravity and then flow radially inward through the gap between the draft tube and the distributor plate. As soon as the particles enter the draft tube, they are exposed to the high speed upward airflow. Particles entering the draft tube are accelerated by the gas-solid drag force and transported upward. When particles and gas exit the draft tube, the gas velocity decreases with expansion of space and a fountain is formed. Finally, particles move downwards in the outer annular region. The particles in the draft tube, annulus, and fountain zones circulate internally in the system, as illustrated by the particle velocities in Figure 5-4.

The velocity profiles of the gas and particulate phase inside the draft tube at different heights are presented in Figure 5-5. It can be seen that the velocity profiles for particles are similar at different axial heights. The axial particle velocity decreases with the radial distance from the draft tube axis, except at the inlet region of the draft tube where the maximum particle velocity is close to the draft tube wall. This is consistent with experimental observations (Saadevandi and Turton, 2004; Zhao et al., 2006). The velocity of gas is almost uniform, preventing the recirculation of particles inside the draft tube.

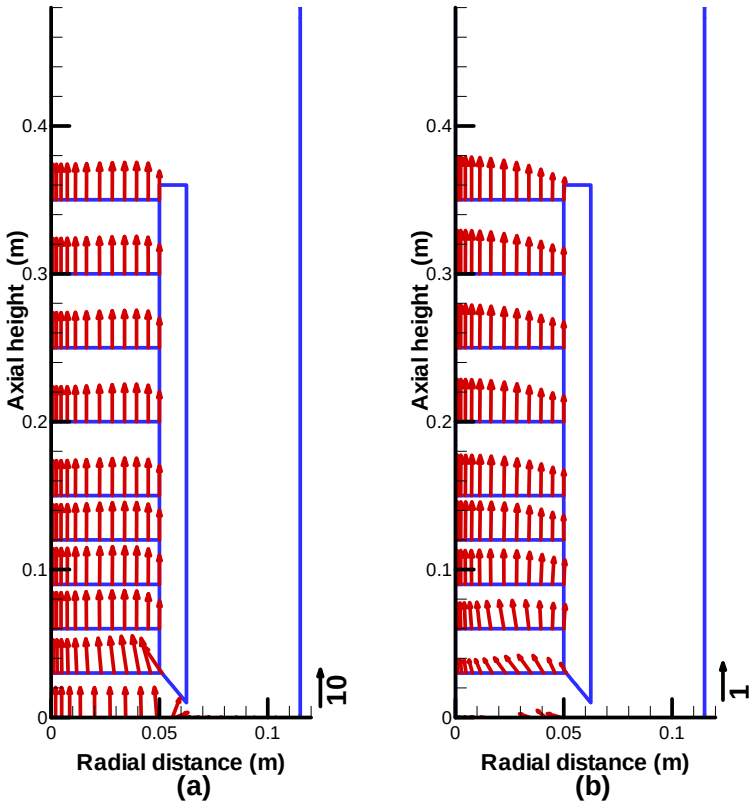

Figure 5-5. Velocity vectors for gas and particles at different heights in draft tube. (a) gas velocity; (b) particle velocity (unit: m/s).

According to Berruti et al. (1988), the solids circulation rate is the most critical variable in predicting the performance of a DTSB. The solids circulation rate calculated for a semicircular

system is compared with experimental results of Saadevandi and Turton (2004). The predicted solids circulation rate, 0.0636 kg/s, agrees well with 0.065 ± 0.004 kg/s reported by these authors. The predicted cross-sectional profiles of the particle volume fraction and velocity in the draft tube are compared with experimental data in Figure 5-6. There is good agreement between simulation and experiment for most of the computational domain. However, as we can see from the figure, the particle velocity in the upper region of the draft tube is somewhat lower than the experimental values. Further comparisons with experimental data are made for the radial profiles of particle volume fraction and velocity in the draft tube at different heights, as shown in Figure 5-7. One possible reason for this discrepancy is that in the experiment, the particles entering the draft tube tend to aggregate at the centre of the inlet region due to the radial velocity. The presence of the front glass face intensifies the aggregation by reflecting the particles, and the voidage in the half-column tends to be lower than in the full-column (He et al., 1994). However, the axisymmetric assumption employed in the current simulation cannot reflect the presence of the front face of this semicircular spouted bed. Another reason for the discrepancy is related to the sensitivity to the restitution coefficient and as discussed below. Consistent with the observation in Figure 5-6, the particle velocities in Figure 5-7 are under-predicted in the upper region of the draft tube. However, they show qualitative agreement with the experimental data. It is believed that the drag model accounts for this under-prediction. Du et al. (2006) studied the influence of drag models on the CFD modeling of spouted beds. Under-predictions of solid velocities in the spout were reported for all the drag models investigated. In their study, the Gidaspow model gave the closest agreement with the experimental data. Similar under-prediction of solid velocities in the spout was reported by Wu and Mujumdar (2007) in a numerical simulation of a spouted bed dryer.

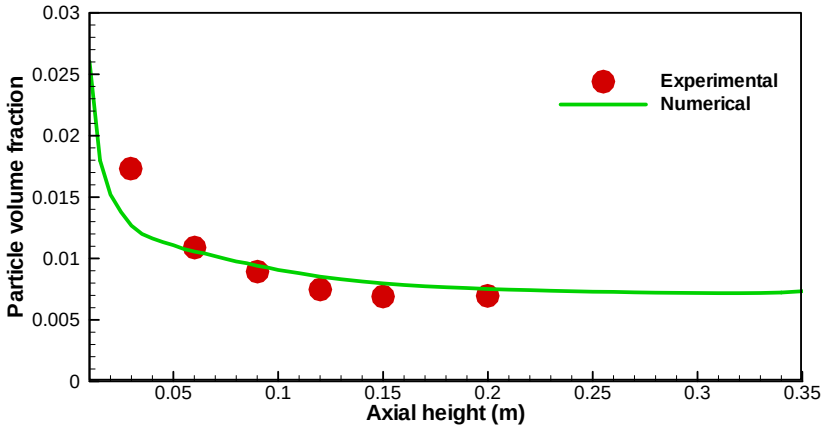

(a)

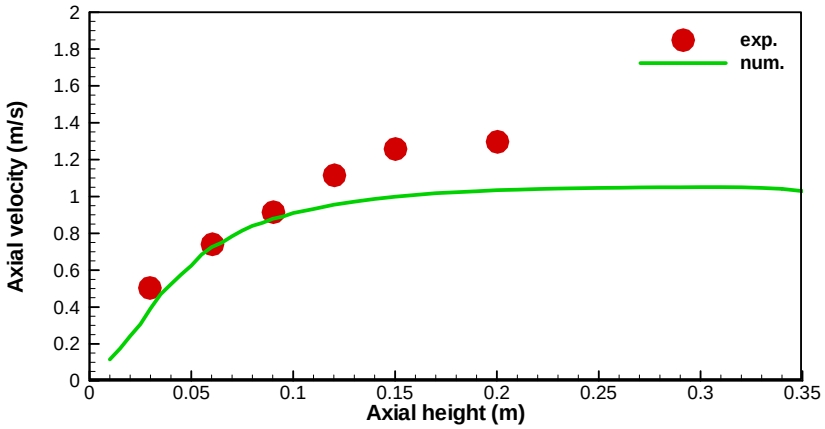

(b)

Figure 5-6. Cross-sectional particle volume fraction (a) and velocity (b) in draft tube.

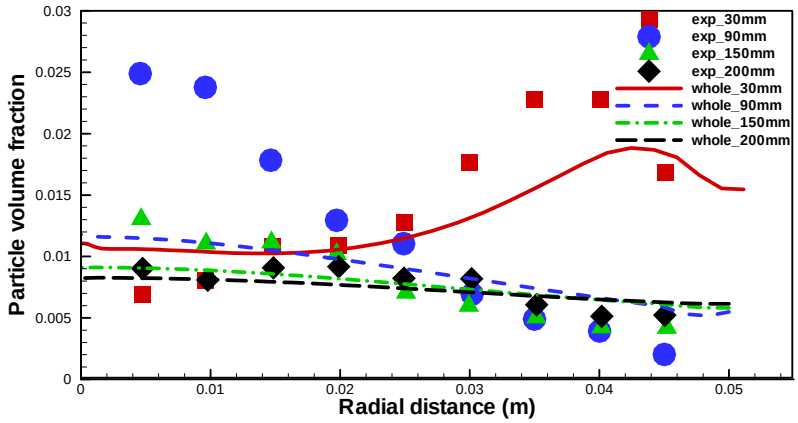

(a)

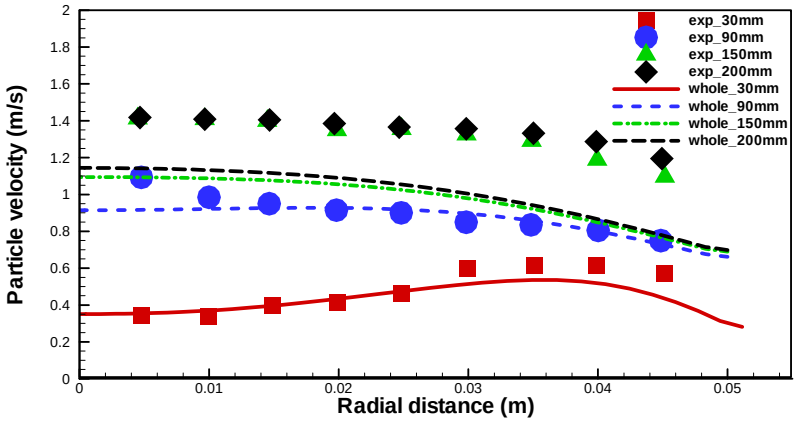

(b)

Figure 5-7. Radial profiles of mean particle volume fraction (a) and axial velocity (b) in draft tube at different heights.

5.4.1.2 Effect of inlet gas flow rate

Six different gas inlet velocities are used in simulations to study the influence of the inlet gas flow rate on the solids circulation rate and flow behaviour in the draft tube. Figure 5-8 shows the average solids circulation rate inside the system. It can be seen that the solids circulation rate increases with the inlet gas velocity, while the rate of increase is decreasing. This trend predicted

by the numerical simulations is consistent with the experimental finding by Ijichi et al. (1998) and Hattori et al. (2004) that the solids circulation rate first increases very quickly and then increases gradually with increasing velocity of the supplied gas in both flat-based semi-cylindrical and full-cylindrical spouted beds with draft tubes. It should be noted that the gap height, which plays an important role in affecting the solids circulation rate, is fixed at 10 mm in all numerical simulations.

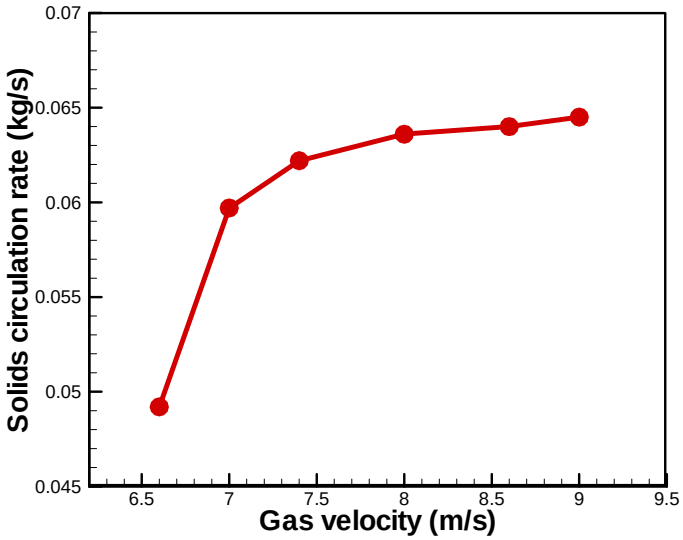

Figure 5-8. Solids circulation rate in draft tube for different gas velocities.

At intermediate gas velocities, the solids circulation rate is determined mainly by the entrainment of particles in the upward gas flow inside the draft tube. As the gas velocity increases, the particles entering the spout tend to be removed immediately; hence, more particles enter the draft tube through the gap. However, at higher gas velocities such as 8 m/s, the solids circulation rate is limited by the solids discharge through the gap instead of the carryover capacity of the gas flow. The discharge of particles from the gap is governed by the slow frictional flow in the compacted annular region. Consequently, the solids circulation rate no longer depends strongly on the gas velocity, as the discharge rate of particles almost reaches its maximum. This differs from conical-based spouted beds, where a certain amount of gas bypasses through the annular

region, and this amount increases with the total gas flow rate. The solids flowability in the annulus increases with the amount of bypassing gas, especially when the particles in the annulus are fluidized (Ijichi et al., 1998; Hattori et al., 2004). In the present setup, however, only a small amount of gas bypasses through the annulus because the gas inlet is much smaller than the draft tube opening. To illustrate this analysis, the gas flow rates in the draft tube and the annulus are plotted in Figure 5-9. The gas flow rate in the annulus is very small, and it remains almost constant with increasing gas velocity. In a flat-based DTSB operated in current condictions, the solids flowability in the annular region is not affected by the gas flow rate through the inner distributor.

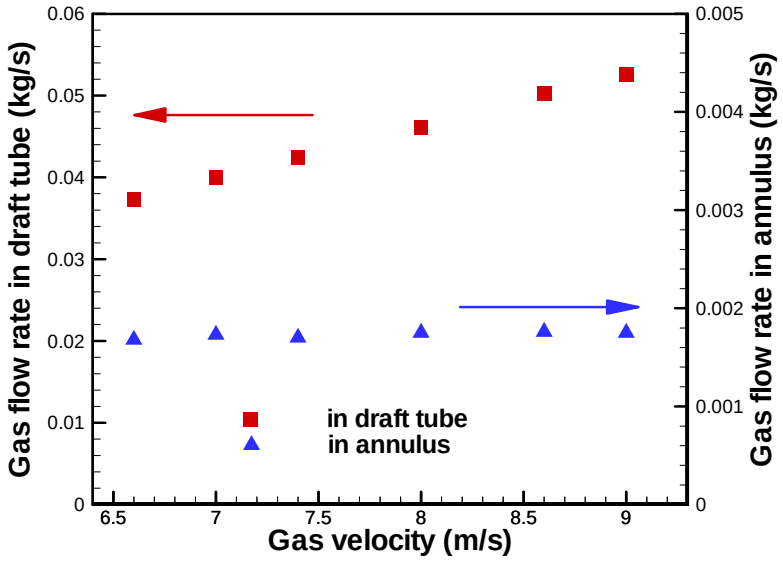

Figure 5-9. Gas flow rate supplied to the system and gas flow rate in annulus.

As the gas flow-rate from the distributor increases, the local voidage increases in the entire draft tube as a consequence of reduced particle residence time inside the tube. It can be easily observed in Figure 5-10, where the contours of particle volume fraction in the bed for different gas velocities are presented. At high gas flow rates, the congregation of particles in the core region becomes weak. It can be expected that particles will segregate towards the wall and form a dilute core region, as typically observed in a riser, if the draft tube is long enough for this flow

pattern to develop. In Figure 5-10, we can also observe that the height of the fountain above the draft tube increases with gas velocity since the particles with higher velocity in the draft tube produce elevated trajectories. The dense region at the top of the fountain as reported in spouted fluidized beds is predicted at low gas velocity and tends to disappear at high gas velocities (He et al., 1994). Similar experimental observations were reported by Karlsson et al. (2006) and Szafran and Kmiec (2007).

5.4.1.3 Effect of restitution coefficient

The restitution coefficient indicates how the relative velocity changes after a collision of two particles. It ranges from zero for perfectly inelastic collisions to one for perfectly elastic collisions. For glass beads of 3 mm in diameter, the restitution coefficient measured from detailed impact measurements is about 0.97 ± 0.01 (Foerster et al., 1994). However, the restitution coefficient is not constant. It has been reported that the restitution coefficient depends on the impact velocity, and it approaches unity when the impact velocity approaches zero (Hussainova et al., 1999). In numerical simulations, this parameter for most particles is usually set in the range of 0.9~0.995 (Samuelsberg and Hjertager, 1996; Goldschmidt et al., 2001; Pain et al., 2002; Lu et al., 2004; Du et al., 2006). Lu et al. (2004) performed a numerical simulation of gas-solid flow in a spouted bed with a restitution coefficient of 0.99 for glass beads. However, Goldschmidt et al. (2001) recommended a value, for this coefficient, from 0.9 to 0.97 for glass beads after numerical investigation of the effect of restitution coefficient on bed dynamics. As no information on particle restitution coefficient was reported in Saadevandi (1996), parametric studies are conducted here to evaluate the effect of the restitution coefficient on our simulations results. The flow patterns for different restitution coefficients are shown in Figure 5-11. Substantial differences can be observed in the contours of particle volume fraction for various values of the restitution coefficient. Decreasing the restitution coefficient leads to lower solids concentration in the draft tube. However, the height of the fountain is almost independent of the restitution coefficient.

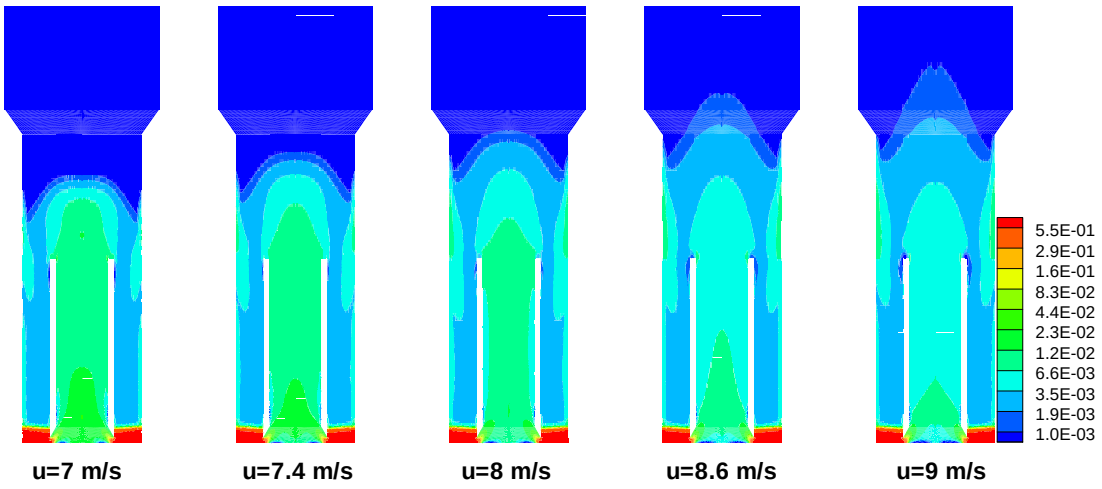

Figure 5-10. Contours of particle volume fraction at different gas velocities.

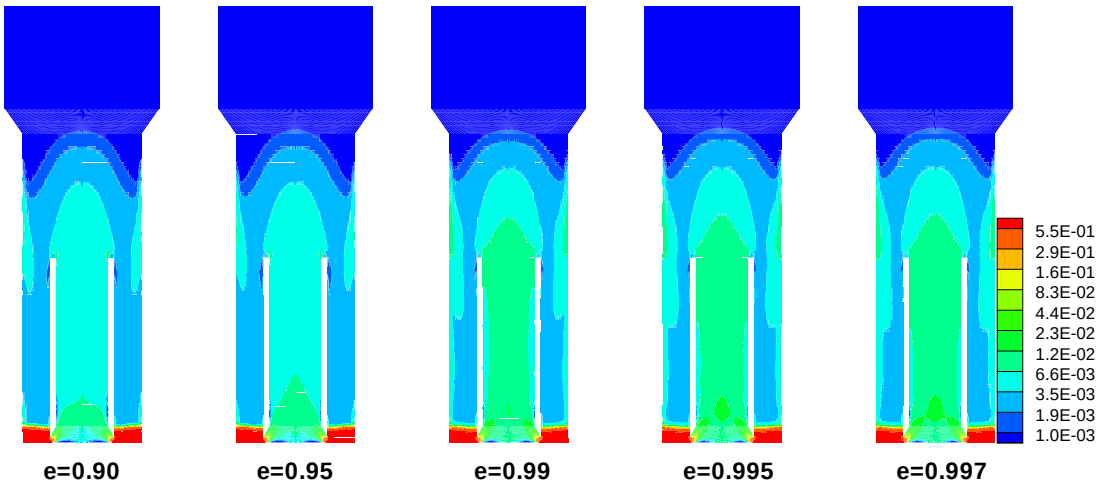

Figure 5-11. Contours of particle volume fraction for different restitution coefficients at a gas velocity of 8 m/s.

The radial profiles of particle volume fraction and axial velocity are compared for different restitution coefficients. A significant increase in solids concentration is observed in Figure 5-12 when the restitution coefficient increases from 0.95 to 0.99. This sensitivity of solids concentration to the restitution coefficient leads to a strong dependence of the solids circulation

rate on the restitution coefficient as well, as shown in Figure 5-13. It can be seen that the sensitivity of the particles circulation rate decreases when the system becomes more inelastic, similar to the trend reported by Liu and Glasser (2006) who performed a parametric investigation of gas-particle flow in a vertical duct.

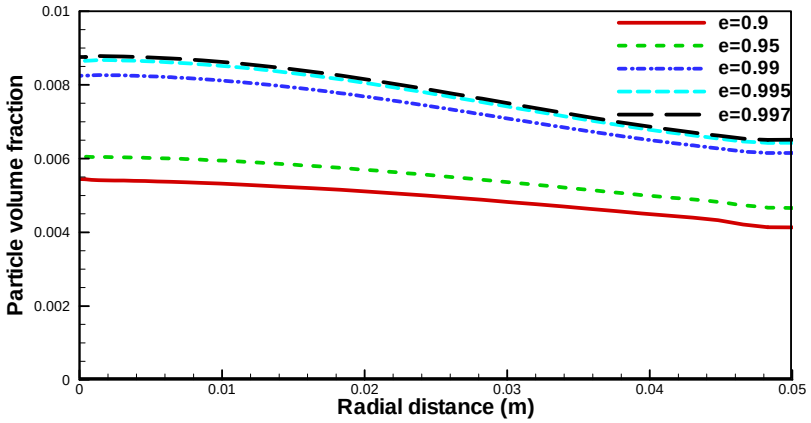

(a)

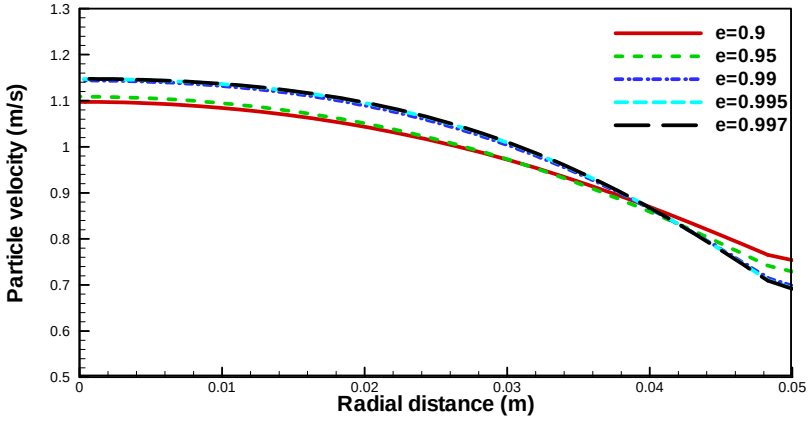

(b)

Figure 5-12. Radial profiles of particle volume fraction (a) and velocity (b) at height of 200 mm for different restitution coefficients.

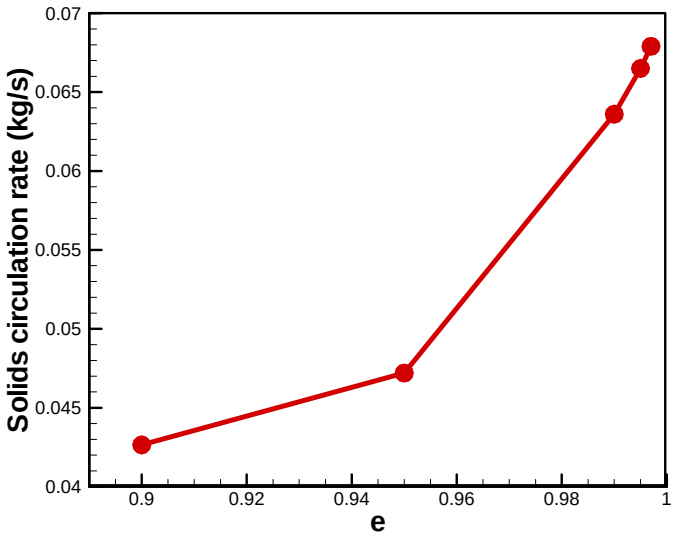

Figure 5-13. Solids circulation rates for difference restitution coefficients at a gas velocity of 8 m/s.

The restitution coefficient characterizes the energy dissipation due to inelastic collisions in the granular flow. Therefore, the restitution coefficient influences the granular temperature and the solid shear viscosity in the granular kinetic model. The granular temperature decreases as the particle collisions become less ideal, i.e. as the restitution coefficient decreases, and the particle flow becomes more viscous. Goldschmidt et al. (2001) found that particles become closely packed in the densest regions of a fluidized bed as collisions become less ideal. Similarly, Taghipour et al. (2005) reported an 8% decrease in bed expansion when the restitution coefficient was reduced from 0.99 to 0.9. In our simulations, we also find that decreasing the restitution coefficient leads to denser solids flow in the annular region where the flow is governed by frictional forces between contacting particles. It becomes more difficult for particles to discharge through the gap into the draft tube so that the solids circulation in the system is hindered.

From the above analyses, it is very likely that the frictional model is responsible for the extreme sensitivity of the flow behaviour to the restitution coefficient. This conclusion can be confirmed

by performing a parametric study without the frictional model. The solids circulation rates are nondimensionalized with that for $e = 0.9$. As demonstrated in Figure 5-14, the sensitivity of the solids circulation rate to the restitution coefficient is moderate when the frictional model is disabled. However, to model the slow, frictional flow in the annulus, an appropriate frictional model is necessary. The available frictional models are discussed in the next section.

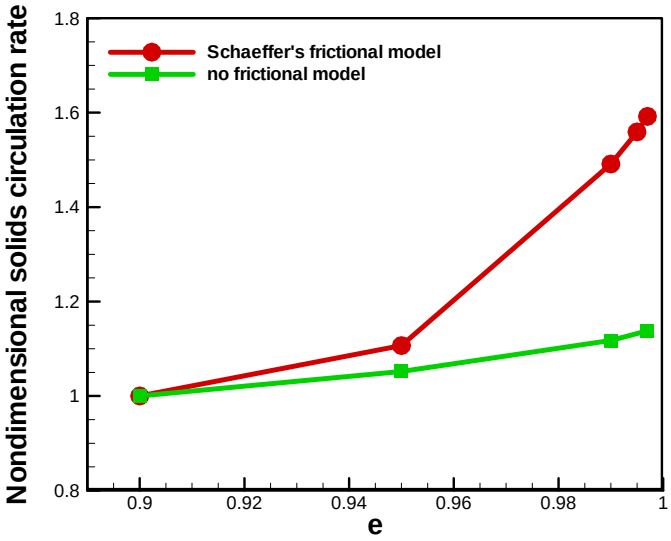

Figure 5-14. Sensitivity of the solids circulation rate to the restitution coefficient with and without frictional model.

As we can see from this parametric study, it is important to choose a reasonable value for the restitution coefficient. Comparison with the solids circulation rate reported experimentally, about 0.065 kg/s, shows that restitution coefficients close to unity provide a good agreement. We choose 0.99 for the restitution coefficient in our remaining simulations.

5.4.1.4 Effect of frictional models

To evaluate the performance of the various frictional models, we incorporate them into Fluent with UDF and carry out a series of simulations with identical operating conditions. Particle volume fraction contours in the annular region are presented in Figure 5-15. It can be seen that

all of the frictional models predict a dense quasi-stagnant region, an area with very slow motion, in the corner, but the shapes of the quasi-stagnant region differ significantly. Both the models of Schaeffer (1987) and Dartevelle (2004) predict the inclined surface of separation of dense particle flow, while the model of Srivastava and Sundaresan (2003) model predicts a fairly flat one. This is because the strain rate fluctuation taken into account by Θ_p / d_p^2 in the Srivastava and Sundaresan model results in much smaller frictional solid viscosity. The flowability in the frictional region is improved, and flow is levelled by the gravitational force more easily. The result from the Dartevelle model presents a unique phenomenon in the gap region: a "tongue-like" relatively dilute region is formed in the annulus. This may be due to the strong shear strain rate at the edge of the draft tube. To investigate this phenomenon, a well designed experiment is necessary. The solids circulation rates are calculated and values for the models of Schaeffer, Dartevelle, and Srivastava and Sundaresan are 0.063, 0.027, and 0.113 kg/s, respectively. The Schaeffer model shows the best agreement with the experiment, provided that the restitution coefficient equals 0.99. For the Srivastava and Sundaresan model, over-estimation of the discharge rate of a two-dimensional bin was reported previously (Srivastava and Sundaresan, 2003).

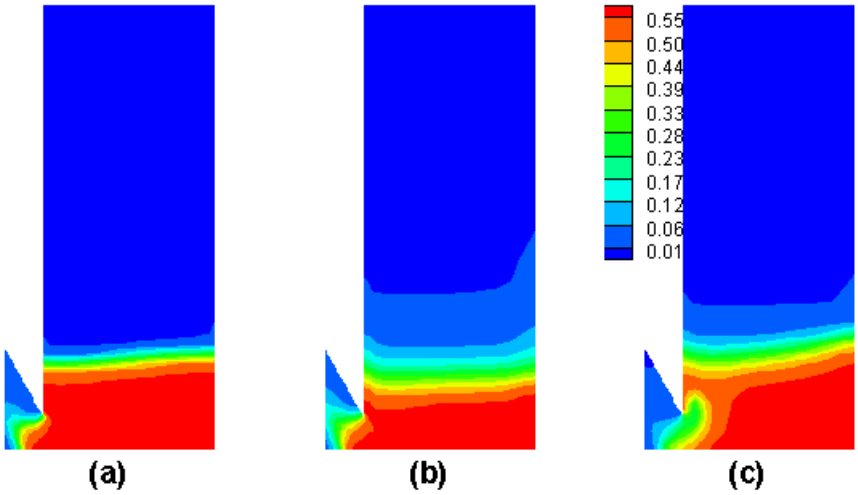

Figure 5-15. Particle volume fraction contours in the stagnant region predicted by different frictional models. (a) Schaeffer (1987); (b) Srivastava and Sundaresan (2003); (c) Dartevelle (2004).

5.4.1.5 Simulation of draft tube only

Due to the importance of the solids circulation rate, we simulated the flow in the draft tube with a controllable circulation rate. This is done by restricting the computational domain to the draft tube only, where the frictional effect is negligible. The boundary conditions are set based on the results from the full domain simulation. The solids circulation rate is controlled by adjusting the inflow through the gap to match the experimental value. Results are compared with the experimental data and with the whole bed simulation, as shown in Figure 5-16. It can be seen that numerical predictions for the particle volume fraction distribution are somewhat improved when the radial particle velocity at the gap is increased slightly to match the experimental solids circulation rate. This indicates that under-prediction of the radial particle velocity at the gap is

another possible reason for the discrepancy in particle volume fraction shown in Figure 5-7, in addition to the analysis above.

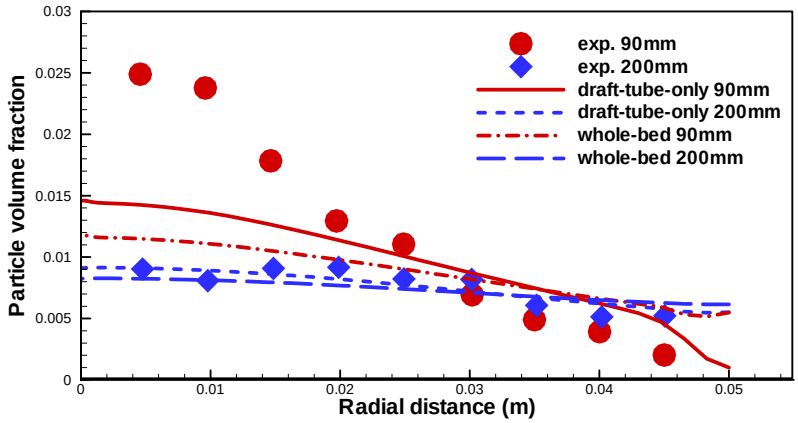

(a)

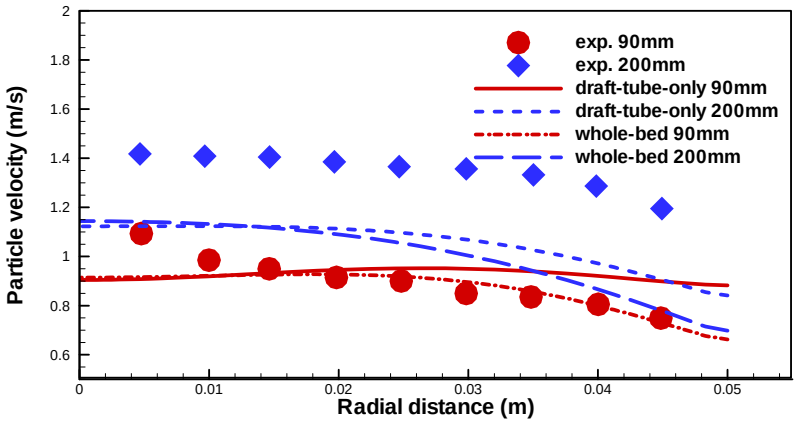

(b)

Figure 5-16. Radial profiles of particle volume fraction (a) and particle velocity (b) from whole-bed and draft-tube-only simulations.

In addition, a parametric study of the restitution coefficient is performed for the draft-tube-only simulation. The radial profiles of the particle volume fraction and the axial velocity at $z = 200$ mm are plotted in Figure 5-17 for different values of the restitution coefficient. In contrast with the results shown in Figure 5-12, the sensitivity of solids concentration to the

restitution coefficient disappears. This confirms our previous analysis that the sensitivity of the flow behaviour to the restitution coefficient arises from the frictional flow in the annular region.

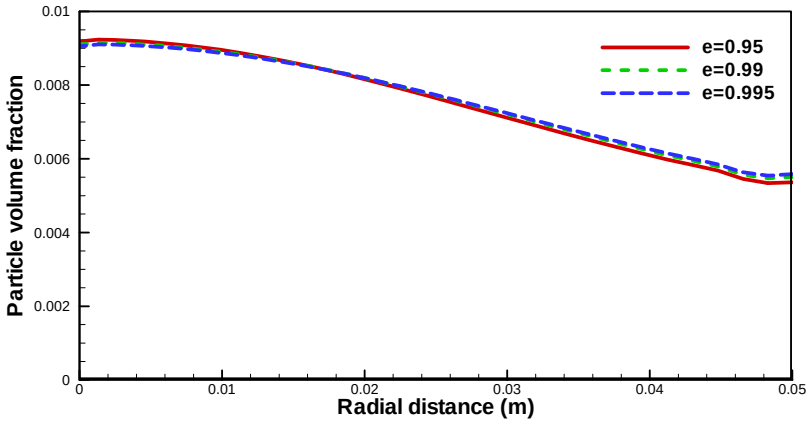

(a)

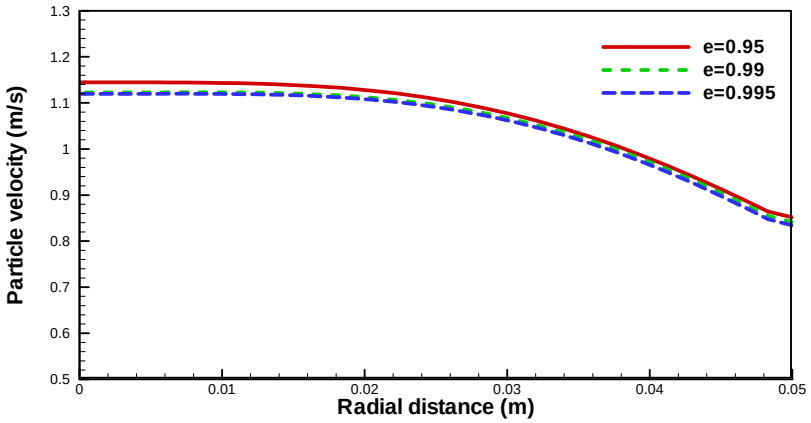

(b)

Figure 5-17. Radial profiles of particle volume fraction (a) and particle velocity (b) at height of 200 mm for different restitution coefficients.

5.4.2 Bottom liquid spray

5.4.2.1 Liquid distribution in the draft tube

A small amount of water spray is introduced into the system at the centre of the gas distributor. The average velocity of droplets is 3.3 m/s; thus, the water flow rate is about 0.06 g/s through the nozzle. Atomization and evaporation of liquid droplets are not currently considered. For simplicity, we only simulate the flow in the draft tube to study the effect of liquid spray on particle velocity and voidage. The liquid content in the annulus region will affect the friction between particles in the real system. However, modeling this effect is beyond the capability of the present model.

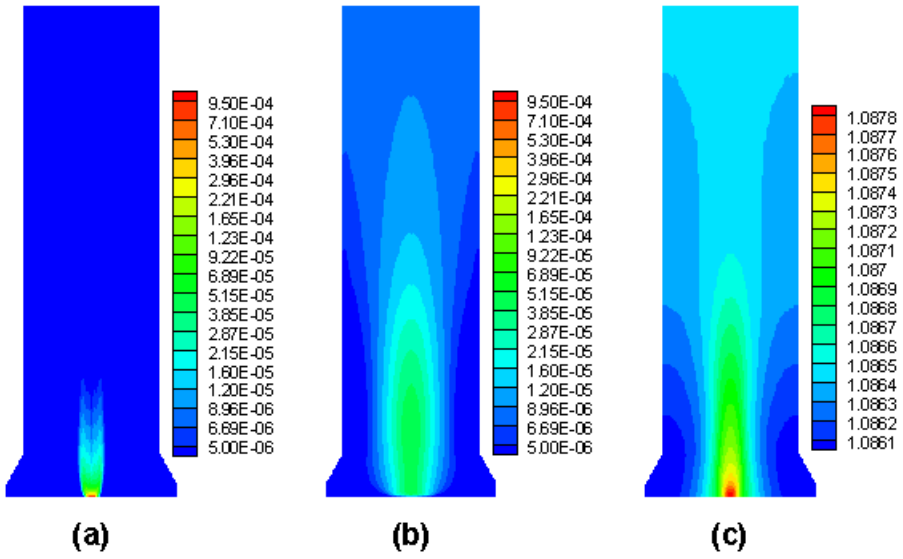

Figure 5-18. Distribution of liquid volume fraction and particle size in draft tube: (a) droplets volume fraction; (b) water film volume fraction; (c) average diameter of particles (mm).

In the draft tube, particles and droplets interact with each other by direct collisions which are assumed to result in coalescence, i.e. droplets attach to particles after collision. The average particle size increases with liquid attachment, as a thin film is formed on the particle. Liquid in the system exists in the form of the droplet phase as well as the liquid component in the

particulate phase. Figure 5-18 shows contours of the mean volume fraction of water and liquid film, and the distribution of average particle size. In Figure 5-18(a), the volume fraction of dispersed droplets decreases rapidly from 0.1% to 0.01% as the spray is injected, indicating that most droplets are captured by particles in the vicinity of the nozzle. As a result, the volume fraction of water existing as liquid film on particles increases near the nozzle as shown in Figure 5-18(b). The particles coated with the liquid film are transported upward by the gas flow and radially by the fluctuating motion. For the small amount of liquid spray considered, the increase of the average particle size is less than $2\,\mu m$.

5.4.2.2 Spray effect on particle velocity and volume fraction

Comparisons of the particle velocity and volume fraction profiles with and without spray are shown in Figure 5-19, at different axial heights. Similar to the experimental observation, there is no significant difference between the results obtained with spray and without spray because of the low spray rate simulated.

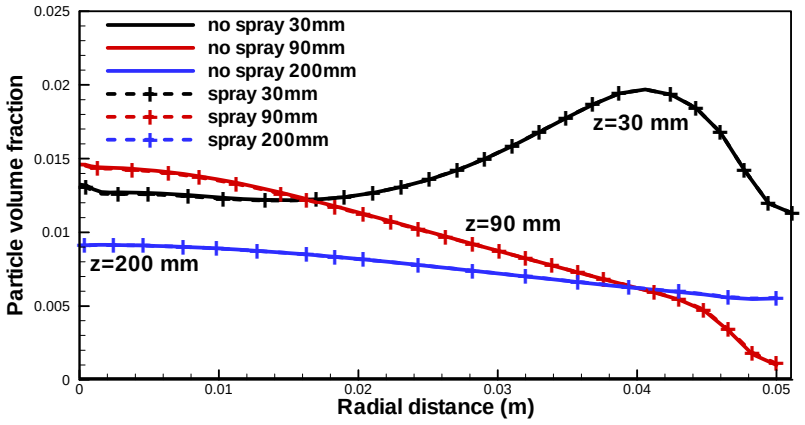

(a)

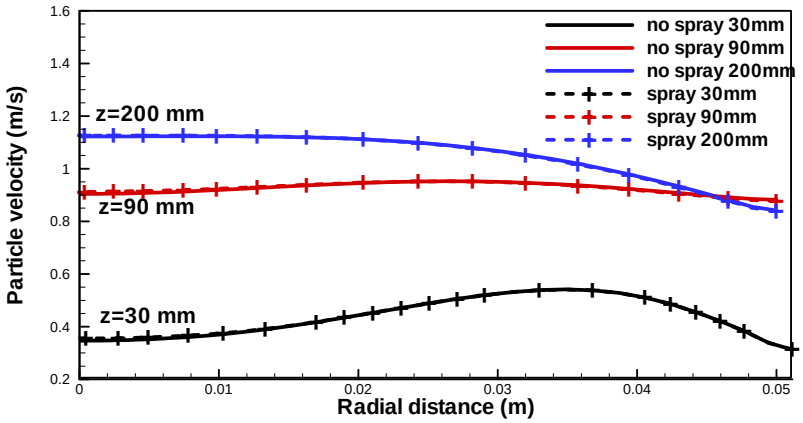

(b)

Figure 5-19. Comparison of particle volume fraction (a) and particle velocity magnitude profiles (b) with and without spray in draft tube at different heights.

For an increased spray flow-rate, the volume fraction of droplets at the spray inlet is increased. Three spray rates of 0.06, 0.25, and 0.6 g/s, respectively, are simulated, and the solid volume fraction and velocity profiles at different axial positions in the draft tube are compared in Figure 5-20. As we can see, the effect of liquid spray becomes more evident at high spray rates, especially in the particle velocity profiles as more momentum is transferred to the particles by collisions. The liquid spray is predict to affect the solid flow mainly in the central region where the liquid concentration is high as shown in Figure 5-18. As the spray rate is further increased, agglomeration becomes important and needs to be considered with appropriate models.

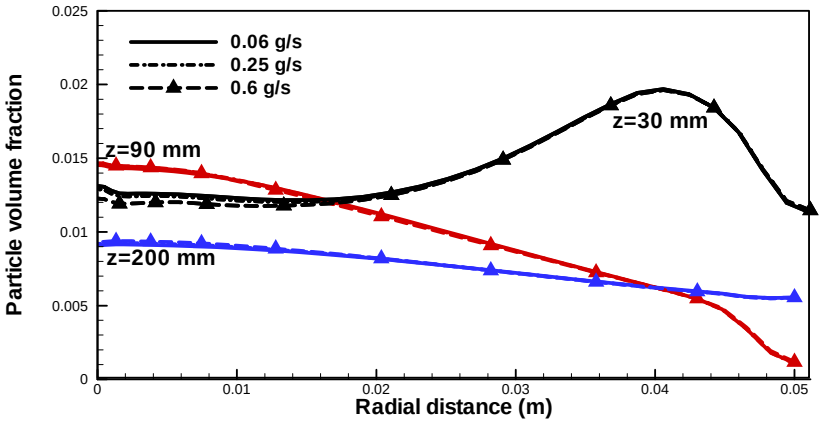

(a)

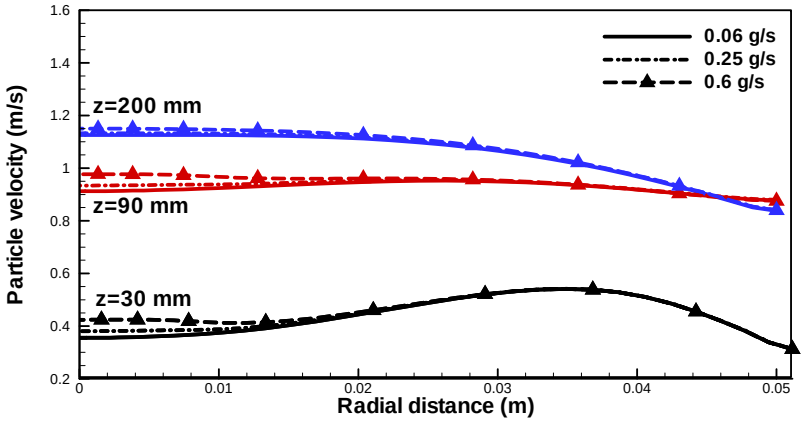

(b)

Figure 5-20. Comparison of particle volume fraction (a) and velocity magnitude profiles (b) at different axial heights in draft tube for three spray rates.

5.5 SUMMARY

In this work, we simulate the gas-solid flow in a flat-based spouted bed with a draft tube. The flow patterns observed in experiments are well predicted by the model. Quantitative comparisons with Saadevandi and Turton's (2004) experiment are performed, and satisfactory agreement is

obtained. The effect of gas velocity on the solids circulation rate is evaluated. The solids circulation rate increases first with increasing velocity, but tends to level off with further increase. For very high gas velocities, the solids circulation rates are entirely dominated by the solids discharge through the gap between the draft tube and the distributor. This finding can be used to guide the design and operation of DTSB systems. Parametric studies of restitution coefficient demonstrate that flow hydrodynamics change dramatically when the restitution coefficient is varied. It is shown that the sensitivity of the flow behaviour to the value of the restitution coefficient arises from the frictional flow in the annular region. Several frictional models are compared in the simulation, and the model of Schaeffer (1987) provides the best agreement with the experimental results.

For low-flow-rate sprays, the interaction between spray droplets and particles is modeled as coalescence upon collision, and the dispersion of wetted particles is described with a transport equation. The effect of liquid spray on the solid volume fraction and velocity in the draft tube is analyzed. Similar to the experimental observations, it is shown that there is no significant effect on the particle volume fraction and velocity profiles for low spray rates. As the liquid spray rate increases, the effect of liquid spray becomes evident in the central core region, especially in the particle velocity profiles. This is our first step in modeling the liquid spray into gas-solid systems. Further improvement to this model will be made in the future, and more practical problems will be modeled.

Chapter 6. EVAPORATIVE SPRAY IN A GAS-SOLID CROSSFLOW

6.1 INTRODUCTION

In **Chapter 5**, a non-evaporative spray in a flat-based DTSB was studied numerically. However, evaporative sprays in the gas-solid flow are commonly encountered in many industrial applications, such as spray dryers, internal combustion engines, fluid coking reactors, and fluid catalytic cracking reactors. In these applications, the injection of liquid sprays into gas-solid systems involves strong three-phase interactions of momentum, heat, and mass transfer. The rapid evaporation of liquid droplets can significantly affect gas-solid mixing, temperature distribution, and flow behaviour, and it plays an important role in most applications by affecting process efficiency and product quality (Fan et al., 2001).

An experimental apparatus for study of the evaporative jet in the dilute gas-solid pneumatic convey was constructed at the New Jersey Institute of Technology (Liu, 2003). This apparatus consisted of a circulating fluidized bed with a simple rectangular column, controllable solids load and flow conditions, and well-defined liquid nitrogen sprays. Detailed information about this experimental setup was provided by Liu (2003), who studied the spray trajectory, spray penetration length, and flow pattern. Specifically, he investigated the effects of geometric and operating parameters, such as nozzle size, nozzle type, injection angle, jetting velocity, and solids loading in his experiments.

In this chapter, the Eulerian-Eulerian multi-fluid model is employed to numerically simulate an evaporative liquid-nitrogen spray into a uniform gas-solid crossflow. The k-epsilon turbulence model with additional terms, taking into account the gas-droplet and gas-particle turbulent interactions, is used to model the transport of turbulence in the gas phase. The transport equation

for the liquid surface area concentration proposed by Iyer et al. (2002), is adopted in the current study to include the droplet size effect. Non-equilibrium droplet heating and evaporation models are utilized to calculate the inter-phase heat and mass transfer rates. These models are incorporated into Fluent 6.3 with user-defined functions (UDF).

The objectives of this part of the work are to obtain a better understanding of the phase interactions and field distributions in the spray region, and to investigate the effect of evaporation on the flow behavior.

6.2 NUMERICAL METHOD

6.2.1 Governing equations

The multi-fluid, Eulerian-Eulerian model based on granular kinetic theory, as stated in **Chapter 2**, is employed. The liquid spray is modeled with the Eulerian approach and governing equations for mass and momentum similar to those in **Chapter 5** are solved. To take into account the mass, momentum, and heat transfer resulting from the phase change due to evaporation of droplets, additional source terms are included in the mass, momentum, and energy equations. Appropriate closure relations are used to close the governing equations. These models are described briefly in the following sections.

6.2.2 Interphase drag

6.2.2.1 Gas-solid and gas-droplet drag forces

For gas-droplet and gas-solid drag forces, the generally accepted expressions for β_{gl} and β_{gp} in equation (6.1) and (6.2) following Issa and Oliveira (1996) and Gidaspow (1994), respectively,

are used. Full details of these two drag models are provided in **Chapter 2** and **Chapter 5**, respectively.

$$\beta_{gl} = \alpha_g \alpha_l \frac{3\rho_g \left|(\vec{V}_g - \vec{V}_l)\right| C_{D,l}}{4 d_l} \tag{6.1}$$

$$\beta_{gp} = \begin{cases} 150\dfrac{\alpha_p(1-\alpha_g)\mu_g}{\alpha_g d_p^2} + 1.75\dfrac{\alpha_p \rho_g \left|\vec{V}_p - \vec{V}_g\right|}{d_p} & \text{if } \alpha_g < 0.8 \\ \dfrac{3}{4} C_{D,p} \alpha_g^{-2.65} \dfrac{\alpha_p \alpha_g \rho_g \left|\vec{V}_p - \vec{V}_g\right|}{d_p} & \text{if } \alpha_g \geq 0.8 \end{cases} \tag{6.2}$$

6.2.2.2 Droplets and solids interaction

The momentum exchange between droplets and particles is hard to model, as study in this field is very limited, especially for strong coupling between heat transfer and evaporation. Wang et al. (2004) incorporated the momentum exchange between droplets and particles into the effective drag coefficient by Mostoufi and Chaouki (1999) when they simulated the evaporative spray jets of liquid nitrogen in concurrent gas-solid flows with a hybrid Eulerian-Lagrangian model. It was assumed that there existed an analogy for the momentum transfer between the droplets in a gas-solid flow and the solids in a gas-solid flow of a fluidized bed. However, the drag correlation by Mostoufi and Chaouki (1999) was originally developed for prediction of the effective drag force experienced by a single particle falling in a fluidized bed of different particles. This effective drag correlation may not be appropriate to model the momentum exchange between droplets and particles due to direct collisions.

There exists very fast evaporation when a small cold droplet of liquid nitrogen collides with a hot particle beyond the Leidenfrost temperature. Upon contact, no wetting can take place considering the Leidenfrost effect (the Leidenfrost effect is a phenomenon in which a liquid, in near contact with a mass significantly hotter than its boiling point, produces an insulating vapor layer which keeps that liquid from boiling rapidly. It is named after Johann Gottlob Leidenfrost, who

discussed this phenomenon in *A Tract About Some Qualities of Common Water* in 1756). The large amount of vapour generated during the collision tends to push the colliding droplet and particle to separate. Though a high rate of evaporation takes place, it is worth noting that the mass loss of droplet during the collision is negligible since vapour density is far less than that of the droplet or particle (Wachters et al., 1966; Karl and Frohn, 2000). Consequently, when bouncing takes place, it is possible to treat it as a collision between two solid particles as the first approximation, without considering deformation or breakup of the droplet during the collision. Hence, the inter-phase drag coefficient between droplets and particles can be written in a similar form as the particle-particle drag coefficient (Syamlal, 1987; Gera et al., 2004)

$$\beta_{lp} = \frac{3}{4}\frac{\left(1+e_{lp}\right)\alpha_l\rho_l\alpha_p\rho_p\left(d_l+d_p\right)^2\left|\vec{V}_l-\vec{V}_p\right|}{\left(\rho_l d_l^3+\rho_p d_p^3\right)} \tag{6.3}$$

where e_{lp} is an effective restitution coefficient to characterize the non-wetting collision between the droplet and the hot particle. However, no direct measurement of this parameter has been reported in the literature. Fortunately, the abundant study on the droplet impinging on a hot surface can be used to estimate the possible value of e_{lp} considering the size ratio between the particle and the droplet in the current problem. It has been reported that the restitution coefficient of a droplet impinging on a hot surface ranges from 0.2 to 0.8, with the value decreasing with increasing Weber number (Hatta et al., 1995; Karl and Frohn, 2000). In the current problem, according to these experimental measurements and after evaluating the collision Weber numbers between spray droplets and particles, a value of 0.8 is assumed for e_{lp}.

6.2.3 Turbulence models

In two-phase flows, the turbulence of the carrier phase (continuous phase) plays an important role in the transport or mixing of the dispersed phase. Correspondingly, when the dispersed phase is introduced into the flow, the turbulence of the continuum phase is modified. Generally, numerical models for the two-phase turbulent flows have been developed along two common

approaches, the Lagrangian-Eulerian approach and the Eulerian-Eulerian approach. A comprehensive review of the numerical models for two-phase turbulent flows has been given by Crowe et al. (1996).

The two-equation $k-\varepsilon$ model has been widely used for simulating single-phase turbulent flows over the past decades, due to its simplicity and relative accuracy in most engineering problems. To model the gas flow with dilute suspension, an extensive amount of work has been performed to modify the $k-\varepsilon$ model with additional terms taking into account interfacial turbulent momentum transfer (Ahmadi and Ma, 1990; Ma and Ahmadi, 1990; Reeks, 1991; Cao and Ahmadi, 1995; Simonin, 1996; Xu and Subramaniam, 2006). Usually, for dilute flows with small particles, the kinetic stresses of the dispersed phase can be determined using a simple "local equilibrium" model, which assumes that the turbulence quantities of the dispersed phase are determined by the turbulence quantities of the carrier phase (Cao and Ahmadi, 1995). However, the information in the literature on three-phase turbulence models is very limited.

6.2.3.1 Turbulence model for gas phase

The $k-\varepsilon$ model is employed to model the turbulence in the gas phase with additional terms to take into account the effect of dispersed phases (droplets and particles). The transport equations for the turbulent kinetic energy k of the gas phase and the dissipation rate of the gas phase turbulent kinetic energy ε are (Launder and Spalding, 1972; Crowe et al., 1996)

$$\frac{\partial}{\partial t}(\alpha_{\mathrm{g}}\rho_{\mathrm{g}}k)+\nabla\cdot(\alpha_{\mathrm{g}}\rho_{\mathrm{g}}\vec{V}_{\mathrm{g}}k)=\nabla\cdot\left(\alpha_{\mathrm{g}}\frac{\mu_{\mathrm{g},t}}{\sigma_k}\nabla k\right)+\alpha_{\mathrm{g}}G-\alpha_{\mathrm{g}}\rho_{\mathrm{g}}\varepsilon+\Pi_{l,k}+\Pi_{p,k} \quad (6.4)$$

$$\frac{\partial}{\partial t}(\alpha_{\mathrm{g}}\rho_{\mathrm{g}}\varepsilon)+\nabla\cdot(\alpha_{\mathrm{g}}\rho_{\mathrm{g}}\vec{V}_{\mathrm{g}}\varepsilon)=\nabla\cdot\left(\alpha_{\mathrm{g}}\frac{\mu_{\mathrm{g},t}}{\sigma_\varepsilon}\nabla\varepsilon\right)+\alpha_{\mathrm{g}}\frac{\varepsilon}{k}(C_1G-C_2\rho_{\mathrm{g}}\varepsilon)+\Pi_{l,\varepsilon}+\Pi_{p,\varepsilon} \quad (6.5)$$

where the turbulent viscosity, $\mu_{\mathrm{g},t}$, is written in terms of the turbulent quantities of the gas phase as

$$\mu_{g,t} = \rho_g C_\mu \frac{k^2}{\varepsilon} \tag{6.6}$$

In equations (6.4) and (6.5), the terms on the left-hand side are the unsteady and the convective terms. The first term on the right-hand side represents the diffusive transport. G is the production of turbulent kinetic energy due to the mean velocity gradients, defined as

$$G = \overline{\overline{\tau}}_{g,t} : \nabla \vec{V}_g \tag{6.7}$$

The third term on the right-hand side of equation (6.4) is the dissipation of the gas phase turbulent kinetic energy. The last two terms on the right-hand side of equations (6.4) and (6.5) represent the damping or destruction of turbulence by the presence of dispersed droplets and particles, which are usually treated with turbulence modulation models. The model constants σ_k, σ_ε, C_1, C_2, and C_μ have standard values for the singe-phase turbulence model. It is believed that the values of these constants depend on the type of particles and the type of flows, and efforts have been made to study the dependence of these parameters on the particle property and loading (Squires and Eaton, 1994; Cao and Ahmadi, 1995). Since this issue is beyond the scope of our current modeling, we use the standard values for these model constants as listed in Table 6-1.

Table 6-1. Constants for the turbulence model.

Constant	σ_k	σ_ε	C_1	C_2	C_μ
Value	1.0	1.3	1.44	1.92	0.09

6.2.3.2 Turbulence model for droplet phase

For gas flow in the presence of dispersed droplets, the term $\Pi_{l,k}$ can be derived from the instantaneous momentum equation of the gas phase (Elghobashi and Abou-Arab, 1983), and it can be written.

$$\Pi_{l,k} = \beta_{gl}\left(k_{gl} - 2k + (\vec{V}_l - \vec{V}_g)\cdot\vec{v}_{l,dr}\right) \tag{6.8}$$

and $\Pi_{l,\varepsilon}$ is modeled (Elghobashi and Abou-Arab, 1983) by,

$$\Pi_{l,\varepsilon} = C_3\frac{\varepsilon}{k}\Pi_{l,k} \tag{6.9}$$

where $C_3 = 1.2$, k_{gl} is the covariance of the velocities of the gas phase and the droplet phase. $\vec{v}_{l,dr}$ is the drift velocity, which represents the dispersion of the dispersed phase by the large turbulent scales of the carrier phase (Simonin, 1990). Different models for the drift velocity have been derived (Deutsch and Simonin, 1991; Reeks, 1992; Reeks, 1993; Peirano and Leckner, 1998). For particles suspended in a homogeneous turbulent flow, the drift velocity can be modeled by the equation (Deutsch and Simonin, 1991)

$$\vec{v}_{l,dr} = -D_{l,dr}\left(\frac{1}{\alpha_l}\nabla\alpha_l - \frac{1}{\alpha_g}\nabla\alpha_g\right) \tag{6.10}$$

where $D_{l,dr}$, the turbulent dispersion coefficient, is modeled as

$$D_{l,dr} = \frac{1}{3}k_{gl}\tau_{l,t}^0 \tag{6.11}$$

$\tau_{l,t}^0$ is the fluid Lagrangian integral time scale, which characterizes the time of interaction between the particle motion and the continuous phase fluctuation. It is related to the characteristic time of the large turbulent eddies of the gas phase, $\tau_{g,t}$, with the relation.

$$\tau_{l,t}^0 = \frac{\tau_{g,t}}{\sqrt{1 + C_\beta\xi^2}} \tag{6.12}$$

where

$$\xi = \frac{3\left|\vec{V}_l - \vec{V}_g\right|^2}{2k} \tag{6.13}$$

and

$$\tau_{g,t} = \frac{3}{2}C_\mu\frac{k}{\varepsilon} \tag{6.14}$$

In equation (6.12), C_β is a constant that depends on the type of flow. It is usually assumed to vary with the angle, θ, between the mean velocity of the dispersed phase and the mean relative velocity, according to

$$C_\beta = 1.8 - 1.35\cos^2(\theta) \tag{6.15}$$

To close equation (6.8), a model for k_{gl} is necessary. A number of different types of models for k_{gl} have been suggested. Some of them are summarized by Lightstone and Hodgson (2004) and Yan et al. (2007). According to these models, the following relation is commonly used

$$\frac{k_{gl}}{k} = C_k \tag{6.16}$$

where C_k is a dimensionless number determined by different time scales in the flow, such as the fluid Lagrangian integral time scale $\tau_{l,t}^0$, and the time scale of the large turbulent eddies $\tau_{g,t}$. Another important time scale is the particle response time, which is related to the inertial effects acting on the dispersed phase, and is defined as

$$\tau_{l,F} = \frac{\alpha_l \rho_l}{\beta_{gl}} \tag{6.17}$$

The expressions for C_k vary from model to model. Nevertheless, there exists a general form in most models (Mostafa and Mongia, 1988; Simonin, 1996; de Bertodano, 1998; Lightstone and Hodgson, 2004), which can be written

$$C_k = 2\frac{\tau_L}{\tau_L + \tau_{l,F}} \tag{6.18}$$

where τ_L is the Lagrangian time scale, which may differ in different models. Here, the model of Simonin (1996) is adopted. Consequently, the turbulent quantities for the dispersed droplet phase are given as follows, consistent with Tchen's theory (Hinze 1975):

$$k_l = \frac{\tau_{l,t}^0}{\tau_{l,t}^0 + \tau_{l,\mathrm{F}}} k \tag{6.19}$$

$$k_{gl} = 2k_l \tag{6.20}$$

$$\mu_{l,t} = \frac{1}{3}\rho_l(\tau_{l,t}^0 k_{gl} + \tau_{l,\mathrm{F}} k_l) \tag{6.21}$$

6.2.3.3 Turbulence model for the particulate phase

For dense gas-solid flows (e.g., fluidized beds), the granular temperature, Θ, for the solid phase is employed to represent the kinetic energy of the random motion of particles. Hence, the transport equation of the granular temperature derived from the kinetic theory as already stated in **Chapter 2**, is used to model the turbulence in the particle movement. In this work, the partial differential equation (2.7) is solved instead of the algebraic formula for the granular temperature.

6.2.4 Mass transfer

6.2.4.1 Without particles

Due to the evaporation of liquid droplets, there exists strong mass transfer between the droplet phase and gas phase. Generally, the evaporation of a single droplet is modeled as

$$\dot{m}_l = -\pi d_l \rho_g D_v Sh \ln(1 + B_M) \tag{6.22}$$

where D_v is the binary diffusivity of the vapour in the gas phase, Sh is the Sherwood number, and B_M is the Spalding mass transfer number, defined as

$$B_M = \frac{Y_s - Y}{1 - Y_s} \tag{6.23}$$

Y_s and Y are the vapour mass fractions at the droplet surface and free stream. At the droplet surface, the vapour mass fraction is calculated from the droplet surface temperature by the Clausius-Clapeyron equilibrium vapour pressure equation (Lefebvre, 1989).

$$Y_s = \frac{1}{1+(\frac{P}{P_{Fs}}-1)\frac{M_g}{M_l}} \tag{6.24}$$

where P_{Fs} is the vapour pressure at the drop surface, P is the ambient pressure, and M_g and M_l are the molecular weights of the gas and liquid, respectively.

To take into account the convective effect of the gas phase on droplet evaporation, the Frössling correlation for the Sherwood number is used.

$$Sh = 2 + 0.6\,\mathrm{Re}_l^{0.5}\,Sc_g^{0.33} \tag{6.25}$$

where $Sc = \nu_g / D_v$ is the Schmidt number.

To achieve the best accuracy of these models, the gas-film thermo-physical properties are evaluated at the reference temperature using the one-third rule of Sparrow and Gregg (1958).

$$T_{ref} = T_l + \frac{T_g - T_l}{3} \tag{6.26}$$

The detailed procedure to calculate the gas-film variable properties is provided by Lefebvre (1989), and this procedure is applied in this study.

Finally, the evaporation source term in the mass conservation equation standing for the mass transfer from the droplet phase to the gas phase due to evaporation is

$$q_{lg,drop} = n_l \dot{m}_l \tag{6.27}$$

where n_l is the number density of droplets. Substituting $n_l = 6\alpha_l / \pi d_l^3$ into (6.27), yields

$$q_{lg,drop} = -\frac{6\alpha_l \rho_g D_v Sh \ln(1+B_M)}{d_l^2} \tag{6.28}$$

6.2.4.2 With particles

Owing to the presence of particles, the evaporation of droplets becomes much more complicated. For simplicity, we neglect the vaporization and diffusion of the droplet into the surrounding air before it reaches the boiling point. Therefore, the evaporation of a single droplet at the boiling point is modeled (Buchanan, 1994) by

$$\dot{m}_l = -\frac{\hbar_{drop} A_{drop} (T_g - T_l)}{L} \tag{6.29}$$

where $\hbar_{drop}$ is the heat transfer coefficient from the surrounding gas-solid mixture to the droplet, $A_{drop} = \pi d_l^2$ is the droplet surface area, and L the latent heat of liquid, T_g, T_l are the temperatures of gas and liquid, respectively. With this equation, the mass transfer of the droplet into the gas phase depends only on the heat transfer from the surrounding mixture of gas and solids.

Simply, the evaporation source terms in mass conservation equations standing for the total mass transfer due to evaporation in a control volume are

$$q_g = -q_l = q_{lg,drop} = \frac{6\alpha_l \hbar_{drop} (T_g - T_l)}{L d_l} \tag{6.30}$$

6.2.5 Heat transfer

6.2.5.1 Gas-droplet heat transfer

The droplet heating and evaporation in the gas flow have been extensively studied (Birouk and Gokalp, 2006; Kolaitis and Founti, 2006; Sazhin, 2006; Sazhin et al., 2006). However, not much

work on the heat transfer between droplets and gas, in the presence of solids, can be found in the literature. Buchanan (1994) analyzed the heat transfer between droplets and gas flow in the presence of solid particles. According to Buchanan's work, for the situation in a riser, with a relatively dilute solid phase and presumably very brief contact between droplets and particles (with droplets acting like hard spheres), the dominant heat transfer mechanism is expected to be conduction through the gas film around the droplet. The effective heat transfer coefficient can be evaluated with an effective Reynolds number to reflect the decrease in the thermal boundary layer around the droplet due to the presence of the dilute solid phase. Accordingly, the expression for the Nusselt number is

$$Nu_{drop} = 2 + 0.6\,\mathrm{Re}_l^{*0.5}\,\mathrm{Pr}_g^{0.33} \tag{6.31}$$

where $\mathrm{Pr}_g = C_{p,g}\mu_g / k_g$ is the Prandtl number, and the effective Reynolds number Re_l^* is calculated by using the gas/solids mixture density instead of the gas density.

$$\mathrm{Re}_l^* = \frac{(\rho_g \alpha_g + \rho_p \alpha_p)\left|\vec{V}_g - \vec{V}_l\right| d_l}{\mu_g} \tag{6.32}$$

When substantial vaporization of the drop occurs, the blowing effect hinders the mass and heat transfer with thickening of both mass and heat boundary layers. A number of correction factors have been introduced to take into account the aforementioned effect (Kolaitis and Founti, 2006). The correction factor proposed by Haywood (1989) is adopted in the current simulation.

$$Nu_{drop} = \frac{2 + 0.6\,\mathrm{Re}_l^{*0.5}\,\mathrm{Pr}_g^{0.33}}{\left(1 + \dfrac{C_{p,g}(T_g - T_l)}{L}\right)^{0.7}} \tag{6.33}$$

The heat transfer between the gas and the droplet phase is assumed to be a function of the temperature difference. Generally, it can be written

$$Q_{gl} = \hbar_{gl}(T_g - T_l) \tag{6.34}$$

where $\hbar_{gl}$ represents the volumetric inter-phase heat transfer coefficient, which is the product of the specific interfacial exchange area and the heat transfer coefficient. For example, the volumetric gas-droplet heat transfer coefficient $\hbar_{gl}$ can be calculated by

$$\hbar_{gl} = \frac{6\alpha_l}{d_l}\hbar_{drop} \tag{6.35}$$

where $\hbar_{drop}$ is the heat transfer coefficient for a single droplet. The heat transfer coefficient between the gas phase and a single droplet can be calculated from the Nusselt number.

$$Nu_{drop} = \frac{\hbar_{drop} d_l}{k_g} \tag{6.36}$$

where k_g is the thermal conductivity of the gas.

6.2.5.2 Gas-particle heat transfer

For the heat transfer between gas and particles, the expression for the Nusselt number from Gunn (1978) is used, which is valid for a wide range of solid volume fractions from 0 to 60%.

$$Nu_{part} = (7 - 10\alpha_g + 5\alpha_g^2)(1 + 0.7\,\mathrm{Re}_p^{0.2}\,\mathrm{Pr}_g^{0.33}) + (1.33 - 2.4\alpha_g + 1.2\alpha_g^2)\,\mathrm{Re}_p^{0.7}\,\mathrm{Pr}_g^{0.33} \tag{6.37}$$

where $\mathrm{Pr}_g = C_{p,g}\mu_g / k_g$ is the Prandtl number. The Reynolds number Re_p is given by

$$\mathrm{Re}_p = \frac{\rho_g \left|\vec{V}_g - \vec{V}_p\right| d_p}{\mu_g} \tag{6.38}$$

Similarly, the heat transfer between the gas and the particulate phase is written as

$$Q_{gp} = \hbar_{gp}(T_g - T_p) \tag{6.39}$$

$\hbar_{gp}$ represents the volumetric inter-phase heat transfer coefficient, calculated by

$$\hbar_{gp} = \frac{6\alpha_p}{d_p}\hbar_{part} \tag{6.40}$$

where $\hbar_{part}$ is the heat transfer coefficient for a single particle, obtained from

$$Nu_{part} = \frac{\hbar_{part} d_p}{k_g} \tag{6.41}$$

6.2.5.3 Particle-droplet heat transfer

When the collision between a hot particle and a droplet takes place, heat transfer and mass transfer occur simultaneously. Unfortunately, little information is available to explain the detailed collision mechanisms including the collision frequency, duration of contact, and heat transfer rate during contact, although several experiments have been performed to measure the evaporation of a droplet in a fluidized bed (Leclere et al., 2001; Leclere et al., 2004). A detailed account of interactions between an evaporating droplet and the hot particle is beyond the capability of the model employed. As indicated in the previous paragraph on calculating the heat transfer between gas and droplet, the particle-droplet heat transfer has already been taken into account by the effective heat transfer coefficient of Buchanan (1994) by assuming that droplets act like hard spheres during collisions.

6.2.6 Surface area concentration

To capture the variation in droplet size due to vaporization, break-up, and coalescence in diesel sprays, Iyer and Abraham (2004, 2005) derived an transport equation for the surface area concentration:

$$\frac{\partial}{\partial t}(L_{S,l}) + \nabla \cdot (L_{S,l}\vec{V}_l) = \nabla \cdot (D_{t,l}\nabla L_{S,l}) + \phi_v + \phi_b + \phi_c \tag{6.42}$$

The surface area concentration, $L_{S,l}$, is the average area of the interface per unit volume in the flow, defined as

$$L_{S,l} = \pi d_l^2 n_l \tag{6.43}$$

$D_{l,t}$ is the turbulent diffusivity, calculated from

$$D_{l,t} = \frac{\mu_{l,t}}{\rho_l Sc_t} \tag{6.44}$$

and ϕ_v, ϕ_b and ϕ_c are the source terms due to vaporization, atomization, droplet breakup, and coalescence, respectively. In the dilute droplet spray, atomization, coalescence, and droplet breakup are neglected. In the current simulation, only evaporation is considered, and the source (sink) term due to evaporation is derived as

$$\phi_v = -\frac{4\rho_g D_v Sh \ln(1+B_M) L_{S,l}}{\rho_l d_l^2} \tag{6.45}$$

The average diameter of the droplet, d_l, can be obtained from the liquid volume fraction and the surface area concentration.

$$d_l = \frac{6\alpha_l}{L_{S,l}} \tag{6.46}$$

6.2.7 Simulation setup

The experimental setup of Liu (2003) at the New Jersey Institute of Technology is simulated in this section. The schematic of the experimental setup is shown in Figure 6-1. The experiment was carried out in a CFB riser with a rectangular cross-section (292 mm × 25.4 mm). The solid particles in the experiments were FCC particles with a bulk density of 1480 kg/m^3 and an average particle size of 70 μm. Liquid nitrogen spray was injected through different nozzles 1.2 m above the distributor, where a fully developed gas-solid suspension was achieved. The mass flow rate, mean velocity, and liquid volume fraction at the spray inlet were reported in the experiment. The temperature field in the spray region was measured using thermocouples. Note that the temperature measured in the experiments was an average mixture temperature that depended on the local heat balance of the thermocouple from the gas thermal convection, the heat transfer due to droplet collision with the thermocouple, and droplet evaporation on it.

Because it was very difficult to interpret the measured temperature, the temperature data were mainly used in the experiments to determine the jet position inside the flow (Liu, 2003).

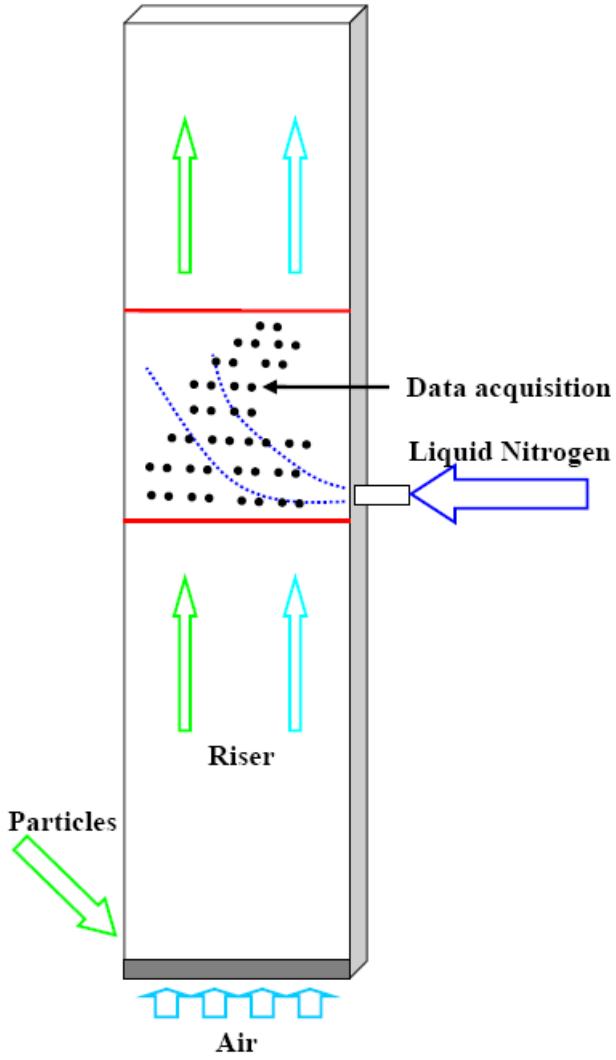

Figure 6-1. Schematic diagram of experimental system of Liu (2003)

In our study, we simulate only part of the system, where liquid nitrogen spray is injected into fully developed gas-solid flow. The simulation test section is 290 mm×150 mm× 25 mm, roughly the test section in the experiment. The computational domain is discretized with a non-uniform grid as shown in Figure 6-2, with 73,200 grid points. Similar to the analytical study for the current experimental system by Zhu et al. (2002) and Liu (2003), where a parametric model for the study of liquid jet evaporation in gas-solid suspension flows was developed,

uniform gas-solid crossflow is assumed since there is no detailed information available on local voidage and velocity of the gas-solid crossflow.

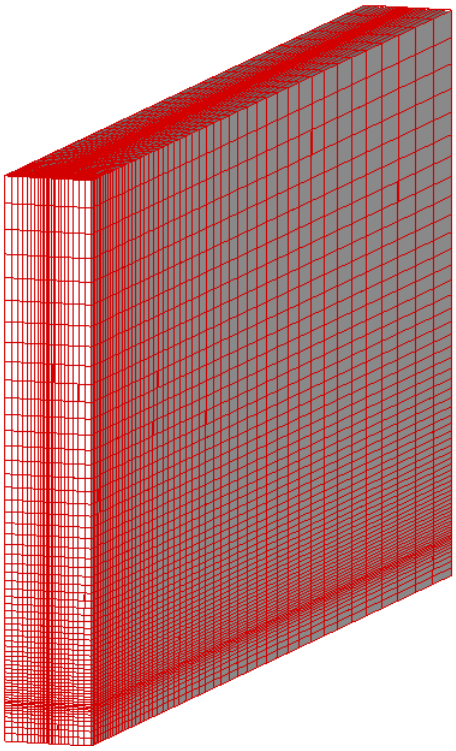

Figure 6-2. Numerical grid used in simulation.

The lateral walls of the bed are modeled using a no-slip boundary condition for the gas phase and a partial slip boundary condition for the solid phase (Johnson and Jackson, 1987). At the top boundary, an outflow boundary condition is applied and particles are free to leave the system. Similar to the analysis in Liu's thesis, uniform gas and solids velocity profiles are specified for the bottom. For the spray inlet, the conditions at the nozzle exit should be applied. However, it is difficult to measure the conditions at the nozzle exit in the experiment. Since it is beyond the scope of the current study to simulate the atomization process of the spray, a uniform droplet size is specified at the spray inlet by assuming the spray has been fully atomized at the nozzle exit. The drop velocity and liquid volume fraction at the spray inlet are set based on experimental measurements.

Due to the difficulties in measurement, the average size of droplets at the nozzle exit was not reported in Liu's experiment. Air-assisted liquid drop atomization is a very complicated process. There is a general understanding of the underlying physical mechanisms of droplet break-up, but detailed quantitative description of the phenomenon is still a challenging problem (Chigier and Reitz., 1998; Lin, 1998). According to Liu and Reitz (1993), drop breakup mechanisms are usually classified with regard to the drop Weber number. There are three regimes observed: bag breakup (6<We<80), stripping breakup (80<We<350), and catastrophic breakup (We>350). Schematic representation of drop breakup mechanisms is shown in Figure 6-3.

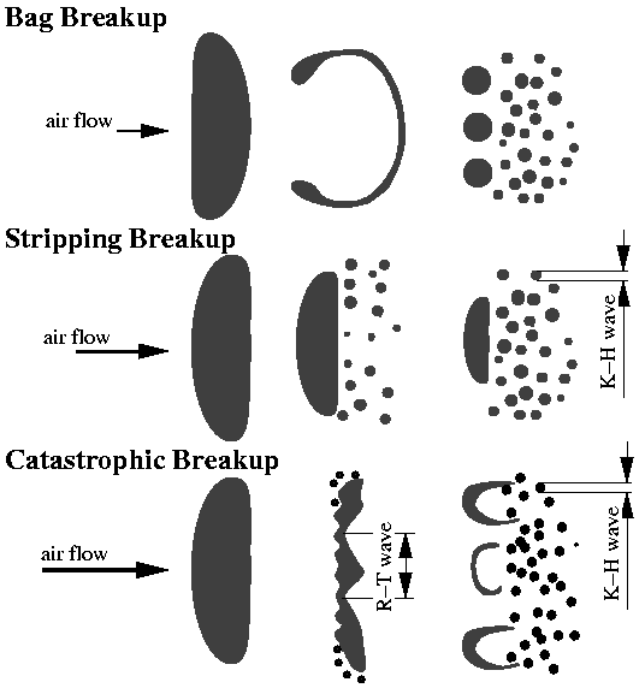

Figure 6-3. Schematic representation of drop breakup mechanisms. (Adapted from Liu and Reitz, 1993).

According to the model developed by Reitz and Diwakar (1986), the droplet undergoes bag breakup when

$$We \equiv \frac{\rho_g u_l^2 r_l}{\sigma} > 6 \tag{6.47}$$

where r_l is the drop radius, σ is the surface tension, and We is the Weber number. Substituting the material properties and spray velocity into equation (6.47), the maximal stable droplet diameter is calculated to be about 25 μm. The spray droplet size of 50 μm is simulated in most cases to study the effects of different parameters, such as solids concentration and jet velocity. However, in order to compare our numerical results with the experimental measurements, a droplet size of 25 μm is used.

The conditions for the simulation obtained from Liu's experiment are summarized in Table 6-2. Conditions such as jet velocity, droplets diameter, and solid concentration are varied in order to study their effects on the flow behaviour.

Table 6-2. Simulation conditions.

Property	**Value**
Particle diameter d_p	70 μm
Droplet diameter at inlet $d_{l,inlet}$	25, 50, 75, and 100 μm
Particle density ρ_p	1480 kg/m^3
Velocity of gas-sold crossflow	0.85 m/s
Temperature of gas-solid crossflow	298 K
Temperature of gas-liquid spray T_l	77 K
Nozzle diameter D_j	1 mm
Spray velocity U_j	33 and 40 m/s
Restitution coefficient e_p	0.95
Restitution coefficient e_{lp}	0.8

6.3 RESULTS AND DISCUSSION

6.3.1 Test cases

6.3.1.1 Particle-laden jet

To test the turbulence model employed in the current study, several simulations with different experiments have been performed. The numerical results are compared with the available experimental data for the particle-laden gas jet in co-current gas flow or stagnant air (Bulzan, 1988; Gillandt et al., 2001; Garcia et al., 2005). The computational domain for all these cases is a rectangular domain with axisymmetric assumption. For the sake of brevity, details on the simulation of these cases are not given here. The conditions of these test cases are summarized in Table 6-3.

Table 6-3. Conditions for test cases.

	Conditions	**Reference**
Case 1	$D_j = 19$ mm; $U_{j,g} = 13.75$ m/s; $U_{j,p} = 13.86$ m/s; $d_p = 39$ μm; $\rho_p = 2500$ kg/m^3; mass loading = 0.2	Bulzan (1988)
Case 2	$D_j = 12$ mm; $U_{j,g} = 15$ m/s; $U_{j,p} = 6.1$ m/s; $d_p = 77.2$ μm; $\rho_p = 2450$ kg/m^3; mass loading = 0.3	Garcia et al. (2005)
Case 3	$D_j = 12$ mm; $U_{j,g} = 7.7$ m/s; $U_{j,p} = 6.4$ m/s; $d_p = 110$ μm; $\rho_p = 2500$ kg/m^3; mass loading = 1.0	Gillandt et al. (2001)

The first data set was for a very dilute particle-laden jet with fine particles obtained by Bulzan (1988). In the experiment, the jet was injected vertically downward from a 19 mm diameter nozzle. The glass beads had an average diameter of 39 μm and mass loading of 0.2 in the jet. Velocity profiles were measured along the centreline axis and within 30 nozzle diameters from

the nozzle exit. Comparison of axial gas and particle velocities along the centreline between numerical simulation and experimental data is shown in Figure 6-4. Further comparison of the axial particle velocity profile is presented in Figure 6-5 at different downstream positions. From these comparisons, it can be seen that good agreement is achieved.

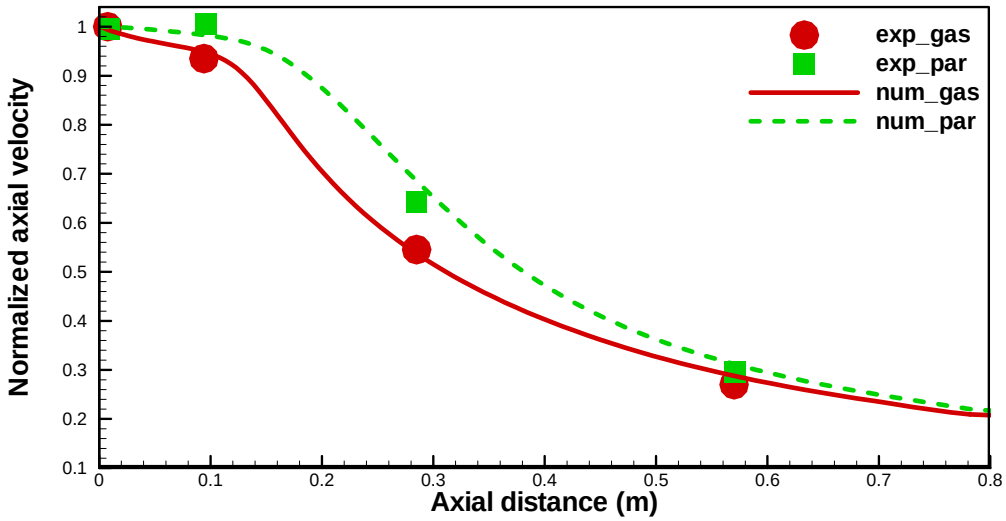

Figure 6-4. Comparison of axial gas and particle velocities along centreline between numerical simulation and experimental data of Bulzan (1988).

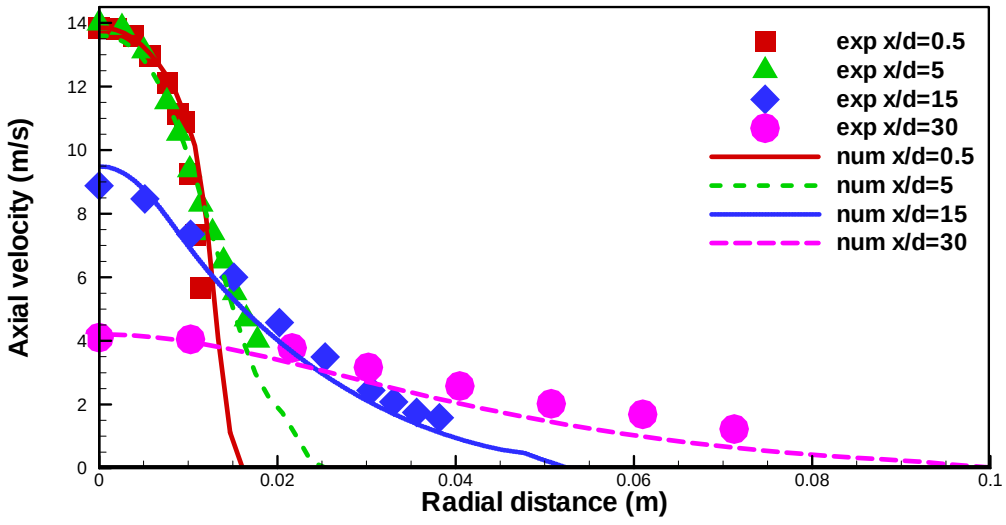

Figure 6-5. Comparison of axial particle velocity profile at different downstream positions between numerical simulation and experimental data of Bulzan (1988).

Comparisons of the gas and solids velocity along the centreline for the other two test cases are shown in Figure 6-6 and Figure 6-7, respectively. Good consistency between numerical simulation and experiment data is obtained. From these three test cases, it can be concluded that the current turbulence model is capable of simulating the turbulent particle-laden jets over a broad range of particle sizes and loadings.

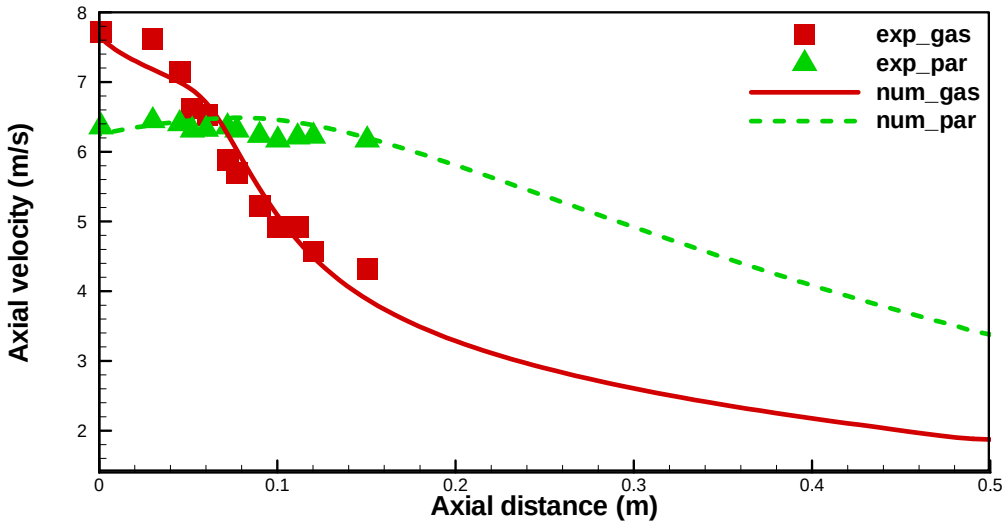

Figure 6-6. Comparison of axial gas and particle velocity along centreline between numerical simulation and experimental data of Garcia et al. (2005).

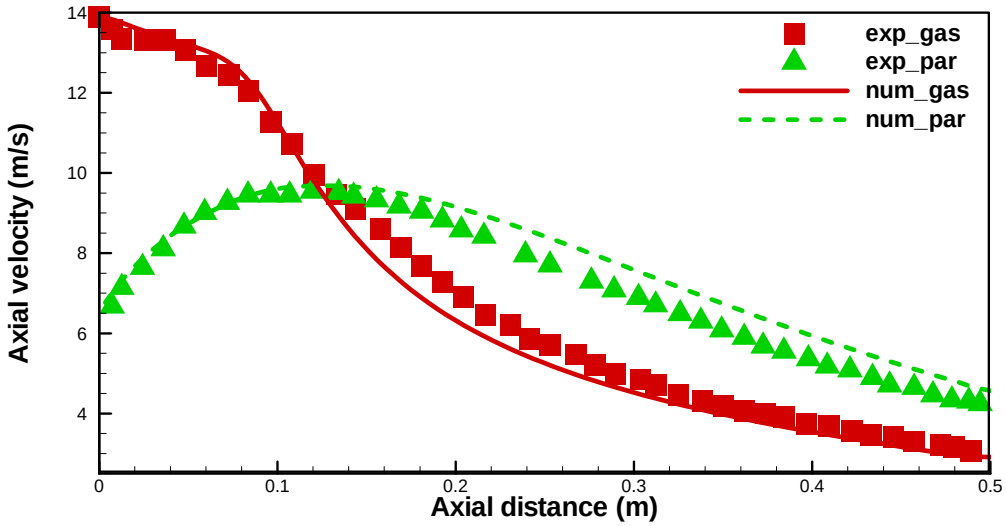

Figure 6-7. Comparison of axial gas and particle velocity along centreline between numerical simulation and experimental data of Gillandt et al. (2001).

6.3.1.2 Evaporating spray in co-current turbulent gas flow

In the current study, the spray evaporation model proposed by Iyer et al. (2002) is employed. This model was originally proposed to study diesel spray for a wide range of ambient and injection conditions. This model is implemented into Fluent 6.3 with User Defined Scalar (UDS) and User Defined Functions (UDF). To evaluate the implementation of the spray evaporation model, an experiment conducted by Sommerfeld and Qiu (1998) is simulated. The experimental setup and its dimensions are shown in Figure 6-8. Heated air was blown from an annular injection tube into a wide test section with an inner diameter of 200 mm and a length of 1.5 m. With a 64 mm outer diameter of the annulus, an expansion ratio of about three was established. Isopropyl alcohol was used to achieve high evaporation rates. Different hollow cone pressure atomisers were mounted in a cylindrical centre-body of the inlet tube to allow different liquid mass flow rates. In order to analyze the spray evolution and evaporation, local droplet size distributions, size-velocity correlations and droplet mass fluxes were measured within the test

section using the phase-Doppler anemometry (Sommerfeld and Qiu, 1998). A detailed description of the test cases, thermodynamic properties of isopropyl vapour and liquid, and the final experimental data are available in an online database of experimental investigations in two-phase flow hosted by Martin-Luther University of Halle-Wittenberg at http://www-mvt.iw.uni-halle.de/index.php? spray_evaporation. The experimental results provided all the required boundary conditions and data to allow testing of numerical calculations of evaporating sprays. For this reason, this experiment has been used as validation tests of several Eulerian-Lagrangian simulations (Chen and Pereira, 1995; Sommerfeld, 1998; Sadiki et al., 2005; Kolaitis and Founti, 2006; Moukalled and Darwish, 2008).

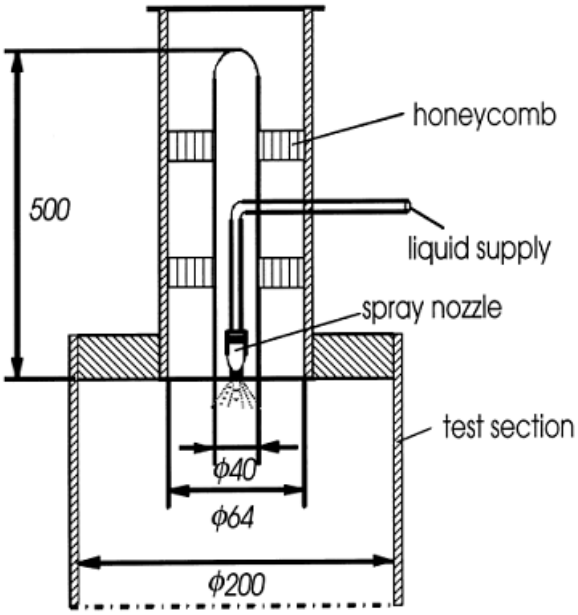

Figure 6-8. Configuration of test section with dimensions in mm. (Adapted from Sommerfeld and Qiu, 1998).

The flow conditions for the case simulated in the current study are summarized in Table 6-4. Detailed numerical results of the flow field are obtained and compared with the available measurements. The radial profiles of droplet axial and radial mean velocities are compared with experimental data in Figures 6-9 and 6-10 at six different axial locations. Overall, the agreement between measurement and computation is reasonably good for both velocity components except

for some small discrepancies. Further comparisons are made for the droplet mass flow rate and mean droplet diameter in Figures 6-11 and 6-12, and both of them are reasonably predicted. The implementation of spray evaporation model is examined by this test case and reasonable consistency with experimental data is obtained.

Table 6-4. Flow conditions from the experimental measurement.

Nozzle holder diameter	Air volume flow rate	Air temperature
40 mm	0.031 m^3/s	373 K
Maximum air velocity	Liquid mass flow rate	Liquid temperature
18 m/s	0.44 g/s	307 K

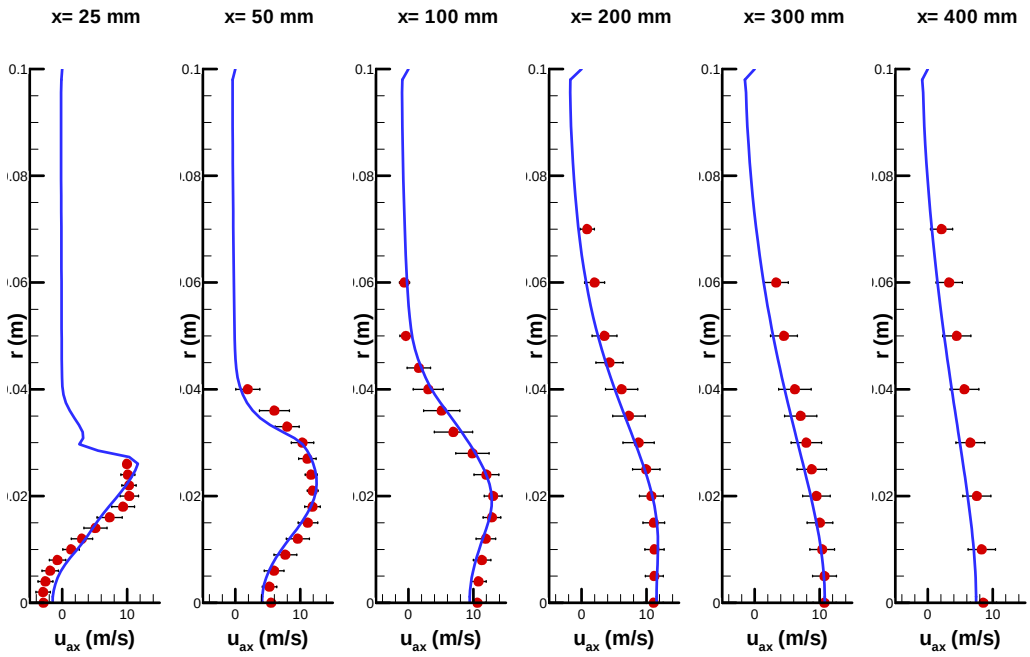

Figure 6-9. Comparison of measurement and simulation for mean axial droplet velocity profiles

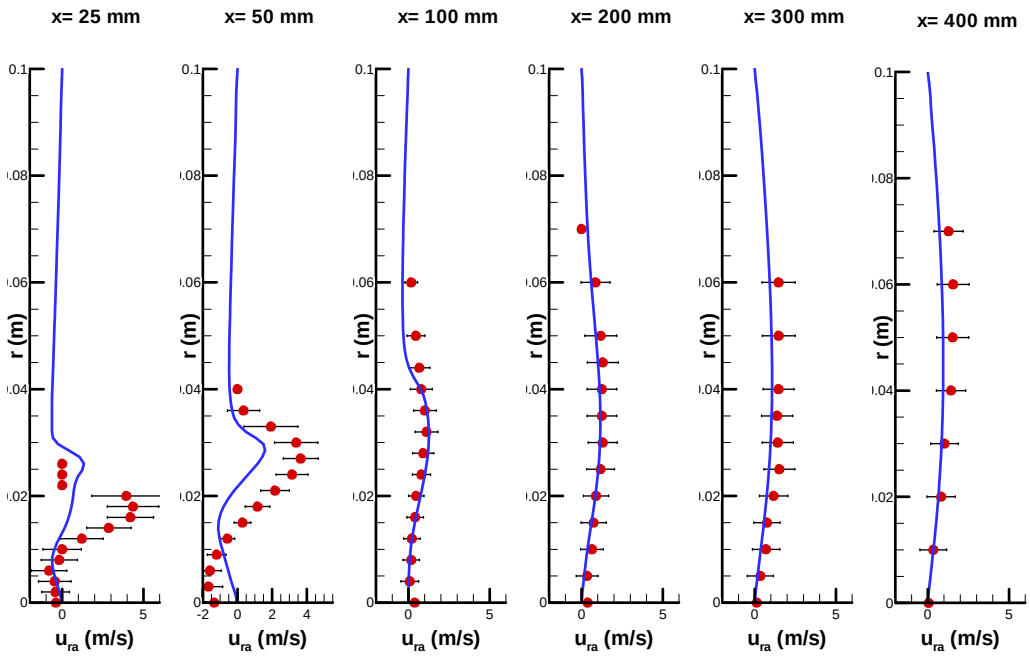

Figure 6-10. Comparison of measurement and simulation for mean radial droplet velocity profiles.

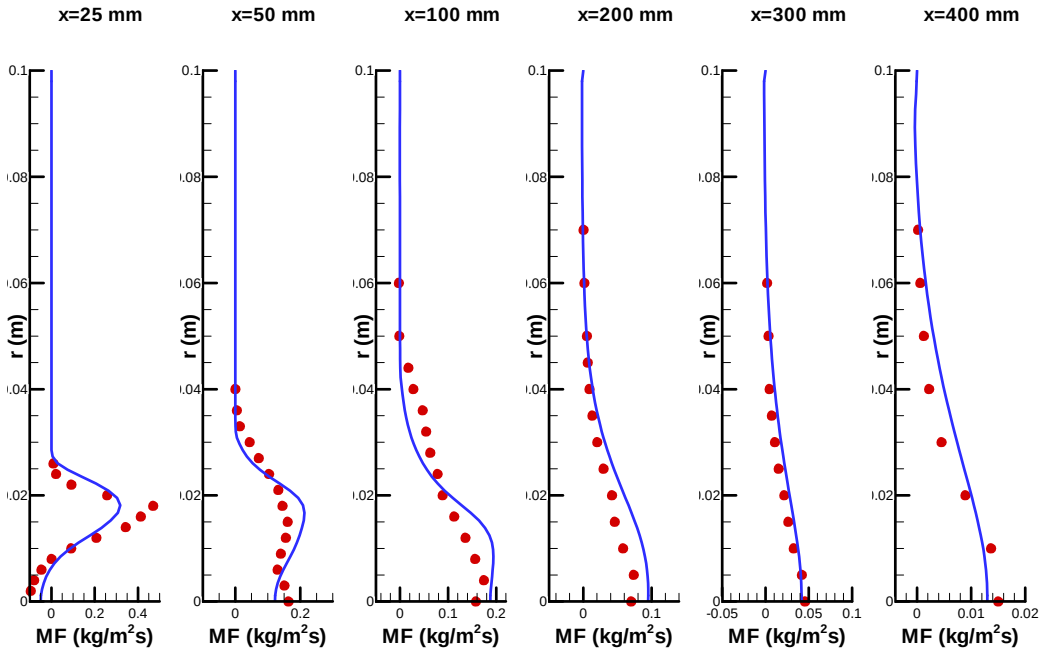

Figure 6-11. Comparison of measurement and simulation for droplet mass flow rate profiles

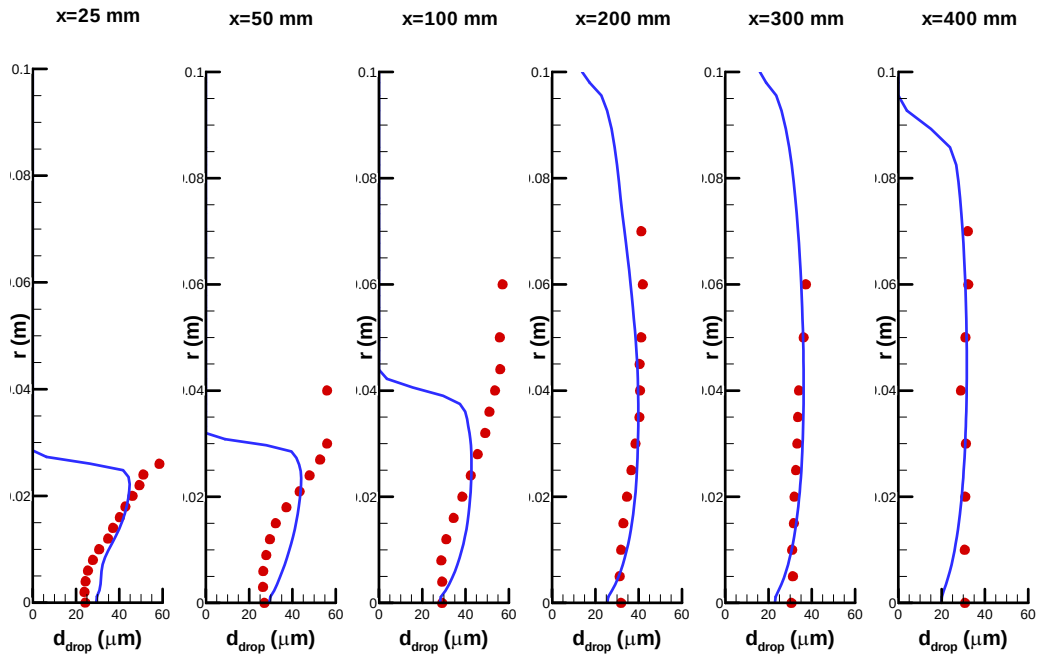

Figure 6-12. Comparison of measurement and simulation for mean droplet diameter distribution.

6.3.2 Evaporative spray in a gas crossflow

6.3.2.1 General spray behaviour

After testing the turbulence model and spray evaporation model, we first simulate the two-phase jet into the gas crossflow. According to the experimental conditions, the two-phase spray of gas and liquid nitrogen is injected into the crossflow with a velocity of 33 m/s. The droplet size is assumed to be 50 μm. The liquid phase volume fraction at the spray inlet is 0.057, which gives a mass flow rate of 1.2 g/s. The liquid volume fraction is shown in Figure 6-13 in the multi-slice view. It can be seen as the jet penetrates into the flow, the liquid volume fraction decreases due to the dispersion and evaporation. A round shape of the jet cross-section can be observed in the figure. The convection effect of the crossflow barely influences the spray cross-section because of the high inertia of the spray jet. It should be noted that the velocity of gas flow is only 0.85 m/s, much smaller than the spray velocity of 33 m/s.

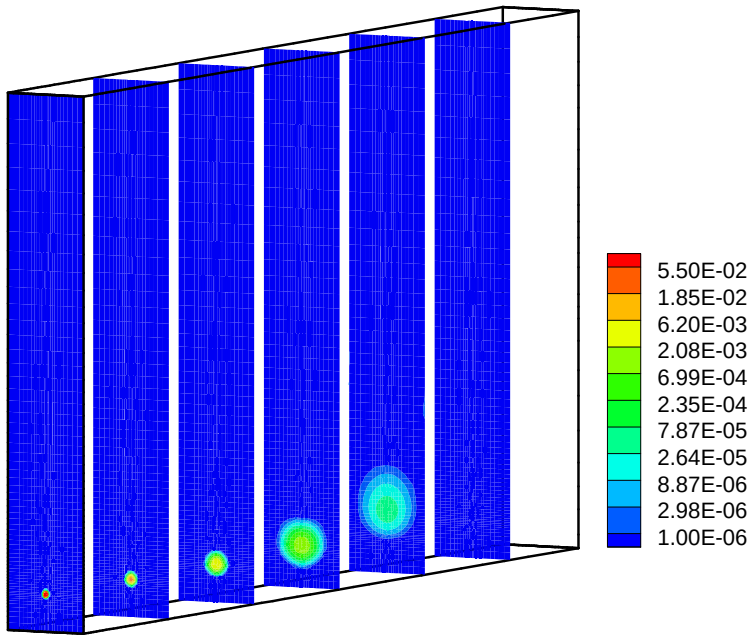

Figure 6-13. Multi-slice view of liquid volume fraction for spray in gas crossflow. (Jet: jet velocity: 33 m/s, liquid volume fraction: 0.057; Crossflow: gas velocity: 0.85 m/s).

The contour of liquid volume fraction in the symmetry plane, where the spray is injected, is shown in Figure 6-14. The liquid volume fraction decreases gradually as the spray penetrates into the crossflow. The spray bends upward due to the crossflow, and the evaporation length of the spray, defined as the spray droplet maximum penetration in the jet direction, can be measured from this plot and is equal to 0.21 m.

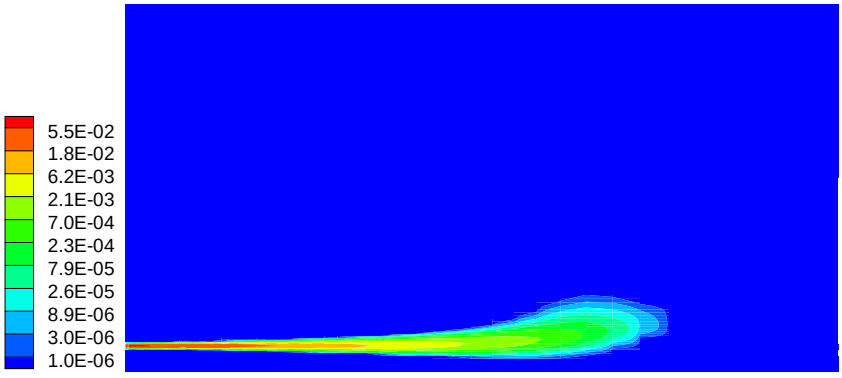

Figure 6-14. Volume fraction of liquid phase in the symmetry plane.

The droplet size distribution in the spray region is shown in Figure 6-15, in the symmetry plane. As the liquid spray penetrates into the crossflow, the droplet sizes decrease gradually due to fast evaporation. The droplets near the spray boundary have the highest evaporation rates because of the high surrounding gas temperature and the low liquid volume fraction, resulting in small droplets there. This result is consistent with the Eulerian-Lagrangian simulation of evaporative spray jets in concurrent gas-solid pipe flows in the literature (Wang et al., 2004)

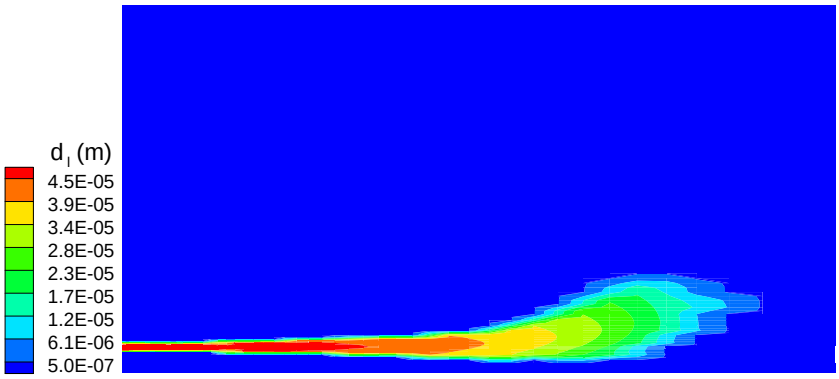

Figure 6-15. Droplet size distribution in the spray region

6.3.2.2 Effect of droplet size

To study the effect of the average droplet size at the spray inlet, four cases with different inlet droplet diameters of 25, 50, 75, and 100 μm are simulated. From the liquid volume fraction contours shown in Figure 6-16, it is evident that the spray evaporation length is greatly affected by the inlet droplet size. The spray evaporation length increases with the inlet droplet size. This is because the evaporation of a single droplet is determined mainly by the droplet size according to the famous D2 law (Lefebvre, 1989). Hence, the long life time and large inertia of a big droplet enable it to penetrate deep into the crossflow. To accurately simulate the liquid spray into a hot crossflow, the droplets size at the spray inlet plays an important role. As we know, the droplets size is mainly determined by the nozzle design and operating conditions (Lefebvre,

1989). Consequently, this result also demonstrates the importance of the spray nozzle in industrial processes.

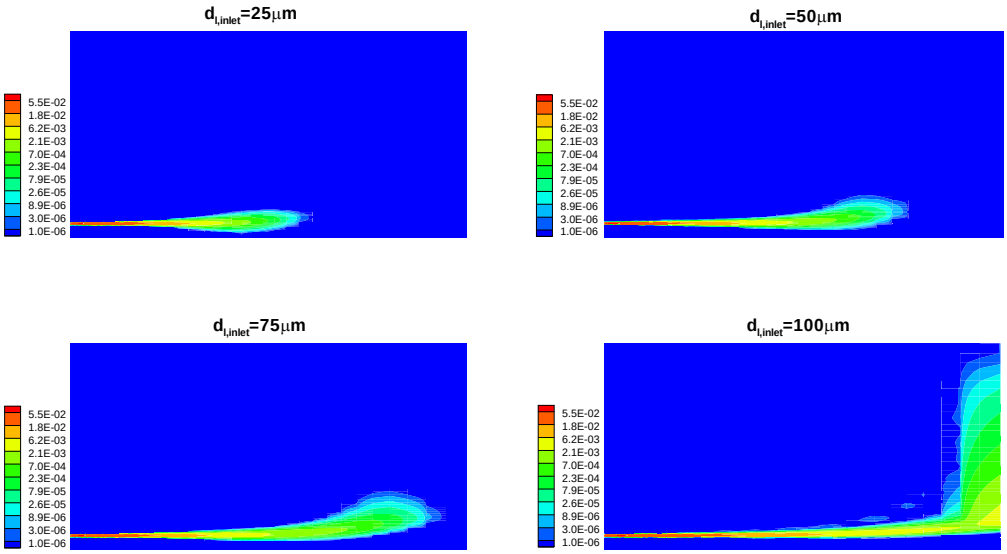

Figure 6-16. Volume fraction of liquid phase for different droplet sizes at spray inlet.

6.3.2.3 Comparison with experiment

The results of the droplet size of 25 μm are compared with the experimental measurement of the spray position. Figure 6-17 shows the comparison, where the symbols represent the jet position measured in the experiment, while the gas temperature contour can be used to determine the jet position in the simulation. In the figure, there is good agreement between our simulation and the experimental results. This agreement can also be viewed as confirming that the choice of stable droplet size prediction from the equation (6.47) is reasonable.

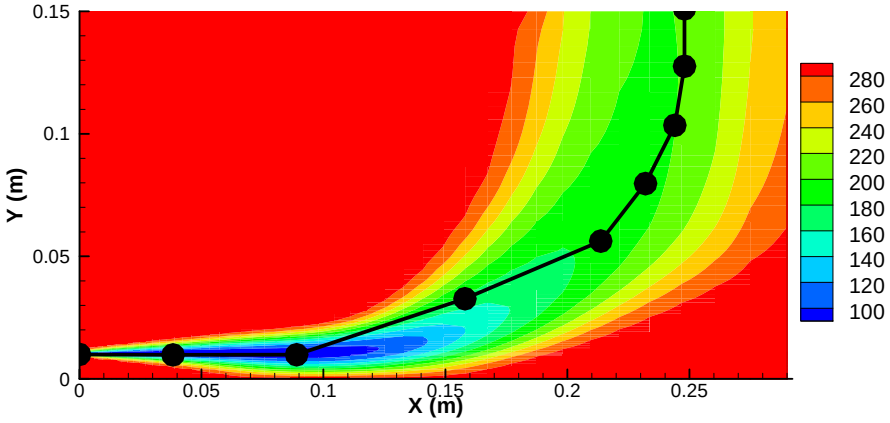

Figure 6-17. Comparison between experimental measurement and numerical simulation for jet position in gas crossflow.

6.3.3 Evaporative spray in a gas-solid crossflow

6.3.3.1 Typical flow behaviour

The evaporative spray in a uniform gas-solid crossflow with a solids concentration of 1% is simulated and discussed in this section. The spray velocity is 33 m/s and the mean droplet size at the spray inlet is 50 μm. The multi-slice view of the liquid phase volume fraction is shown in Figure 6-18. Compared with Figure 6-14, jet penetration decreases greatly due to the presence of particles. In addition, the shape of the jet deviates strongly from the round shape for the jet in the gas crossflow. This is because the presence of solid particles augments the convection effect from the crossflow and affects the shape of the jet cross-section.

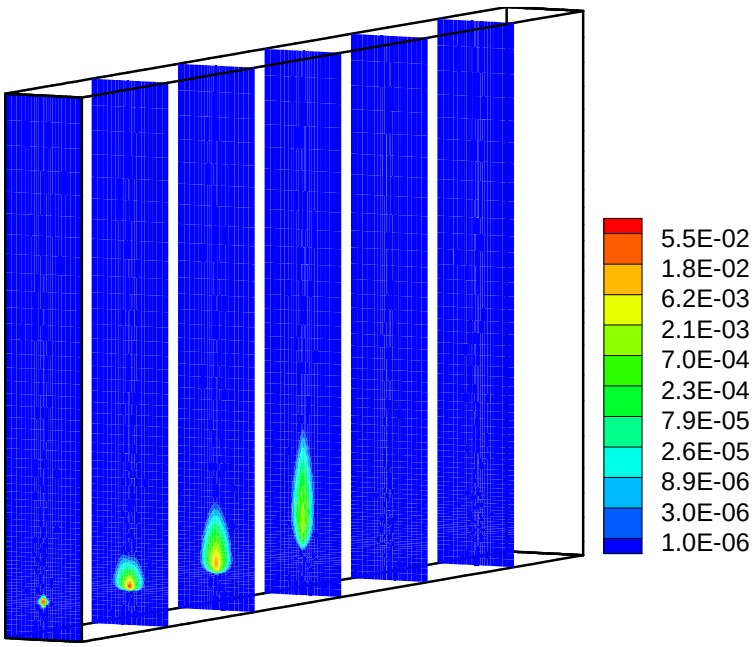

Figure 6-18. Multi-slice view of liquid volume fraction for spray in gas-solid crossflow. (Jet: jet velocity: 33m/s, liquid volume fraction: 0.057; Crossflow: solid concentration: 0.01, gas-solid velocity: 0.85 m/s).

Figure 6-19 shows the liquid volume fraction in the symmetry plane. Due to the presence of particles, the evaporation of droplets is enhanced, resulting in a shorter evaporation length compared to the case without particles. In addition, because of the high momentum in the crossflow, the bending angle of the spray is higher than for the case without particles.

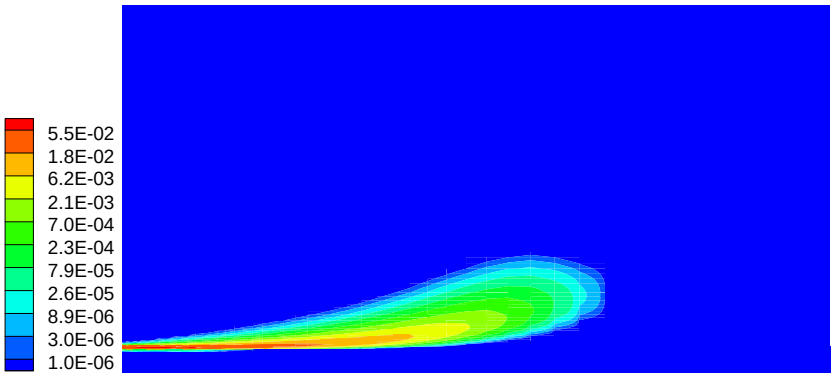

Figure 6-19. Volume fraction of liquid phase in the symmetry plane for spray in gas-solid crossflow. (Jet: jet velocity: 33m/s, liquid volume fraction: 0.057; Crossflow: solid concentration: 0.01, gas-solid velocity: 0.85 m/s).

Figure 6-20 presents the solid phase volume fraction in the symmetry plane. From this figure, it can be seen that liquid evaporation produces a large amount of vapour, which dilutes the solids flow in the jet region and pushes the particles away to form a compact zone around the jet. This is very apparent in the slice views of the solid volume fraction contour in the jet direction as shown in Figure 6-21, where a shell-like dense region surrounding the spray jet can be observed.

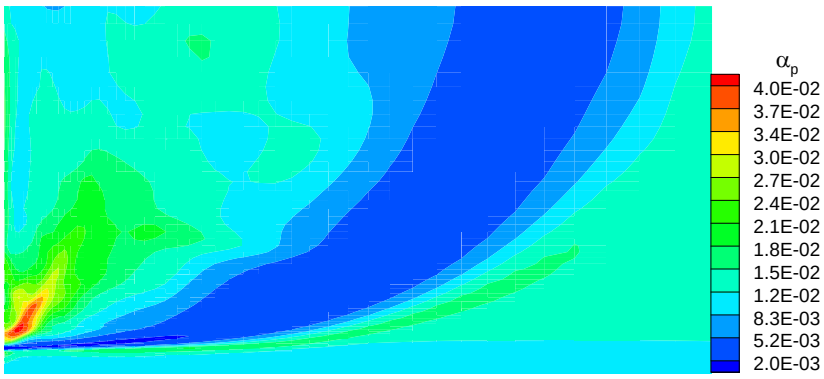

Figure 6-20. Volume fraction of solid phase in the symmetry plane for spray in gas-solid crossflow.

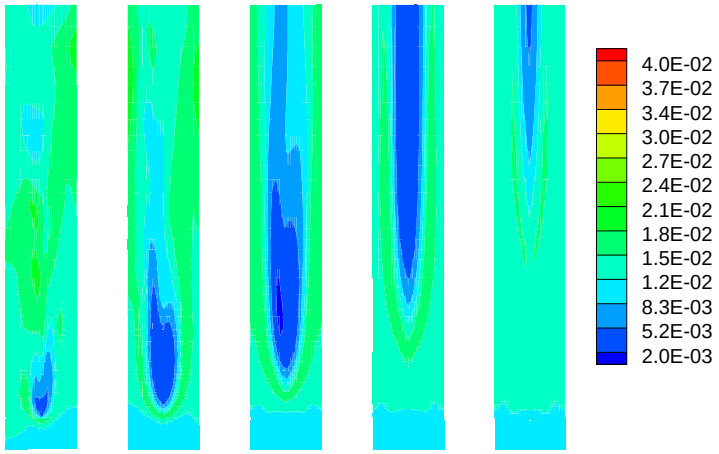

Figure 6-21. Volume fraction of solid phase in cross-planes along jet direction (X = 0.05, 0.1, 0.15, 0.2, 0.25 m from left to right, respectively).

6.3.3.2 Effect of solids concentration

To study the effect of the solids concentration on the spray structure, contours of the liquid volume fraction are shown in Figure 6-22 for solids concentrations of 0, 1% and 5%. For these cases, the spray conditions are fixed, i.e. spray velocity of 33 m/s, droplet size of 50 μm, and liquid volume fraction of 0.057. It is obvious that the spray evaporation length is reduced as the solids concentration increases. With the presence of solids in the crossflow, the spray expansion angle tends to increase with the solids concentration as more particles are entrained by the spray. In addition, the spray-bending angle increases with increasing solids concentration. All the phenomena observed here qualitatively agree with the experimental observation, except for the spray expansion angle, which could not be measured experimentally (Liu, 2003).

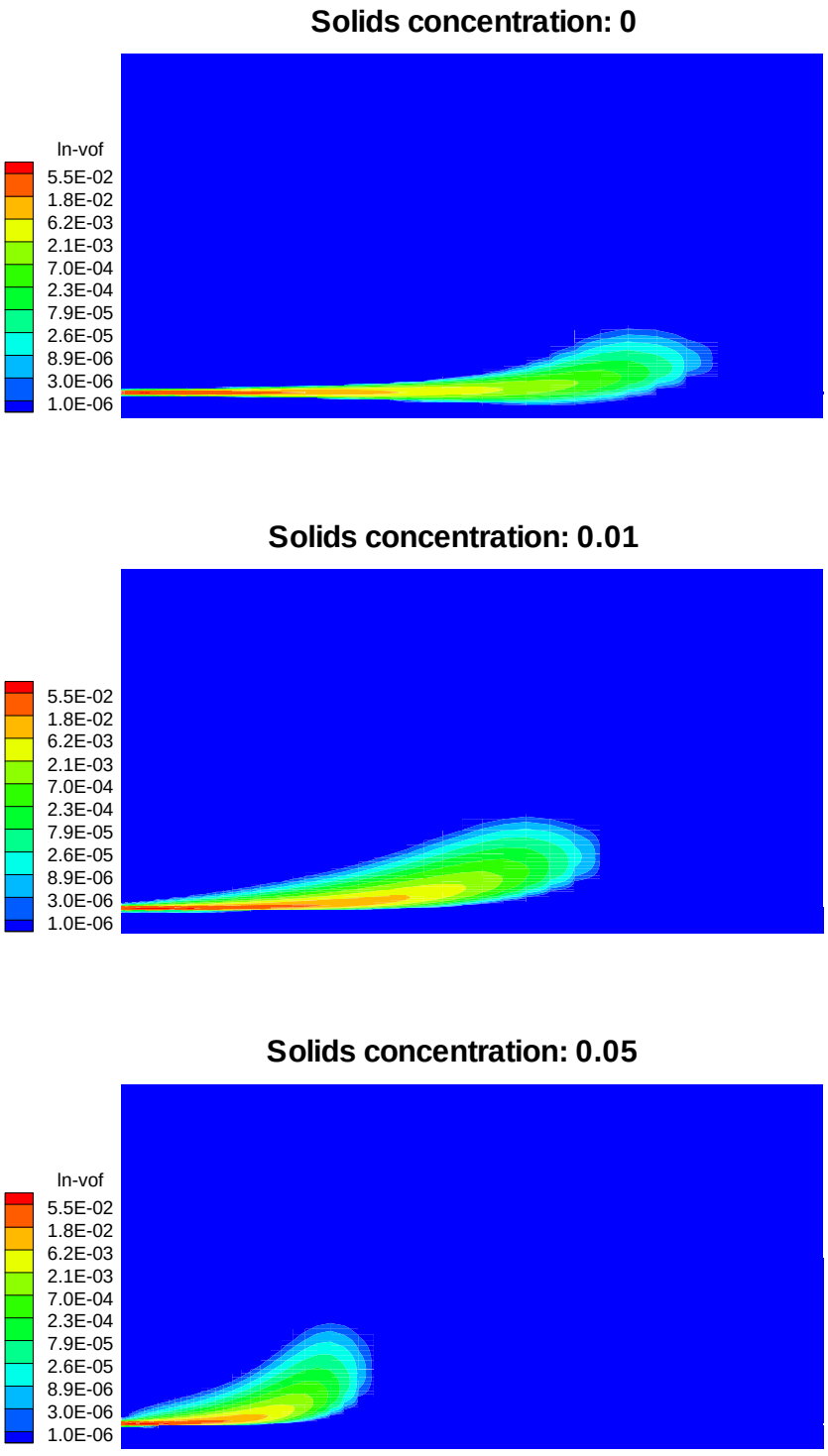

Figure 6-22. Volume fraction of liquid phase at different solids concentrations. (Jet: jet velocity: 33 m/s, liquid volume fraction: 0.057; Crossflow: gas-solid velocity: 0.85 m/s).

6.3.3.3 *Effect of spray velocity*

Two spray velocities of 33 and 40 m/s are simulated to evaluate the effect of the jet velocity on the spray behaviour. For these two cases, all parameters are maintained the same except for the spray velocity. The contours of liquid volume fraction for these two jet velocities are shown in Figure 6-23. The spray evaporation length increases with spray velocity because of the increased spray momentum at the inlet. By carefully examining the spray expansion angles, it can be found that the jet expansion angle decreases slightly with increasing jet velocity. This trend is consistent with experimental observations for a vertical gas jet (Cleaver et al, 1995) and our previous numerical simulation for a horizontal gas jet in a fluidized bed (Li et al., 2008).

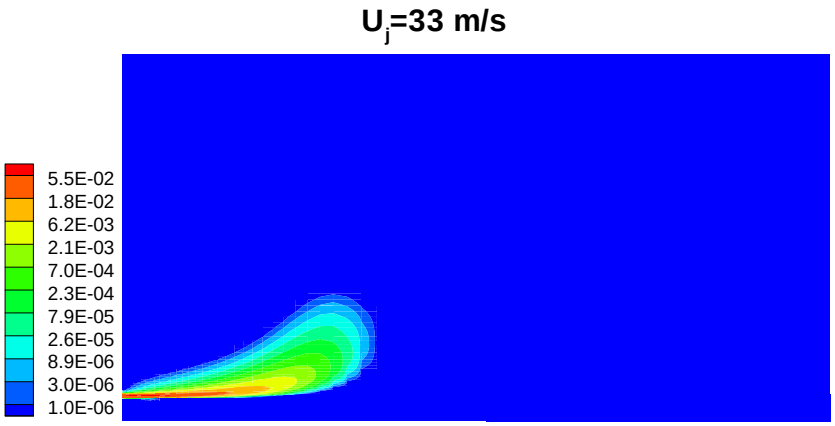

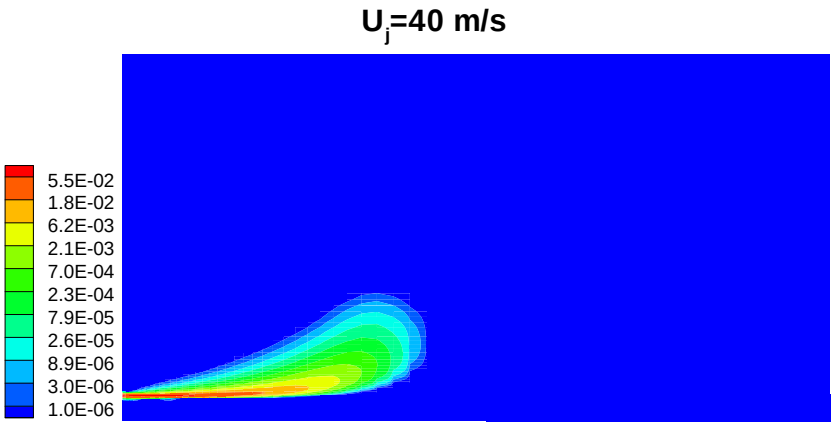

Figure 6-23. Volume fraction of liquid phase for spray velocity of 33 and 40 m/s. (Jet: liquid volume fraction: 0.057; Crossflow: solids concentration: 0.05, gas-solid velocity: 0.85 m/s).

6.3.3.4 Comparison with experiment

Figure 6-24 compares of the numerical simulation with the experimental measurement of jet positions for solids concentration of 0.5%, 1%, and 2.1%. In all these cases, the droplet diameter at the spray inlet is 25 μm, and the liquid volume fraction is 5.7%. Although the spray-bending angles are slightly over-predicted, reasonable agreement between our simulation and the experiment can be observed. Many factors may lead to over-predictions in the spray-bending angle, for example, uncertainty in droplet size and non-uniformity of crossflow. In addition, the inability to model large droplets in the spray is another possible reason for the over-prediction. Again, the effect of the solids concentration on the jet behaviour is illustrated in the figure.

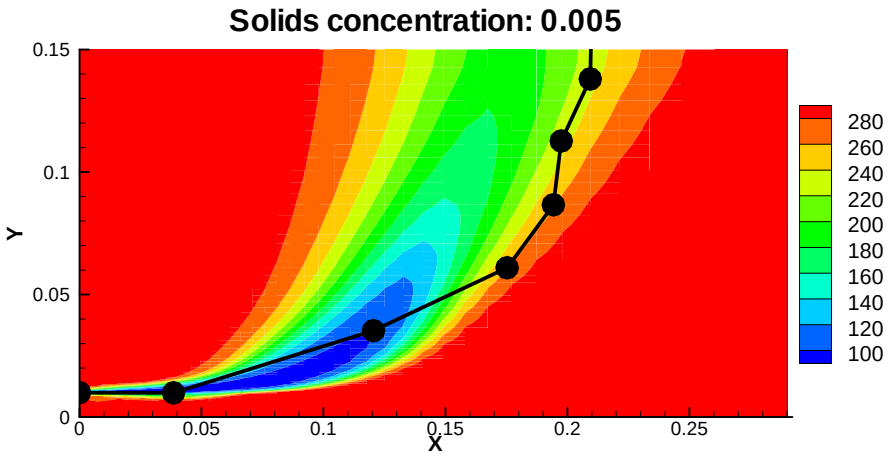

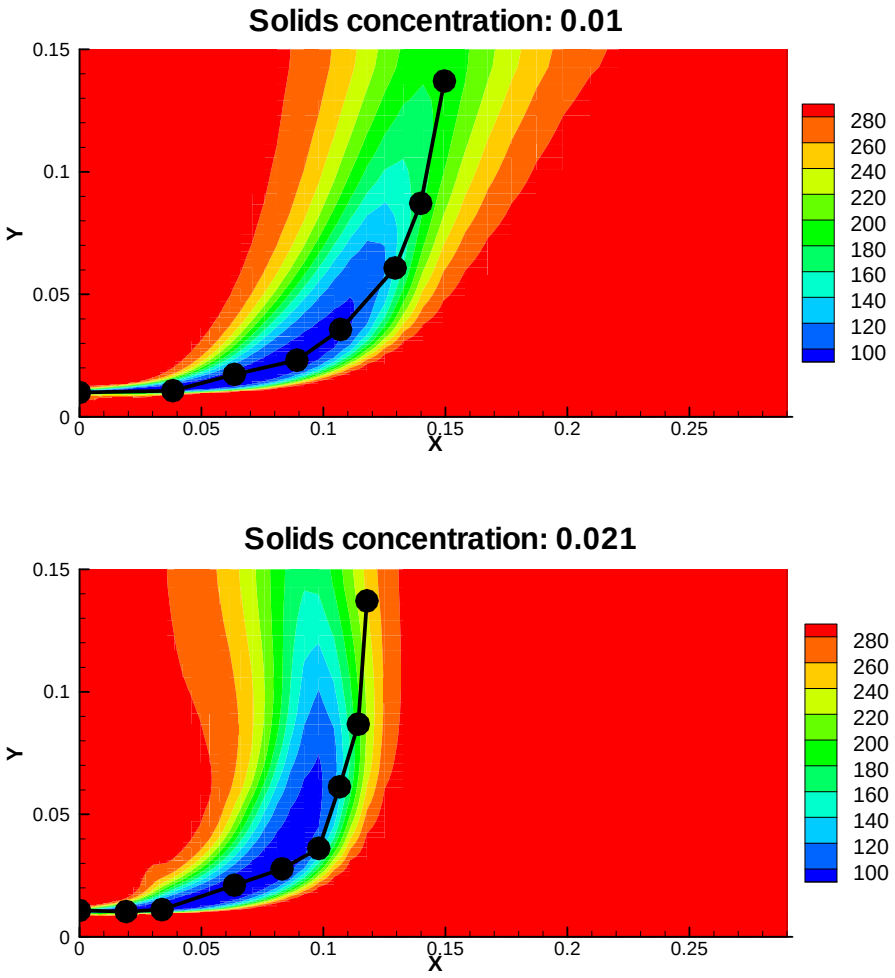

Figure 6-24. Comparison between experimental measurement and numerical simulation for jet position in gas-solid crossflow.

6.4 SUMMARY

In this chapter, three-dimensional simulations of an evaporating gas-liquid spray into a gas-solid crossflow are performed. The gas, solid, and liquid phases are modeled with a Eulerian-Eulerian model and appropriate correlations for inter-phase interaction and heat, mass transfer are used. The implementation of these models into Fluent 6.3 has been carefully compared with available experimental data.

General features of the evaporative spray and qualitative trends are predicted in our simulation, and the predicted results agree reasonably well with the experimental observations. The predicted spray positions are quantitatively compared with experimental measurements for different solids concentrations, and fair agreement has been obtained. In our simulations, we find that particles affect the spray structure in evaporation length, jet cross-sectional shape, spray-bending angle, and expansion angle. The spray evaporation length increases with jet velocity and inlet droplet size, and decreases with increasing solids loading in the crossflow. Evaporation of the spray droplets plays an important role in affecting the flow behaviour by forming a shell-like dense region around the spray jet.

Chapter 7. EVAPORATIVE SPRAY IN A RISER

7.1 INTRODUCTION

In **Chapter 6**, the following assumptions were used to simplify the analysis:

(a) The droplet size of liquid spray was assumed to be uniform at the spray inlet, and coalescence and atomization of the spray droplets in the crossflow were neglected.

(b) The interaction between droplets and particles was simply described as collision, and the momentum exchange between these two phases was simply modeled with a particle-particle drag coefficient.

(c) The effect of particles on heat transfer was only taken into account by an effective heat transfer coefficient between gas-solid mixture and droplets.

(d) The gas-solid crossflow was considered to be uniform with a uniform velocity profile and constant solids concentration.

Although reasonable agreement between our numerical results and the experiment has been obtained, further investigation and improvement for some of the aforementioned assumptions are needed, especially when we want to extend our models to more general problems, for example, complex flows in industrial applications. This motivates the work in this chapter.

The objective of this chapter is to extend the work in **Chapter 6** to develop a more complete model capable of accounting for the complex interactions between hot particles and cold droplets in riser flows based on available empirical correlations and experimental observations in the literature. With the newly developed model, we intend to simulate the evaporating water spray in a hot high-density riser and achieve a better understanding of the hydrodynamics of these complex phenomena. To model the liquid injection into FCC risers, the interactions including

momentum and energy exchange between the injected spray droplets and FCC particles must be correctly taken into account. However, there is no detailed explanation of the collision mechanism and the associated transfer phenomenon in the literature, although many engineering process operations involve the collision of liquid droplets with solid particles at high temperatures. Before the modelling work is introduced, a brief review of previous work on the droplet-particle interaction is given.

Recently, Ge and Fan (2006) performed three-dimensional direct numerical simulations for the film-boiling contact of a moving particle and a liquid droplet with the level-set method. In their study, normal and oblique collisions between the droplet and the particle were simulated and compared with the experimental data. With film-boiling evaporation upon contact, the droplet undergoes spreading, recoiling, and rebounding during non-wetting contact. In their numerical study, they found that the particle size had a significant effect on the dynamics in a normal collision.

Due to the difficulty in modeling, the momentum exchange between droplets and particles with strong coupling heat transfer and evaporation are often neglected in the modeling of liquid injection in a riser (Gao et al., 2001; Chang and Zhou, 2003; Nayak et al., 2005). Wang et al. (2004) incorporated the momentum exchange between droplets and particles into the effective gas drag coefficient by Mostoufi and Chaouki (1999) when modelling the evaporative spray jets of liquid nitrogen in concurrent gas-solid flows.

Heat transfer between droplets and the surroundings is expected to be enhanced by the presence of particles. Buchanan (1994) did extensive work on the heat-transfer coefficients of gas/solids and liquid/gas/solids systems based on the hypothesis of direct contact, convective heat transfer, and radiative heat transfer. He proposed a correlation for the heat transfer coefficient to describe the convective heat transfer through a gas layer between the droplet and particles due to the

Leidenfrost effect, which has been used extensively in numerical simulations of FCC riser flows (Gupta and Rao, 2003; Berry et al., 2004; Wang et al., 2004). Chang and Zhou (2003) developed a collision heat transfer model for predicting the heat transfer between particles and droplets. In this model, the heat flux from particles to droplets per unit volume was proportional to the number densities of particles and droplets, particle thermal conductivity, conduction distance, and mean temperature difference. According to the authors, the model was closed by an empirical proportionality constant. To capture the key features of heat transfer between the liquid droplet and the gas-solid mixture, Nayak et al. (2005) developed a phenomenological model to predict the heat transfer coefficient of droplet vaporization in a gas-solid flow by relating the evaporation rate of the droplet with the collision frequency, heat capacity, latent heat, relative velocity, and phase temperature.

7.2 EXPERIMENTAL SETUP

The experiments of Gehrke and Wirth (2008) were conducted in a pilot-plant scale model CFB unit of diameter of 0.19 m and height 11.3 m. The riser of spent FCC particles was operated at a temperature of 300°C with a mass flux of 180 kg/m^{2}s at two superficial gas velocities: 5 and 10 m/s. Water was injected into the middle of the reactor via a single fluid nozzle. Two nozzles with different spray droplet sizes and spray patterns were used in the experiments. The spray angles for both the hollow cone and the full cone spray were the same, 60 degrees in the free environment, and the average droplet sizes $d_{v,90}$ were 269 and 466 μm, respectively. Capacitance probes were used to analyze the solid concentration and mass flux, and thermocouples were employed to measure the temperature in the system. In the experiment, profiles of solids concentration as well as solid mass flux distribution inside the riser at different heights with and without liquid spray were measured to study the interaction between the spray and the upstream solids flow. The spray border was determined with thermocouples and capacitance probes to investigate the radial spray profile. A schematic of the experimental setup

is shown in Figure 7-1; a detailed description of the experimental setup as well as experimental results were provided by Gehrke and Wirth (2007a, 2007b, 2008). In this chapter, we simulate only a section of the riser, shown in the inset of Figure 7-1.

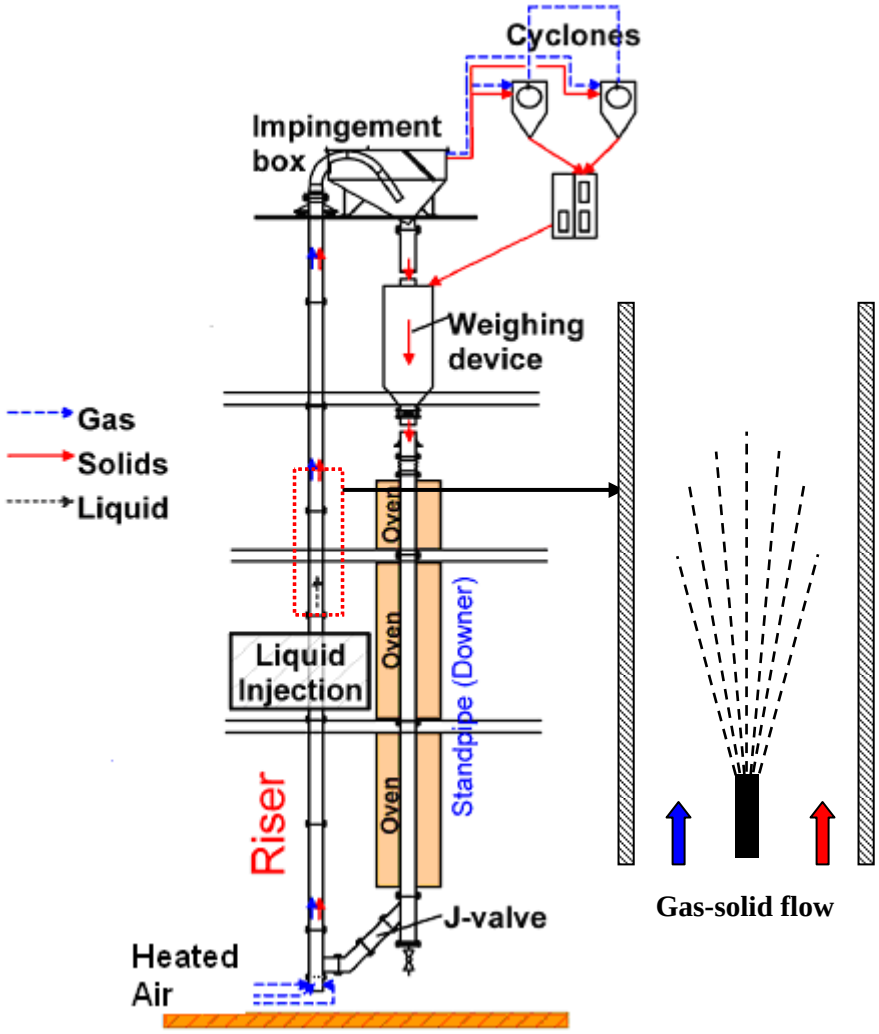

Figure 7-1. Schematic of experimental setup. (Adapted from Gehrke and Wirth, 2007b).

7.3 NUMERICAL METHOD

7.3.1 Governing equations

To model the evaporative water spray in the riser, the gas, liquid and solid phases are treated as an inter-penetrating continuum with a Eulerian approach, and the following assumptions are made. The particles are inert spheres and considered to be mono-sized, and do not absorb any liquid. In some circumstances, particles can be trapped inside large droplets to form agglomerates when collision occurs. In this circumstance, spray droplets and the trapped particles are treated as a droplet/agglomerate mixture phase. The interactions between droplets and agglomerates, i.e. coalescence and breakup, are neglected because of their low concentrations.

Governing equations of mass, momentum and energy for each phase can be written in a similar way to what was done in previous simulations. Constitutive relations based on granular kinetic theory are used to close the governing equations for the solid phase, and turbulence models detailed in **Chapter 6** are employed. Only the additional models taking into account the mass, momentum and heat transfer resulting from complex interactions between droplets and hot particles are described here.

7.3.2 Inter-phase momentum exchange

For gas-droplet and gas-solid drag forces, the generally accepted expressions for β_{gl} and β_{gp} following Issa and Oliveira (1996) and the Gidaspow drag model are used. Full details of these two drag models can be found in **Chapter 2** and **Chapter 5**, respectively.

It is very difficult to model the momentum exchange between droplets and particles, as investigations in this field are very limited, especially for strong coupling heat transfer and

evaporation. Here, a phenomenological model is developed to describe the momentum exchange. According to the collision modes by Fan (2004), the collision of a particle and a droplet of different sizes may experience different contact modes. In the present study, it is reasonable to assume that the small particle may rebound or the particle may penetrate into the droplet and be retained inside, as schematically illustrated in Figure 7-2. In the latter circumstance, the particles trapped in the droplet are assumed to form an agglomerate. When bouncing takes place, it is reasonable to treat the interaction between the droplet and the particle as a collision between two rigid bodies to model the momentum exchange. For this purpose, an expression for the droplet-particle momentum transfer due to collision is derived in **Appendix A** based on recent numerical simulations of Ge and Fan (2006, 2007).

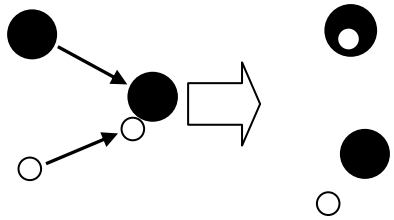

Figure 7-2. Schematic of collision between a droplet and a particle (solid circle: droplet; hollow circle: particle).

Similar to the gas-droplet and the gas-particle momentum exchanges, the droplet-particle momentum exchange is expressed as the product of a drag coefficient and the relative slip velocity between the solid and the droplet phase.

$$M_{lp} = -M_{pl} = \beta_{lp}(\vec{V}_l - \vec{V}_p) \tag{7.1}$$

where

$$\beta_{lp} = (1-\gamma)\varphi\frac{3}{4}\frac{(1+e_{lp})\alpha_l\rho_l\alpha_p\rho_p(d_l+d_p)^2\left|\vec{V}_l-\vec{V}_p\right|}{\left(\rho_l d_l^3+\rho_p d_p^3\right)} \tag{7.2}$$

Here γ is the particles collection efficiency by the droplet and expresses the probability of particles to be trapped by the droplet upon collision; φ is a lump factor to take into account the decrease of momentum exchange due to oblique collisions; e_{lp} is the effective restitution coefficient of a normal collision between the droplet and the particle. Equation (7.2) is slightly different from the solid-solid drag correlation used in **Chapter 6.** In equation (7.2), the particles collection efficiency γ, and the lump factor φ are introduced to characterize the collision between a small particle and a large droplet. Discussion of the introduction of γ and φ can be found in the next section and in **Appendix A**, respectively**.**

7.3.3 Mass and heat transfer between phases

In the current problem, there are different mechanisms for mass transfer between different phases. Mass is transferred from the droplet/agglomerate phase to the gas phase when evaporation takes place. Meanwhile, there exists mass transfer between the droplet/agglomerate phase and the particle phase due to collisions.

7.3.3.1 Mass transfer due to collisions

The mass transfer from the solid phase to the droplet/agglomerate phase due to collisions is proportional to the collision frequency and the particles collection efficiency, and it can be expressed as:

$$q_{pl,c} = \gamma m_p f_{lp} \tag{7.3}$$

where $m_p = \rho_p \pi d_p^3 / 6$ is the mass of a single particle and f_{lp} is the frequency of collision between the droplet and solid particle in per unit volume. The frequency of collision can be approximated (Iyer and Abraham, 2005; Nayak et al., 2005) by

$$f_{lp} = \frac{\pi}{4} n_l n_p (d_p + d_l)^2 \left| \vec{V}_l - \vec{V}_p \right| \tag{7.4}$$

where n_l and n_p are the numbers of drops and particles per unit volume. Rewriting n_l and n_p in terms of volume fractions, equation (7.4) becomes

$$f_{lp} = \frac{\pi}{4}\left(\frac{6\alpha_l}{\pi d_l^3}\right)\left(\frac{6\alpha_p}{\pi d_p^3}\right)(d_p + d_l)^2 \left|\vec{V}_l - \vec{V}_p\right| \tag{7.5}$$

The particle collection efficiency, γ, introduced here is analogous to the adhesion probability for small droplets hitting a solid surface (Heinrich et al., 2003). Similar to the adhesion probability, the collection efficiency depends on the wetting properties and the kinetic energy of the colliding bodies, as well as sizes. Due to the complex and strong coupling between hydrodynamic and thermodynamic factors during collision, such as a deformable interface, film boiling heat transfer, and phase changes, the theoretical analysis of this parameter is difficult. In the absence of experimental information on the particles collection efficiency, it is practical to treat this parameter as adjustable.

7.3.3.2 Mass transfer due to evaporation

Owing to the presence of particles, the evaporation of the droplet becomes even more complex. For simplicity, we neglect the vaporization and diffusion of the droplet into the surrounding air before it reaches the boiling point. The evaporation of a single droplet at the boiling point is modeled (Buchanan, 1994) as

$$\dot{m}_{drop} = -\frac{\hbar_{drop,mix} A_{drop} (T_g - T_l)}{L} \tag{7.6}$$

where $\hbar_{drop,mix}$ is the coefficient of heat transfer from the surrounding gas-solid mixture to a droplet, $A_{drop} = \pi d_l^2$ is the droplet surface area and L is the latent heat of liquid, T_g, T_l are temperatures of gas and liquid, respectively. The mass transfer rate from the droplet phase to the gas phase due to evaporation in a control volume is written as

$$q_{lg,drop} = \frac{6\alpha_l \hbar_{drop,mix}(T_g - T_l)}{Ld_l} \tag{7.7}$$

In the above expressions, evaporation resulting from the contacts of particles and droplets when bouncing collisions take place, is taken into account with an effective heat transfer coefficient $\hbar_{drop}$, discussed in the next section. When the particle is trapped into a droplet at the boiling point upon collision, the mass transfer is

$$\dot{m}_{part} = -\frac{\hbar_{part} A_{part}(T_p - T_l)}{L} \tag{7.8}$$

where $\hbar_{part}$ is the coefficient of heat transfer from the trapped particle to liquid, $A_{part} = \pi d_p^2$ is the particle surface area and T_p is the temperature of the particle. Similarly, we obtain

$$q_{lg,part} = n_{p,l} \frac{\hbar_{part} A_{part}(T_p - T_l)}{L} \tag{7.9}$$

where $n_{p,l}$ is the number density of particles in the droplet/agglomerate phase.

Considering the evaporation of the agglomerate, some particles are released from the agglomerate due to the decrease of the amount of liquid in the agglomerate. Calculation of this part of mass transfer $q_{lp,e}$ is straightforward, with the assumption that the volume fraction of liquid in the agglomerate is equal to $1-\alpha_{p,pack}$, where $\alpha_{p,pack}$ is the particle volume faction at the packing state (Leclere et al., 2001). It should be noted that agglomeration is a very complicated process and the current consideration is only a first approximation. Consequently, the source terms in mass conservation equations are closed by

$$q_g = q_{lg,drop} + q_{lg,part} \tag{7.10}$$

$$q_l = q_{pl,c} - q_{lp,e} - q_{lg,drop} - q_{lg,part} \tag{7.11}$$

$$q_p = q_{lp,e} - q_{pl,c} \tag{7.12}$$

7.3.4 Heat transfer between phases

The heat transfer between any two phases is assumed to be a function of the temperature difference. Generally, it can be written as

$$Q_{mn} = \hbar_{mn}(T_m - T_n) \tag{7.13}$$

Here m, n can be g, l and p; $\hbar_{mn}$ represents the volumetric inter-phase heat transfer coefficient, which is the product of the specific interfacial exchange area and the heat transfer coefficient. For example, the volumetric gas-particle and gas-droplet heat transfer coefficient $\hbar_{gp}$ and $\hbar_{gl}$ can be calculated by

$$\hbar_{gp} = \frac{6\alpha_p}{d_p}\hbar_{part} \tag{7.14}$$

$$\hbar_{gl} = \frac{6\alpha_l}{d_l}\hbar_{drop} \tag{7.15}$$

Usually, the gas-solid or gas-droplet heat transfer coefficient is calculated from the dimensionless Nusselt number.

$$Nu_{part} = \frac{\hbar_{part} d_p}{k_g} \tag{7.16}$$

$$Nu_{drop} = \frac{\hbar_{drop} d_l}{k_g} \tag{7.17}$$

where k_g is the thermal conductivity of the gas.

For the heat transfer between gas and particle, the expression for the Nusselt number from Gunn (1978) is used, applicable for a wide range of solid volume fractions between 0 and 60%.

$$Nu_{part} = (7 - 10\alpha_g + 5\alpha_g^2)(1 + 0.7\,\mathrm{Re}_p^{0.2}\,\mathrm{Pr}^{0.33}) + (1.33 - 2.4\alpha_g + 1.2\alpha_g^2)\,\mathrm{Re}_p^{0.7}\,\mathrm{Pr}^{0.33} \quad (7.18)$$

where $\mathrm{Pr} = C_{p,g}\mu_g / k_g$ is the Prandtl number, and the Reynolds number, Re_p, is

$$\mathrm{Re}_p = \frac{\rho_g \left|\vec{V}_g - \vec{V}_p\right| d_p}{\mu_g} \quad (7.19)$$

The heat transfer between gas and droplet in the presence of solids was analyzed by Buchanan (1994). The expression for the Nusselt number is

$$Nu_{drop} = \frac{2 + 0.6\,\mathrm{Re}_l^{*0.5}\,\mathrm{Pr}^{0.33}}{\left(1 + \dfrac{C_{p,g}(T_g - T_l)}{L}\right)^{0.7}} \quad (7.20)$$

where the effective Reynolds number Re_l^* is defined by

$$\mathrm{Re}_l^* = \frac{(\rho_g \alpha_g + \rho_p \alpha_p)\left|\vec{V}_g - \vec{V}_l\right| d_l}{\mu_g} \quad (7.21)$$

When the droplet collides with hot particles, a large amount of vapour is produced due to the strong heat transfer upon collision (Ge and Fan, 2006). Nayak et al. (2005) developed a phenomenological model to characterize the amount of heat transferred during the collision with vapour generation. It can be written as

$$\Delta E = \phi \frac{\pi}{6} d_p^3 \rho_{vapor} L \quad (7.22)$$

Here, the solid particle in contact with a droplet is assumed to get pushed back when vapour of volume ϕ times the particle volume is generated. The overall heat transfer from particles to droplets due to collisions can be estimated as a product of the collision frequency per unit volume and the energy transferred per collision (Nayak et al., 2005).

$$\hbar_{pl} = \phi \frac{1.5\alpha_p \alpha_l \rho_{vapor} L \left|\vec{V}_l - \vec{V}_p\right|}{(T_p - T_l) d_l} \left(1 + \frac{d_p}{d_l}\right)^2 \quad (7.23)$$

Finally, we have

$$\hbar_{drop,mix} = \hbar_{drop} + \hbar_{pl} \tag{7.24}$$

For the particles trapped inside the agglomerate, thermal equilibrium is assumed. To achieve the best accuracy of these models, the gas-film thermo-physical properties are evaluated at the reference temperature using the one-third rule (Sparrow and Gregg, 1958).

7.3.5 Spray evaporation

In the present study, we model the evaporative spray with a population balance model. In the spray, the number density of droplets $n(l;\vec{x},t)$ is a function of diameter l, spatial position $\vec{x}$ and time t. The diameter is usually referred to as an internal coordinate in contrast to spatial position and time, which are external coordinates. Consequently, the volume fraction of the liquid phase can be written as

$$\alpha_l = \int_0^\infty n(l;\vec{x},t)\frac{\pi}{6}l^3 dl \tag{7.25}$$

The transport equation for the number density is given by

$$\frac{\partial}{\partial t}\left[n(l;\vec{x},t)\right] + \nabla\cdot\left[n(l;\vec{x},t)\vec{V}_l\right] + \frac{\partial}{\partial l}\left[n(l;\vec{x},t)G\right] = S(l;\vec{x},t) \tag{7.26}$$

where $\vec{V}_l$ is the velocity of the liquid phase solved from the momentum equation, G is the droplet growth rate based on the diameter, defined as

$$G = \frac{\partial l}{\partial t} \tag{7.27}$$

The growth rate of the droplet size due to evaporation and agglomeration can be easily obtained with the assumption that both droplet and agglomerate are spherical. Hence, a simple correlation can be derived with geometric consideration:

$$G = \frac{2G_V}{\pi l^2} \tag{7.28}$$

where G_V is the growth rate of the droplet/agglomerate volume resulting from the mass transfer due to evaporation and agglomeration.

In equation (7.26), the source term $S(l;\vec{x},t)$ represents the changes in the droplet size distribution due to coalescence and breakup. It is usually written as

$$S(l;\vec{x},t) = B^c(l;\vec{x},t) - D^c(l;\vec{x},t) + B^b(l;\vec{x},t) - D^b(l;\vec{x},t) \qquad (7.29)$$

The $B^c(l;\vec{x},t)$ and $D^c(l;\vec{x},t)$ are the birth and death rates of the droplet due to coalescence, $B^b(l;\vec{x},t)$ and $D^b(l;\vec{x},t)$ are the birth and death rates of the droplet due to breakup. In the present modeling of evaporative thin spray, the phenomena related to coalescence and breakup of droplets are neglected for simplicity as these interactions are supposed to have negligible effect on the spray evolution (Chang and Zhou, 2003). We do not cover the details of the source terms due to coalescence and breakup of spray droplets as these phenomena are neglected in the current study. Hence, the right hand side of equation (7.26) becomes zero. However, the effects of coalescence and breakup of droplets can be investigated with appropriate models in future work.

To solve the general population balance equation, the most common approach is the discrete method, also known as the classes or sectional method. The basic idea of this method is to represent the continuous particle size distribution in terms of a set of discrete size classes or bins (Ramkrishna, 2000). Equation (7.26) can then be written in terms of the number density of each size bin as

$$\frac{\partial}{\partial t}\left[\rho_l N_i(\vec{x},t)\right] + \nabla\cdot\left[\rho_l N_i(\vec{x},t)\vec{V}_l\right] + \frac{\partial}{\partial l}\left[\rho_l N_i(\vec{x},t) G_i\right] = \rho_l S(l_i;\vec{x},t) \qquad (7.30)$$

where $N_i(\vec{x},t)$ is the number density of bin l_i, defined as $N_i(\vec{x},t) = \int_{l_i}^{l_{i+1}} n(l,\vec{x},t)dl$. By introducing the volume faction of each size bin $\alpha_{l,i} = N_i(\vec{x},t)V_i$, equations (7.30) can be converted to

$$\frac{\partial}{\partial t}\left(\rho_l \alpha_{l,i}\right) + \nabla \cdot \left(\rho_l \alpha_{l,i} \vec{V}_l\right) + \frac{\partial}{\partial l}\left(\frac{\rho_l \alpha_{l,i} G_i}{V_i}\right) = \rho_l V_i S(l_i; \vec{x}, t) \tag{7.31}$$

where $V_i = \pi l_i^3 / 6$ is the volume of the droplet size l_i. There are several schemes for the discretization of size bins as reviewed by Vanni (2000). A simple approach is to divide the droplets into bins such that the volume of each bin satisfied $V_{i+1} / V_i = 2^q$ where $q = 1, 2, ...$ and is referred to as the ratio factor.

7.3.6 Simulation setup

The governing equations and constitutive correlations in the above paragraphs are solved in Fluent 6.3. The proposed phenomenological heat and mass transfer models are incorporated into Fluent 6.3 with user-defined functions (UDF). In addition, species transport equations are solved for the vapour in the gas phase and the water in the droplet/agglomerate phase.

The problem is simplified as an axisymmetric two-dimensional problem. The domain of 2 m height and 0.095 m width is discretized with a non-uniform structured grid as illustrated in Figure 7-3. This domain is only a section of the riser since the spray has a minor effect on the flow upstream. The liquid spray is introduced from a nozzle of 15 mm diameter. The minimal size of a control volume near the spray nozzle is about 1 mm in radial direction and 5 mm in axial direction. Note that the full domain simulation of the riser is not performed for two reasons: Firstly, the computational cost of a full three-dimensional simulation of the flow in a riser would be extremely high. Secondly, accurate numerical simulation of the gas-solid flow in a riser is very difficult as several challenges exist in this field, for example, turbulence of the gas and solid phases and drag reduction due to cluster phenomena.

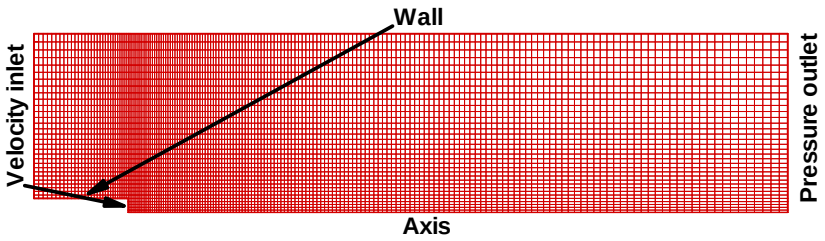

Figure 7-3. Grid and boundary conditions.

We perform a grid independence study of three grids with grid point numbers of 2000, 6150, and 24600. By evaluating the distributions of gas, liquid, and solid in the flow, it has been demonstrated that the grid number has only a small influence on the simulation results. In the following paragraphs, most of the simulations are carried out on the grid with 6150 grid points.

The parameters for numerical simulation are summarized in Table 7-1. Most of them are obtained from the experiment. Properties which are not listed in the table, for example, gas density and viscosity, are calculated with appropriate correlations. Studies for adjustable parameters used in the current model are performed and will be presented in the section on numerical simulation results.

Table 7-1. The experimental conditions for numerical simulation.

Parameter	**Description**	**value**
T_g	Gas temperature	573 K
T_p	Particle temperature	573 K
T_l	Liquid temperature	313 K
d_p	Diameter of particles	65 μm
d_l	Diameter of droplets	254 μm
ρ_p	Density of particles	1600 kg/m^3

Parameter	Description	value
ρ_l	Density of droplets	1000 kg/m^3
Q_{spray}	Spray volume flow rate	60 l/m
u_l	Spray velocity	23.6 m/s
e_p	Restitution coefficient	0.95

The boundary conditions are also illustrated in Figure 7-3. The axis of symmetry is treated with the axis boundary condition, where the velocity gradients for all phases and the granular temperature gradient along the radial direction are zero. For the inlet boundaries of the gas-solid flow and the liquid spray, the velocity and volume fraction are set based on available experimental measurement or calculation from experimental conditions. In the experiment, the solid volume fraction and solid flux at different heights inside the riser were measured via capacitance probes (Gehrke 2008). With these measurements, the velocity of the solid phase can be calculated. Since a direct measurement of the gas velocity is very difficult (Moran and Glicksman, 2003), it is estimated from the slip velocity according to the well-known Richardson-Zaki correlation by assuming the balance between the drag and gravity force, as follows:

$$\frac{u_{slip}}{u_t} = \alpha_g^{n(\mathrm{Re})-1} \tag{7.32}$$

where u_t is the terminal velocity of the particle and

$$n(\mathrm{Re}) = \begin{cases} 4.65 & \mathrm{Re}_t < 0.2 \\ 4.35\,\mathrm{Re}_t^{-0.03} & 0.2 \le \mathrm{Re}_t < 1 \\ 4.45\,\mathrm{Re}_t^{-0.1} & 1 \le \mathrm{Re}_t < 500 \\ 2.4 & \mathrm{Re}_t > 500 \end{cases}$$

For example, the inlet boundary conditions of solid volume fraction and velocities determined with this procedure for superficial gas velocity of 10 m/s are shown in Figure 7-4.

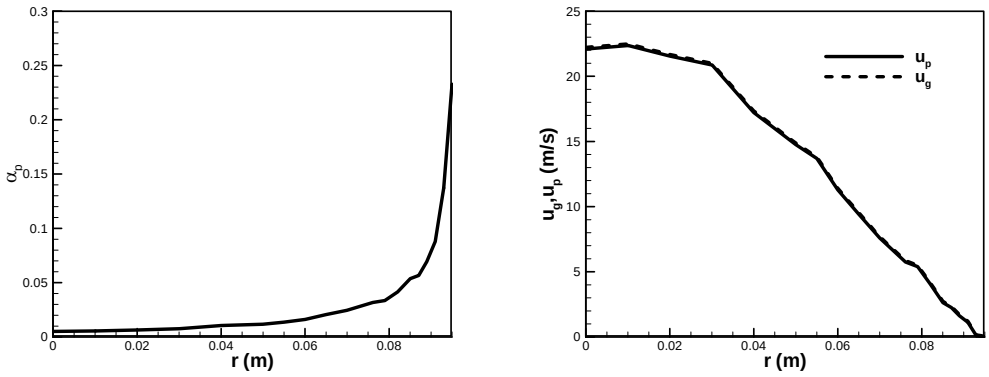

Figure 7-4. Inlet boundary conditions of solid volume fraction (left) and velocities of gas and particles (right) calculated based on experimental measurements.

The droplet exit velocity from the nozzle is assumed to be equal to the theoretical maximum discharge velocity corresponding to the total pressure difference across the nozzle (Ronsse et al., 2007).

$$u_{spray} = \sqrt{\frac{2\Delta P}{\rho_l}} \tag{7.33}$$

The inlet volume fraction of the liquid spray is then calculated from the liquid volume flow rate of the spray and the average droplet size reported in the experiment is used to specify the inlet boundary conditions for the population balance equations.

A non-slip boundary condition for the gas phase is set for all the walls. For the solid phase, the partial slip boundary condition suggested by Johnson and Jackson (1987) is employed. The free slip boundary condition for the droplet phase is set for the wall. As for the top outlet boundary, the pressure outlet is used, which allows the particles and droplets to leave the bed freely.

7.4 RESULTS AND DISCUSSION

7.4.1 Comparison with the experiment

Two cases with different superficial gas velocities of 5 and 10 m/s in the riser are simulated and the numerical results are compared with the available experimental measurements for a hollow cone spray. Inlet boundary conditions for gas, solid, and liquid spray are set based on the procedure described above. The spray velocity is 27 m/s, and the droplet volume fraction is 0.004 for both cases. For the hollow cone single fluid spray, the hollow cone angle is set to be 60 degree for both cases according to the experiment. The droplet diameter $d_{v,90}$ at the spray inlet reported in the experiment was 269 μm. This is defined such that 90% of the total liquid volume is in drops of diameter smaller than $d_{v,90}$ (Lefebvre, 1989). It is larger than the Sauter mean diameter usually used in the numerical simulations. A droplet size distribution shown in Figure 7-5 is used in the simulation, which gives a mean droplet size of 235 μm and $d_{v,90}$ of 254 μm (Lefebvre, 1989).

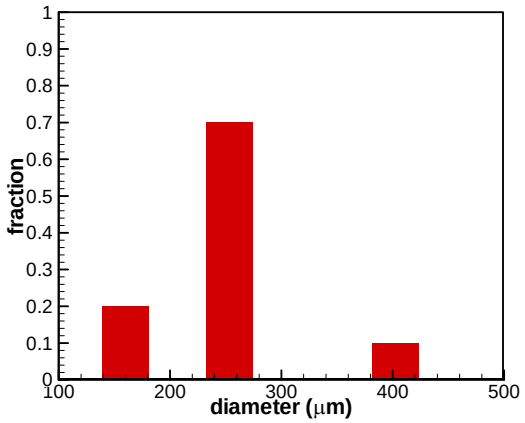

Figure 7-5. Droplet size distribution at the spray inlet used in numerical simulations

Figure 7-6 shows the contours of the field variables: the liquid volume fraction, solid volume fraction, mass fraction of steam, and gas and solid temperatures, for the spray injection into the

riser with a superficial gas velocity of 5 m/s. A typical flow pattern of the hollow cone spray can be observed in Figure 7-6 (a). The spray expands after leaving the inlet. However, the spray loses its expansion trend in the far region from the inlet because of the interaction with the co-current gas-solid flow. The liquid volume fraction decreases due to evaporation. It should be noted that the radial distance shown in Figure 7-6 is stretched, and the angle observed in the figure is larger than it should be. In the vicinity of the spray inlet, the spray droplets are soon heated up to the boiling point. Then the spray starts to evaporate and a large amount of vapour is generated, as shown in Figure 7-6 (c). In many systems, the steam concentration distribution is critical to the determination of the chemical reactions in the reactor. Here, it is revealed that the excessive vapour production resulting from the rapid droplet evaporation is mixed into the surrounding gas stream, which not only changes the local velocities of gas and solids, but also dilutes the solids flow, see Figure 7-6 (b). Particles are pushed off to the wall by spray droplets through collisions and the solids concentration inside the hollow spray cone is low. In the annulus, the solids concentration decreases along the height because of the dilution effect of the vapour. Due to the limitation of the axisymmetric assumption used in the current simulation, the radial movement of solids is restricted and an extremely low solids concentration along the axis is predicted. In the spray region, both gas and solids cool down as they transfer sensible and latent heat to the droplets, as shown in Figure 7-6 (d) and (e). The mixing of the gas-solid at a high temperature and the steam at a low temperature leads to the formation of a low temperature region, which is in line with the vapour concentration. Again, a low temperature along the axis is predicted for both gas and solid temperature distributions due to the low solids concentration there.

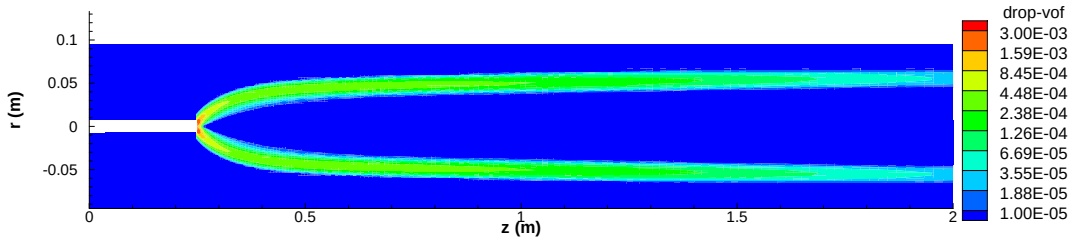

(a)

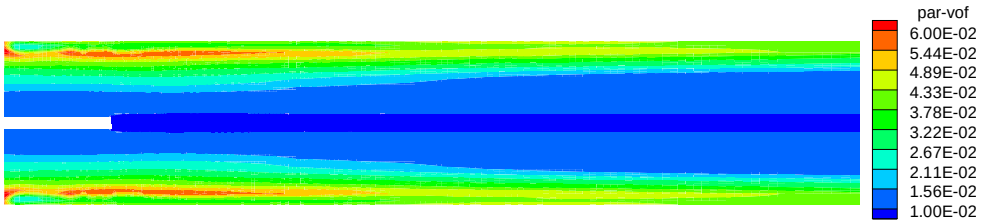

(b)

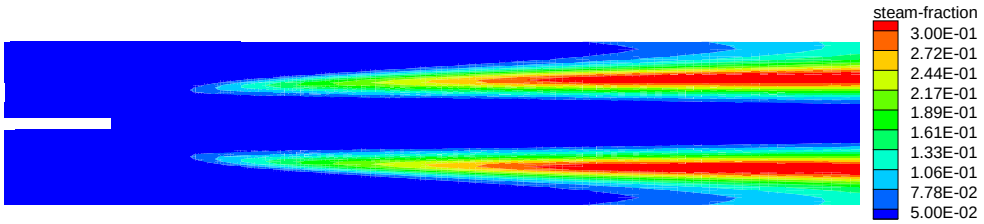

(c)

(d)

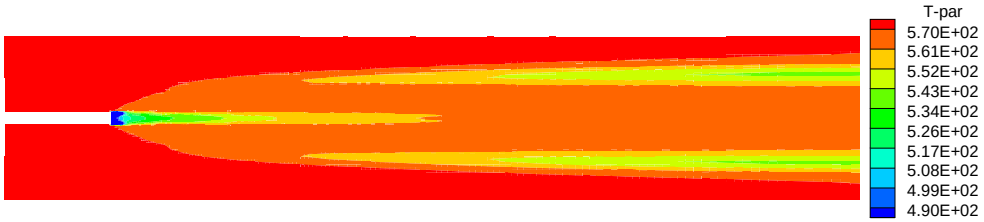

(e)

Figure 7-6. Contours of liquid volume fraction (a), solid volume fraction (b), steam mass fraction (c), gas temperature (d), and solid temperature (e) for the case with a superficial gas velocity of 5 m/s.

Results for the spray injection into the riser with a superficial gas velocity of 10 m/s are shown in Figure 7-7. Phenomena similar to those in the previous discussion are observed in the figure. However, there are some differences. Compared with the spray shown in Figure 7-6 for the riser with a superficial gas velocity of 5 m/s, the spray has a larger expansion for the case with a superficial gas velocity of 10 m/s. This is mainly because the solids concentration is higher in the core region when the riser is operated with a low superficial gas velocity while the solids circulation flow rate maintains constant. This is shown in Figure 7-8, where the solid volume fraction profiles measured in the experiment at the inlet are shown for both cases. As solid particles play an important role in the evaporation of spray droplets, less vapour is generated and its dilution effect on the solids flow weakens accordingly. Similar influence on the temperature distributions can be observed.

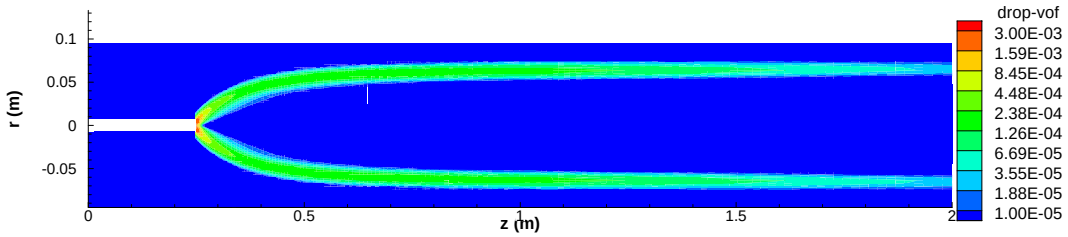

(a)

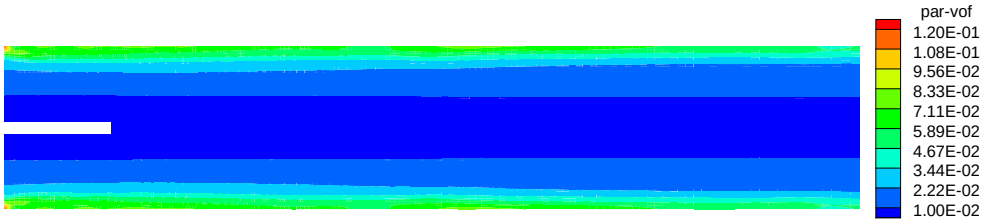

(b)

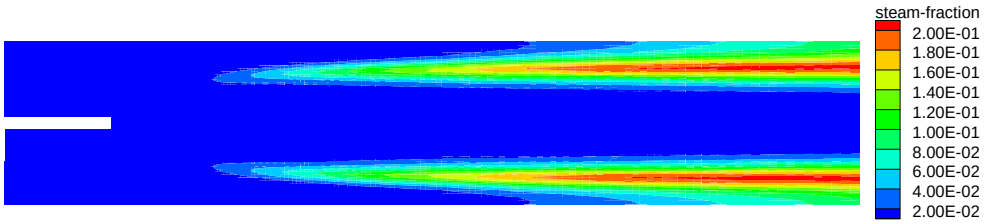

(c)

(d)

(e)

Figure 7-7. Contours of liquid volume fraction (a), solid volume fraction (b), steam mass fraction (c), gas temperature (d), and solids temperature (e) for the case with a superficial gas velocity of 10 m/s.

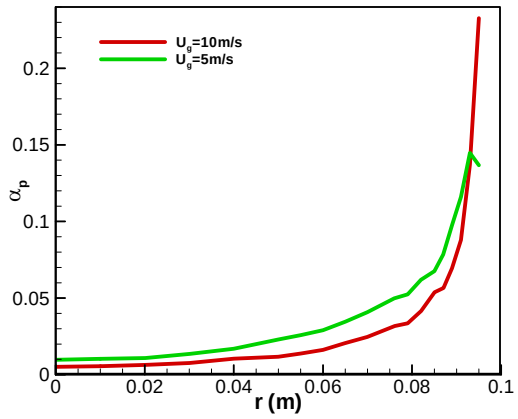

Figure 7-8. Solid volume fraction at the inlet for different superficial gas velocities.

In the experiment, the spray borderline was detected from both the temperature profile and the solid concentration profile measured with the thermocouple and the capacitance probe, respectively (Gehrke and Wirth, 2008). The signal measured by the capacitance probes characterized the existence of particles and water. It was unfortunately not possible to split the raw signal into "solid" and "liquid" parts. However, a steep rise in the signal was detected at the spray borderline as the liquid led to a significantly higher signal change than the solids alone. To compare with the experimental measurement of the spray borderline, the liquid volume fraction profile 140 mm above the spray nozzle is compared with the spray profile measured by the capacitance probes in Figures 7-9 and 7-10 for these two superficial gas velocities. To facilitate direct comparison, magnitudes of both the experimental data and numerical results are scaled. In these figures, the position and width of the peak region can be used to characterize the spray borderline and spray width. From these two figures, reasonable agreement can be observed.

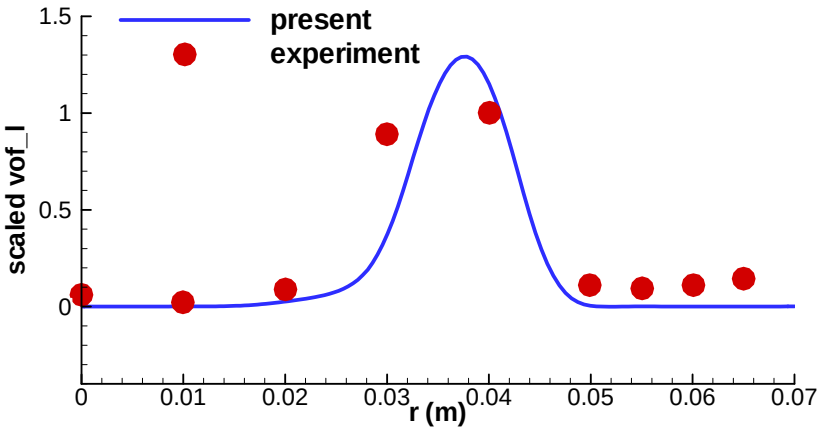

Figure 7-9. Comparison of spray profiles at 140 mm above spray nozzle for superficial gas velocity of 5 m/s.

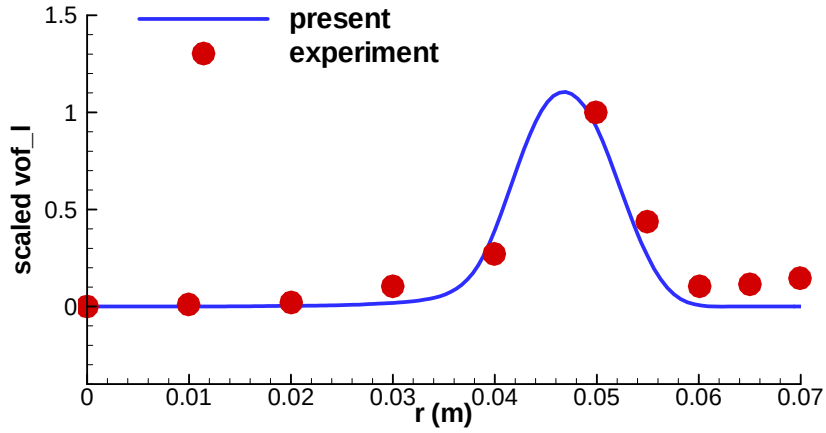

Figure 7-10. Comparison of spray profiles at 140 mm above spray nozzle for superficial gas velocity of 10 m/s.

In the experiments, the spray length was about 1 m (Gehrke and Wirth, 2007a). The current numerical simulation predicts a spray evaporation length of 2 m or so, which is much higher than the experimental measurement. The reasons are briefly discussed here. As stated in the previous paragraphs, the average solid volume fraction and velocity are used as the inlet boundary condition in the simulation. An axisymmetric steady gas-solid flow is assumed in the riser. With

this assumption, the radial movement of gas and solids across the centre of the riser are prevented. These movements are very strong, though the radial movements from different directions are counteracted in a time-averaged sense. Consequently, the collisions between the solids and spray droplets resulting from crossflow of solids are not correctly modeled as the collision frequency is calculated with the time-averaged solids concentration and velocity field. This has no influence on the momentum exchange in the time-averaged sense. However, it has a very significant impact on the heat transfer and evaporation as the contributions from the radial movements of particles from different directions cannot be cancelled as those field variables are scalars. The heat transfer between spray droplets and the surrounding gas-solid mixture is greatly enhanced by the radial solids movement, hence accelerating the evaporation. This leads to the high spray evaporation length predicted in the current simulation. Note that the heat transfer rate does not affect the spray expansion, especially in the first half of the spray. This is demonstrated below. In the computation, the values of 0.5, 0.3, 0.05, and 14 are used respectively for adjustable parameters - the restitution coefficient e_{lp}, correction factor φ, particles collection efficiency γ, and parameter ϕ. The influences of these parameters are discussed in the next section with respect to the spray expansion and the evaporation length.

7.4.2 Parametric study

7.4.2.1 Effect of φ and e_{lp}

In modeling the interaction between droplets and particles, restitution coefficient e_{lp} and correction factor φ are not well defined due to the absence of experimental or theoretical evidence. In **Appendix A**, the value of 0.4 for φ is based on the simulation of Ge and Fan (2006) simulation for the collision between a 1.2 mm droplet and a 1.2 mm particle. Hence, a value around 0.4 is suggested for φ in the current study. Based on the Ge and Fan's numerical simulation of a collision between a moving droplet and a hot particle, the restitution coefficient

can be estimated to be 0.58 for that specific condition. In addition, according to the experimental investigations of the interaction of a small liquid droplet impinging on a rigid surface above the Leidenfrost temperature, the reported restitution coefficients are dependent on the Weber number, and are in the range of 0.4-0.8 (Karl and Frohn, 2000) and 0.2-0.6 (Hatta et al., 1995) for the conditions tested.

A parametric study is necessary to assess the influence of these parameters on the flow hydrodynamics. Since these two parameters have a similar effect on the inter-phase drag coefficient, for simplicity, the parametric study is performed for only one parameter. Here, e_{lp} is fixed at 0.5 and simulations for different values of φ are performed. The liquid volume fraction distributions for different values of φ are shown in Figure 7-11. The effect of φ is significant as it increases from 0.2 to 0.5. The expansion angle of the spray, which determines the effective interaction zone of the spray, decreases greatly with increasing φ. As discussed in **Appendix A**, the higher the value of φ, the more momentum is exchanged during the collision between a droplet and a particle. However, because of the low volume fraction of the droplet phase in the riser, φ has only a minimal effect on the solid volume fraction distribution.

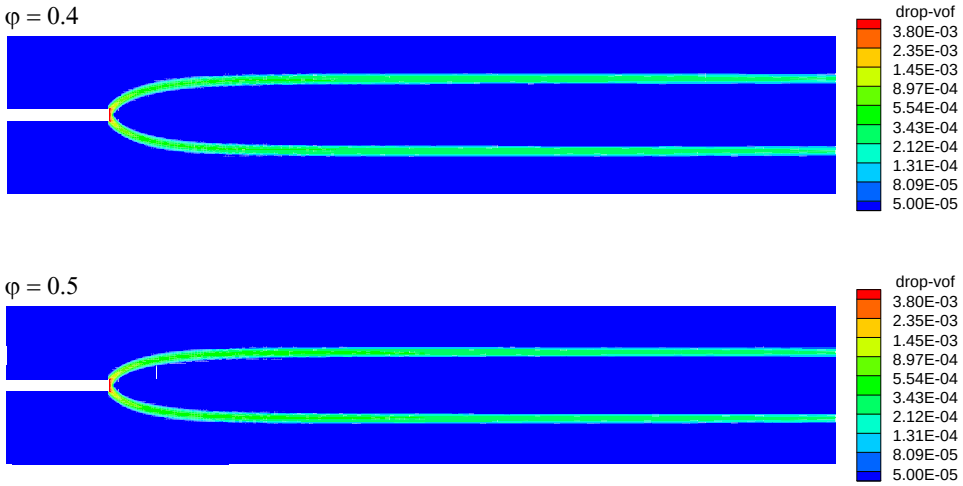

Figure 7-11. Liquid volume fraction distributions for different values of φ. (Simulation conditions: $d_p = 160$ μm; $e_{ls} = 0.5$; $\gamma = 0$; $\phi = 14$).

7.4.2.2 Effect of γ

The particle collection efficiency γ characterizes the probability of a particle to be trapped by a droplet during collision. The particle collection efficiency is expected to be small when strong evaporation takes place. Particles trapped by a single droplet can form an agglomerate. Therefore, to some extent, this parameter represents the agglomeration tendency. Moreover, it affects the inter-phase momentum transfer between the droplet and solid phases as shown by equation (7.1).

Figure 7-12 shows the liquid volume fraction distributions for different γ. In the present model, the droplets and agglomerates are modelled as a mixture phase with two different species. For $\gamma = 0$, there is no coalescence between droplets and particles upon collision. Due to evaporation, the droplet size decreases when travelling in the riser. This is reflected by the decreasing volume fraction along the height. For $\gamma = 0.05$ and 0.1, a certain number of particles are trapped in the droplet phase in the form of agglomerates. Hence the volume fraction of the droplet phase tends to increase slightly, which comprises the decrease caused by evaporation. In the figure, we can

also observe that different values of γ have negligible influence on the spray expansion. Without further experimental or theoretical evidence, we assume γ to be 0.05 in our simulations.

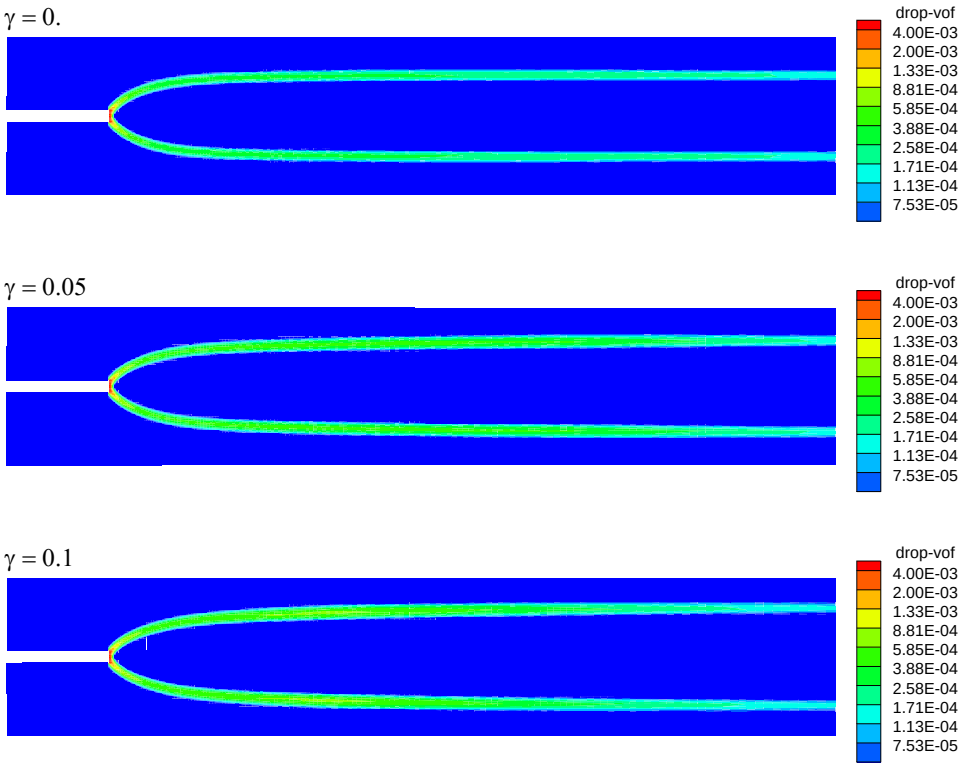

Figure 7-12. Liquid volume fraction distributions for different values of γ. (Simulation conditions: $d_p = 160$ μm; $e_{ls} = 0.5$; $\varphi = 0.3$; $\phi = 14$).

7.4.2.3 Effect of ϕ

When a hot solid particle collides with a large liquid droplet, the vapour generated at contact tries to push the solid particle away from the drop. The actual physics of this process are very complex and the amount of vapour generated during this process is believed to depend on the thermodynamic properties of the liquid, vapour, and solid, such as the latent heat of the liquid, heat capacity, and conductivity for each phase, as well as the temperature difference and

collision velocity. An analytical expression for this parameter is not possible in the absence of independent experimental information. Nayak et al. (2005) introduced the parameter ϕ to characterize the amount of vapour and suggested treating it as an adjustable parameter.

Figure 7-13 shows the liquid volume fraction distributions for a broad range of ϕ: 5, 14, 50, and 100. However, even for $\phi = 100$, the mass of vapour generated during the collision is less than 1% of the mass of droplet. It is obvious that the value of ϕ affects the evaporation of the droplet. For high ϕ, more vapour is generated during the collision and the droplet evaporates faster, leading to a decreased spray evaporation length. However, it has little effect on the spray expansion as illustrated in Figure 7-13. This is because the spray boundary is mainly determined by the interaction between the liquid spay and the gas-solid flow through the inter-phase drag force, while fast evaporation only indirectly affects the behavior through decreasing droplet size in the drag correlations. Without appropriate experimental data to determine the value of ϕ, the value of 14 suggested by Nayak et al. (2005) is used in our simulations since the particles in our study are similar to those in their work.

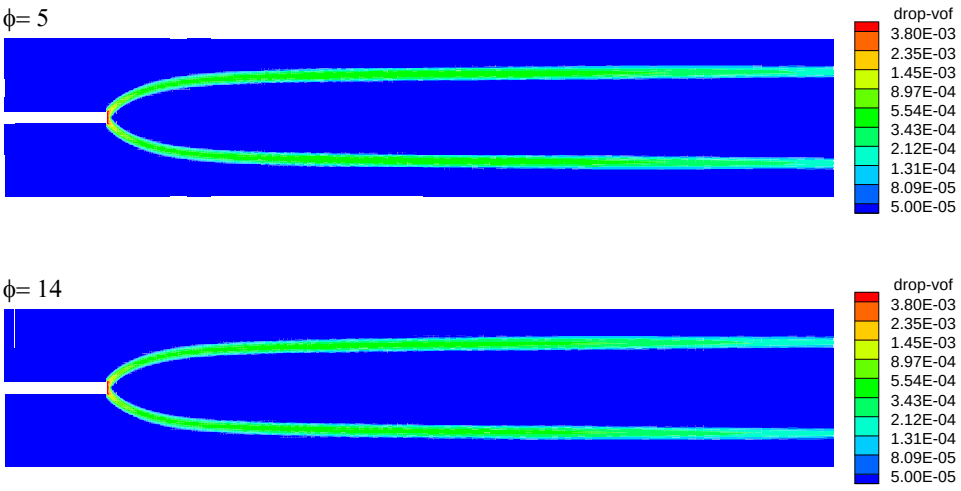

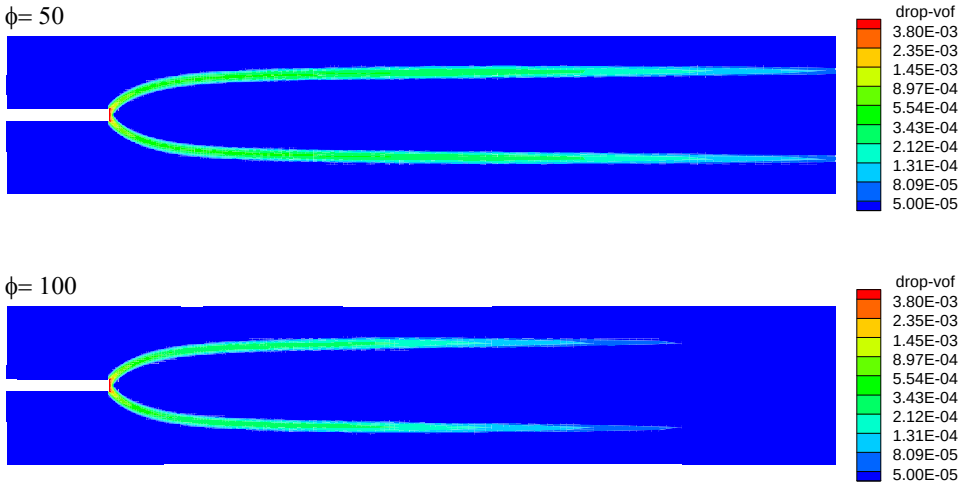

Figure 7-13. Liquid volume fraction distributions for different values of ϕ (Simulation conditions: $e_{ls} = 0.5;\ \varphi = 0.3;\ \gamma = 0.05$)

7.4.3 Influence of the operating parameter

7.4.3.1 Effect of droplet diameter

In the experiment, the droplet diameter $d_{v,90}$ of 269 μm was reported for the hollow cone spray nozzle (Gehrke and Wirth, 2008). It is larger than the Sauter mean diameter commonly used in the numerical simulations (Lefebvre, 1989). Since no information on the droplet size distribution is reported, it is assumed to be uniform at the spray inlet, and effect of droplet size on the spray behaviour in the riser flow is investigated. Three droplet diameters of 100, 160, and 253 μm are simulated and the liquid volume fraction distributions for these cases are presented in Figure 7-14. It can be observed that the spray expansion is strongly influenced by the droplet diameter at the spray inlet. For large droplets, the high inertia enables deep penetration into the gas-solid flow, causing a wide spray expansion. This result is also consistent with our finding in **Chapter 6**. It is interesting to note that the spray evaporation length tends to decrease for a large droplet size because the solids concentration in the annulus region of the riser is very high. As a result,

the evaporation of droplets is greatly enhanced as the spray expands into the dense annulus region.

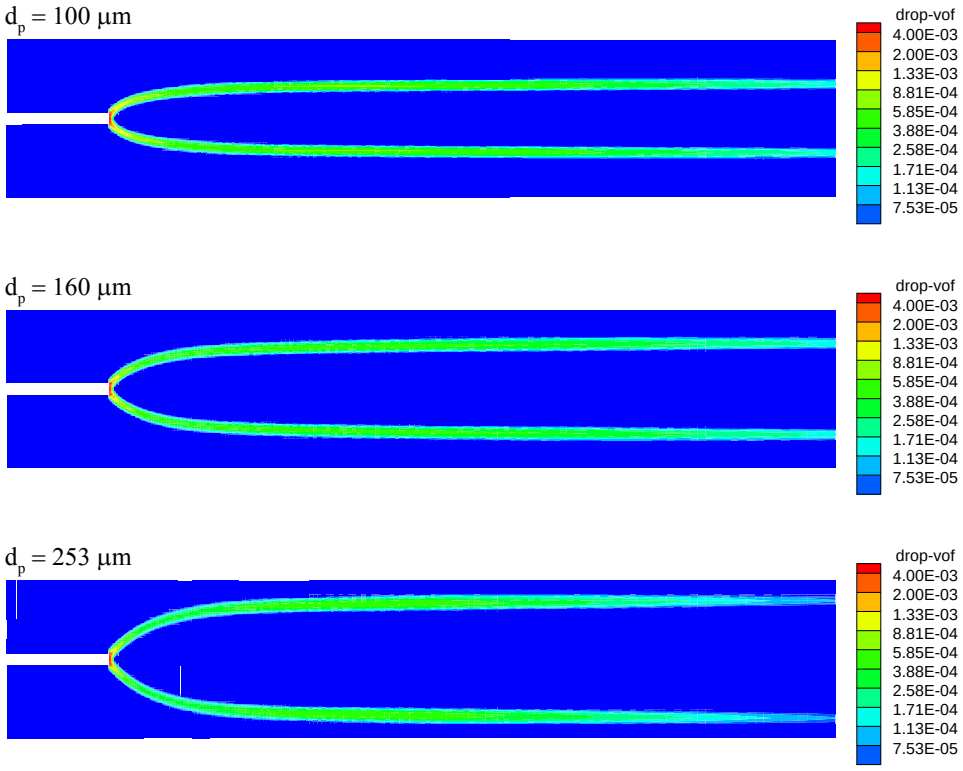

Figure 7-14. Liquid volume fraction distributions for different droplet sizes. (Simulation conditions: $e_{ls} = 0.5;\ \varphi = 0.3;\ \gamma = 0.05;\ \phi = 14$).

7.4.3.2 Effect of bed temperature

The effect of bed temperature is portrayed for temperatures of 473, 573, and 673 K in Figure 7-15. When the bed temperature increases, the evaporation of droplets is enhanced and the spray evaporation length decreases as a consequence. It can be observed that the bed temperature has negligible influence on the spray expansion in the co-current gas-solid flow. It should be noted that the solid circulation rate is kept constant in the current simulations, while the bed temperature is expected to affect the solid circulation rate in a circulating fluidized bed as the properties of fluidizing gas change. To some extent, it would affect the spray behaviour as well.

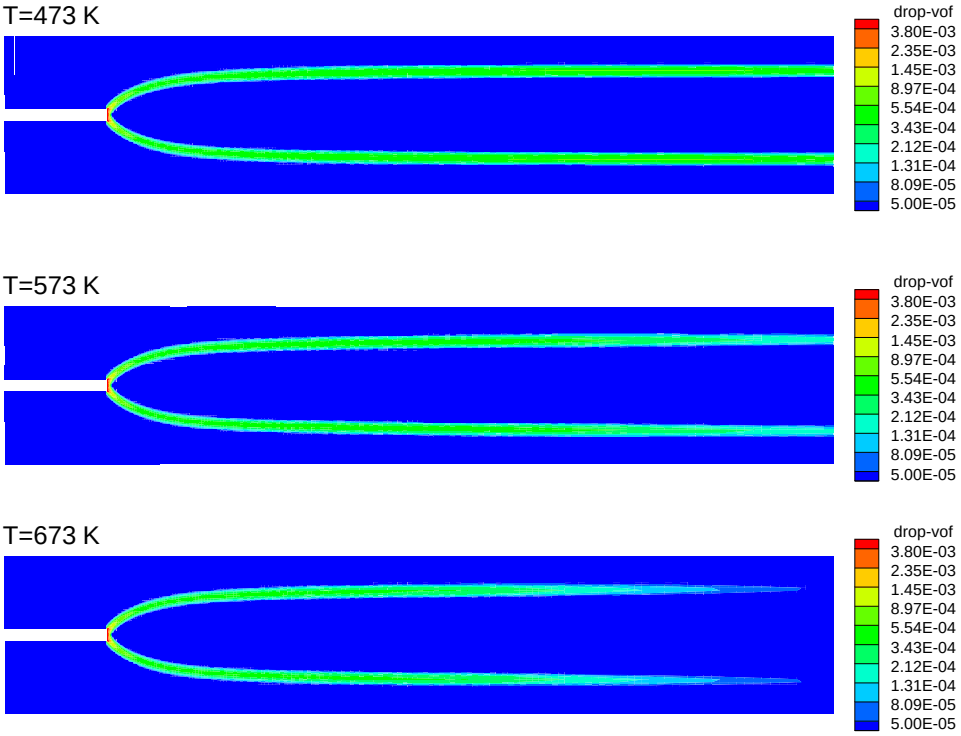

Figure 7-15. Liquid volume fraction distributions for different bed temperatures. (Simulation conditions: $e_{ls} = 0.5;\ \varphi = 0.3;\ \gamma = 0.05;\ \phi = 14$).

7.4.3.3 Effect of spray angle

Figure 7-16 shows the liquid volume fraction distributions in the gas-solid flow for the hollow cone spray with different spray opening angles of 60, 90, and 120 degrees. The spray opening angle has more impact on the spray expansion in the region close to the spray inlet. The spray expansion slightly increases for wide-spray angles, and droplets interact with more particles in the annulus region of the riser. As a result, the spray evaporation lengths decrease for wide spray angles.

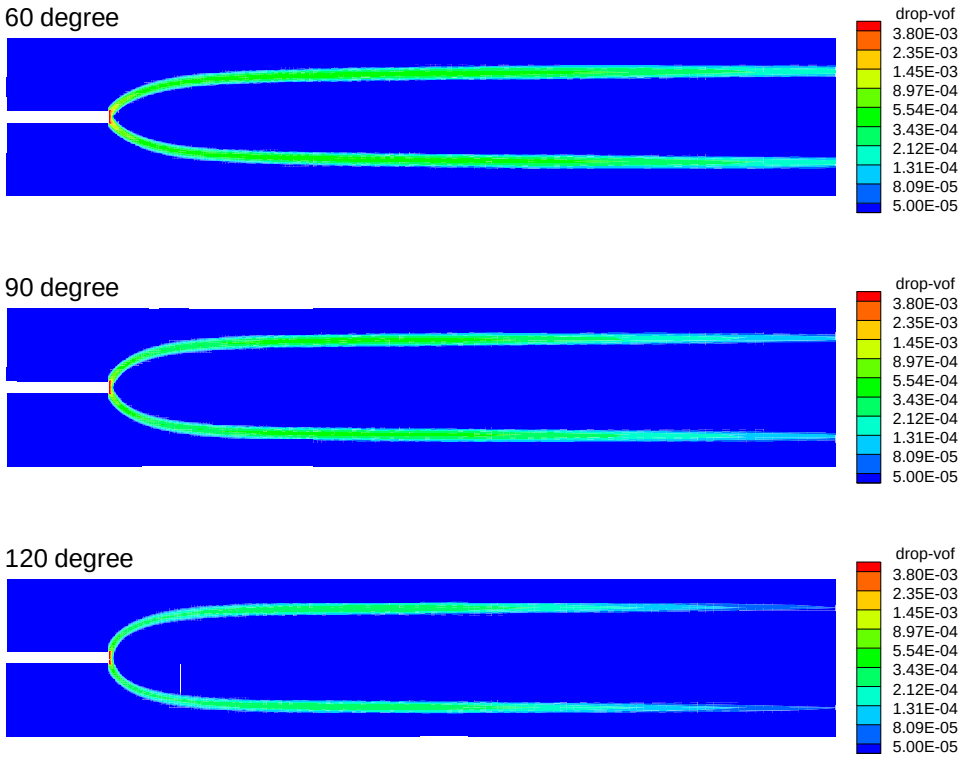

Figure 7-16. Liquid volume fraction distributions for different spray opening angles. (Simulation conditions: $e_{ls} = 0.5;\ \varphi = 0.3;\ \gamma = 0.05$).

7.5 SUMMARY

In this chapter, a model is developed to investigate the hydrodynamics of an evaporative spray in the hot gas-solid flow. In this model, sub-models for the interaction between droplets and particles including the momentum exchange and heat and mass transfer are proposed based on available experimental observations, as well as the numerical results of Ge and Fan (2006). Several parameters are introduced to model the complex interaction between the cold evaporative spray and the hot gas-solid flow.

Simulation of an evaporative water spray through a hollow cone spray nozzle in a riser operated at an elevated temperature is conducted with appropriate assumptions. Comparison with the

available experimental measurement of the spray expansion is performed, and reasonable agreement is obtained. Due to the limitation of the axisymmetric assumption used in our simulation, the evaporation length of the spray is over-predicted. To accurately simulate this problem, a three-dimensional simulation of the whole system, not feasible with our current computational resources, is suggested for the future. In addition, the influences of several adjustable parameters in the model are investigated in the parametric study, and possible values are suggested for those parameters. Finally, the effects of operating conditions such as droplet size, bed temperature, and spray angle are evaluated with the current model.

Chapter 8. CONCLUSIONS AND RECOMMENDATIONS

8.1 SUMMARY AND CONCLUSIONS

Numerical simulations of the gas/spray jet interaction with fluidized beds have been carried out for different configurations. It is shown that CFD codes can be used to model various two-phase and three-phase flows. The work includes two parts: gas jets in bubbling fluidized beds and the liquid spray in gas-solid flows.

8.1.1 Gas jets in bubbling fluidized beds

Three-dimensional numerical simulations are performed for single and multiple gas jets into bubbling fluidized beds. Key conclusions are as follows:

- Three-dimensional numerical simulation is conducted for a single horizontal gas jet issuing into a cylindrical gas-solid fluidized bed of FCC particles. By extending the model of McKeen and Pugsley (2003a), a non-uniform scale factor on Gibilaro's inter-phase drag model taking into account the effect of agglomerates of fine FCC particles, is incorporated into the numerical tool. The predicted bed heights and voidage distribution are consistent with experimental observations. The jet penetration lengths and expansion angles of different jet velocities are in good agreement with published experimental data and empirical correlations. This is encouraging with respect to the validity of this scaled drag model for the simulation of FCC fluidized beds. This model can be incorporated efficiently into numerical tools to simulate FCC particles operated in the bubbling fluidization regime.

- Single and multiple horizontal gas jets in a rectangular bubbling fluidized bed of coke particles are studied numerically. Various jet velocities and jet arrangements were simulated. Our numerical predictions agree well with experimental trends and observations. The interactions between the gas jet and surrounding gas, solids, bubbles, and other jets are also studied numerically. Ultimately, a better understanding of the jet behaviour is achieved through these numerical simulations.

- The influence of the secondary gas injection on the flow hydrodynamics in a bubbling fluidized bed is examined. It is shown that secondary gas injection can strongly affect the hydrodynamics above the injection level if the secondary injection flow rate is high enough, while its effect is nearly negligible below the injection level. According to the investigations of voidage and velocity distribution resulting from the secondary gas injection, the jet penetration depth plays an important role in affecting the bed hydrodynamics. When jets penetrate deep into the bed, it is found that the introduction of a secondary gas injection can promote solids circulation inside the bed by bringing more particles upward into the core region. However, at higher jetting flow rates and deeper penetrations, slugging tends to take place, which may lead to the gas bypassing through the bed. In our simulations, a decrease in mean bubble size is observed for low-flow-rate secondary gas injections, and it is more significant when the secondary gas is injected through several jets with a moderate penetration depth. This decrease in bubble size leads to improved gas-solid contacting; hence, it can be used to increase the conversion for a mass-transfer limited reaction.

- The mixing of secondary gas with bed materials is studied by introducing tracer gas from secondary injections into the bubbling fluidized bed. To understand the mixing behaviour, both unsteady and steady results are analyzed. At the injection level, the tracer distribution is non-uniform. Within a short distance above the injection, the tracer becomes uniformly distributed. Gas back-mixing is observed in all simulations, prominent near the wall due to

downward flow of solids. For the cases studied, gas back-mixing tends to decrease as the secondary gas flow rate increases. For an identical secondary gas flow rate, it has been demonstrated that better contacting between the tracer gas and solid particles is achieved when the secondary gas is injected through a distributed jet arrangement than for a single jet.

8.1.2 Spray in fluidized beds

To study the liquid spray in some gas-solid systems, several experimental setups are simulated with appropriate assumptions and models. Key conclusions are as follows:

- For low-flow-rate bottom sprays into a flat-based spouted bed with a draft tube, the interaction between spray droplets and particles is modeled as coalescence upon collision, and the dispersion of wetted particles is described with a transport equation. The effect of liquid spray on the solid volume fraction and velocity in the draft tube is analyzed. Similar to the experimental observations, it is shown that there is no significant effect on the particle volume fraction and velocity profiles. As the liquid spray rate increases, the effect of liquid spray becomes evident in the central core region, especially in the particle velocity profiles.

- Three-dimensional simulations are performed for an evaporating gas-liquid spray into a gas-solid crossflow. Appropriate models are chosen to model the interactions between evaporative spray droplets and particles, as well as inter-phase heat and mass transfer, and careful comparison with available experimental data is performed step by step. General features of the evaporative spray and qualitative trends are predicted. It is found that particles affect the spray structure in terms of the evaporation length, cross sectional shape of spray jet, spray-bending angle, and expansion angle. The spray evaporation length increases with jet velocity and inlet droplets size and decreases with increasing solids loading in the crossflow. In addition, evaporation plays an important role in affecting the flow behaviour.

- A more complicated model is developed for the hydrodynamics of the evaporative spray in a hot gas-solid flow. In this model, the phenomenological sub-models for the interaction between the droplet and particles, including momentum exchange and heat and mass transfer are proposed based on available experimental observations and numerical simulations in the literature. Several parameters are introduced to model the complex interaction between the cold evaporative spray and the hot gas-solid flow. Simulation of an evaporative water spray through a hollow cone spray nozzle in a riser operated at an elevated temperature is conducted with appropriate assumptions. Preliminary comparison with available experimental measurements of spray expansion is performed, and reasonable agreement is obtained. The influences of the adjustable parameters in the model are investigated in a parametric study, and appropriate values for those parameters are suggested. In addition, the effects of operating conditions such as droplet size, bed temperature, and spray angle are evaluated with the current model, and reasonable trends are predicted. It is demonstrated that the numerical simulations with the proposed models are capable of shedding some light on the details of the evaporative spray in gas-solid flows to provide better understanding. With sufficient computational resources, the numerical simulation could be used to design and optimize gas/spray injection in fluidized bed reactors.

8.2 ORIGINAL CONTRIBUTIONS

- Three-dimensional numerical simulations of horizontal gas jets in a fluidized bed are conducted. This is the first three-dimensional numerical study on horizontal gas jets in fluidized beds in the published literature.

- The interactions between the gas jet and surrounding gas, solids, bubbles, and other jets that are difficult to investigate in experiments are studied numerically. A better understanding of the interaction between the horizontal gas injection and the fluidized beds from hydrodynamics and

mixing points of view has been achieved through numerical studies, which has not been thoroughly studied in the previous numerical work in the literature.

- Attempts are made to simulate the non-evaporative and evaporative sprays in different gas-solid systems with available models. Some new models are proposed for this purpose. Our models focus on the direct interactions between droplets and particles, such as momentum exchange and heat transfer. The predictions agree reasonably well with the experimental measurements. Overall, despite some remaining questions in the modeling, we have been able to shed some light on the gas/spray jet interaction with different fluidized bed systems.

- The current study highlights areas needing further investigation, such as scale-up, the mechanism of droplet-particle collision over the Leidenfrost temperature, and agglomeration. To validate the current CFD models, comparison with more independent experiments is needed (Grace and Taghipour, 2004).

8.3 RECOMMENDATIONS

Several future research topics on jet-bed interaction are suggested here:

Scale-up study. Very commonly in the literature, both experiments and numerical simulations are for small-scale systems. Although the conclusions on jet-bed interaction from small-scale systems may be also applicable to large industrial scale plants, some investigations on scale-up are required.

Agglomeration. In the current study, agglomeration is neglected in most simulations. However, it is believed to be vital in many industrial applications, such as the fluid coking proces and coating. Therefore, a study of agglomeration could have practical significance.

Droplet-particle collision over the Leidenfrost temperature. The fundamental mechanisms of droplet-particle collision over the Leidenfrost temperature are far from being fully understood. Very careful collision experiments or detailed numerical simulations on droplet-particle collision would be beneficial.

Extension of the current models. The models presented in this research are only an attempt to describe the complex phenomena of evaporating spray into a hot gas-solid flow. Some assumptions introduced into the models need further investigation to justify their applicability, and parameters used in the model need to be measured in carefully designed experiments.

REFERENCES

Adegoroye, A., Paterson, N., Li, X., Morgan, T., Herod, A.A., et al, (2004). The characterisation of tars produced during the gasification of sewage sludge in a spouted bed reactor. Fuel, 83,(14-15) 1949-1960.

Ahmadi, G., and Ma, D., (1990). A thermodynamical formulation for dispersed multiphase turbulent flows.1. Basic theory. International Journal of Multiphase Flow, 16,(2) 323-340.

Al-Sherehy, F., (2002). Distributed addition of gaseous reactants in fluidized beds. PhD thesis. University of British Columbia, Vancouver.

Al-Sherehy, F., Grace, J.R., and Adris, A.E., (2004). Gas mixing and modeling of secondary gas distribution in a bench-scale fluidized bed. AIChE Journal, 50,(5) 922-936.

Anderson, T.B., and Jackson, R., (1967). A fluid mechanical description of fluidized beds. Industrial & Engineering Chemistry Fundamentals, 6,(4) 527-539.

Anderson, T.B., and Jackson, R., (1969). A fluid mechanical description of fluidized beds - comparison of theory and experiment. Industrial & Engineering Chemistry Fundamentals, 8,(1) 137-144.

Ariyapadi, S., Berruti, F., Briens, C., McMillan, J., and Zhou, D., (2004). Horizontal penetration of gas-liquid spray jets in gas-solid fluidized beds. International Journal of Chemical Reactor Engineering, 2,(A22)

Ariyapadi, S., Holdsworth, D.W., Norley, C.J.D., Berruti, F., and Briens, C., (2003). Digital X-ray imaging technique to study the horizontal injection of gas-liquid jets into fluidized beds. International Journal of Chemical Reactor Engineering, 1,(A56)

Arsenijevic, Z.L., Grbavcic, Z.B., and Garic-Grulovic, R.V., (2004). Drying of suspensions in the draft tube spouted bed. Canadian Journal of Chemical Engineering, 82,(3) 450-464.

Atkinson, J.H., and Bransby, P.L., (1978). The Mechanics of Soils: An Introduction to Critical State Soil Mechanics. McGraw-Hill, pp. 375.

Aulton, M., Aulton, M., Cole, G., Cole, G., and Hogan, J., (1995). Introduction and overview of pharmaceutical coating. In: Pharmaceutical Coating Technology, pp. 1 - 5.

Behie, L.A., Bergougn.Ma, Baker, C.G.J., and Bulani, W., (1970). Jet momentum dissipation at a grid of a large gas fluidized bed. Canadian Journal of Chemical Engineering, 48,(2) 158-161.

Benjelloun, F., Liegeois, R., and Vanderschuren, J., (1995). Penetration length of horizontal gas jets into atmospheric fluidized beds. Presented at Fluidization VIII: Proceedings of the Eighth Engineering Foundation Conference on Fluidization, Tours, France. p. 239-246.

Benyahia, S., Syamlal, M., and O'Brien, T.J., (2005). Evaluation of boundary conditions used to model dilute, turbulent gas/solids flows in a pipe. Powder Technology, 156,(2-3) 62-72.

Benyahia, S., Syamlal, M., and O'Brien, T.J., (2006). Extension of Hill-Koch-Ladd drag correlation over all ranges of Reynolds number and solids volume fraction. Powder Technology, 162,(2) 166-174.

Benyahia, S., Syamlal, M., and O'Brien, T.J., (2007). Summary of MFIX Equations 2005-4. pp.

Berruti, F., Muir, J.R., and Behie, L.A., (1988). Solids circulation in a spout-fluid bed with draft tube. Canadian Journal of Chemical Engineering, 66,(12) 919-923.

Berry, T.A., McKeen, T.R., Pugsley, T.S., and Dalai, A.K., (2004). Two-dimensional reaction engineering model of the riser section of a fluid catalytic cracking unit. Industrial & Engineering Chemistry Research, 43,(18) 5571-5581.

Bi, H.T., Ellis, N., Abba, I.A., and Grace, J.R., (2000). A state-of-the-art review of gas-solid turbulent fluidization. Chemical Engineering Science, 55,(21) 4789-4825.

Birouk, M., and Gokalp, I., (2006). Current status of droplet evaporation in turbulent flows. Progress in Energy and Combustion Science, 32,(4) 408-423.

Bruhns, S., and Werther, J., (2005). An investigation of the mechanism of liquid injection into fluidized beds. AIChE Journal, 51,(3) 766-775.

Buchanan, J.S., (1994). Analysis of heating and vaporization of feed droplets in fluidized catalytic cracking risers. Industrial & Engineering Chemistry Research, 33,(12) 3104-3111.

Bulzan, D.L., (1988). Particle-laden weakly swirling free jets: Measurement and prediction, NASA Technical Memorandum 100881. pp.

Cammarata, L., Lettieri, P., Micale, G.D.M., and Colman, D., (2003). 2D and 3D CFD simulations of bubbling fluidized beds using Eulerian-Eulerian models. International Journal of Chemical Reactor Engineering, 1,(A48)

Campbell, C.S., (1997). Self-diffusion in granular shear flows. Journal of Fluid Mechanics, 348 85-101.

Cao, J., and Ahmadi, G., (1995). Gas-particle 2-phase turbulent-flow in a vertical duct. International Journal of Multiphase Flow, 21,(6) 1203-1228.

Carnahan, N.F., and Starling, K.E., (1969). Equation of state for non-attracting rigid spheres. Journal of Chemical Physics, 51,(2) 635-642.

Chang, S.L., Lottes, S.A., Zhou, C.Q., Bowman, B.J., and Petrick, M., (2001). Numerical study of spray injection effects on the heat transfer and product yields of FCC riser reactors. Journal of Heat Transfer-Transactions of the ASME, 123,(3) 544-555.

Chang, S.L., and Zhou, C.Q., (2003). Simulation of FCC riser flow with multiphase heat transfer and cracking reactions. Computational Mechanics, 31,(6) 519-532.

Chapman, S., and Cowling, T.G., (1970). The mathematical theory of non-uniform gases: an account of the kinetic theory of viscosity, thermal conduction, and diffusion in gases. Cambridge: University Press, pp. 423.

Chen, L.B., and Weinstein, H., (1993). Shape and extent of the void formed by a horizontal jet in a fluidized-bed. AIChE Journal, 39,(12) 1901-1909.

Chen, X.Q., and Pereira, J.C.F., (1995). Prediction of evaporating spray in anisotropically turbulent gas-flow. Numerical Heat Transfer Part A-Applications, 27,(2) 143-162.

Chen, Y.M., (2006). Recent advances in FCC technology. Powder Technology, 163,(1-2) 2-8.

Chigier, N., and Reitz., R.D., (1998). Regimes of jet break-up and break-up mechanisms (physical aspects). In: Recent advances in spray combustion: spray atomization and drop burning phenomena, ed. KK Kuo, pp. 109-135: American Institute of Aeronautics and Astronautics.

Cho, Y.J., Namkung, W., Kim, S.D., and Park, S.W., (1994). Effect of secondary air Injection on axial solid holdup distribution in a circulating fluidized-bed. Journal of Chemical Engineering of Japan, 27,(2) 158-164.

Christensen, D., Nijenhuis, J., van Ommen, J.R., and Coppens, M.O., (2008a). Influence of distributed secondary gas injection on the performance of a bubbling fluidized-bed reactor. Industrial & Engineering Chemistry Research, 47,(10) 3601-3618.

Christensen, D., Nijenhuis, J., Van Ornmen, J.R., and Coppens, M.O., (2008b). Residence times in fluidized beds with secondary gas injection. Powder Technology, 180,(3) 321-331.

Christensen, D., Vervloet, D., Nijenhuis, J., van Wachem, B.G.M., van Ommen, J.R., and Coppens, M.O., (2008c). Insights in distributed secondary gas injection in a bubbling fluidized bed via discrete particle simulations. Powder Technology, 183,(3) 454-466.

Chyang, C.S., Chang, C.H., and Chang, J.H., (1997). Gas discharge modes at a single horizontal nozzle in a two-dimensional fluidized bed. Powder Technology, 90,(1) 71-77.

Cleaver, J.A.S., Ghadiri, M., Tuponogov, V.G., Yates, J.G., and Cheesman, D.J., (1995). Measurement of jet angles in fluidized-beds. Powder Technology, 85,(3) 221-226.

Copan, J., Clarke, N., and Berruti, F., (2001). The interaction of single- and two-phase jets and fluidized beds. Presented at Fluidization X, Proceedings of the Engineering Foundation Conference on Fluidization, Beijing, China. p. 77-84.

Crowe, C.T., Troutt, T.R., and Chung, J.N., (1996). Numerical models for two-phase turbulent flows. Annual Review of Fluid Mechanics, (28) 11-43.

Dartevelle, S., (2004). Numerical modeling of geophysical granular flows: 1. A comprehensive approach to granular rheologies and geophysical multiphase flows. Geochemistry Geophysics Geosystems, 5.

Das Sharma, S., Pugsley, T., and Delatour, R., (2006). Three-dimensional CFD model of the deaeration rate of FCC particles. AIChE Journal, 52,(7) 2391-2400.

de Bertodano, M.A.L., (1998). Two fluid model for two-phase turbulent jets. Nuclear Engineering and Design, 179,(1) 65-74.

Deardorf, J.W., (1971). Magnitude of subgrid scale eddy coefficient. Journal of Computational Physics, 7,(1) 120-133.

Deen, N.G., Annaland, M.V., Van der Hoef, M.A., and Kuipers, J.A.M., (2007). Review of discrete particle modeling of fluidized beds. Chemical Engineering Science, 62,(1-2) 28-44.

Demichele, G., Elia, A., and Massimilla, L., (1976). Interaction between jets and fluidized-beds. Quaderni Dell Ingegnere Chimico Italiano, 12,(6) 155-162.

deOliveira, W.P., Freire, J.T., and Coury, J.R., (1997). Analysis of particle coating by spouted bed process. International Journal of Pharmaceutics, 158,(1) 1-9.

Deshmukh, S.A.R.K., Annaland, M.V., and Kuipers, J.A.M., (2007). Gas back-mixing studies in membrane assisted bubbling fluidized beds. Chemical Engineering Science, 62,(15) 4095-4111.

Deutsch, E., and Simonin, O., (1991). Large eddy simulation applied to the motion of particles in stationary homogeneous fluid turbulence. Turbulence Modification in Multiphase Flows AMSE FED, (110) 35-42.

Dewettinck, K., Deroo, L., Messens, W., and Huyghebaert, A., (1998). Agglomeration tendency during top-spray fluidized bed coating with gums. Food Science and Technology-Lebensmittel-Wissenschaft & Technologie, 31,(6) 576-584.

Dewettinck, K., and Huyghebaert, A., (1998). Top-spray fluidized bed coating: Effect of process variables on coating efficiency. Food Science and Technology-Lebensmittel-Wissenschaft & Technologie, 31,(6) 568-575.

Dewettinck, K., and Huyghebaert, A., (1999). Fluidized bed coating in food technology. Trends in Food Science & Technology, 10,(4-5) 163-168.

Di Felice, R., (1994). The voidage function for fluid particle interaction systems. International Journal of Multiphase Flow, 20,(1) 153-159.

Difelice, R., (1994). The voidage function for fluid particle interaction systems. International Journal of Multiphase Flow, 20,(1) 153-159.

Donald, A., Bi, H.T., Grace, J.R., and Lim, C.J., (2004). Penetration of single and multiple horizontal jets into fluidized beds. Presented at Fluidization XI, Ischia. p. 171-178.

Donida, M.W., and Rocha, S.C.S., (2002). Coating of urea with an aqueous polymeric suspension in a two-dimensional spouted bed. Drying Technology, 20,(3) 685-704.

Donida, M.W., Rocha, S.C.S., and Bartholomeu, F., (2005). Influence of polymeric suspension characteristics on the particle coating in a spouted bed. Drying Technology, 23,(9-11) 1811-1823.

Du, W., Bao, X.J., Xu, J., and Wei, W.S., (2006). Computational fluid dynamics (CFD) modeling of spouted bed: Influence of frictional stress, maximum packing limit and coefficient of restitution of particles. Chemical Engineering Science, 61,(14) 4558-4570.

Elghobashi, S.E., and Abou-Arab, T.W., (1983). A two-equation turbulence model for two-phase flows. Physics of Fluids, 26,(4) 931-938.

Enwald, H., Peirano, E., and Almstedt, A.E., (1996). Eulerian two-phase flow theory applied to fluidization. International Journal of Multiphase Flow, (22) 21-66.

Ergun, S., (1952). Fluid flow through packed columns. Chemical Engineering Progress, 48 89-94.

Fan, L.-S., (2004). Gas-liquid-solid fluidization: Perspectives. International Journal of Chemical Reactor Engineering, (2) P5.

Fan, L.-S., and Zhu, C., (1998). Principles of gas-solid flows. Cambridge; New York: Cambridge University Press, pp. 557.

Fan, L.S., Lau, R., Zhu, C., Vuong, K., Warsito, W., et al, (2001). Evaporative liquid jets in gas-liquid-solid flow system. Chemical Engineering Science, 56,(21-22) 5871-5891.

Felli, V., Berruti, F., Briens, C., and Chan, E., (2003). Injection of a liquid spray into a gas-solid fluidized bed: measurement of solids entrainment into the spray. CRE IX, Quebec City.

Filla, M., Massimilla, L., and Vaccaro, S., (1983). Gas jets in jluidized-beds - the Influence of particle-size, shape and density on gas and solids entrainment. International Journal of Multiphase Flow, 9,(3) 259-267.

Fluent, (2006). FLUENT 6.3 Documentation. Fluent Inc.,

Foerster, S.F., Louge, M.Y., Chang, A.H., and Allia, K., (1994). Measurements of the Collision Properties of Small Spheres. Physics of Fluids, 6,(3) 1108-1115.

Gao, J.S., Xu, C.M., Lin, S.X., Yang, G.H., and Guo, Y.C., (2001). Simulations of gas-liquid-solid 3-phase flow and reaction in FCC riser reactors. AIChE Journal, 47,(3) 677-692.

Garcia, J.A., Calvo, E., Palacin, J.I.G., Santolaya, J.L., and Aisa, L., (2005). Local measurements in a particle laden jet generated by a convergent nozzle. Fluid Dynamics,

Ge, Y., and Fan, L.S., (2006). Three-dimensional direct numerical simulation for film-boiling contact of moving particle and liquid droplet. Physics of Fluids, 18,(11) 117104.

Ge, Y., and Fan, L.S., (2007). Droplet-particle collision mechanics with film-boiling evaporation. Journal of Fluid Mechanics, (573) 311-337.

Gehrke, S., and Wirth, K.E., (2007a). Evaporating liquid in a high-density riser. Presented at International Congress on Particle Technology, Nuremberg, Germany.

Gehrke, S., and Wirth, K.E., (2007b). Liquid feed injection in a high density riser. Presented at The 12th International Conference on Fluidization - New Horizons in Fluidization Engineering. p. 79-86.

Gehrke, S., and Wirth, K.E., (2008). Riser flow pattern with liquid feed injection at elevated temperature. Presented at 9th International Conference on Circulating Fluidized Beds, Hamburg, Germany.

Geldart, D., (1972). Effect of particle-size and size distribution on behavior of gas-fluidized beds. Powder Technology, 6,(4) 201-215.

Gelderbloom, S.J., Gidaspow, D., and Lyczkowski, R.W., (2003). CFD simulations of bubbling/collapsing fluidized beds for three Geldart groups. AIChE Journal, 49,(4) 844-858.

Gera, D., Gautam, M., Tsuji, Y., Kawaguchi, T., and Tanaka, T., (1998). Computer simulation of bubbles in large-particle fluidized beds. Powder Technology, 98,(1) 38-47.

Gera, D., Syamlal, M., and O'Brien, T.J., (2004). Hydrodynamics of particle segregation in fluidized beds. International Journal of Multiphase Flow, 30,(4) 419-428.

Gibilaro, L.G., (2001). Fluidization-dynamics: the formulation and applications of a predictive theory for the fluidized state. Boston: Butterworth-Heinemann, pp. 232.

Gidaspow, D., (1986). Hydrodynamics of fluidization and heat transfer: super computer modelling. Applied Mechanics Review, (39) 1-23.

Gidaspow, D., (1994). Multiphase flow and fluidization: continuum and kinetic theory descriptions. Boston: Academic Press, pp. 467.

Gidaspow, D., and Ettehadieh, B., (1983). Fluidization in two-dimensional beds with a jet.2. Hydrodynamic modeling. Industrial & Engineering Chemistry Fundamentals, 22,(2) 193-201.

Gidaspow, D., Syamlal, M., and Seo, Y., (1986). Hydrodynamics of fluidization of single and binary size particles: supercomputer modeling. Presented at the Fifth Engineering Conference on Fluidization. p. 1-8.

Gillandt, I., Fritsching, U., and Bauckhage, K., (2001). Measurement of phase interaction in dispersed gas/particle two-phase flow. International Journal of Multiphase Flow, 27,(8) 1313-1332.

Gilliland, E.R., and Mason, E.A., (1952). Gas mixing in beds of fluidized solids. Journal of Industrial and Engineering Chemistry, (44) 218-224.

Goldschmidt, M.J.V., Kuipers, J.A.M., and van Swaaij, W.P.M., (2001). Hydrodynamic modelling of dense gas-fluidised beds using the kinetic theory of granular flow: effect of coefficient of restitution on bed dynamics. Chemical Engineering Science, 56,(2) 571-578.

Goossens, W.R.A., (1998). Classification of fluidized particles by Archimedes number. Powder Technology, 98,(1) 48-53.

Grace, J.R., (1986). Contacting modes and behavior classification of gas - solid and other 2-phase suspensions. Canadian Journal of Chemical Engineering, 64,(3) 353-363.

Grace, J.R., and Lim, C.J., (1987). Permanent jet formation in beds of particulate solids. Canadian Journal of Chemical Engineering, 65,(1) 160-162.

Grace, J.R., and Taghipour, F., (2004). Verification and validation of CFD models and dynamic similarity for fluidized beds. Powder Technology, 139,(2) 99-110.

Gray, D.D., and Stiles, J.M., (1988). On the constitutive relation for frictional flow of granular materials,Topical Report U.S. Department of Energy. pp. 29.

Gray, M.R., (2002). Fundamentals of bitumen coking processes analogous to granulations: A critical review. Canadian Journal of Chemical Engineering, 80,(3) 393-401.

Gray, M.R., Le, T., McCaffrey, W.C., Berruti, F., Soundararajan, S., et al, (2001). Coupling of mass transfer and reaction in coking of thin films of an Athabasca vacuum residue. Industrial & Engineering Chemistry Research, 40,(15) 3317-3324.

Gunn, D.J., (1978). Transfer of heat or mass to particles in fixed and fluidized-beds. International Journal of Heat and Mass Transfer, 21,(4) 467-476.

Gupta, A., and Rao, D.S., (2001). Model for the performance of a fluid catalytic cracking (FCC) riser reactor: effect of feed atomization. Chemical Engineering Science, 56,(15) 4489-4503.

Gupta, A., and Rao, D.S., (2003). Effect of feed atomization on FCC performance: simulation of entire unit. Chemical Engineering Science, 58,(20) 4567-4579.

Hammond, D.G., Lampert, L.F., Mart, C.J., Massenzio, S.F., Phillips, G.E., et al, (2003). Review of FLUID COKING and FLEXICOKING Technologies. Presented at Sixth Topical Conference on Refining Processing Tutorial on Reside Upgrading American Institute of Chemical Engineers 2003 Spring National Meeting.

Hansen, K.G., Solberg, T., and Hjertager, B.H., (2004). A three-dimensional simulation of gas/particle flow and ozone decomposition in the riser of a circulating fluidized bed. Chemical Engineering Science, 59,(22-23) 5217-5224.

Hatta, N., Fujimoto, H., Takuda, H., Kinoshita, K., and Takahashi, O., (1995). Collision dynamics of a water droplet impinging on a rigid surface above the Leidenfrost temperature. ISIJ International, 35,(1) 50-55.

Hattori, H., Ito, S., Onezawa, T., Yamada, K., and Yanai, S., (2004). Fluid and solids flow affecting the solids circulation rate in spouted beds with a draft-tube. Journal of Chemical Engineering of Japan, 37,(9) 1085-1091.

Hattori, H., and Takeda, K., (1978). Side-Outlet Spouted Bed with Inner Draft-Tube for Small-Sized Solid Particles. Journal of Chemical Engineering of Japan, 11,(2) 125-129.

Haywood, R.J., Nafziger, R., and Renksizbulut, M., (1989). A detailed examination of gas and liquid phase transient processes in convective droplet evaporation. Journal of Heat Transfer, 111,(2) 495-502.

He, P., and Salcudean, M., (1994). A numerical method for 3D viscous incompressible flows using nonorthogonal grids. International Journal for Numerical Methods in Fluids, 18,(5) 449-469.

He, Y.L., Lim, C.J., Grace, J.R., Zhu, J.X., and Qin, S.Z., (1994). Measurements of voidage profiles in spouted beds. Canadian Journal of Chemical Engineering, 72,(2) 229-234.

Heinrich, S., Blumschein, J., Henneberg, M., Ihlow, M., Peglow, M., and Morl, L., (2003). Study of dynamic multi-dimensional temperature and concentration distributions in liquid-sprayed fluidized beds. Chemical Engineering Science, 58,(23-24) 5135-5160.

Hemati, A., Cherif, R., Saleh, K., and Pont, V., (2003). Fluidized bed coating and granulation: influence of process-related variables and physicochemical properties on the growth kinetics. Powder Technology, 130,(1-3) 18-34.

Henrique, C., Batrouni, G., and Bideau, D., (2001). Diffusion as a mixing mechanism in granular materials. Physical Review E, 6301,(1).

Hill, R.J., Koch, D.L., and Ladd, A.J.C., (2001). The first effects of fluid inertia on flows in ordered and random arrays of spheres. Journal of Fluid Mechanics, (448) 213-241.

Hinze, J.O., (1975). Turbulence. McGraw-Hill Publishing Co., New York.

Hong, R., Li, H., Li, H., and Wang, Y., (1997). Studies on the inclined jet penetration length in a gas-solid fluidized bed. Powder Technology, (92) 205-212.

Hong, R.Y., Guo, Q.J., Luo, G.H., Zhang, J.Y., and Ding, J., (2003). On the jet penetration height in fluidized beds with two vertical jets. Powder Technology, 133,(1-3) 216-227.

Hoomans, B.P.B., Kuipers, J.A.M., Briels, W.J., and vanSwaaij, W.P.M., (1996). Discrete particle simulation of bubble and slug formation in a two-dimensional gas-fluidised bed: A hard-sphere approach. Chemical Engineering Science, 51,(1) 99-118.

Howard, J.R., (1989). Fluidized bed technology: principles and applications. Bristol, England; New York: A. Hilger, pp. 214.

Hrenya, C.M., and Sinclair, J.L., (1997). Effects of particle-phase turbulence in gas-solid flows. AIChE Journal, 43,(4) 853-869.

Hsiau, S.S., and Hunt, M.L., (1993). Kinetic-theory analysis of flow-induced particle diffusion and thermal conduction in granular material flows. Journal of Heat Transfer-Transactions of the ASME, 115,(3) 541-548.

Huanpeng, L., Wentie, L., Jianxiang, Z., Ding, J., Xiujian, Z., and Huilin, L., (2004). Numerical study of gas-solid flow in a precalciner using kinetic theory of granular flow. Chemical Engineering Journal, 102,(2) 151.

Hussainova, I., Kubarsepp, J., and Shcheglov, I., (1999). Investigation of impact of solid particles against hardmetal and cermet targets. Tribology International, 32,(6) 337-344.

Iddir, H., and Arastoopour, H., (2005). Modeling of multitype particle flow using the kinetic theory approach. AIChE Journal, 51,(6) 1620-1632.

Ijichi, K., Miyauchi, M., Uemura, Y., and Hatate, Y., (1998). Characteristics of flow behavior in semi-cylindrical spouted bed with draft tube. Journal of Chemical Engineering of Japan, 31,(5) 677-682.

Ishii, M., (1975). Thermo-fluid dynamic theory of two-phase flow. Paris Eyrolles, pp. 248.

Issa, R.L., and Oliveira, P.J., (1996). Validation of two-fluid model in shear-free mixing layers. ASME-PUBLICATIONS-FED, (236), 112-120.

Iyer, V., and Abraham, A., (2005). Two-fluid modeling of spray penetration and dispersion under diesel engine conditions. Atomization and Sprays, 15,(3) 249-269.

Iyer, V., and Abraham, J., (2003). An evaluation of a two-fluid Eulerian-liquid Eulerian-gas model for diesel sprays. Journal of Fluids Engineering-Transactions of the ASME, 125,(4) 660-669.

Iyer, V.A., Abraham, J., and Magi, V., (2002). Exploring injected droplet size effects on steady liquid penetration in a Diesel spray with a two-fluid model. International Journal of Heat and Mass Transfer, 45,(3) 519-531.

Jenkins, J.T., and Savage, S.B., (1983). A theory for the rapid flow of identical, smooth, nearly elastic, spherical-particles. Journal of Fluid Mechanics, 130,(May) 187-202.

Johansson, K., van Wachem, B.G.M., and Almstedt, A.E., (2006). Experimental validation of CFD models for fluidized beds: Influence of particle stress models, gas phase compressibility and air inflow models. Chemical Engineering Science, 61,(5) 1705-1717.

Johnson, P.C., and Jackson, R., (1987). Frictional collisional constitutive relations for antigranulocytes-materials, with application to plane shearing. Journal of Fluid Mechanics, (176) 67-93.

Johnson, P.C., Nott, P., and Jackson, R., (1990). Frictional collisional equations of motion for particulate flows and their application to chutes. Journal of Fluid Mechanics, (210) 501-535.

Jones, D.S.J., Pujadó, P.R., and MyiLibrary. 2006. Handbook of petroleum processing. pp. xiv, 1353 p. Dordrecht: Springer.

Jono, K., Ichikawa, H., Miyamoto, M., and Fukumori, Y., (2000). A review of particulate design for pharmaceutical powders and their production by spouted bed coating. Powder Technology, 113,(3) 269-277.

Karl, A., and Frohn, A., (2000). Experimental investigation of interaction processes between droplets and hot walls. Physics of Fluids, 12,(4) 785-796.

Karlsson, S., Bjorn, I.N., Folestad, S., and Rasmuson, A., (2006). Measurement of the particle movement in the fountain region of a Wurster type bed. Powder Technology, 165,(1) 22-29.

Kim, J.H., and Shakourzadeh, K., (2000). Analysis and modelling of solid flow in a closed loop circulating fluidized bed with secondary air injection. Powder Technology, 111,(3) 179-185.

Knoebig, T., and Werther, J., (1999). Horizontal reactant injection into large-scale fluidized bed reactors - Modeling of secondary air injection into a circulating fluidized bed combustor. Chemical Engineering & Technology, 22,(8) 656-659.

Knowlton, T.M., Karri, S.B.R., and Issangya, A., (2005). Scale-up of fluidized-bed hydrodynamics. Powder Technology, 150,(2) 72-77.

Koksal, A., Golriz, M.R., and Hamdullahpur, F., (2008). Effect of staged air on heat transfer in circulating fluidized beds. Applied Thermal Engineering, 28,(8-9) 1008-1014.

Koksal, M., and Hamdullahpur, F., (2004). Gas mixing in circulating fluidized beds with secondary air injection. Chemical Engineering Research & Design, 82,(A8) 979-992.

Kolaitis, D.I., and Founti, M.A., (2006). A comparative study of numerical models for Eulerian-Lagrangian simulations of turbulent evaporating sprays. International Journal of Heat and Fluid Flow, 27,(3) 424-435.

Konduri, R.K., Altwicker, E.R., and Morgan, M.H., (1999). Design and scale-up of a spouted-bed combustor. Chemical Engineering Science, 54,(2) 185-204.

Kono, H.O., (1989). Transport in fluidized particle systems. In: Transport processes in engineering, ed. LK Doraiswamy, AD Mujumdar, pp. 1-30

Kunii, D.o., and Levenspiel, O., (1991). Fluidization engineering. Boston: Butterworth-Heinemann, pp. 491.

Launder, B.E., and Spalding, D.B., (1972). Lectures in mathematical models of turbulence. London, New York: Academic Press, pp. 7, 169.

Leclere, K., Briens, C., Gauthier, T., Bayle, J., Bergougnou, M., and Guigon, P., (2001). Liquid vaporization in a fluidized bed. Industrial & Engineering Chemistry Research, 40,(23) 5415-5420.

Leclere, K., Briens, C., Gauthier, T., Bayle, J., Guigon, P., and Bergougnou, M., (2004). Experimental measurement of droplet vaporization kinetics in a fluidized bed. Chemical Engineering and Processing, 43,(6) 693-699.

Lefebvre, A.H., (1989). Atomization and sprays. New York: Hemisphere Pub. Corp., pp. 421.

Li, J., and Kuipers, J.A.M., (2002). Effect of pressure on gas-solid flow behavior in dense gas-fluidized beds: a discrete particle simulation study. Powder Technology, 127,(2) 173-184.

Li, J.H., and Weinstein, H., (1989). An experimental comparison of gas backmixing in fluidized-eeds across the regime spectrum. Chemical Engineering Science, 44,(8) 1697-1705.

Li, T., Pougatch, K., Salcudean, M., and Grecov, D., (2008). Numerical simulation of horizontal jet penetration in a three-dimensional fluidized bed. Powder Technology, 184,(1) 89-99.

Lightstone, M.F., and Hodgson, S.M., (2004). Turbulence modulation in gas-particle flows: A comparison of selected models. Canadian Journal of Chemical Engineering, 82,(2) 209-219.

Limtrakul, S., Chalermwattanatai, A., Unggurawirote, K., Tsuji, Y., Kawaguchi, T., and Tanthapanichakoon, W., (2003). Discrete particle simulation of solids motion in a gas-solid fluidized bed. Chemical Engineering Science, 58,(3-6) 915-921.

Lin, S.P., (1998). Regimes of jet break-up and break-up mechanisms (mathematical aspects). In: Recent advances in spray combustion: spray atomization and drop burning phenomena, ed. KK Kuo, pp. 137-160: American Institute of Aeronautics and Astronautics.

Link, J.M., Godlieb, W., Deen, N.G., and Kuipers, J.A.M., (2007). Discrete element study of granulation in a spout-fluidized bed. Chemical Engineering Science, 62,(1-2) 195-207.

Link, K.C., (1996). Wirbelschicht Spruehgranulation: Untersuchung der Granulatbildung an einer frei schwebenden Einzelpartikel. Universitaet Karlsruhe (TH), Karlsruhe.

Liu, A.B., and Reitz, R., (1993). Mechanisms of air-assisted liquid atomization. Atomization and Sprays, 3,(1) 55-75.

Liu, G., (2003). Evaporatiing crossflow sprays in gas-solid flows. New Jersey Institute of Technology, New Jersey.

Liu, X., and Glasser, B.J., (2006). A parametric investigation of gas-particle flow in a vertical duct. AIChE Journal, 52,(3) 940-956.

Lu, H.L., and Gidaspow, D., (2003). Hydrodynamics of binary fluidization in a riser: CFD simulation using two granular temperatures. Chemical Engineering Science, 58,(16) 3777-3792.

Lu, H.L., He, Y.R., Liu, W.T., Ding, J.M., Gidaspow, D., and Bouillard, J., (2004). Computer simulations of gas-solid flow in spouted beds using kinetic-frictional stress model of granular flow. Chemical Engineering Science, 59,(4) 865-878.

Lun, C., and Savage, S., (1986). The effects of an impact velocity dependent coefficient of restitution on stresses developed by sheared granular materials. ACTA Mechanica, 63,(1) 15.

Lun, C.K.K., Savage, S.B., Jeffrey, D.J., and Chepurniy, N., (1984). Kinetic theories for granular flow - inelastic particles in couette flow and slightly inelastic particles in a general flowfield. Journal of Fluid Mechanics, 140,(Mar) 223-256.

Ma, D., and Ahmadi, G., (1990). A thermodynamical formulation for dispersed multiphase turbulent flows.2. Simple shear flows for dense mixtures. International Journal of Multiphase Flow, 16,(2) 341-351.

Maronga, S.J., and Wnukowski, P., (1998). The use of humidity and temperature profiles in optimizing the size of fluidized bed in a coating process. Chemical Engineering and Processing, 37,(5) 423-432.

Maronga, S.J., and Wnukowski, P., (2001). Growth kinetics in particle coating by top-spray fluidized bed systems. Advanced Powder Technology, 12,(3) 371-391.

Marschall, K.J., and Mleczko, L., (1999). CFD modeling of an internally circulating fluidized-bed reactor. Chemical Engineering Science, 54,(13-14) 2085-2093.

Marzocchella, A., and Arena, U., (1996). Hydrodynamics of a circulating fluidized bed operated with different secondary air injection devices. Powder Technology, 87,(3) 185-191.

Massimilla, L., (1985). Gas jets in fluidized beds. In: Fluidization, ed. JF Davidson, R Clift, D Harrison, pp. 133-172. London: Academic Press.

Mathur, K.B., and Epstein, N., (1974). Spouted beds. New York: Academic Press, pp. xv, 304 p.

McKeen, T., and Pugsley, T., (2003a). Simulation and experimental validation of a freely bubbling bed of FCC catalyst. Powder Technology, 129,(1-3) 139-152.

McKeen, T., and Pugsley, T., (2003b). Simulation of cold flow FCC stripper hydrodynamics at small scale using computational fluid dynamics. International Journal of Chemical Reactor Engineering, 1,(A18).

Merry, J.M.D., (1971). Penetration of a horizontal gas jet into a fluidised bed. Transactions of the Institution of Chemical Engineers and the Chemical Engineer, 49,(4) 189-195.

Merry, J.M.D., (1975). Penetration of vertical jets into fluidized-beds. AIChE Journal, 21,(3) 507-510.

Missen, R.W., Mims, C.A., and Saville, B.A., (1999). Introduction to chemical reaction engineering and kinetics. New York: J. Wiley, pp. xviii, 672 p.

Molerus, O., (1982). Interpretation of Geldart type-a, type-B, type-C and type-D powders by taking into account interparticle cohesion forces. Powder Technology, 33,(1) 81-87.

Moran, J.C., and Glicksman, L.R., (2003). Mean and fluctuating gas phase velocities inside a circulating fluidized bed. Chemical Engineering Science, 58,(9) 1867-1878.

Mostafa, A.A., and Mongia, H.C., (1988). On the interaction of particles and turbulent fluid-flow. International Journal of Heat and Mass Transfer, 31,(10) 2063-2075.

Mostoufi, N., and Chaouki, J., (1999). Prediction of effective drag coefficient in fluidized beds. Chemical Engineering Science, 54,(7) 851-858.

Mostoufi, N., and Chaouki, J., (2000). On the axial movement of solids in gas-solid fluidized beds. Chemical Engineering Research & Design, 78,(A6) 911-920.

Moukalled, F., and Darwish, M., (2008). Numerical prediction of dispersion and evaporation of liquid sprays in gases flowing at all speeds. Numerical Heat Transfer Part B-Fundamentals, 54,(3) 185-212.

Muir, J.R., Berruti, F., and Behie, L.A., (1990). Solids circulation in spouted and spout-fluid beds with draft-tubes. Chemical Engineering Communications, (88) 153-171.

Musmarra, D., (2000). Influence of particle size and density on the jet penetration length in gas fluidized beds. Industrial & Engineering Chemistry Research, 39,(7) 2612-2617.

Nayak, S.V., Joshi, S.L., and Ranade, V.V., (2005). Modeling of vaporization and cracking of liquid oil injected in a gas-solid riser. Chemical Engineering Science, 60,(22) 6049-6066.

Nguyen, H.V., Potter, O.E., Dent, D.C., and Whitehead, A.B., (1981). Gas backmixing in large fluidized-beds containing tube assemblies. AIChE Journal, 27,(3) 509-514.

Nguyen, H.V., Whitehead, A.B., and Potter, O.E., (1977). Gas backmixing, solids movement, and bubble activities in large-scale fluidized-beds. AIChE Journal, 23,(6) 913-922.

Nolan, G.T., and Kavanagh, P.E., (1992). Computer-simulation of random packing of hard-spheres. Powder Technology, 72,(2) 149-155.

Nowak, Z.P., and Salcudean, M., (1996). Turbulent flow calculations by the nonlinear multi-grid method. Zeitschrift Fur Angewandte Mathematik Und Mechanik, 76,(8) 463-469.

Pain, C.C., Mansoorzadeh, S., Gomes, J.L.M., and de Oliveira, C.R.E., (2002). A numerical investigation of bubbling gas-solid fluidized bed dynamics in 2-D geometries. Powder Technology, 128,(1) 56-77.

Panda, R.C., Zank, J., and Martin, H., (2001). Modeling the droplet deposition behavior on a single particle in fluidized bed spray granulation process. Powder Technology, 115,(1) 51-57.

Patankar, S.V., (1980). Numerical heat transfer and fluid flow. New York: McGraw-Hill,

Paulo, M., Rocha, S.C.S., and Lisboa, A.C.L., (2006). Modeling and experimental analysis of polydispersed particles coating in spouted bed. Chemical Engineering and Processing, 45,(11) 965-972.

Peirano, E., and Leckner, B., (1998). Fundamentals of turbulent gas-solid flows applied to circulating fluidized bed combustion. Progress in Energy and Combustion Science, 24,(4) 259-296.

Peirano, E., Delloume, V., Johnsson, F., Leckner, B., and Simonin, O., (2002). Numerical simulation of the fluid dynamics of a freely bubbling fluidized bed: influence of the air supply system. Powder Technology, 122,(1) 69-82.

Pitman, E.B., and Schaeffer, D.G., (1987). Stability of time-dependent compressible antigranulocytes flow in 2 dimensions. Communications on Pure and Applied Mathematics, 40,(4) 421-447.

Portela, L.M., and Oliemans, R.V.A., (2006). Possibilities and limitations of computer simulations of industrial turbulent dispersed multiphase flows. Flow Turbulence and Combustion, 77,(1-4) 381-403.

Pougatch, K. 2005. Equations for the Eulerian multiphase model. Personal Communication.

Qureshi, M.M.R., and Zhu, C., (2006). Crossflow evaporating sprays in gas-solid flows: Effect of aspect ratio of rectangular nozzles. Powder Technology, 166,(2) 60-71.

Rajan, S., and Christoff, J.D., (1982). Effect of horizontal air jet penetration on the combustion of coal in a fluidized-bed. Journal of Energy, 6,(2) 125-131.

Ramkrishna, D., (2000). Population balances: theory and applications to particulate systems in engineering. San Diego, Calif.: Academic Press, pp. xvi, 355 p.

Ran, X., Wei, F., Wang, Z.W., and Jin, Y., (2001). Lateral solids dispersion in a high-density riser with swirling air flow. Powder Technology, 121,(2-3) 123-130.

Reeks, M.W., (1991). On a kinetic-equation for the transport of particles in turbulent flows. Physics of Fluids A-Fluid Dynamics, 3,(3) 446-456.

Reeks, M.W., (1992). On the continuum equations for dispersed particles in nonuniform flows. Physics of Fluids A-Fluid Dynamics, 4,(6) 1290-1303.

Reeks, M.W., (1993). On the constitutive relations for dispersed particles in nonuniform flows.1. Dispersion in a simple shear-flow. Physics of Fluids A-Fluid Dynamics, 5,(3) 750-761.

Reitz, R.D., and Diwakar, R., (1986). Effect of drop break-up on fuel sprays,SAE Report 860469. pp.

Rhodes, M.J., Wang, X.S., Nguyen, M., Stewart, P., and Liffman, K., (2001). Use of discrete element method simulation in studying fluidization characteristics: influence of interparticle force. Chemical Engineering Science, 56,(1) 69-76.

Ronsse, F., Pieters, J.G., and Dewettinck, K., (2007). Numerical spray model of the fluidized bed coating process. Drying Technology, 25,(9) 1491-1514.

Saadevandi, B.A., (1996). The use of imaging techniques to study the hydrodynamics of particle motion in a fluidized bed coating device in the region of the liquid spray. West Virginia University.

Saadevandi, B.A., and Turton, R., (2004). Particle velocity and voidage profiles in a draft tube equipped spouted-fluidized bed coating device. Chemical Engineering Communications, 191,(10) 1379-1400.

Sadiki, A., Chrigui, M., Janicka, J., and Maneshkarimi, M.R., (2005). Modeling and simulation of effects of turbulence on vaporization, mixing and combustion of liquid-fuel sprays. Flow Turbulence and Combustion, 75,(1-4) 105-130.

Saleh, K., Steinmetz, D., and Hemati, A., (2003). Experimental study and modeling of fluidized bed coating and agglomeration. Powder Technology, 130,(1-3) 116-123.

Samuelsberg, A., and Hjertager, B.H., (1996). An experimental and numerical study of flow patterns in a circulating fluidized bed reactor. International Journal of Multiphase Flow, 22,(3) 575-591.

Savage, S.B., (1983). Granular flows down rough inclines - review and extension. In: Mechanics of Granular Materials: New Model and Constitutive Relations, pp. 261-282.

Savage, S.B., (1998). Analyses of slow high-concentration flows of granular materials. Journal of Fluid Mechanics, 377 1-26.

Sazhin, S.S., (2006). Advanced models of fuel droplet heating and evaporation. Progress in Energy and Combustion Science, 32,(2) 162-214.

Sazhin, S.S., Kristyadi, T., Abdelghaffar, W.A., and Heikal, M.R., (2006). Models for fuel droplet heating and evaporation: Comparative analysis. Fuel, 85,(12-13) 1613-1630.

Schaeffer, D.G., (1987). Instability in the evolution-equations describing incompressible antigranulocytes Flow. Journal of Differential Equations, 66,(1) 19-50.

Schofield, A.N., and Wroth, P., (1968). Critical state soil mechanics. New York: McGraw-Hill, pp. xix, 310.

Shakhova, N.A., (1968). Discharge of turbulent jets into a fluidized bed. Journal of Engineering Physics and Thermophysics, 14,(1) 32-36.

Simonin, O., (1990). Eulerian formulation for particle dispersion in turbulent two-phase flows. p. 156-166.

Simonin, O., (1996). Continuum modelling of dispersed two-phase flows. Lecture series - van Kareman Institute for fluid dynamics, 2 K1-K47.

Sinclair, J.L., and Jackson, R., (1989). Gas-particle flow in a vertical pipe with particle-particle interactions. AIChE Journal, 35,(9) 1473-1486.

Skouby, D.C., (1999). Hydrodynamic studies in a 0.45-m riser with liquid feed injection. AIChE Symposium Series, (321) 67-70.

Smolders, K., and Baeyens, J., (2001). Gas fluidized beds operating at high velocities: a critical review of occurring regimes. Powder Technology, 119,(2-3) 269-291.

Sommerfeld, M., (1998). Analysis of isothermal and evaporating turbulent sprays by phase-Doppler anemometry and numerical calculations. International Journal of Heat and Fluid Flow, 19,(2) 173-186.

Sommerfeld, M., and Qiu, H.H., (1998). Experimental studies of spray evaporation in turbulent flow. International Journal of Heat and Fluid Flow, 19,(1) 10-22.

Song, X.Q., Bi, H.T., Lim, C.J., Grace, J.R., Chan, E., et al, (2004). Hydrodynamics of the reactor section in fluid cokers. Powder Technology, 147,(1-3) 126-136.

Song, X.Q., Grace, J.R., Bi, H., Lim, C.J., Chan, E., et al, (2005). Gas mixing in the reactor section of fluid cokers. Industrial & Engineering Chemistry Research, 44,(16) 6067-6074.

Spalding, D.B., (1980). Numerical computation of multiphase flow and heat transfer. In: Recent advances in numerical methods in fluids, ed. K Morgan, C Taylor, pp. 139-168. Swansea: Pineridge Press.

Sparrow, E.M., and Gregg, J.L., (1958). The variable fluid-property in free convection. Transactions of the ASME, (80) 879-886.

Squires, K.D., and Eaton, J.K., (1994). Effect of selective modification of turbulence on 2-equation models for particle-laden turbulent flows. Journal of Fluids Engineering-Transactions of the ASME, 116,(4) 778-784.

Srivastava, A., and Sundaresan, S., (2003). Analysis of a fractional-kinetic model for gas-particle flow. Powder Technology, 129,(1-3) 72-85.

Stephens, G.K., Sinclair, R.J., and Potter, O.E., (1967). Gas exchange between bubbles and dense phase in a fluidized bed. Powder Technology, (1) 157-163.

Syamlal, M. 1987. The particle-particle drag term in a multiparticle model of fluidization. pp. 25

Syamlal, M., and O'Brien, T.J., (1989). Computer simulation of bubbles in a fluidized bed. AIChE Symposium Series, (85) 22-31.

Syamlal, M., and O'Brien, T.J., (2003). Fluid dynamic simulation of O-3 decomposition in a bubbling fluidized bed. AIChE Journal, 49,(11) 2793-2801.

Syamlal, M., Rogers, W., and Brien, T.J.O., (1993). MFIX documentation: Theory guide, U.S. Department of Energy (DOE), Morgantown Energy Technology Center, Morgantown, West Virginia. pp.

Szafran, R.G., and Kmiec, A., (2004). CFD modeling of heat and mass transfer in a spouted bed dryer. Industrial & Engineering Chemistry Research, 43,(4) 1113-1124.

Szafran, R.G., and Kmiec, A., (2007). Periodic fluctuations of flow and porosity in spouted beds. Transport in Porous Media, 66,(1-2) 187-200.

Szafran, R.G., Kmiec, A., and Ludwig, W., (2005). CFD modeling of a spouted-bed dryer hydrodynamics. Drying Technology, 23,(8) 1723-1736.

Taghipour, F., Ellis, N., and Wong, C., (2005). Experimental and computational study of gas-solid fluidized bed hydrodynamics. Chemical Engineering Science, 60,(24) 6857-6867.

Tardos, G.I., (1997). A fluid mechanistic approach to slow, frictional flow of powders. Powder Technology, 92,(1) 61-74.

Tchen, C.M., (1947). Mean value and correlation problems connected with the motion of small particles suspended in a turbulent fluid. Delft University of Technology.

Tsuji, Y., Kawaguchi, T., and Tanaka, T., (1993). Discrete particle simulation of 2-dimensional fluidized-bed. Powder Technology, 77,(1) 79-87.

Tsuo, Y.P., and Gidaspow, D., (1990). Computation of flow patterns in circulating fluidized-beds. AIChE Journal, 36,(6) 885-896.

Turton, R., Bhatia, A., Hakim, H., Subramanian, G., and Norman, L., (2001). Research in particle coating and agglomeration at West Virginia University. Powder Technology, 117,(1-2) 139-148.

Tyler, J., and Mees, P., (1999). Using CFD to model the interaction of a horizontal feed jet on fluidized bed hydrodynamics. Presented at Second International Conference on CFD in the Minerals and Process Industries, Australia. p. 113-117.

Utter, B., and Behringer, R.P., (2004). Self-diffusion in dense granular shear flows. Physical Review E, 69,(3).

Vaccaro, S., (1997). Analysis of the variables controlling gas jet expansion angles in fluidized beds. Powder Technology, 92,(3) 213-222.

Vaccaro, S., Musmarra, D., and Petrecca, M., (1997). Evaluation of the jet penetration depth in gas-fluidized beds by pressure signal analysis. International Journal of Multiphase Flow, 23,(4) 683-698.

Valverde, J.M., Castellanos, A., and Quintanilla, M.A.S., (2001). Self-diffusion in a gas-fluidized bed of fine powder. Physical Review Letters, 86,(14) 3020-3023.

Van Deemter, J.J., (1985). Mixing. Presented at Fluidization. p. 331.

van Wachem, B.G.M., Schouten, J.C., van den Bleek, C.M., Krishna, R., and Sinclair, J.L., (2001). Comparative analysis of CFD models of dense gas-solid systems. AIChE Journal, 47,(5) 1035-1051.

van Willigen, F.K., Christensen, D., van Ommen, J.R., and Coppens, M.O., (2005). Imposing dynamic structures on fluidised beds. Catalysis Today, 105,(3-4) 560-568.

Vanni, M., (2000). Approximate population balance equations for aggregation-breakage processes. Journal of Colloid and Interface Science, 221,(2) 143-160.

Varol, M., and Atimtay, A.T., (2007). Combustion of olive cake and coal in a bubbling fluidized bed with secondary air injection. Fuel, 86,(10-11) 1430-1438.

Wachters, L.H., Bonne, H., and Vannouhu, H.J., (1966). Heat transfer from a hot horizontal plate to sessile water drops in spherodial state. Chemical Engineering Science, 21,(10) 923-936.

Wang, X.H., Zhu, C., and Ahluwalia, R., (2004). Numerical simulation of evaporating spray jets in concurrent gas-solids pipe flows. Powder Technology, 140,(1-2) 56-67.

Wen, C.Y., and Yu, Y.H., (1966). Mechanics of fluidization. Presented at Chemical Engineering Progress Symposium Series. p. 100-111.

Werther, J., and Bruhns, S., (2004). 3-D Modeling of Liquid Injection into Fluidized Beds. International Journal of Chemical Reactor Engineering, 2,(A31).

Wu, Z.H., and Mujumdar, A.S., (2007). Simulation of the hydrodynamics and drying in a spouted bed dryer. Drying Technology, 25,(1-3) 59-74.

Wurster, D.E. 1953. Method of applying coating onto edible tablets or the like *USA Patent No. 2 648 609.*

Xu, Y., and Subramaniam, S., (2006). A multiscale model for dilute turbulent gas-particle flows based on the equilibration of energy concept. Physics of Fluids, 18,(3).

Xuereb, C., Laguerie, C., and Baron, T., (1991a). Behavior of horizontal or inclined continuous jets gas-injected into a fluidized-bed.1. Morphology of the jets. Powder Technology, 67,(1) 43-56.

Xuereb, C., Laguerie, C., and Baron, T., (1991b). Behavior of horizontal or inclined continuous jets introduced to a fluidized-bed by a gas.2. Gas velocity profiles in horizontal jets. Powder Technology, 64,(3) 271-283.

Yadav, N.K., Kulkarni, B.D., and Doraiswamy, L.K., (1994). Experimental evaluation and modeling of agglomerating fine powder fluidized-beds. Industrial & Engineering Chemistry Research, 33,(10) 2412-2420.

Yan, F., Lightstone, M.F., and Wood, P.E., (2007). Numerical study on turbulence modulation in gas-particle flows. Heat and Mass Transfer, 43,(3) 243-253.

Yang, N., Wang, W., Ge, W., and Li, J.H., (2003). CFD simulation of concurrent-up gas-solid flow in circulating fluidized beds with structure-dependent drag coefficient. Chemical Engineering Journal, 96,(1-3) 71-80

Yang, W.C., (2007). Modification and re-interpretation of Geldart's classification of powders. Powder Technology, 171,(2) 69-74.

Yang, W.C., and Keairns, D.L., (1979). Estimating the jet penetration depth of multiple vertical grid jets. Industrial & Engineering Chemistry Fundamentals, 18,(4) 317-320.

Yu, A.B., and Xu, B.H., (2003). Particle-scale modelling of gas-solid flow in fluidisation. Journal of Chemical Technology and Biotechnology, 78,(2-3) 111-121.

Zenz, F.A., (1968). Bubble formation and grid design. IChemE Symposium Series, (30) 136-139.

Zhang, K., Zhang, J.Y., and Zhang, B.J., (2004). CFD simulation of jet behaviour and voidage profile in a gas-solid fluidized bed. International Journal of Energy Research, 28,(12) 1065-1074.

Zhao, X.L., Yao, Q., and Li, S.Q., (2006). Effects of draft tubes on particle velocity profiles in spouted beds. Chemical Engineering & Technology, 29,(7) 875-881.

Zhu, C., Liu, G.L., Wang, X., and Fan, L.S., (2002). A parametric model for evaporating liquid jets in dilute gas-solid flows. International Journal of Multiphase Flow, 28,(9) 1479-1495.

Zhu, C., Wang, X.H., and Fan, L.S., (2000). Effect of solids concentration on evaporative liquid jets in gas-solid flows. Powder Technology, 111,(1-2) 79-82.

Zimmermann, S., and Taghipour, F., (2005). CFD modeling of the hydrodynamics and reaction kinetics of FCC fluidized-bed reactors. Industrial & Engineering Chemistry Research, 44,(26) 9818-9827.

Appendix A. MODELLING OF LIQUID-SOLID INTERACTION

To start the derivation by considering the collision between two rigid, non-rotating spherical particles as shown in Figure A-1, we can calculate the momentum exchange during the collision by

$$\delta\vec{M}_c = \frac{(1+e_{lp})m_l m_p \left|\vec{U}_r \cdot \vec{k}\right|}{m_l + m_p}\vec{k} \tag{A.1}$$

Here $\vec{k}$ is the unit vector directed from the centre of the first particle to the second one, $\vec{n}$ is the unit vector of relative velocity $\vec{U}_r$ and e_{lp} is the restitution coefficient between these two particles, m_l and m_p are the masses of two particles respectively.

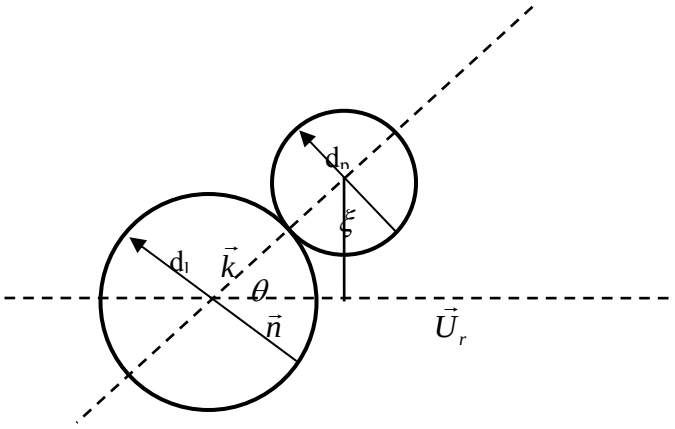

Figure A-1. Schematic of the collision between two particles

Assuming that particles slide during a collision, the momentum change due to friction can be obtained according to Coulomb's law of friction

$$\delta\vec{M}_f = C_{f,lp}\frac{(1+e_{lp})m_l m_p \left|\vec{U}_r \cdot \vec{k}\right|}{m_l + m_p}\vec{t} \tag{A.2}$$

Here $\vec{t}$ is the unit vector normal to $\vec{k}$, and $C_{f,lp}$ is the coefficient of friction between the colliding particles.

The total rate of momentum exchange can be calculated with the consideration of axial symmetry of the volume

$$\Delta\vec{M} = \vec{n}\int_0^{\frac{d_l+d_p}{2}} \frac{(1+e_{lp})m_l m_p \left|\vec{U}_r \cdot \vec{k}\right|}{m_l + m_p}\left[\left(\vec{k}\cdot\vec{n}\right) + C_{f,lp}\left(\vec{t}\cdot\vec{n}\right)\right] 2\pi\xi n_l n_p \left|\vec{U}_r\right| d\xi \qquad \text{(A.3)}$$

To perform this integration, the angle θ between $\vec{k}$ and $\vec{n}$ is introduced. Simply, we have

$$\vec{k}\cdot\vec{n} = \cos\theta \qquad \text{(A.4)}$$

and

$$\sin\theta = \frac{2\xi}{d_l + d_p} \qquad \text{(A.5)}$$

Finally, we get

$$\Delta\vec{M} = \vec{n}\frac{2\pi(1+e_{lp})m_l m_p n_l n_p \left|\vec{U}_r\right|^2}{m_l + m_p}\frac{(d_l + d_p)^2}{16}\left(1 + C_{f,lp}\frac{\pi}{4}\right) \qquad \text{(A.6)}$$

Substitute the expressions for number densities and weight of the particles, the total momentum exchange rate is

$$\Delta\vec{M} = \frac{3(1+e_{lp})\left(\frac{\pi}{2} + C_{f,lp}\frac{\pi^2}{8}\right)\rho_l\rho_p\alpha_l\alpha_p(d_l + d_p)^2\left|\vec{U}_r\right|^2}{2\pi\left(\rho_l d_l^3 + \rho_p d_p^3\right)}\vec{n} \qquad \text{(A.7)}$$

This expression is consistent with the available particle-particle drag correlations for the dilute regime (Gidaspow et al., 1986; Syamlal, 1987).

In the above derivation of the momentum exchange between two particles, the restitution coefficient is assumed to be a constant, only dependant on the material properties of the particles. However, it is no longer valid in the collision between a particle and a droplet. The dependency of the restitution coefficient on the Weber number has been reported in many experiments of a droplet impinging on a hot surface (Hatta et al., 1995; Karl and Frohn, 2000). In other words, the

restitution coefficient is dependent on the droplet velocity. Inherently, the restitution coefficient between a droplet and a hot particle could be even more complicated. It is expected that we have

$$e_{lp} = \tilde{F}(We) \tag{A.8}$$

where the Weber number We is defined as

$$We = \frac{\rho_l u_r^2 d_l}{\sigma} \tag{A.9}$$

σ is surface tension of droplet and $u_r = U_r \cos\theta$. Equation (A.8) can be further written into

$$e_{lp} = F(\vec{U}_r \cdot \vec{k}) = F(U_r \cos\theta) \tag{A.10}$$

For normal collision, we have

$$e_{lp,0} = F(U_r) \tag{A.11}$$

It has been reported that the restitution coefficient decreased with an increasing Weber number in experiments for a droplet impinging on a hot surface (Hatta et al., 1995; Karl and Frohn, 2000). Consequently, we expect

$$e_{lp} \geq e_{lp,0} \tag{A.12}$$

With the free-slip boundary on the particle surface formed by the vapour layer in mind, the friction between the droplet and particle is neglected. Then, the projection of momentum change δM on $\vec{n}$ becomes

$$\delta M_n = \frac{(1+e_{lp}) m_l m_p \left|\vec{U}_r \cdot \vec{k}\right|}{m_l + m_p} \vec{k} \cdot \vec{n} \tag{A.13}$$

Equation (A.13) can be non-dimensionalized with the momentum change of the normal collision as

$$\frac{\delta M_n}{\delta M_{n,0}} = \frac{(1+e_{lp})\cos^2\theta}{1+e_{lp,0}} \tag{A.14}$$

where $\delta M_{n,0}$ is the momentum exchange for the normal collision. By assuming $e_{lp} = e_{lp,0}$, equation (A.14) can be simplified and plotted in Figure A-2. The simulated momentum changes during the collisions between a 1.2 mm droplet and a 1.2 mm hot particle by Ge and Fan (2006) are also plotted in Figure A-2. It is obvious that the momentum exchange during oblique collisions is much lower than the prediction by equation (A.14) with the scenario of a constant restitution coefficient $e_{lp} = e_{lp,0}$.

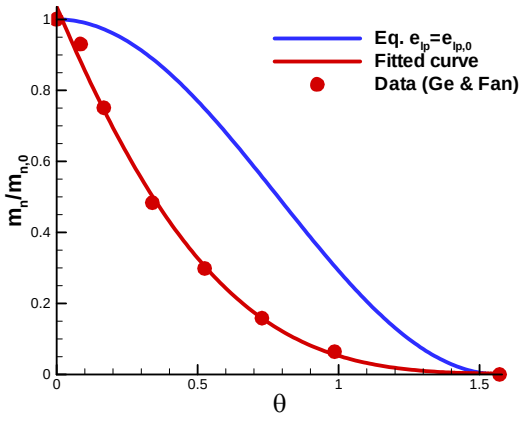

Figure A-2. Non-dimensional momentum changes during oblique collisions of a droplet and a particle

In our analysis, it is assumed that the collision takes place in an infinitely short time. However, in both experimental observations and numerical simulations, the collision usually takes a few milliseconds. During the period of oblique collision, a significant displacement of the droplet from its initial collision position on the particle was observed in Ge and Fan's simulation and this displacement was more evident for the collision with a large obliquity (Ge and Fan, 2007). It is schematically shown in Figure A-3, where Δl is the displacement. This phenomenon prohibits the momentum exchange during the collision and is responsible for the difference between the analytical solution and numerical simulation presented in Figure A-2.

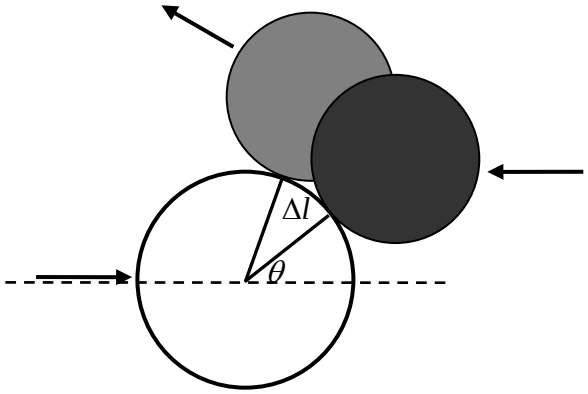

Figure A-3. Displacement of the droplet from its initial collision position during oblique collision (black circle: droplet upon contact; gray circle: droplet upon departure)

Roughly, the displacement Δl of the droplet from its initial collision position on the particle can be estimated by

$$\Delta l = \tau \left| \vec{U}_r \cdot \vec{t} \right| \tag{A.15}$$

where τ is the contact time, which can be estimated by the first order vibration period of the droplet

$$\tau = \pi r_l \sqrt{\frac{\rho_l r_l}{\sigma}} \tag{A.16}$$

where r_l is the droplet radius, and σ is the surface tension. Hence, a displacement in angle $\Delta\theta$ can be defined as

$$\Delta\theta = \frac{\Delta l}{r_p} \tag{A.17}$$

which can be used to characterize the deviation of the droplet-particle collision from the rigid particle-particle collision. From equation (A.17), it can be seen that the displacement is more significant for the collision between a big droplet and a small particle than the collision between a small droplet and a big particle.

To take into account the aforementioned phenomenon, as well as the variable restitution coefficient state as equation (A.8) with a lumped coefficient ζ, the momentum exchange during collision between a particle and a droplet can be written as

$$\delta\vec{M}_c = \zeta \frac{(1+e_{lp,0})m_l m_p \left|\vec{U}_r \cdot \vec{k}\right|}{m_l + m_p}\vec{k} \tag{A.18}$$

Similar to equation (A.3), the following expression is obtained after integration, which models the total momentum exchange rate.

$$\Delta\vec{M} = \varphi\frac{3}{4}\frac{(1+e_{lp,0})\rho_l\rho_p\alpha_l\alpha_p(d_l+d_p)^2\left|\vec{U}_r\right|^2}{\rho_l d_l^3 + \rho_p d_p^3}\vec{n} \tag{A.19}$$

Here φ is introduced as a correction factor resulting from the integration of ζ. For the collision between a 1.2 mm droplet and a 1.2 mm particle, the calculated value of φ is 0.4 based on Ge and Fan's data (Ge and Fan, 2006). To determine other values of φ, carefully designed experiments or numerical simulation is needed.